

UNIVERSITÀ DEGLI STUDI DI PISA  
SCUOLA DI DOTTORATO IN SCIENZE DI BASE “GALILEO GALILEI”  
DOTTORATO IN MATEMATICA - XXV CICLO



Ph.D. Thesis

**Finite volume central schemes for a two-phase  
compressible model with application to gas-liquid  
Riemann problems and magma ascent dynamics**

GIUSEPPE LA SPINA

Advisor:  
Dr. Mattia de' Michieli Vitturi

DIRETTORE DELLA SCUOLA DI DOTTORATO: Prof. Fabrizio Broglia  
SETTORE SCIENTIFICO-DISCIPLINARE: MAT/08 Analisi Numerica

---

ACADEMIC YEAR 2014



---

## ABSTRACT

---

In this thesis a multidimensional compressible two-phase flow model with two pressures, two velocities and a single temperature is studied. The system of partial differential equations, derived using the theory of thermodynamically compatible systems, is written in conservative form and the hyperbolicity of the system is shown. Furthermore, for a more complete analysis, the characteristic polynomial is computed. The single temperature model is also compared with the classical Baer–Nunziato model, showing that, although they can be written in similar way, they present important differences.

In order to solve the governing equations, several numerical schemes for the discretization in space, based on the finite volume methods, are considered. Several numerical fluxes, the Lax–Friedrichs, the Generalized FORCE, the Kurganov and Tadmor, the Kurganov, Noelle and Petrova and finally a modification of the Lax–Friedrichs numerical fluxes are introduced. For the discretization in time, two approaches for solving the system of partial differential equations, the splitting and the Runge–Kutta approach, are presented. All the numerical schemes are implemented using the open source CFD (Computational Fluid Dynamics) toolbox “OpenFOAM”(Open source Field Operation And Manipulation, developed by OpenCFD Ltd).

After the definition of the physical model and of the numerical methods, the robustness, the correctness and the accuracy of the proposed schemes are investigated performing several monodimensional and multidimensional well-known numerical tests in presence of rarefaction and shock waves. Two shock–bubble interaction experiments have been reproduced numerically, comparing the results with laboratory observations. The results show a really good agreement between the simulation and the laboratory experiments. The physical model appears to be accurate and the numerical methods robust, being able to properly resolve detailed flow features as shock-wave refractions, reflections and diffractions.

Finally, an application of the single temperature model to the volcanological field is presented, proposing a new model for the initial stages of magma ascent in a conduit during explosive eruptions. The magma ascent model is derived from the single temperature model adding a new transport equation for the gas dissolved in the liquid phase and showing through the calculation of the characteristic polynomial that the new equation does not alter the hyperbolicity of the system. Using one of the numerical schemes proposed, the initial phases of an explosive eruption at Soufrière Hills Volcano are simulated, focusing the attention on the effect of disequilibrium processes.

To conclude, in the appendix, the derivation of the single temperature model using the thermodynamically compatible systems is presented and some details regarding the implementation of the numerical schemes proposed in this thesis using the OpenFOAM framework are given.



---

## CONTENTS

---

<b>ABSTRACT</b>	iii
<b>1 INTRODUCTION</b>	1
<b>2 SINGLE TEMPERATURE TWO-PHASE FLOW MODEL</b>	5
<b>2.1 Governing equations</b>	7
<b>2.1.1 Entropy balance</b>	9
<b>2.2 Characteristic analysis</b>	13
<b>2.2.1 Primitive variable formulation</b>	14
<b>2.2.2 Derivatives analysis</b>	20
<b>2.2.3 Eigenvalues numerical estimation</b>	21
<b>2.2.4 Simplified models</b>	22
<b>2.3 Equation of state</b>	23
<b>2.4 Comparison of models</b>	25
<b>3 NUMERICAL SCHEMES</b>	27
<b>3.1 Splitting approach</b>	28
<b>3.1.1 Numerical methods for homogeneous systems of conservation laws</b>	29
<b>3.1.1.1 Lax-Friedrichs numerical fluxes</b>	31
<b>3.1.1.2 GForce numerical fluxes</b>	31
<b>3.1.1.3 Kurganov, Noelle, Petrova numerical fluxes</b>	32
<b>3.1.1.4 Kurganov and Tadmor numerical fluxes</b>	35
<b>3.1.1.5 Modification of the Lax-Friedrichs numerical fluxes</b>	35
<b>3.1.2 Integration of the source terms</b>	36
<b>3.1.2.1 Velocity Relaxation</b>	36
<b>3.1.2.2 Pressure Relaxation</b>	37
<b>3.1.2.3 Phase exchange</b>	39
<b>3.1.2.4 Gravitational force</b>	41
<b>3.2 Runge-Kutta approach</b>	41
<b>3.2.1 Computation of the solution using IMEX DIRK schemes</b>	45
<b>3.2.2 Derivative approximation through complex numbers</b>	45
<b>4 NUMERICAL TESTS</b>	49
<b>4.1 Linear reconstruction</b>	49
<b>4.2 One dimensional four rarefaction problem</b>	50
<b>4.3 One dimensional four shock problem</b>	60
<b>4.4 One dimensional air-water shock problem</b>	69
<b>4.5 One dimensional sonic point test problem</b>	78
<b>4.6 One dimensional cavitation tube problem</b>	86
<b>4.7 Conclusions</b>	95
<b>5 MULTIDIMENSIONAL APPLICATIONS</b>	97
<b>5.1 Air-Water Explosion problem 2D</b>	98
<b>5.2 Shock-Bubble interaction problem 2D</b>	102
<b>5.2.1 R22 bubble</b>	102
<b>5.2.2 Helium bubble</b>	105
<b>5.3 Conclusions</b>	107

<b>6 VOLCANOLOGICAL APPLICATION</b>	<b>109</b>
<b>6.1 Conduit model</b>	<b>110</b>
6.1.1 Characteristic analysis	114
<b>6.2 Constitutive equations</b>	<b>115</b>
6.2.1 Volatiles and solubility	115
6.2.2 Magma Rheology	116
6.2.3 Magma fragmentation	117
6.2.4 Pressure relaxation	118
6.2.5 Relative velocity	119
<b>6.3 Numerical Tests</b>	<b>120</b>
6.3.1 Explosive Eruptions at Soufrière Hills Volcano	121
6.3.1.1 Instantaneous pressure and velocity relaxations	123
6.3.1.2 Finite rate pressure and velocity relaxations	130
6.3.2 Conclusions	136
<b>7 CONCLUSIONS</b>	<b>139</b>
<b>A THERMODYNAMICALLY COMPATIBLE SYSTEMS</b>	<b>143</b>
<b>B OPENFOAM IMPLEMENTATION</b>	<b>147</b>
<b>B.1 Pre-requisites</b>	<b>148</b>
<b>B.2 Solvers overview</b>	<b>152</b>
B.2.1 Splitting approach solver: <i>twoPhaseCentralFoam</i>	152
B.2.2 Runge-Kutta approach solver: <i>twoPhaseCentralFoamDIRK</i>	160
<b>BIBLIOGRAPHY</b>	<b>163</b>

---

## LIST OF FIGURES

---

Figure 1	Schematic illustration of the linear reconstruction obtained using minmod limiter. . . . .	30
Figure 2	Schematic illustration of the fully discrete scheme of Kurganov, Noelle and Petrova. . . . .	32
Figure 3	Normalized relative error of the derivative approximations with respect the exact value. . . . .	48
Figure 4	Four Rarefaction - Reference solutions . . . . .	51
Figure 5	Four Rarefaction - Comparison between the reference solution for the mixture density, and the solutions computed using the splitting approach with LF, LMod, GF, KT and KNP numerical fluxes	52
Figure 6	Four Rarefaction - Comparison between the reference solution for the mixture density, and the solutions computed using the DIRK schemes IEE, ARS, LRR and BPR, all in conjunction with the LF numerical fluxes. . . . .	52
Figure 7	Four Rarefaction - Comparison between the reference solution for the mixture density, and the solutions computed using the DIRK schemes IEE, ARS, LRR and BPR, all in conjunction with the LMod numerical fluxes. . . . .	53
Figure 8	Four Rarefaction - Comparison between the reference solution for the mixture density, and the solutions computed using the DIRK schemes IEE, ARS, LRR and BPR, all in conjunction with the GF numerical fluxes. . . . .	53
Figure 9	Four Rarefaction - Comparison between the reference solution for the mixture density, and the solutions computed using the DIRK schemes IEE, ARS, LRR and BPR, all in conjunction with the KT numerical fluxes. . . . .	53
Figure 10	Four Rarefaction - Comparison between the reference solution for the mixture density, and the solutions computed using the DIRK schemes IEE, ARS, LRR and BPR, all in conjunction with the KNP numerical fluxes. . . . .	54
Figure 11	Four Rarefaction - Comparison between the reference solution for the mixture density, and the solutions computed using the DIRK IEE scheme in conjunction with LF, LMod, GF, KT and KNP numerical fluxes. . . . .	54
Figure 12	Four Rarefaction - Comparison between the reference solution for the mixture density and the solutions obtained using different number of cells for the domain discretization: 250, 500, 1000 and 2000 cells. . . . .	54
Figure 13	Four Shock - Reference solutions. . . . .	61

Figure 14	Four Shock - Comparison between the reference solution for the mixture density, and the solutions computed using the splitting approach with LF, LMod, GF, KT and KNP numerical fluxes. . . . .	62
Figure 15	Four Shock - Comparison between the reference solution for the mixture density, and the solutions computed using the DIRK schemes IEE and BPR, all in conjunction with the LF numerical fluxes. . . . .	62
Figure 16	Four Shock - Comparison between the reference solution for the mixture density, and the solutions computed using the DIRK schemes IEE, ARS, LRR and BPR, all in conjunction with the LMod numerical fluxes. . . . .	62
Figure 17	Four Shock - Comparison between the reference solution for the mixture density, and the solutions computed using the DIRK schemes IEE, ARS, LRR and BPR, all in conjunction with the GF numerical fluxes. . . . .	63
Figure 18	Four Shock - Comparison between the reference solution for the mixture density, and the solutions computed using the DIRK schemes IEE, ARS, LRR and BPR, all in conjunction with the KT numerical fluxes. . . . .	63
Figure 19	Four Shock - Comparison between the reference solution for the mixture density, and the solutions computed using the DIRK schemes IEE, ARS, LRR and BPR, all in conjunction with the KNP numerical fluxes. . . . .	63
Figure 20	Four Shock - Comparison between the reference solution for the mixture density, and the solutions computed using the DIRK BPR scheme in conjunction with LF, LMod, GF, KT and KNP numerical fluxes. . . . .	64
Figure 21	Four Shock - Comparison between the reference solution for the mixture density and the solutions obtained using different number of cells for the domain discretization: 250, 500, 1000 and 2000 cells. . . . .	64
Figure 22	Air-Water Shock - Reference solutions. . . . .	70
Figure 23	Air-Water Shock - Comparison between the reference solution for the mixture density, and the solutions computed using the splitting approach with LF, LMod, GF, KT and KNP numerical fluxes. . . . .	71
Figure 24	Air-Water Shock - Comparison between the reference solution for the mixture density, and the solutions computed using the splitting approach and the interfaces relaxations with LF, LMod, GF, KT and KNP numerical fluxes. . . . .	71
Figure 25	Air-Water Shock - Comparison between the reference solution for the mixture density, and the solutions computed using the DIRK schemes IEE, ARS, LRR and BPR, all in conjunction with the LMod numerical fluxes. . . . .	71
Figure 26	Air-Water Shock - Comparison between the reference solution for the mixture density, and the solutions computed using the DIRK schemes IEE, ARS, LRR and BPR, all in conjunction with the GF numerical fluxes. . . . .	72

Figure 27	Air-Water Shock - Comparison between the reference solution for the mixture density, and the solutions computed using the DIRK schemes IEE, ARS, LRR and BPR, all in conjunction with the KT numerical fluxes. . . . .	72
Figure 28	Air-Water Shock - Comparison between the reference solution for the mixture density, and the solutions computed using the DIRK schemes IEE, ARS, LRR and BPR, all in conjunction with the KNP numerical fluxes. . . . .	72
Figure 29	Air-Water Shock - Comparison between the reference solution for the mixture density, and the solutions computed using the DIRK ARS scheme in conjunction with LMod, GF, KT, and KNP numerical fluxes. . . . .	73
Figure 30	Air-Water Shock - Comparison between the reference solution for the mixture density and the solutions obtained using different number of cells for the domain discretization: 250, 500, 1000 and 2000 cells. . . . .	73
Figure 31	Sonic Point - Reference solutions. . . . .	79
Figure 32	Sonic Point - Comparison between the reference solution for the mixture density, and the solutions computed using the splitting approach and the predictor/corrector strategy with LF, LMod, GF, KT and KNP numerical fluxes. . . . .	80
Figure 33	Sonic Point - Comparison between the reference solution for the mixture density, and the solutions computed using the DIRK schemes IEE, ARS, LRR and BPR, all in conjunction with the LMod numerical fluxes. . . . .	80
Figure 34	Sonic Point - Comparison between the reference solution for the mixture density, and the solutions computed using the DIRK schemes IEE, ARS, LRR and BPR, all in conjunction with the GF numerical fluxes. . . . .	80
Figure 35	Sonic Point - Comparison between the reference solution for the mixture density, and the solutions computed using the DIRK schemes IEE, ARS, LRR and BPR, all in conjunction with the KT numerical fluxes. . . . .	81
Figure 36	Sonic Point - Comparison between the reference solution for the mixture density, and the solutions computed using the DIRK schemes IEE, ARS, LRR and BPR, all in conjunction with the KNP numerical fluxes. . . . .	81
Figure 37	Sonic Point - Comparison between the reference solution for the mixture density, and the solutions computed using the DIRK LRR scheme in conjunction with LMod, GF, KT and KNP numerical fluxes. . . . .	81
Figure 38	Sonic Point - Comparison between the reference solution for the mixture density and the solutions obtained using different number of cells for the domain discretization: 250, 500, 1000 and 2000 cells. . . . .	82
Figure 39	Cavitation Tube - Reference solutions. . . . .	88

Figure 40	Cavitation Tube - Comparison between the reference solution for the mixture density, and the solutions computed using the splitting approach and the predictor/corrector strategy with LF, LF-Mod, GF, KT and KNP numerical fluxes. . . . .	89
Figure 41	Cavitation Tube - Comparison between the reference solution for the mixture density, and the solutions computed using the DIRK schemes IEE, ARS, LRR and BPR, all in conjunction with the LF-Mod numerical fluxes. . . . .	89
Figure 42	Cavitation Tube - Comparison between the reference solution for the mixture density, and the solutions computed using the DIRK schemes IEE, ARS, LRR and BPR, all in conjunction with the GF numerical fluxes. . . . .	89
Figure 43	Cavitation Tube - Comparison between the reference solution for the mixture density, and the solutions computed using the DIRK schemes IEE, ARS, LRR and BPR, all in conjunction with the KT numerical fluxes. . . . .	90
Figure 44	Cavitation Tube - Comparison between the reference solution for the mixture density, and the solutions computed using the DIRK schemes IEE, ARS, LRR and BPR, all in conjunction with the KNP numerical fluxes. . . . .	90
Figure 45	Cavitation Tube - Comparison between the reference solution for the mixture density, and the solutions computed using the DIRK BPR scheme in conjunction with LFMod, GF, KT and KNP numerical fluxes. . . . .	90
Figure 46	Cavitation Tube - Comparison between the reference solution for the mixture density and the solutions obtained using different number of cells for the domain discretization: 1000, 2000, 4000 and 8000 cells. . . . .	91
Figure 47	Air-Water Explosion: Emulated Schlieren images generated from the numerical results plotting $ \nabla \rho $ in a nonlinear graymap at different times. . . . .	99
Figure 48	Air-Water Explosion: Emulated Schlieren image generated from the numerical results plotting $ \nabla \rho $ in a nonlinear graymap at time $2.5 \times 10^{-4}$ s. . . . .	100
Figure 49	Air-Water Explosion: Comparison between the reference solution for the mixture density obtained from the monodimensional test Air-Water Shock problem and those obtained from this test considering a grid of $2000 \times 2000$ cells and extracting the data in the domain $(x, y) \in (0, 1) \times \{0\}$ . . . . .	101
Figure 50	Schematic illustration of the domain and of the initial conditions used for the Shock-Bubble interaction problem. . . . .	102
Figure 51	R22 bubble - Part 1: comparison between the numerical results (left panels) and laboratory experiments (right panels). . . . .	104
Figure 52	R22 bubble - Part 2: comparison between the numerical results (left panels) and laboratory experiments (right panels). . . . .	105
Figure 53	Helium bubble - Part 1: comparison between the numerical results (left panels) and laboratory experiments (right panels). . . . .	107

Figure 54	Helium bubble - Part 2: comparison between the numerical results (left panels) and laboratory experiments (right panels). . . . .	108
Figure 55	Schematic illustration of the conduit in the first stages of an eruption. . . . .	111
Figure 56	Initial profiles of pressure and bubbles volume fraction for the simulated eruption of Soufrière Hills Volcano. . . . .	122
Figure 57	Profiles of pressure, volume fraction of bubbles, velocity, fragmentation efficiency, temperature and mixture density at different times assuming a single pressure and velocity and no mass transfer. . . . .	124
Figure 58	Fragmentation level and discharge rate at the top and at the bottom of the conduit and its maximum value as function of time assuming a single pressure and velocity and no mass transfer. . . . .	125
Figure 59	Profiles of pressure, volume fraction of bubbles, velocity, fragmentation efficiency, temperature and mixture density at different times assuming a single pressure and velocity and equilibrium mass transfer. . . . .	126
Figure 60	Fragmentation level and discharge rate at the top and at the bottom of the conduit and its maximum value as function of time assuming a single pressure and velocity and equilibrium mass transfer. . . . .	127
Figure 61	Profiles of dissolved water content $x_d$ and the equilibrium value $x_d^{eq}$ at $t = 1000$ s assuming a single pressure and velocity and a finite rate exsolution. . . . .	127
Figure 62	Profiles of pressure, volume fraction of bubbles, velocity, fragmentation efficiency, temperature and mixture density at different times assuming a single pressure and velocity and a disequilibrium mass transfer. . . . .	128
Figure 63	Fragmentation level and discharge rate at the top and at the bottom of the conduit and its maximum value as function of time assuming a single pressure and velocity and a disequilibrium mass transfer. . . . .	129
Figure 64	Profiles of mixture pressure, pressure difference between gas and melt phase, volume fraction of the bubbles, fragmentation efficiency, melt and gas velocity, temperature and mixture density at different times (up to 200 s) assuming the disequilibrium of pressures and velocities and no mass transfer. . . . .	131
Figure 65	Fragmentation level and discharge rate at the top and at the bottom of the conduit and its maximum value as function of time assuming the disequilibrium of pressures and velocities and no mass transfer. . . . .	132
Figure 66	Profiles of mixture pressure, pressure difference between gas and melt phase, volume fraction of the bubbles, fragmentation efficiency, melt and gas velocity, temperature and mixture density at different times assuming the disequilibrium of pressures and velocities and equilibrium mass transfer. . . . .	133

Figure 67	Fragmentation level and discharge rate at the top and at the bottom of the conduit and its maximum value as function of time assuming the disequilibrium of pressures and velocities and equilibrium mass transfer. . . . .	134
Figure 68	Profiles of mixture pressure, pressure difference between gas and melt phase, volume fraction of the bubbles, fragmentation efficiency, melt and gas velocity, temperature and mixture density at different times assuming the disequilibrium of pressures, velocities and mass transfer. . . . .	135
Figure 69	Fragmentation level and discharge rate at the top and at the bottom of the conduit and its maximum value as function of time assuming the disequilibrium of pressures, of velocities and of mass transfer. . . . .	136
Figure 70	Laser Induced Cavitation Problem: Preliminary results presented at ICNAAM 2013 (de' Michieli Vitturi et al., 2013b) . . . . .	140
Figure 71	Photographies of a laboratory experiment of a shock-tube filled with gas and particles performed at the School of Earth and Exploration of the Arizona State University. . . . .	141
Figure 72	Schematic representation of two adjacent cells. . . . .	149
Figure 73	Schematic representation of a two-dimensional grid with uniform step-size. . . . .	154

---

## LIST OF TABLES

---

Table 1	Tableau Implicit-Explicit Euler IEE(1,1,1) . . . . .	44
Table 2	Tableau Asher, Ruuth, Spiteri ARS(2,2,2) . . . . .	44
Table 3	Tableau Liotta, Romano, Russo LRR(3,2,2) . . . . .	44
Table 4	Tableau Boscarino, Pareschi, Russo BPR(5,3,3) . . . . .	44
Table 5	Parameters of the equation of state for water and air. . . . .	50
Table 6	Four Rarefaction - Relative errors between the reference mixture density and those computed using the splitting approach. . . . .	56
Table 7	Four Rarefaction - Relative errors between the reference mixture density and those computed using the DIRK IEE scheme. . . . .	56
Table 8	Four Rarefaction - Relative errors between the reference mixture density and those computed using the DIRK ARS scheme. . . . .	56
Table 9	Four Rarefaction - Relative errors between the reference mixture density and those computed using the DIRK LRR scheme. . . . .	57
Table 10	Four Rarefaction - Relative errors between the reference mixture density and those computed using the DIRK BPR scheme. . . . .	57
Table 11	Four Rarefaction - Convergence rates for the mixture density computed with different domain discretization using the splitting approach. . . . .	57
Table 12	Four Rarefaction - Convergence rates for the mixture density computed with different domain discretization using the DIRK IEE scheme. . . . .	58
Table 13	Four Rarefaction - Convergence rates for the mixture density computed with different domain discretization using the DIRK ARS scheme. . . . .	58
Table 14	Four Rarefaction - Convergence rates for the mixture density computed with different domain discretization using the DIRK LRR scheme. . . . .	58
Table 15	Four Rarefaction - Convergence rates for the mixture density computed with different domain discretization using the DIRK BPR scheme. . . . .	59
Table 16	Four Shock - Relative errors between the reference mixture density and those computed using the splitting approach. . . . .	65
Table 17	Four Shock - Relative errors between the reference mixture density and those computed using the DIRK IEE scheme. . . . .	66
Table 18	Four Shock - Relative errors between the reference mixture density and those computed using the DIRK ARS scheme. . . . .	66
Table 19	Four Shock - Relative errors between the reference mixture density and those computed using the DIRK LRR scheme. . . . .	66
Table 20	Four Rarefaction - Relative errors between the reference mixture density and those computed using the DIRK BPR scheme . . . . .	67

Table 21	Four Shock - Convergence rates for the mixture density computed with different domain discretization using the splitting approach. . . . .	67
Table 22	Four Shock - Convergence rates for the mixture density computed with different domain discretization using the DIRK IEE scheme. . . . .	67
Table 23	Four Shock - Convergence rates for the mixture density computed with different domain discretization using the DIRK ARS scheme. . . . .	68
Table 24	Four Shock - Convergence rates for the mixture density computed with different domain discretization using the DIRK LRR scheme. . . . .	68
Table 25	Four Shock - Convergence rates for the mixture density computed with different domain discretization using the DIRK BPR scheme. . . . .	68
Table 26	Air-Water Shock - Relative errors between the reference mixture density and those computed using the splitting approach. . . . .	74
Table 27	Air-Water Shock - Relative errors between the reference mixture density and those computed using the DIRK IEE scheme. . . . .	75
Table 28	Air-Water Shock - Relative errors between the reference mixture density and those computed using the DIRK ARS scheme. . . . .	75
Table 29	Air-Water Shock - Relative errors between the reference mixture density and those computed using the DIRK LRR scheme. . . . .	75
Table 30	Air-Water Shock - Relative errors between the reference mixture density and those computed using the DIRK BPR scheme. . . . .	76
Table 31	Air-Water Shock - Convergence rates for the mixture density computed with different domain discretization using the splitting approach. . . . .	76
Table 32	Air-Water Shock - Convergence rates for the mixture density computed with different domain discretization using the DIRK IEE scheme. . . . .	77
Table 33	Air-Water Shock - Convergence rates for the mixture density computed with different domain discretization using the DIRK ARS scheme. . . . .	77
Table 34	Air-Water Shock - Convergence rates for the mixture density computed with different domain discretization using the DIRK LRR scheme. . . . .	77
Table 35	Air-Water Shock - Convergence rates for the mixture density computed with different domain discretization using the DIRK BPR scheme. . . . .	78
Table 36	Sonic Point - Relative errors between the reference mixture density and those computed using the splitting approach. . . . .	83
Table 37	Sonic Point - Relative errors between the reference mixture density and those computed using the DIRK IEE scheme. . . . .	83
Table 38	Sonic Point - Relative errors between the reference mixture density and those computed using the DIRK ARS scheme. . . . .	83
Table 39	Sonic Point - Relative errors between the reference mixture density and those computed using the DIRK LRR scheme. . . . .	84
Table 40	Sonic Point - Relative errors between the reference mixture density and those computed using the DIRK BPR scheme. . . . .	84
Table 41	Sonic Point - Convergence rates for the mixture density computed with different domain discretization using the splitting approach. . . . .	84

Table 42	Sonic Point - Convergence rates for the mixture density computed with different domain discretization using the DIRK IEE scheme. . . . .	85
Table 43	Sonic Point - Convergence rates for the mixture density computed with different domain discretization using the DIRK ARS scheme. . . . .	85
Table 44	Sonic Point - Convergence rates for the mixture density computed with different domain discretization using the DIRK LRR scheme. . . . .	85
Table 45	Sonic Point - Convergence rates for the mixture density computed with different domain discretization using the DIRK BPR scheme. . . . .	86
Table 46	Parameters of the equation of state for water and water vapor. . . . .	87
Table 47	Cavitation Tube - Relative errors between the reference mixture density and those computed using the splitting approach . . . . .	91
Table 48	Cavitation Tube - Relative errors between the reference mixture density and those computed using the DIRK IEE scheme. . . . .	92
Table 49	Cavitation Tube - Relative errors between the reference mixture density and those computed using the DIRK ARS scheme. . . . .	92
Table 50	Cavitation Tube - Relative errors between the reference mixture density and those computed using the DIRK LRR scheme. . . . .	92
Table 51	Cavitation Tube - Relative errors between the reference mixture density and those computed using the DIRK BPR scheme. . . . .	93
Table 52	Cavitation Tube - Convergence rates for the mixture density computed with different domain discretization using the splitting approach. . . . .	93
Table 53	Cavitation Tube - Convergence rates for the mixture density computed with different domain discretization using the DIRK IEE scheme. . . . .	93
Table 54	Cavitation Tube - Convergence rates for the mixture density computed with different domain discretization using the DIRK ARS scheme. . . . .	94
Table 55	Cavitation Tube - Convergence rates for the mixture density computed with different domain discretization using the DIRK LRR scheme. . . . .	94
Table 56	Cavitation Tube - Convergence rates for the mixture density computed with different domain discretization using the DIRK BPR scheme. . . . .	94
Table 57	Parameters of the equation of state for R22, He and air. . . . .	102
Table 58	Parameters of the conduit model used for the simulated eruption of Soufrière Hills Volcano. . . . .	121
Table 59	Parameters of the equation of state for melt and gas. . . . .	122
Table 60	Syntax of some mathematical operations in OpenFOAM . . . . .	148
Table 61	Syntax for some differential operators in OpenFOAM. . . . .	150



---

## INTRODUCTION

---

Fluid dynamics is a branch of physics that study the motion of the fluids. It has several subdisciplines, including aerodynamics (the study of air and other gases in motion) and hydrodynamics (the study of liquids in motion). Fluid dynamics has a wide range of applications, including calculating forces and moments on aircraft, determining the mass flow rate of oil through pipelines, predicting weather patterns, understanding nebulae in interstellar space and reportedly modeling fission weapon detonation. Some of its principles are even used in traffic engineering, where traffic is treated as a continuous fluid.

Depending on how many different phases form the fluid, we can distinguish two main categories of problems: single-phase or multiphase flows. In particular, in this thesis, the attention is focused on the study of two-phase compressible fluids and on their application to the volcanological field, describing the ascent of magma in volcanic conduits. Even considering a fluid with only two distinct phases, there is a wide range of different flows. In fact, the two-phase flows can be divided into three main branches (Ishii, 1975): gas-liquid flows (bubbly flows, separated flows, gas-droplet flows), gas-solid flows (gas-particle flows, fluidized beds), liquid-solid flows (slurry flows, sediment transport). These categories of two-phase flows are very different from each others, but the thing that connects all of them is the presence of an interface that separates the two phases. The correct mathematical and numerical treatment of interfaces is a central problem in the theory of two-phase flows.

The most straightforward approach would be to model the interface between the phases explicitly in the model. With this kind of approach we consider separate regions occupied by one phase only (Hou et al., 1999; Scardovelli and Zaleski, 1999; Tryggvason et al., 2001). Sometimes, instead, the detailed knowledge of the positions of phase interfaces is not necessary, for example in case of dispersed flows with a large number of droplets, bubbles, or particles. The system of governing equations for such models is obtained by volume and time averaging of the single-phase equations, and consists of two continuity, two momentum, and two energy equations for both phases (Baer and Nunziato, 1986; Drew and Passman, 1999; Ishii, 1975; Stewart and Wendroff, 1984). Another possibility is to consider an intermediate approach, in which we assume that, for each volume of fluid considered, there can be both phases at the same time with a proper volume fraction. As in the previous models, the governing equations are based on the averaging theory for each phase, and consist of two continuity, two momentum, and two energy equations and, in addition, one equation for the volume fraction (Andrianov et al., 2003; Saurel and Abgrall, 1999; Saurel and Le Métayer, 2001; Zein et al., 2010).

In recent years a new approach has been developed using the theory of thermodynamically compatible systems (Romenski et al., 2007; Romenski and Toro, 2004). With this approach we do not consider the governing equations for each phase separately, but we solve the continuity, momentum and energy equations for the whole mixture. Furthermore, to determine the internal state of the medium, additional differential equations must be provided (for example balance laws for the volume fraction, for the mass fraction and for the relative velocity).

However, whatever approach is used, the governing equations result in a system of partial differential equations (PDEs) whose solutions exhibit rich and complex structures. Unfortunately, closed analytical expressions for their solutions can be found only in very special circumstances and these are mostly of limited theoretical and practical interest. Thus, it has become a common practice to employ numerical methods to approximate the solutions of the PDEs. The most used numerical methods can be divided in three categories: finite difference, finite volume and finite element methods. In finite difference methods the differential operators of the PDEs are approximated using a truncation of the Taylor series expansion and a pointwise domain discretization. Finite volume methods are based on an integral formulation of the PDEs where the domain is partitioned in discrete “volumes” or cells, assuming that the solution in each cell is approximated by the volume average in the cell. Finally, with finite element methods, the PDEs system is transformed in a variational problem for which the solution is obtained as a combination of a set of piecewise continuous functions.

In this thesis, in particular, only finite volume methods will be considered. In the last three decades finite volume numerical methods for single phase flow have seen the development of high-resolution numerical schemes such as shock-capturing methods (Kurganov et al., 2001; Liu and Tadmor, 1998; Nessyahu and Tadmor, 1990; Roe, 1981; Sod, 1978). Shock-capturing methods are numerical schemes that are able to reproduce the propagation of discontinuities (shock waves) in the solution. These methods are oscillation-free near shock waves and retain high orders of accuracy in smooth parts of the flow. The shock-capturing methods may be classified into two categories: upwind and central shock-capturing schemes. In general with an upwind scheme we attempt to discretize hyperbolic partial differential equations using numerical fluxes based on the direction determined by the sign of the characteristic speeds. The origin of upwind methods can be traced back to the work of Courant, Isaacson, and Rees, in which they proposed the CIR method (Courant et al., 1952). Later Godunov (1959) and afterwards Harten et al. (1983) generalized CIR method, which is a first-order upwind scheme. The Godunov method regards the solution within each cell as a cell average instead of representing the solution in discrete form as pointwise values. Thus one can think of this method as the first conservative finite volume method. This integral average is fundamentally linked with the conservative nature of the scheme which overcomes the disadvantage of traditional non-conservative methods. The interaction between two local constant states constitutes a Riemann problem and its solution can be calculated exactly or approximately for most hyperbolic systems. Then the solution to each local Riemann problem is used to calculate the inter-cell flux, which is used to update the solution to the next time level. The key point for the implementation of an upwind scheme is the knowledge of the complete eigenstructure of the system of PDE.

With the central schemes, instead, hyperbolic partial differential equations are discretized using central differencing. The main advantage of these methods is that they

do not require the knowledge of the complete eigenstructure of the system of PDE, but only the spectral radius (Kurganov and Tadmor, 2000; Nessyahu and Tadmor, 1990) or at most the minimum and maximum eigenvalues (Kurganov et al., 2001). Furthermore, central schemes are much simple to implement with respect to the upwind schemes. However, in order to use central schemes, the hyperbolic partial differential equations have to be written in conservative (divergent) form. There is a significant body of literature regarding central schemes, for example Arminjon et al. (2002); Arminjon and Touma (2005); Bianco et al. (1999); Del Zanna et al. (2002); Kurganov and Petrova (2001); Levy et al. (1999, 2002); Lie and Noelle (2003); Toro (2009) to name just a few.

For a single-phase compressible flow, the governing equations are already written in divergent form, therefore the use of central schemes is straightforward. Things become more complicated when multiphase flow models are considered. Following the models proposed by Baer and Nunziato (1986), the hyperbolic partial differential equations cannot be written in conservative form, thus central schemes cannot be used. For this reason, upwind schemes are widely adopted in multiphase flow modeling (Andrianov et al., 2003; Saurel and Abgrall, 1999; Saurel and Le Métayer, 2001; Tokareva and Toro, 2010; Zein et al., 2010). The presence of non-conservative terms posed a mathematical difficulties when wishing to allow for discontinuous solutions of the two-phase system (Andrianov and Warnecke, 2004; Dal Maso et al., 1995; François and François, 1999; Lefloch and Tzavaras, 1999). In Pelanti and LeVeque (2006); Saito et al. (2003) an assumption of dilute flow is adopted to drop the non-conservative terms of the system.

At the same time, a big effort was made in finding a new multiphase flow model written in conservative form. The turning point there was with the work of Godunov and Romensky (1995), that continued later in the articles of Romensky (1998) and in Romensky (2001), in which the class of thermodynamically compatible systems was presented. Every system belonging to this class is generated from a thermodynamic potential alone and has an additional conservation law as a consequence. Besides, every system can be reduced to a symmetric hyperbolic form and can be written in conservative form. Using the theory of thermodynamically compatible systems it is possible to derive new governing equations for multiphase flow written in divergent form. This approach has reached a grown popularity in the last ten years with a significant increase in the number of publications (La Spina and de' Michieli Vitturi, 2012; Resnyansky, 2003, 2006; Resnyansky et al., 2011; Resnyansky and Bourne, 2004; Romenski et al., 2010, 2007; Romenski and Toro, 2004; Romenski et al., 2003; Zeidan, 2003, 2011; Zeidan et al., 2007; Zeidan and Slaouti, 2009).

In this thesis, a compressible two-phase flow model with two pressures, two velocities and a single temperature derived using the theory of thermodynamically compatible systems is presented. The governing equations for this model form a hyperbolic system of partial differential equations coupled with source terms that include the presence of external forces and interphase exchange terms. Due to the divergent form of the system, high resolution shock-capturing central scheme are adopted to solve the governing equations.

Furthermore, we remark that the conservative form of the equations provided by the adoption of the theory of thermodynamically compatible systems is valid for both dilute or dense regimes without the need of neglecting some terms. For this reason, the two-phase flow model presented in this thesis is also an ideal base for the development of a magma ascent model for explosive eruptions, where very different regimes are present.

The past decade has seen much progress in modeling magma ascent processes during explosive eruptions (Clarke et al., 2002a,b; Dufek and Bergantz, 2005; Koyaguchi and Mitani, 2005; Kozono and Koyaguchi, 2009; Macedonio et al., 2005; Massol and Jaupart, 1999; Massol et al., 2001; Mastin, 2002; Melnik and Sparks, 2002b; Melnik, 2000; Papale, 2001; Proussevitch and Sahagian, 1998; Sahagian, 2005; Woods and Koyaguchi, 1994). In contrast to the modeling of effusive eruptions, where changes in the solutions are more gentle, explosive eruptions require a proper treatment of shock and rarefaction waves to estimate the depth of magma fragmentation. Furthermore, a model for explosive eruptions should be able to properly describe very different regimes: a bubbly flow region where the gas is the dispersed phase with low volume fractions (below the fragmentation level), and a gas-pyroclasts region where the gas is the continuous carrier phase (above the fragmentation level).

The thesis is organized as follows:

- In Chapter 2 the governing equations for a compressible two-phase flow model with a common temperature are introduced. From the governing equations, a balance law for entropy coupled with a non-negative source term is derived. Then the characteristic analysis, through the computation of the characteristic polynomial, is presented. Furthermore, to close the system, some equations of state are provided and finally the presented model is compared with the classical Baer and Nunziato model.
- In Chapter 3 we introduce some high resolution shock-capturing central schemes to solve the governing equations presented before. Two family of schemes, based respectively on the splitting approach and on the Runge-Kutta approach, are presented.
- In Chapter 4 several monodimensional numerical simulations, performed to validate and compare the schemes proposed in this work, are shown. All the schemes are implemented using the open source CFD toolbox OpenFOAM.
- In Chapter 5 some multidimensional tests are reported. Here we reproduce numerically some laboratory experiments, comparing the observed data with the numerical results.
- In Chapter 6 we present a preliminary application of the model and of the numerical schemes to the volcanological world. Furthermore some numerical simulation are reported.
- In Chapter 7 the conclusions are drawn.
- Finally, in the Appendix the derivation of the governing equations using the theory of thermodynamically compatible systems is reported. Furthermore, we give some detail regarding the implementation of the numerical schemes presented in this thesis.

# 2

---

## SINGLE TEMPERATURE TWO-PHASE FLOW MODEL

---

Multiphase flow modeling is one of the most challenging research areas in computational and applied mathematics and intensive efforts have been done in the recent decades in the development of advanced models and numerical methods. Common formulations of mathematical models of multiphase flows are originated in Baer and Nunziato (1986); Ishii (1975) and are based on the averaging theory. The governing equations of such models consist of the balance equations for density, momentum and energy of each phase, and phase interaction is taken into account by the additional algebraic and differential source terms. The model proposed by Baer and Nunziato (1986) and studied by Embid and Baer (1992) stimulated further modifications of the governing equations and the development of new approaches in the modeling of two-phase flows, see for example Guillard and Duval (2007); Pelanti and LeVeque (2006); Saurel and Abgrall (1999); Stewart and Wendroff (1984); Zein et al. (2010). A multidimensional version of the governing equations of Baer-Nunziato-type models for two-phase flow is the following:

$$\frac{\partial}{\partial t} (\alpha_i \rho_i) + \nabla \cdot (\alpha_i \rho_i \vec{u}_i) = \Theta_i, \quad (2.1)$$

$$\frac{\partial}{\partial t} (\alpha_i \rho_i \vec{u}_i) + \nabla \cdot (\alpha_i \rho_i \vec{u}_i \otimes \vec{u}_i + \alpha_i P_i) = P_I \nabla(\alpha_i) + \Gamma_i, \quad (2.2)$$

$$\frac{\partial}{\partial t} \left[ \alpha_i \rho_i \left( e_i + \frac{|\vec{u}_i|^2}{2} \right) \right] + \nabla \cdot \left[ \alpha_i \rho_i \vec{u}_i \left( e_i + \frac{|\vec{u}_i|^2}{2} \right) + \alpha_i P_i \vec{u}_i \right] = P_I \vec{u}_I \nabla(\alpha_i) + \Omega_i, \quad (2.3)$$

$$\frac{\partial}{\partial t} (\alpha_1) + \vec{u}_I \nabla \cdot (\alpha_1) = \Phi_1. \quad (2.4)$$

Let us describe the physical meaning of each variable (the subscript  $i = 1, 2$  refers to phase 1 and phase 2 respectively):  $\rho_i$  is the density,  $\vec{u}_i$  is the velocity,  $P_i$  is the pressure,  $e_i$  is the specific internal energy and  $\alpha_i$  is the volume fraction, which satisfy the relation  $\alpha_1 + \alpha_2 = 1$ . The source terms  $\Theta_i$ ,  $\Gamma_i$ ,  $\Omega_i$  and  $\Phi_1$  are terms related to the interaction between the two phases and the external forces while  $P_I$  and  $\vec{u}_I$  represent averaged values of the interfacial pressure and velocity over the two-phase control volume. In the Baer-Nunziato-type models the interfacial pressure is defined as the mixture pressure, while the interfacial velocity is defined as the velocity of the center of mass.

In the previously cited works and references therein the mathematical properties of differential equations of two-phase flow models were studied and a variety of test problems have been solved numerically. It is proved that the differential equations of

the model are hyperbolic and this guarantees a solvability of certain classes of initial-boundary-value problems. As already discussed, one of the major disadvantage of Baer-Nunziato-type models is that not all equations can be written in a conservative (divergent) form (for example Eqs. (2.2)–(2.4)). Note that the divergent form of equations is very attractive because it allows us to apply known mathematical tools and accurate numerical methods to study problems of practical interest.

Another phenomenological approach, based on the theory of thermodynamically compatible system of conservation laws was first proposed in Godunov and Romensky (1995) to formulate the governing equations of compressible multiphase flow. Here, the mixture is assumed as a continuum in which a multiphase character of a flow is taken into account by introducing new phenomenological variables beyond the classical density, momentum and energy. With this approach we do not consider the governing equations for each phase separately, but we solve the continuity, momentum and energy equations for the whole mixture. Furthermore, to determine the internal state of the medium, additional differential equations must be provided (for example balance laws for the volume fraction, for the mass fraction and for the relative velocity). The governing equations form a hyperbolic system of partial differential equations in conservative form and these can be rewritten as a set of subsystems of conservation laws for each phase coupled by interface exchange terms. In general the two-phase flow thermodynamically compatible equations differ from the Baer-Nunziato-type equations, but for simplest one-dimensional isentropic flows they coincide (Romenski and Toro, 2004).

In addition to the difficulties in obtaining a conservative form for their governing equations, multiphase flow problems, even in the case of two-phase flow, become challenging when relaxation processes are considered (for example pressures and/or velocities relaxations). That is why many papers are devoted to the development of simplified models which are obtained introducing additional constraints (Kreeft and Koren, 2010; Murrone and Guillard, 2005). These constraints usually represent the assumption that the relaxation time to the equilibrium state is very small compared with the characteristic time of the process under consideration. As a rule these constraints consist in the requirement that the pressures, velocities or temperatures must be equal in the two phases. In recent years a two-phase models with gas-liquid transition have been developed in Le Métayer et al. (2005), where phase transitions is introduced with the use of discontinuities derived from the conservation laws. This approach requires a detailed knowledge of properties of discontinuous solutions and its numerical realization is quite complicated. Actually the phase transition in two-phase model can also be accounted as an irreversible process with high rate of relaxation. In Zein et al. (2010) a simplified two-phase model is proposed in which an equality of phase Gibbs potentials is proposed in addition to the phase velocities, pressures and temperatures equalities. It is important to note that the phase transition itself occurs only in the neighborhood of critical pressures and temperatures. If the temperature and the pressure are far from the critical values then the equality of phase Gibbs potentials is not valid. That is why it is reasonable to design a phase transition model with the use of kinetics of phase mass transfer. Such an approach is used in Resnyansky et al. (2011) for the description of continuous phase transition in polytetrafluoroethylene.

In this chapter an extension of the two-phase flow model with two pressures, two velocities and a single temperature, which has been proposed in Romenski et al. (2010) and studied in La Spina and de' Michieli Vitturi (2012), is presented. These governing

equations are derived using the principles of extended thermodynamics (Godunov and Romenskii, 2003; Romenski et al., 2003; Romensky, 1998) and the resulting system forms a system of partial differential equations written in conservative form, which can be reduced to a symmetric hyperbolic system (see Appendix A). The derivation of this special form is based on the existence of an additional energy conservation law, which represent the first law of thermodynamics for the given system.

## 2.1 GOVERNING EQUATIONS

In the two-phase model, each phase can be characterized by its own parameters of state. The phase volume fractions in the mixture are denoted with  $\alpha_1$  and  $\alpha_2$ , which satisfy the saturation constraint  $\alpha_1 + \alpha_2 = 1$ . Phase mass densities are  $\rho_1$ ,  $\rho_2$ , while the velocities are  $\vec{u}_1$  and  $\vec{u}_2$ .

We introduce also the notation  $s_i$  for the phase specific entropy and  $e_i$  for the specific internal energy and we assume that the equations of state for each phase  $e_i$  are known function of the density  $\rho_i$  and entropy  $s_i$ :

$$e_i = e_i(\rho_1, s_i). \quad (2.5)$$

From the equations of state, the phase pressures  $P_i$  and the temperatures  $T_i$  are computed as follows:

$$P_i = \rho_i^2 \frac{\partial e_i}{\partial \rho_i}, \quad T_i = \frac{\partial e_i}{\partial s_i}. \quad (2.6)$$

In this thesis we assume that the two phases are in thermal equilibrium, thus we set

$$T = T_1 = T_2.$$

Finally, the following mixture parameters of state, connected with the individual phase parameters, are introduced:

$$\begin{aligned} \rho &= \alpha_1 \rho_1 + \alpha_2 \rho_2, & c &= c_1 = \frac{\alpha_1 \rho_1}{\rho}, & P &= \alpha_1 P_1 + \alpha_2 P_2 \\ \vec{u} &= c_1 \vec{u}_1 + c_2 \vec{u}_2, & \vec{w} &= \vec{u}_1 - \vec{u}_2, & e &= c_1 e_1 + c_2 e_2, \\ E &= e + c(1 - c) \frac{|\vec{w}|^2}{2}. \end{aligned} \quad (2.7)$$

Using these notations, the system of governing equations can be written as

$$\frac{\partial \mathbf{U}}{\partial t} + \nabla \cdot \mathbf{F}(\mathbf{U}) = \mathbf{S}(\mathbf{U}), \quad (2.8)$$

where

$$\mathbf{U} = (\rho, \rho \alpha_1, \rho_1 \alpha_1, \rho \vec{u}, \vec{w}, \rho(E + |\vec{u}|^2/2))^T \quad (2.9)$$

is the vector of the conservative variables,  $\mathbf{F}(\mathbf{U})$  is the vector of the fluxes of the conservative variables and  $\mathbf{S}(\mathbf{U})$  is the vector of the source terms which takes into account the interphase exchange terms and the external forces.

More in detail, the mixture mass conservation law can be written as:

$$\frac{\partial}{\partial t} (\rho) + \nabla \cdot (\rho \vec{u}) = 0. \quad (2.10)$$

The balance law for the volume fraction of the first phase is:

$$\frac{\partial}{\partial t} (\rho \alpha_1) + \nabla \cdot (\rho \alpha_1 \vec{u}) = -\phi, \quad (2.11)$$

where  $\phi$  is the pressure relaxation defined as a function of the pressures difference and of a pressure relaxation rate  $\tau^{(p)}$  by

$$\phi = \frac{1}{\tau^{(p)}} (P_2 - P_1).$$

This term represents the phase pressure equalizing through the process of pressure wave propagation in dispersed phase and its interaction with the interface boundaries.

The mass conservation law for the first phase is:

$$\frac{\partial}{\partial t} (\rho_1 \alpha_1) + \nabla \cdot (\rho_1 \alpha_1 \vec{u}_1) = -\rho \theta, \quad (2.12)$$

where  $\theta$  is defined as

$$\theta = \frac{1}{\tau^{(c)}} \left( \mu_1 - \mu_2 + (1 - 2c) \frac{|\vec{w}|^2}{2} \right),$$

$\mu_1$  and  $\mu_2$  are the phase chemical potentials (or Gibbs free energies)

$$\mu_1 = e_1 + \frac{P_1}{\rho_1} - s_1 T, \quad \mu_2 = e_2 + \frac{P_2}{\rho_2} - s_2 T,$$

$\vec{w} = \vec{u}_1 - \vec{u}_2$  is the relative velocity and  $\tau^{(c)}$  is a phase exchange relaxation rate. We remark that in the original model presented in Romenski et al. (2010) there is no mass transfer between the phases and consequently there is no source term in the mass conservation law for the first phase.

The mixture momentum equation is:

$$\frac{\partial}{\partial t} (\rho \vec{u}) + \nabla \cdot [\vec{u}_1 \otimes (\rho_1 \alpha_1 \vec{u}_1) + \vec{u}_2 \otimes (\rho_2 \alpha_2 \vec{u}_2) + (\alpha_1 P_1 + \alpha_2 P_2) \mathbf{I}] = \rho \vec{g}, \quad (2.13)$$

where  $\vec{g}$  is the gravity vector,  $\mathbf{I}$  is the three dimensional identity matrix and  $\otimes$  is the tensor product.

The relative velocity balance law is:

$$\begin{aligned} \frac{\partial}{\partial t} (\vec{w}) + \nabla \cdot \left[ \frac{\vec{u}_1 \otimes \vec{u}_1}{2} - \frac{\vec{u}_2 \otimes \vec{u}_2}{2} + \left( e_1 + \frac{P_1}{\rho_1} - e_2 - \frac{P_2}{\rho_2} - (s_1 - s_2) T \right) \mathbf{I} \right] &= \\ &= -\frac{1}{\rho} \vec{\lambda}_0 - \vec{u} \times \vec{\omega}, \end{aligned} \quad (2.14)$$

where the interfacial friction  $\vec{\lambda}_0$  is defined as a function of the velocity relaxation rate  $\tau^{(f)}$ , the mass fraction  $c$  and the relative velocity  $\vec{w}$ :

$$\vec{\lambda}_0 = \frac{1}{\tau^{(f)}} c (1 - c) \vec{w}.$$

In the case of dispersed particle flow the velocity relaxation represents the Stokes drag force in the phase momentum equations.

In the equation (2.14) the artificial vector  $\vec{\omega}$  is introduced, as it is done in Romenski et al. (2007), to save a conservation-law form of the equation. Furthermore, this variable can be treated as a source terms in the equation for the relative velocity (Romenski et al., 2010).

The conservation energy law is written as:

$$\begin{aligned} \frac{\partial}{\partial t} \left[ \rho \left( E + \frac{|\vec{u}|^2}{2} \right) \right] + \nabla \cdot \left[ \alpha_1 \rho_1 \vec{u}_1 \left( e_1 + \frac{|\vec{u}_1|^2}{2} + \frac{P_1}{\rho_1} \right) + \right. \\ \left. + \alpha_2 \rho_2 \vec{u}_2 \left( e_2 + \frac{|\vec{u}_2|^2}{2} + \frac{P_2}{\rho_2} \right) - \rho c (1-c) \vec{w} (s_1 - s_2) T \right] = \rho (\vec{u} \cdot \vec{g}). \end{aligned} \quad (2.15)$$

Finally, we have the steady state equation

$$\nabla \times \vec{w} = \vec{\omega}. \quad (2.16)$$

Therefore, using the notations presented in Eq. (2.7), the vector of the fluxes can be written as

$$\mathbf{F}(\mathbf{U}) = \begin{pmatrix} \rho \vec{u} \\ \rho \alpha_1 \vec{u} \\ \rho_1 \alpha_1 \vec{u}_1 \\ \vec{u}_1 \otimes (\rho_1 \alpha_1 \vec{u}_1) + \vec{u}_2 \otimes (\rho_2 \alpha_2 \vec{u}_2) + (\alpha_1 P_1 + \alpha_2 P_2) \mathbf{I} \\ \frac{\vec{u}_1 \otimes \vec{u}_1}{2} - \frac{\vec{u}_2 \otimes \vec{u}_2}{2} + \left( e_1 + \frac{P_1}{\rho_1} - e_2 - \frac{P_2}{\rho_2} - (s_1 - s_2) T \right) \mathbf{I} \\ \sum_{i=1}^2 \left[ \alpha_i \rho_i \vec{u}_i \left( e_i + \frac{|\vec{u}_i|^2}{2} + \frac{P_i}{\rho_i} \right) \right] - \rho c (1-c) \vec{w} (s_1 - s_2) T \end{pmatrix}, \quad (2.17)$$

while the vector of the source terms can be expressed as

$$\mathbf{S}(\mathbf{U}) = \begin{pmatrix} 0 \\ -\frac{1}{\tau^{(p)}} (P_2 - P_1) \\ -\frac{1}{\tau^{(c)}} \rho \left( \mu_1 - \mu_2 + (1-2c) \frac{|\vec{w}|^2}{2} \right) \\ \frac{\rho \vec{g}}{\tau^{(f)}} \\ -\frac{1}{\tau^{(f)}} \left[ \frac{c(1-c)}{\rho} (\vec{u}_1 - \vec{u}_2) \right] - \vec{u} \times \vec{\omega} \\ \rho (\vec{u} \cdot \vec{g}) \end{pmatrix}. \quad (2.18)$$

### 2.1.1 Entropy balance

From now on, for simplicity, we only consider the monodimensional case and, in this way, the steady-state equation (2.16) and the term  $\vec{u} \times \vec{\omega}$  in the relative velocity balance equation can be neglected, obtaining the following system:

$$\frac{\partial}{\partial t} (\rho) + \frac{\partial}{\partial x} (\rho u) = 0, \quad (2.19)$$

$$\frac{\partial}{\partial t} (\rho \alpha_1) + \frac{\partial}{\partial x} (\rho \alpha_1 u) = -\phi, \quad (2.20)$$

$$\frac{\partial}{\partial t}(\rho_1\alpha_1) + \frac{\partial}{\partial x}(\rho_1\alpha_1 u_1) = -\rho\theta, \quad (2.21)$$

$$\frac{\partial}{\partial t}(\rho u) + \frac{\partial}{\partial x}[\rho_1\alpha_1(u_1)^2 + \rho_2\alpha_2(u_2)^2 + \alpha_1 P_1 + \alpha_2 P_2] = -\rho g, \quad (2.22)$$

$$\frac{\partial}{\partial t}(w) + \frac{\partial}{\partial x}\left[\frac{(u_1)^2}{2} - \frac{(u_2)^2}{2} + e_1 + \frac{P_1}{\rho_1} - e_2 - \frac{P_2}{\rho_2} - (s_1 - s_2)T\right] = -\frac{1}{\rho}\lambda_0, \quad (2.23)$$

$$\begin{aligned} & \frac{\partial}{\partial t}\left[\rho\left(E + \frac{u^2}{2}\right)\right] + \frac{\partial}{\partial x}\left[\alpha_1\rho_1u_1\left(e_1 + \frac{(u_1)^2}{2} + \frac{P_1}{\rho_1}\right) + \right. \\ & \left. + \alpha_2\rho_2u_2\left(e_2 + \frac{(u_2)^2}{2} + \frac{P_2}{\rho_2}\right) - \rho c(1-c)w(s_1 - s_2)T\right] = -\rho ug. \end{aligned} \quad (2.24)$$

It is shown here that, from the system of equations (2.19)–(2.24), it is possible to write an equation for the balance of the total mixture entropy  $S$ , defined as

$$S = c_1s_1 + c_2s_2.$$

To derive this balance equation, first we have to write an equivalent nonconservative form of the equations (2.19)–(2.24).

From the mixture mass conservation we have:

$$\frac{\partial\rho}{\partial t} + \rho\frac{\partial u}{\partial x} + u\frac{\partial\rho}{\partial x} = 0 \implies \frac{d\rho}{dt} + \rho\frac{\partial u}{\partial x} = 0, \quad (2.25)$$

where we have introduced the material derivative  $d/dt = \partial/\partial t + u\partial/\partial x$ .

Expanding the second equation for balance of the volume of the first equation, we have

$$\begin{aligned} & \rho\frac{\partial\alpha_1}{\partial t} + \alpha_1\frac{\partial\rho}{\partial t} + \alpha_1\frac{\partial\rho u}{\partial x} + \rho u\frac{\partial\alpha_1}{\partial x} = -\phi \\ & \Downarrow \\ & \alpha_1\left(\frac{\partial\rho}{\partial t} + \frac{\partial\rho u}{\partial x}\right) + \rho\left(\frac{\partial\alpha_1}{\partial t} + u\frac{\partial\alpha_1}{\partial x}\right) = -\phi \\ & \Downarrow \\ & \left(\frac{\partial\alpha_1}{\partial t} + u\frac{\partial\alpha_1}{\partial x}\right) = -\frac{\phi}{\rho} \\ & \Downarrow \\ & \frac{d\alpha_1}{dt} = -\frac{\phi}{\rho}. \end{aligned} \quad (2.26)$$

Writing the mass conservation equation for the first phase in terms of the mixture parameters  $\rho$  and  $c$  we obtain:

$$\frac{\partial(c\rho)}{\partial t} + \frac{\partial(c\rho u_1)}{\partial x} = -\rho\theta \quad (2.27)$$

and expanding the derivatives and using the relationship  $u_1 = u + (1 - c)w$  we get

$$\begin{aligned} \rho \frac{\partial c}{\partial t} + c \frac{\partial \rho}{\partial t} + c \frac{\partial \rho u}{\partial x} + \rho u \frac{\partial c}{\partial x} + \frac{\partial}{\partial x}(\rho c(1 - c)w) &= -\rho \theta \\ \downarrow \\ c \left( \frac{\partial \rho}{\partial t} + \frac{\partial \rho u}{\partial x} \right) + \rho \left( \frac{\partial c}{\partial t} + u \frac{\partial c}{\partial x} \right) + \frac{\partial}{\partial x}(\rho c(1 - c)w) &= -\rho \theta \\ \downarrow \\ \rho \frac{dc}{dt} + \frac{\partial}{\partial x}(\rho c(1 - c)w) &= -\rho \theta. \end{aligned} \quad (2.28)$$

Now, rewriting the mixture momentum equation in a more compact form, we have

$$\frac{\partial \rho u}{\partial t} + \frac{\partial}{\partial x} (\rho u^2 + P + \rho c(1 - c)w^2) = \rho g. \quad (2.29)$$

Expanding the derivatives we can write

$$\begin{aligned} \rho \frac{\partial u}{\partial t} + u \frac{\partial \rho}{\partial t} + u \frac{\partial \rho u}{\partial x} + \rho u \frac{\partial u}{\partial x} + \frac{\partial}{\partial x}(P + \rho c(1 - c)w^2) &= \rho g \\ \downarrow \\ \rho \left( \frac{\partial \rho}{\partial t} + \frac{\partial \rho u}{\partial x} \right) + \rho \left( \frac{\partial u}{\partial t} + u \frac{\partial u}{\partial x} \right) + \frac{\partial}{\partial x}(P + \rho c(1 - c)w^2) &= \rho g \\ \downarrow \\ \rho \frac{du}{dt} + \frac{\partial P}{\partial x} + \frac{\partial}{\partial x}(\rho c(1 - c)w^2) &= \rho g. \end{aligned} \quad (2.30)$$

We observe that the sum of the velocities can be written in terms of  $c$ ,  $u$  and  $w$  as

$$u_1 + u_2 = 2u - 2cw + w \quad (2.31)$$

and from this identity we can rewrite the first two terms on the spatial derivative of the relative velocity equation in the following way:

$$\frac{u_1^2}{2} - \frac{u_2^2}{2} = \frac{w}{2}(u_1 + u_2) = \frac{w}{2}(2u - 2cw + w) = uw + (1 - 2c)\frac{w^2}{2}. \quad (2.32)$$

Now, substituting the previous expression in the equation for the relative velocity, we have:

$$\begin{aligned} \frac{\partial w}{\partial t} + u \frac{\partial w}{\partial x} + w \frac{\partial u}{\partial x} + \\ + \frac{\partial}{\partial x} \left( (1 - 2c)\frac{w^2}{2} + e_1 + \frac{P_1}{\rho_1} - e_2 - \frac{P_2}{\rho_2} - (s_1 - s_2)T \right) &= -\frac{1}{\rho} \lambda_0 \\ \downarrow \\ \frac{dw}{dt} + w \frac{\partial u}{\partial x} + \frac{\partial}{\partial x} \left( (1 - 2c)\frac{w^2}{2} + \mu_1 - \mu_2 \right) &= -\frac{1}{\rho} \lambda_0. \end{aligned} \quad (2.33)$$

With the notation for the internal energy of the mixture  $E$  introduced in Eq. (2.7), i.e.

$$E = e(\alpha_1, \rho, c, S) + c(1 - c)\frac{w^2}{2}, \quad (2.34)$$

the energy equation can be written in the form:

$$\begin{aligned} \frac{\partial}{\partial t} \left[ \rho \left( E + \frac{u^2}{2} \right) \right] + \frac{\partial}{\partial x} \left[ \rho u \left( E + \frac{u^2}{2} \right) + uP + \rho uw(c(1-c)w) + \right. \\ \left. + \rho \left( \mu_1 - \mu_2 + (1-2c)\frac{w^2}{2} \right) (c(1-c)w) \right] = \rho ug. \end{aligned} \quad (2.35)$$

For the first two terms of the energy equation we can write:

$$\begin{aligned} \frac{\partial}{\partial t} \left( \rho \left( E + \frac{u^2}{2} \right) \right) + \frac{\partial}{\partial x} \left[ \rho u \left( E + \frac{u^2}{2} \right) \right] = \\ = \rho \frac{\partial}{\partial t} \left( E + \frac{u^2}{2} \right) + \left( E + \frac{u^2}{2} \right) \frac{\partial \rho}{\partial t} + \rho u \frac{\partial}{\partial x} \left( E + \frac{u^2}{2} \right) + \left( E + \frac{u^2}{2} \right) \frac{\partial \rho u}{\partial x} = \\ = \left( E + \frac{u^2}{2} \right) \left( \frac{\partial \rho}{\partial t} + \frac{\partial \rho u}{\partial x} \right) + \rho \left( \frac{\partial E}{\partial t} + u \frac{\partial E}{\partial x} \right) + \rho \left( \frac{\partial}{\partial t} \frac{u^2}{2} + u \frac{\partial}{\partial x} \frac{u^2}{2} \right) = \\ = \rho \frac{dE}{dt} + \rho u \left( \frac{\partial u}{\partial t} + u \frac{\partial u}{\partial x} \right) = \\ = \rho \frac{dE}{dt} + \rho u \frac{du}{dt} = \\ = \rho \frac{dE}{dt} - u \left( \frac{\partial p}{\partial x} + \frac{\partial}{\partial x} (\rho c(1-c)w^2) - \rho g \right). \end{aligned} \quad (2.36)$$

Now, substituting in the energy equation, we have:

$$\begin{aligned} \rho \frac{dE}{dt} + \frac{\partial u P}{\partial x} - u \frac{\partial P}{\partial x} + \frac{\partial}{\partial x} (\rho uw^2 c(1-c)) - u \frac{\partial}{\partial x} (\rho c(1-c)w^2) + \\ + \frac{\partial}{\partial x} \left( \rho \left( \mu_1 - \mu_2 + (1-2c)\frac{w^2}{2} \right) (c(1-c)w) \right) + \rho ug = \rho ug \\ \Downarrow \\ \rho \frac{dE}{dt} + P \frac{\partial u}{\partial x} + \rho c(1-c)w^2 \frac{\partial u}{\partial x} + \\ + \frac{\partial}{\partial x} \left( \rho \left( \mu_1 - \mu_2 + (1-2c)\frac{w^2}{2} \right) (c(1-c)w) \right) = 0 \end{aligned} \quad (2.37)$$

and, using the formula

$$dE = E_{\alpha_1} d\alpha_1 + E_\rho d\rho + E_c dc + E_w dw + E_S dS,$$

we find

$$\frac{dS}{dt} = \frac{1}{E_S} \left( \frac{dE}{dt} - E_{\alpha_1} \frac{d\alpha_1}{dt} - E_\rho \frac{d\rho}{dt} - E_c \frac{dc}{dt} - E_w \frac{dw}{dt} \right). \quad (2.38)$$

The partial derivatives of  $E$  follow directly from the definition written in (2.34):

$$\begin{aligned} E_c &= \frac{\partial E}{\partial c} = e_c + (1 - 2c) \frac{w^2}{2} = \mu_1 - \mu_2 + (1 - 2c) \frac{w^2}{2}, \\ E_w &= \frac{\partial E}{\partial w} = c(1 - c)w, \quad E_\alpha = \frac{\partial E}{\partial \alpha} = \frac{P_1 - P_2}{\rho}, \\ E_\rho &= \frac{\partial E}{\partial \rho} = \frac{1}{\rho^2} P, \quad E_S = \frac{\partial E}{\partial S} = T. \end{aligned} \quad (2.39)$$

We observe that the source terms for the pressure relaxation, the phase change and the relative velocity are strictly related to  $E_\alpha$ ,  $E_c$  and  $E_w$  respectively.

Now, substituting the expressions for the material derivatives found in (2.26), (2.28), (2.30), (2.33), and (2.37) and the partial derivatives of  $E$  in (2.38), we obtain

$$\begin{aligned} \frac{dS}{dt} &= \frac{1}{T} \left[ -\frac{P}{\rho} \frac{\partial u}{\partial x} - c(1 - c)w^2 \frac{\partial u}{\partial x} - \right. \\ &\quad - \frac{1}{\rho} \frac{\partial}{\partial x} \left( \rho \left( \mu_1 - \mu_2 + (1 - 2c) \frac{w^2}{2} \right) (c(1 - c)w) \right) + \frac{P_1 - P_2}{\rho} \frac{\phi}{\rho} + \frac{1}{\rho^2} P \rho \frac{\partial u}{\partial x} + \\ &\quad + \left( \mu_1 - \mu_2 + (1 - 2c) \frac{w^2}{2} \right) \frac{1}{\rho} \left[ \frac{\partial}{\partial x} (\rho c(1 - c)w) + \frac{\rho}{\tau^{(c)}} \left( \mu_1 - \mu_2 + (1 - 2c) \frac{w^2}{2} \right) \right] + \\ &\quad \left. + c(1 - c)w \left( w \frac{\partial u}{\partial x} + \frac{\partial}{\partial x} \left( (1 - 2c) \frac{w^2}{2} + \mu_1 - \mu_2 \right) + \frac{1}{\rho} \lambda_0 \right) \right], \end{aligned} \quad (2.40)$$

or, in an equivalent more compact form

$$\begin{aligned} \frac{dS}{dT} &= \frac{1}{T} \left[ -\frac{P}{\rho} \frac{\partial u}{\partial x} - w E_w \frac{\partial u}{\partial x} - \frac{1}{\rho} \frac{\partial \rho E_c E_w}{\partial x} + E_\alpha \frac{\phi}{\rho} + \right. \\ &\quad + \frac{P}{\rho} \frac{\partial u}{\partial x} + \frac{E_c}{\rho} \frac{\partial \rho E_w}{\partial x} + \frac{E_c^2}{\tau^{(c)}} + E_w w \frac{\partial u}{\partial x} + E_w \frac{\partial E_c}{\partial x} + \frac{E_w}{\rho} \lambda_0 \left. \right]. \end{aligned} \quad (2.41)$$

From this equation, after some cancellation, we obtain the desired entropy balance law

$$\begin{aligned} \frac{dS}{dt} &= \frac{1}{T} \left( E_\alpha \frac{\phi}{\rho} + \frac{E_c^2}{\tau^{(c)}} + \frac{E_w}{\rho} \lambda_0 \right) = \\ &= \frac{1}{T} \left[ \frac{(P_1 - P_2)^2}{\rho \tau^{(p)}} + \frac{1}{\tau^{(c)}} \left( \mu_1 - \mu_2 + (1 - 2c) \frac{w^2}{2} \right)^2 + \frac{c^2 (1 - c)^2 w^2}{\tau^{(f)} \rho^2} \right]. \end{aligned} \quad (2.42)$$

We notice that the right hand side in the above equation, which represents the entropy production, is a non-negative quantity.

## 2.2 CHARACTERISTIC ANALYSIS

In this section the mathematical properties of the one-dimensional version of the model are studied and an eigenvalues analysis is presented. An approximated analysis

of the eigenvalues of the jacobian of the fluxes vector, under the assumption of zero relative velocity, has been illustrated in Romenski et al. (2003).

Here we show that, rewriting the system using an appropriate set of conservative variables, the analysis can be done explicitly.

### 2.2.1 Primitive variable formulation

First of all, we rewrite the system of equations (2.19)–(2.24) in an equivalent quasilinear form

$$\frac{\partial \mathbf{V}}{\partial t} + B(\mathbf{V}) \frac{\partial \mathbf{V}}{\partial x} = \mathbf{Z}(\mathbf{V}), \quad (2.43)$$

where  $\mathbf{V}$  is the vector of primitive variables

$$\mathbf{V} = (\alpha_1, S, \rho_1, \rho_2, u_1, u_2)^T. \quad (2.44)$$

To obtain the matrix  $B(\mathbf{V})$  we have to derive the equations of conservation for the primitive variables in quasilinear form. For the volume fraction  $\alpha_1$ , from equation (2.26), we have:

$$\frac{\partial \alpha_1}{\partial t} + u \frac{\partial \alpha_1}{\partial x} = -\frac{\phi}{\rho}. \quad (2.45)$$

As it has been shown in the previous section, the equation for the entropy can be written as:

$$\frac{\partial S}{\partial t} + u \frac{\partial S}{\partial x} = \frac{1}{T} \left[ \frac{(P_1 - P_2)^2}{\rho \tau^{(p)}} + \frac{\left( \mu_1 - \mu_2 + (1 - 2c) \frac{w^2}{2} \right)^2}{\tau^{(c)}} + \frac{c^2 (1 - c)^2 w^2}{\rho^2 \tau^{(f)}} \right]. \quad (2.46)$$

From the mass conservation of the first phase (2.21), we can write:

$$\begin{aligned} \frac{\partial \rho_1 \alpha_1}{\partial t} + \frac{\partial \rho_1 u_1 \alpha_1}{\partial x} &= -\rho \theta \\ \downarrow \\ \alpha_1 \frac{\partial \rho_1}{\partial t} + \alpha_1 \frac{\partial \rho_1 u_1}{\partial x} + \rho_1 \frac{\partial \alpha_1}{\partial t} + \rho_1 u_1 \frac{\partial \alpha_1}{\partial x} &= -\rho \theta \\ \downarrow \\ \alpha_1 \frac{\partial \rho_1}{\partial t} + \alpha_1 \frac{\partial \rho_1 u_1}{\partial x} + \rho_1 \frac{\partial \alpha_1}{\partial t} + \rho_1 u \frac{\partial \alpha_1}{\partial x} + \rho_1 (u_1 - u) \frac{\partial \alpha_1}{\partial x} &= -\rho \theta \\ \downarrow \\ \rho_1 \left( \frac{\partial \alpha_1}{\partial t} + u \frac{\partial \alpha_1}{\partial x} \right) + \alpha_1 \left( \frac{\partial \rho_1}{\partial t} + \frac{\partial \rho_1 u_1}{\partial x} \right) + \rho_1 \left( \frac{\alpha_2 \rho_2}{\rho} (u_1 - u_2) \right) \frac{\partial \alpha_1}{\partial x} &= -\rho \theta \\ \downarrow \\ \rho_1 \left( -\frac{\phi}{\rho} \right) + \alpha_1 \left( \frac{\partial \rho_1}{\partial t} + \rho_1 \frac{\partial u_1}{\partial x} + u_1 \frac{\partial \rho_1}{\partial x} \right) + \alpha_2 \frac{\rho_1 \rho_2}{\rho} (u_1 - u_2) \frac{\partial \alpha_1}{\partial x} &= -\rho \theta \\ \downarrow \\ \frac{\partial \rho_1}{\partial t} + \rho_1 \frac{\partial u_1}{\partial x} + u_1 \frac{\partial \rho_1}{\partial x} + \frac{\alpha_2 \rho_1 \rho_2}{\alpha_1 \rho} (u_1 - u_2) \frac{\partial \alpha_1}{\partial x} &= \frac{\rho_1 \phi}{\alpha_1 \rho} - \frac{\rho}{\alpha_1} \theta. \end{aligned} \quad (2.47)$$

In the same way we obtained the quasi-linear equations for  $\rho_1$ , we have the following equation for  $\rho_2$ :

$$\frac{\partial \rho_2}{\partial t} + \rho_2 \frac{\partial u_2}{\partial x} + u_2 \frac{\partial \rho_2}{\partial x} + \frac{\alpha_1 \rho_1 \rho_2}{\alpha_2 \rho} (u_1 - u_2) \frac{\partial \alpha_1}{\partial x} = \frac{\rho}{\alpha_2} \theta - \frac{\rho_2 \phi}{\alpha_2 \rho}. \quad (2.48)$$

About the first phase velocity, using the mass conservation of the first phase (2.21) we have

$$\frac{\partial \alpha_1 \rho_1 u_1}{\partial t} = u_1 \frac{\partial \alpha_1 \rho_1}{\partial t} + \alpha_1 \rho_1 \frac{\partial u_1}{\partial t} = u_1 \left[ -\rho \theta - \frac{\partial}{\partial x} (\rho_1 \alpha_1 u_1) \right] + \alpha_1 \rho_1 \frac{\partial u_1}{\partial t}. \quad (2.49)$$

Now, from the mixture momentum equation (2.22), we get

$$\begin{aligned} & \frac{\partial (\alpha_1 \rho_1 u_1 + \alpha_2 \rho_2 u_2)}{\partial t} + \frac{\partial}{\partial x} (\alpha_1 \rho_1 u_1^2 + \alpha_2 \rho_2 u_2^2 + \alpha_1 P_1 + \alpha_2 P_2) = \rho g \\ & \qquad \qquad \qquad \Downarrow \\ & \alpha_1 \rho_1 \frac{\partial u_1}{\partial t} + u_1 \frac{\partial \alpha_1 \rho_1}{\partial t} + \alpha_2 \rho_2 \frac{\partial u_2}{\partial t} + u_2 \frac{\partial \alpha_2 \rho_2}{\partial t} + \\ & + \alpha_1 \rho_1 u_1 \left( \frac{\partial}{\partial x} u_1 \right) + u_1 \frac{\partial}{\partial x} (\alpha_1 \rho_1 u_1) + \alpha_2 \rho_2 u_2 \left( \frac{\partial}{\partial x} u_2 \right) + u_2 \frac{\partial}{\partial x} (\alpha_2 \rho_2 u_2) + \\ & + (P_1 - P_2) \frac{\partial}{\partial x} \alpha_1 + \alpha_1 \frac{\partial}{\partial x} P_1 + \alpha_2 \frac{\partial}{\partial x} P_2 = \rho g \\ & \qquad \qquad \qquad \Downarrow \\ & u_1 \left( \frac{\partial \alpha_1 \rho_1}{\partial t} + \frac{\partial}{\partial x} \alpha_1 \rho_1 u_1 \right) + u_2 \left( \frac{\partial \alpha_2 \rho_2}{\partial t} + \frac{\partial}{\partial x} \alpha_2 \rho_2 u_2 \right) + \\ & + \alpha_1 \rho_1 \left( \frac{\partial u_1}{\partial t} + u_1 \frac{\partial}{\partial x} u_1 \right) + \alpha_2 \rho_2 \left( \frac{\partial u_2}{\partial t} + u_2 \frac{\partial}{\partial x} u_2 \right) + \\ & + (P_1 - P_2) \frac{\partial}{\partial x} \alpha_1 + \alpha_1 \frac{\partial}{\partial x} P_1 + \alpha_2 \frac{\partial}{\partial x} P_2 = \rho g. \end{aligned} \quad (2.50)$$

Using equations (2.19)–(2.21) we obtain

$$\begin{aligned} & u_1 (-\rho \theta) + u_2 (\rho \theta) + \\ & + \alpha_1 \rho_1 \left( \frac{\partial u_1}{\partial t} + u_1 \frac{\partial}{\partial x} u_1 \right) + \alpha_2 \rho_2 \left( \frac{\partial u_2}{\partial t} + u_2 \frac{\partial}{\partial x} u_2 \right) + \\ & + (P_1 - P_2) \frac{\partial}{\partial x} \alpha_1 + \alpha_1 \frac{\partial}{\partial x} P_1 + \alpha_2 \frac{\partial}{\partial x} P_2 = \rho g \\ & \qquad \qquad \qquad \Downarrow \\ & \frac{\alpha_1 \rho_1}{\alpha_2 \rho_2} \left( \frac{\partial u_1}{\partial t} + u_1 \frac{\partial}{\partial x} u_1 \right) + \left( \frac{\partial u_2}{\partial t} + u_2 \frac{\partial}{\partial x} u_2 \right) + \\ & + \frac{(P_1 - P_2)}{\alpha_2 \rho_2} \frac{\partial}{\partial x} \alpha_1 + \frac{\alpha_1}{\alpha_2 \rho_2} \frac{\partial}{\partial x} P_1 + \frac{1}{\rho_2} \frac{\partial}{\partial x} P_2 = \frac{\rho}{\alpha_2 \rho_2} (g + \theta(u_1 - u_2)). \end{aligned} \quad (2.51)$$

Summing the equation for the relative velocity (2.23) to the last equation above, we get

$$\begin{aligned}
 & \left(1 + \frac{\alpha_1 \rho_1}{\alpha_2 \rho_2}\right) \left(\frac{\partial u_1}{\partial t} + u_1 \frac{\partial}{\partial x} u_1\right) + \frac{\partial}{\partial x} \left(e_1 - e_2 + \frac{P_1}{\rho_1} - \frac{P_2}{\rho_2} - (s_1 - s_2)T\right) + \\
 & + \frac{(P_1 - P_2)}{\alpha_2 \rho_2} \frac{\partial}{\partial x} \alpha_1 + \frac{\alpha_1}{\alpha_2 \rho_2} \frac{\partial}{\partial x} P_1 + \frac{1}{\rho_2} \frac{\partial}{\partial x} P_2 = \frac{\rho}{\alpha_2 \rho_2} (g + \theta(u_1 - u_2)) - \frac{1}{\rho} \lambda_0 \\
 & \quad \Downarrow \\
 & \frac{\partial u_1}{\partial t} + u_1 \frac{\partial}{\partial x} u_1 + \frac{\alpha_2 \rho_2}{\rho} \frac{\partial}{\partial x} \left(e_1 - e_2 + \frac{P_1}{\rho_1} - \frac{P_2}{\rho_2} - (s_1 - s_2)T\right) + \\
 & + \frac{(P_1 - P_2)}{\rho} \frac{\partial}{\partial x} \alpha_1 + \frac{\alpha_1}{\rho} \frac{\partial}{\partial x} P_1 + \frac{\alpha_2}{\rho} \frac{\partial}{\partial x} P_2 = (g + \theta(u_1 - u_2)) - \frac{\alpha_2 \rho_2}{\rho^2} \lambda_0.
 \end{aligned} \tag{2.52}$$

Now, from the thermodynamic identity

$$Tds_i = de_i - \frac{P_i}{\rho_i^2} d\rho_i, \tag{2.53}$$

we have

$$d \left( e_i + \frac{P_i}{\rho_i} - s_i T \right) = de_i + \frac{1}{\rho_i} dP_i - \frac{P_i}{\rho_i^2} d\rho_i - s_i dT - T ds_i = \frac{1}{\rho_i} dP_i - s_i dT, \tag{2.54}$$

and, substituting Eq. (2.54) in the last equation of (2.52), we obtain the equation for the velocity of the first phase:

$$\begin{aligned}
 & \frac{\partial u_1}{\partial t} + u_1 \frac{\partial}{\partial x} u_1 + \frac{\alpha_2 \rho_2}{\rho} \left( \frac{1}{\rho_1} \frac{\partial}{\partial x} P_1 - s_1 \frac{\partial}{\partial x} T - \frac{1}{\rho_2} \frac{\partial}{\partial x} P_2 + s_2 \frac{\partial}{\partial x} T \right) + \\
 & + \frac{(P_1 - P_2)}{\rho} \frac{\partial}{\partial x} \alpha_1 + \frac{\alpha_1}{\rho} \frac{\partial}{\partial x} P_1 + \frac{\alpha_2}{\rho} \frac{\partial}{\partial x} P_2 = (g + \theta(u_1 - u_2)) - \frac{\alpha_2 \rho_2}{\rho^2} \lambda_0 \\
 & \quad \Downarrow \\
 & \frac{\partial u_1}{\partial t} + u_1 \frac{\partial}{\partial x} u_1 + \left( \frac{\alpha_2 \rho_2}{\rho_1 \rho} + \frac{\alpha_1}{\rho} \right) \frac{\partial}{\partial x} P_1 + \left( -\frac{1}{\rho_2} \frac{\alpha_2 \rho_2}{\rho} + \frac{\alpha_2}{\rho} \right) \frac{\partial}{\partial x} P_2 + \\
 & + \frac{(P_1 - P_2)}{\rho} \frac{\partial}{\partial x} \alpha_1 + \frac{\alpha_2 \rho_2}{\rho} (s_2 - s_1) \frac{\partial}{\partial x} T = (g + \theta(u_1 - u_2)) - \frac{\alpha_2 \rho_2}{\rho^2} \lambda_0 \\
 & \quad \Downarrow \\
 & \frac{\partial u_1}{\partial t} + u_1 \frac{\partial}{\partial x} u_1 + \frac{1}{\rho_1} \frac{\partial}{\partial x} P_1 + \frac{(P_1 - P_2)}{\rho} \frac{\partial}{\partial x} \alpha_1 + \\
 & + \frac{\alpha_2 \rho_2}{\rho} (s_2 - s_1) \frac{\partial}{\partial x} T = (g + \theta(u_1 - u_2)) - \frac{\alpha_2 \rho_2}{\rho^2} \lambda_0.
 \end{aligned} \tag{2.55}$$

Finally, subtracting the relative velocity equation (2.23) from the previous equation we find the equation for the velocity of the second phase

$$\begin{aligned}
 & \frac{\partial u_2}{\partial t} + u_2 \frac{\partial}{\partial x} u_2 + \frac{1}{\rho_2} \frac{\partial}{\partial x} P_2 + \frac{(P_1 - P_2)}{\rho} \frac{\partial}{\partial x} \alpha_1 - \\
 & - \frac{\alpha_1 \rho_1}{\rho} (s_2 - s_1) \frac{\partial}{\partial x} T = (g + \theta(u_1 - u_2)) + \frac{\alpha_1 \rho_1}{\rho^2} \lambda_0.
 \end{aligned} \tag{2.56}$$

Now, from the equations obtained for the primitive variables  $[\alpha_1, S, \rho_1, \rho_2, u_1, u_2]$ , we can finally write the single-temperature model in the following non conservative quasi-linear form:

$$\begin{aligned}
& \frac{\partial \alpha_1}{\partial t} + u \frac{\partial \alpha_1}{\partial x} = -\frac{\phi}{\rho} \\
& \frac{\partial S}{\partial t} + u \frac{\partial S}{\partial x} = \\
& = \frac{1}{T} \left[ \frac{(P_1 - P_2)^2}{\rho \tau^{(p)}} + \frac{1}{\rho \tau^{(c)}} \left( \mu_1 - \mu_2 + (1 - 2c) \frac{w^2}{2} \right)^2 + \frac{c^2(1 - c)^2}{\rho^2} \zeta \right] \\
& \frac{\partial \rho_1}{\partial t} + \frac{\alpha_2 \rho_2 \rho_1}{\alpha_1 \rho} (u_1 - u_2) \frac{\partial \alpha_1}{\partial x} + u_1 \frac{\partial \rho_1}{\partial x} + \rho_1 \frac{\partial u_1}{\partial x} = \frac{\rho_1 \phi}{\alpha_1 \rho} - \frac{\rho}{\alpha_1} \theta \\
& \frac{\partial \rho_2}{\partial t} + \frac{\alpha_1 \rho_1 \rho_2}{\alpha_2 \rho} (u_1 - u_2) \frac{\partial \alpha_1}{\partial x} + u_2 \frac{\partial \rho_2}{\partial x} + \rho_2 \frac{\partial u_2}{\partial x} = -\frac{\rho_2 \phi}{\alpha_2 \rho} + \frac{\rho}{\alpha_2} \theta \quad (2.57) \\
& \frac{\partial u_1}{\partial t} + u_1 \frac{\partial u_1}{\partial x} + \frac{1}{\rho_1} \frac{\partial P_1}{\partial x} + \frac{P_1 - P_2}{\rho} \frac{\partial \alpha_1}{\partial x} - c_2(s_1 - s_2) \frac{\partial T}{\partial x} = \\
& = (g + \theta(u_1 - u_2)) - \frac{\alpha_2 \rho_2}{\rho^2} \lambda_0 \\
& \frac{\partial u_2}{\partial t} + u_2 \frac{\partial u_2}{\partial x} + \frac{1}{\rho_2} \frac{\partial P_2}{\partial x} + \frac{P_1 - P_2}{\rho} \frac{\partial \alpha_1}{\partial x} + c_1(s_1 - s_2) \frac{\partial T}{\partial x} = \\
& = (g + \theta(u_1 - u_2)) + \frac{\alpha_1 \rho_1}{\rho^2} \lambda_0.
\end{aligned}$$

In order to have the system in the desired form (2.43), we have to express the derivatives  $\partial P_i / \partial x$  and  $\partial T / \partial x$  as functions of the derivatives of the primitive variables with respect to  $x$ . We observe that, because of the equal phase temperatures, one can derive phase entropy  $s_i$  as a function of volume fraction  $\alpha_1$ , phase densities and mixture entropy ( $s_1 = \tilde{s}_1(\alpha_1, \rho_1, \rho_2, S)$ ,  $s_2 = \tilde{s}_2(\alpha_1, \rho_1, \rho_2, S)$ ), by solving the system of equations

$$T_1 = \frac{\partial(e_1(\rho_1, s_1))}{\partial s_1} = T, \quad T_2 = \frac{\partial(e_2(\rho_2, s_2))}{\partial s_2} = T, \quad c_1 s_1 + c_2 s_2 = S. \quad (2.58)$$

From the first two equations, solving for  $s_1$  and  $s_2$ , we can find  $s_1 = \bar{s}_1(\rho_1, T)$  and  $s_2 = \bar{s}_2(\rho_2, T)$ . Now, substituting in the last equation and solving for  $T$ , we can find

$$T = \tilde{T}(\alpha_1, \rho_1, \rho_2, S). \quad (2.59)$$

Then, we can define  $\tilde{s}_1$  and  $\tilde{s}_2$  as

$$\tilde{s}_1 = \bar{s}_1(\rho_1, \tilde{T}), \quad \tilde{s}_2 = \bar{s}_2(\rho_2, \tilde{T}),$$

and, from the equations of state, we can write the phase pressures and the common temperature as

$$\tilde{P}_i(\alpha_1, \rho_1, \rho_2, S) = P_i(\rho_i, \tilde{s}_i), \quad \tilde{T}(\alpha_1, \rho_1, \rho_2, S) = T_i(\rho_i, \tilde{s}_i),$$

and their derivatives with respect to  $x$  as

$$\frac{\partial T}{\partial x} = \frac{\partial \tilde{T}}{\partial \alpha_1} \frac{\partial \alpha_1}{\partial x} + \frac{\partial \tilde{T}}{\partial \rho_1} \frac{\partial \rho_1}{\partial x} + \frac{\partial \tilde{T}}{\partial \rho_2} \frac{\partial \rho_2}{\partial x} + \frac{\partial \tilde{T}}{\partial S} \frac{\partial S}{\partial x} \quad (2.60)$$

$$\frac{\partial P_i}{\partial x} = \frac{\partial \tilde{P}_i}{\partial \alpha_1} \frac{\partial \alpha_1}{\partial x} + \frac{\partial \tilde{P}_i}{\partial \rho_1} \frac{\partial \rho_1}{\partial x} + \frac{\partial \tilde{P}_i}{\partial \rho_2} \frac{\partial \rho_2}{\partial x} + \frac{\partial \tilde{P}_i}{\partial S} \frac{\partial S}{\partial x}. \quad (2.61)$$

Substituting them in the quasi-linear system (2.57), we can finally write the matrix  $B(\mathbf{V})$  as

$$B = \begin{bmatrix} u & 0 & 0 & 0 & 0 & 0 \\ 0 & u & 0 & 0 & 0 & 0 \\ b_{3,1} & 0 & u_1 & 0 & \rho_1 & 0 \\ b_{4,1} & 0 & 0 & u_2 & 0 & \rho_2 \\ b_{5,1} & b_{5,2} & \frac{1}{\rho_1} \frac{\partial \tilde{P}_1}{\partial \rho_1} - c_2(s_1 - s_2) \frac{\partial \tilde{T}}{\partial \rho_1} & \frac{1}{\rho_1} \frac{\partial \tilde{P}_1}{\partial \rho_2} - c_2(s_1 - s_2) \frac{\partial \tilde{T}}{\partial \rho_2} & u_1 & 0 \\ b_{6,1} & b_{6,2} & \frac{1}{\rho_2} \frac{\partial \tilde{P}_2}{\partial \rho_1} + c_1(s_1 - s_2) \frac{\partial \tilde{T}}{\partial \rho_1} & \frac{1}{\rho_2} \frac{\partial \tilde{P}_2}{\partial \rho_2} + c_1(s_1 - s_2) \frac{\partial \tilde{T}}{\partial \rho_1} & 0 & u_2 \end{bmatrix}, \quad (2.62)$$

where

$$b_{3,1} = c_2 \frac{\rho_1}{\alpha_1} (u_1 - u_2), \quad (2.63)$$

$$b_{4,1} = c_1 \frac{\rho_2}{\alpha_2} (u_1 - u_2), \quad (2.64)$$

$$b_{5,1} = \frac{P_1 - P_2}{\rho} + \frac{1}{\rho_1} \frac{\partial \tilde{P}_1}{\partial \alpha_1} - c_2(s_1 - s_2) \frac{\partial \tilde{T}}{\partial \alpha_1}, \quad (2.65)$$

$$b_{5,2} = \frac{1}{\rho_1} \frac{\partial \tilde{P}_1}{\partial S} - c_2(s_1 - s_2) \frac{\partial \tilde{T}}{\partial S}, \quad (2.66)$$

$$b_{6,1} = \frac{P_1 - P_2}{\rho} + \frac{1}{\rho_2} \frac{\partial \tilde{P}_2}{\partial \alpha_1} + c_1(s_1 - s_2) \frac{\partial \tilde{T}}{\partial \alpha_1}, \quad (2.67)$$

$$b_{6,2} = \frac{1}{\rho_2} \frac{\partial \tilde{P}_2}{\partial S} + c_1(s_1 - s_2) \frac{\partial \tilde{T}}{\partial S}. \quad (2.68)$$

Due to the structure of the matrix  $B$ , the equation for the eigenvalues does not depend on the coefficients  $b_{i,j}$  defined in Eqs. (2.63)–(2.68) and it takes the form

$$\pi(\lambda) = (u - \lambda)^2 \cdot \det(A - \lambda I), \quad (2.69)$$

where the matrix  $A$  is

$$A = \begin{bmatrix} u_1 & 0 & \rho_1 & 0 \\ 0 & u_2 & 0 & \rho_2 \\ \frac{1}{\rho_1} \frac{\partial \tilde{P}_1}{\partial \rho_1} - c_2(s_1 - s_2) \frac{\partial \tilde{T}}{\partial \rho_1} & \frac{1}{\rho_1} \frac{\partial \tilde{P}_1}{\partial \rho_2} - c_2(s_1 - s_2) \frac{\partial \tilde{T}}{\partial \rho_2} & u_1 & 0 \\ \frac{1}{\rho_2} \frac{\partial \tilde{P}_2}{\partial \rho_1} + c_1(s_1 - s_2) \frac{\partial \tilde{T}}{\partial \rho_1} & \frac{1}{\rho_2} \frac{\partial \tilde{P}_2}{\partial \rho_2} + c_1(s_1 - s_2) \frac{\partial \tilde{T}}{\partial \rho_2} & 0 & u_2 \end{bmatrix}. \quad (2.70)$$

The characteristic polynomial of  $A$  is  $\tilde{\pi}(\lambda) = \sum_{i=0}^4 a_i \lambda^i$  where

$$a_4 = 1,$$

$$a_3 = -(2u_1 + 2u_2),$$

$$a_2 = \left( u_1^2 + u_2^2 + 4u_1u_2 - \frac{\partial \tilde{P}_1}{\partial \rho_1} - \frac{\partial \tilde{P}_2}{\partial \rho_2} - c_1\rho_2(s_1 - s_2) \frac{\partial \tilde{T}}{\partial \rho_2} + c_2\rho_1(s_1 - s_2) \frac{\partial \tilde{T}}{\partial \rho_1} \right),$$

$$a_1 = - \left( 2u_1u_2^2 + 2u_1^2u_2 - 2u_2 \frac{\partial \tilde{P}_1}{\partial \rho_1} - 2u_1 \frac{\partial \tilde{P}_2}{\partial \rho_2} - \right.$$

$$\left. - 2c_1\rho_2u_1(s_1 - s_2) \frac{\partial \tilde{T}}{\partial \rho_2} + 2c_2\rho_1u_2(s_1 - s_2) \frac{\partial \tilde{T}}{\partial \rho_1} \right),$$

$$a_0 = \left( u_1^2u_2^2 - u_2^2 \frac{\partial \tilde{P}_1}{\partial \rho_1} - u_1^2 \frac{\partial \tilde{P}_2}{\partial \rho_2} - c_1\rho_2u_1^2(s_1 - s_2) \frac{\partial \tilde{T}}{\partial \rho_2} + c_2\rho_1u_2^2(s_1 - s_2) \frac{\partial \tilde{T}}{\partial \rho_1} + \right.$$

$$\left. + \frac{\partial \tilde{P}_1}{\partial \rho_1} \frac{\partial \tilde{P}_2}{\partial \rho_2} - \frac{\partial \tilde{P}_1}{\partial \rho_2} \frac{\partial \tilde{P}_2}{\partial \rho_1} + c_1\rho_2(s_1 - s_2) \frac{\partial \tilde{P}_1}{\partial \rho_1} \frac{\partial \tilde{T}}{\partial \rho_2} - c_1\rho_2(s_1 - s_2) \frac{\partial \tilde{P}_1}{\partial \rho_2} \frac{\partial \tilde{T}}{\partial \rho_1} + \right.$$

$$\left. + c_2\rho_1(s_1 - s_2) \frac{\partial \tilde{P}_2}{\partial \rho_1} \frac{\partial \tilde{T}}{\partial \rho_2} - c_2\rho_1(s_1 - s_2) \frac{\partial \tilde{P}_2}{\partial \rho_2} \frac{\partial \tilde{T}}{\partial \rho_1} \right).$$

We observe that it is possible to write the characteristic polynomial  $\tilde{\pi}(\lambda)$  in the more compact form

$$\tilde{\pi}(\lambda) = \pi_1(\lambda) \cdot \pi_2(\lambda) - \pi_3, \quad (2.71)$$

where

$$\pi_1(\lambda) = \lambda^2 - 2u_1\lambda + u_1^2 - \frac{\partial \tilde{P}_1}{\partial \rho_1} + c_2\rho_1(s_1 - s_2) \frac{\partial \tilde{T}}{\partial \rho_1},$$

$$\pi_2(\lambda) = \lambda^2 - 2u_2\lambda + u_2^2 - \frac{\partial \tilde{P}_2}{\partial \rho_2} - c_1\rho_2(s_1 - s_2) \frac{\partial \tilde{T}}{\partial \rho_2}, \quad (2.72)$$

$$\pi_3 = \left( \frac{\partial \tilde{P}_2}{\partial \rho_1} + c_1\rho_2(s_1 - s_2) \frac{\partial \tilde{T}}{\partial \rho_1} \right) \cdot \left( \frac{\partial \tilde{P}_1}{\partial \rho_2} - c_2\rho_1(s_1 - s_2) \frac{\partial \tilde{T}}{\partial \rho_2} \right).$$

### 2.2.2 Derivatives analysis

In order to obtain the coefficients of the characteristic polynomial, we need to evaluate the derivatives  $\partial \tilde{P}_i / \partial \rho_j$  and  $\partial \tilde{T} / \partial \rho_j$ , and consequently the solution of the system (2.58) for  $\tilde{s}_1$  and  $\tilde{s}_2$ . This can be done by solving the system of equations (2.58) for  $\tilde{s}_1$  and  $\tilde{s}_2$ , in order to write explicitly an the expressions for  $\tilde{P}_i(\alpha_1, \rho_1, \rho_2, S)$  and  $\tilde{T}(\alpha_1, \rho_1, \rho_2, S)$ .

we show here that is possible to write the two derivatives only in terms of the original equation of state (2.5), i.e. without the need of evaluating explicitly the terms  $\tilde{s}_1$  and  $\tilde{s}_2$ .

Using the definition of  $\tilde{T}$ , we can write:

$$\frac{\partial \tilde{T}}{\partial \rho_j} = \frac{\partial}{\partial \rho_j} T_j(\rho_j, \tilde{s}_j) = \frac{\partial T_j}{\partial \rho_j} + \frac{\partial T_j}{\partial s_j} \frac{\partial \tilde{s}_j}{\partial \rho_j}. \quad (2.73)$$

Now, from the system of equations (2.58), we define the function  $G$  as:

$$G(\alpha_1, \rho_1, \rho_2, \tilde{s}_2, S) = c_1 T_{1,\rho_1}^{-1}(T_2(\rho_2, \tilde{s}_2)) + c_2 \tilde{s}_2 - S = 0, \quad (2.74)$$

where  $T_{1,\rho_1}^{-1}(\cdot)$  is the inverse function of  $T_1(\rho_1, \cdot)$  with respect to the entropy  $s_1$  (i.e.  $s_1 = T_{1,\rho_1}^{-1}(T)$ ) and, using the implicit function theorem, we can write

$$\begin{aligned} \frac{\partial \tilde{s}_2}{\partial \rho_2} &= -\frac{G_{\rho_2}}{G_{\tilde{s}_2}} = -\frac{\frac{\partial c_1}{\partial \rho_2} T_{1,\rho_1}^{-1}(T_2(\rho_2, \tilde{s}_2)) + c_1 \frac{\partial T_{1,\rho_1}^{-1}}{\partial T} \frac{\partial T_2}{\partial \rho_2} + \frac{\partial c_2}{\partial \rho_2} s_2}{c_1 \frac{\partial T_{1,\rho_1}^{-1}}{\partial T} \frac{\partial T_2}{\partial s_2} + c_2} = \\ &= -\frac{\frac{\partial c_1}{\partial \rho_2} s_1 + c_1 \frac{\partial T_2}{\partial \rho_2} / \frac{\partial T_1}{\partial s_1} + \frac{\partial c_2}{\partial \rho_2} s_2}{c_1 \frac{\partial T_2}{\partial s_2} / \frac{\partial T_1}{\partial s_1} + c_2} = -\frac{\frac{\partial c_1}{\partial \rho_2} (s_1 - s_2) + c_1 \frac{\partial T_2}{\partial \rho_2} / \frac{\partial T_1}{\partial s_1}}{c_1 \frac{\partial T_2}{\partial s_2} / \frac{\partial T_1}{\partial s_1} + c_2} = \\ &= -\frac{\frac{\partial c_1}{\partial \rho_2} (s_1 - s_2) \frac{\partial T_1}{\partial s_1} + c_1 \frac{\partial T_2}{\partial \rho_2}}{c_1 \frac{\partial T_2}{\partial s_2} + c_2 \frac{\partial T_1}{\partial s_1}}. \end{aligned} \quad (2.75)$$

In the same way, from the system of equations (2.58), we define the function  $H$  as:

$$H(\alpha_1, \rho_1, \rho_2, \tilde{s}_1, S) = c_2 T_{2,\rho_2}^{-1}(T_1(\rho_1, \tilde{s}_1)) + c_1 \tilde{s}_1 - S = 0, \quad (2.76)$$

and we obtain

$$\begin{aligned}
\frac{\partial \tilde{s}_1}{\partial \rho_1} &= -\frac{H_{\rho_1}}{H_{\tilde{s}_1}} = -\frac{\frac{\partial c_2}{\partial \rho_1} T_{2,\rho_2}^{-1}(T_1(\rho_1, \tilde{s}_1)) + c_2 \frac{\partial T_{2,\rho_2}^{-1}}{\partial T} \frac{\partial T_1}{\partial \rho_1} + \frac{\partial c_1}{\partial \rho_1} s_1}{c_2 \frac{\partial T_2^{-1}}{\partial T} \frac{\partial T_1}{\partial s_1} + c_1} = \\
&= -\frac{\frac{\partial c_2}{\partial \rho_1} s_2 + c_2 \frac{\partial T_1}{\partial \rho_2} / \frac{\partial T_2}{\partial s_2} + \frac{\partial c_1}{\partial \rho_1} s_1}{c_2 \frac{\partial T_1}{\partial s_1} / \frac{\partial T_2}{\partial s_2} + c_1} = -\frac{\frac{\partial c_2}{\partial \rho_1} (s_1 - s_2) + c_2 \frac{\partial T_1}{\partial \rho_1} / \frac{\partial T_2}{\partial s_2}}{c_2 \frac{\partial T_1}{\partial s_1} / \frac{\partial T_2}{\partial s_2} + c_1} = \\
&= -\frac{\frac{\partial c_2}{\partial \rho_1} (s_1 - s_2) \frac{\partial T_2}{\partial s_2} + c_2 \frac{\partial T_1}{\partial \rho_1}}{c_2 \frac{\partial T_1}{\partial s_1} + c_1 \frac{\partial T_2}{\partial s_2}}.
\end{aligned} \tag{2.77}$$

Now, expanding the derivatives of  $\tilde{P}_i$ , we can write

$$\begin{aligned}
\frac{\partial \tilde{P}_i}{\partial \rho_j} &= \frac{\partial}{\partial \rho_j} P_i(\rho_i, \tilde{s}_i) = \delta_{ij} \frac{\partial P_i}{\partial \rho_j} + \frac{\partial P_i}{\partial s_i} \frac{\partial \tilde{s}_i}{\partial \rho_j} = \\
&= \delta_{ij} C_j^2 + \left[ \frac{\partial}{\partial s_i} \left( \rho_i^2 \frac{\partial e_i(\rho_i, s_i)}{\partial \rho_i} \right) \right] \frac{\partial \tilde{s}_i}{\partial \rho_j} = \\
&= \delta_{ij} C_j^2 + \rho_i^2 \frac{\partial T_i}{\partial \rho_i} \frac{\partial \tilde{s}_i}{\partial \rho_j},
\end{aligned} \tag{2.78}$$

where  $C_i$  is the isentropic sound speed of the  $i$ -th phase defined as

$$C_i = \sqrt{\frac{\partial P_i(\rho_i, s_i)}{\partial \rho_i}}. \tag{2.79}$$

We observe that, to evaluate the expressions we have found for the derivatives  $\partial \tilde{P}_i / \partial \rho_j$  and  $\partial \tilde{T} / \partial \rho_j$ , it is requested only the knowledge of the sound speeds  $C_i$  and of the partial derivatives of the temperatures, both defined in terms of the original equations of state (2.5)–(2.6). Furthermore, being  $T_i = T_i(\rho_i, s_i)$ , we have, independently from the particular choice of the equations of state,

$$\frac{\partial T_i}{\partial s_i} = \frac{T_i}{c_{v,i}}, \quad \frac{\partial T_i}{\partial \rho_i} = \frac{T_i \Gamma_i}{\rho_i}, \tag{2.80}$$

where  $c_{v,i}$  is the specific heat capacity at constant volume of the  $i$ -th phase and  $\Gamma_i$  is the Grüneisen coefficient, defined in Menikoff and Plohr (1989) as a function of the thermal expansion coefficient and the isothermal compressibility.

### 2.2.3 Eigenvalues numerical estimation

Due to the complexity of the equations, the development of exact or approximate Riemann solvers for the two-phase single temperature model can be a difficult task. In

particular, the evaluation of the eigenvalues and the eigenvectors of the matrix  $B$  can be very expensive from a computational point of view. An alternative way to find the solution is to apply central schemes, that are not tied on the specific eigenstructure of the problem. The only characteristic information necessary for the construction of the central schemes is the knowledge of the largest positive and negative local propagation speeds. Thus, we have to evaluate the largest and smallest roots of the characteristic polynomial  $\tilde{\pi}(\lambda)$ .

First of all, we observe that, due to the fact that the system of equations (2.19)–(2.24) is hyperbolic (which follows from the derivation of the governing equations using the principle of thermodynamically compatible systems), the characteristic polynomial  $\tilde{\pi}(\lambda)$  has four real roots  $\lambda_1 \leq \lambda_2 \leq \lambda_3 \leq \lambda_4$ . Now, being the coefficient  $a_4 > 0$ , we have:

$$\tilde{\pi}(\lambda) > 0 \text{ and } \frac{\partial^2 \tilde{\pi}}{\partial \lambda^2}(\lambda) > 0 \quad \text{for } \lambda < \lambda_1 \text{ or } \lambda > \lambda_4. \quad (2.81)$$

The positivity of both the polynomial and its second derivative ensures that the iterative Newton's method

$$x_{n+1} = x_n - \frac{\tilde{\pi}(x_n)}{\tilde{\pi}'(x_n)},$$

with a starting point  $x_0 < \lambda_1$ , converges to the smallest eigenvalue  $\lambda_1$ , and with a starting point  $x_0 > \lambda_4$ , converges to the largest eigenvalue  $\lambda_4$ . The initial guess  $x_0$  can be easily determined using the Gershgorin circle theorem, or with a lower and upper estimates of the solutions of the characteristic polynomial.

#### 2.2.4 Simplified models

We analyze here the eigenvalues of the Jacobian matrix in some particular case with additional hypothesis that simplify the model.

First, we consider the case with a single velocity, i.e.  $u_1 = u_2 = u$ , corresponding to analytical solution obtained with a relative velocity relaxation ( $\lambda_0 = +\infty$ ). With this assumption the characteristic polynomial  $\tilde{\pi}(\lambda)$  takes the following form:

$$\left[ y - \left( \frac{\partial \tilde{P}_1}{\partial \rho_1} - c_2 \rho_1 (s_1 - s_2) \frac{\partial \tilde{T}}{\partial \rho_1} \right) \right] \left[ y - \left( \frac{\partial \tilde{P}_2}{\partial \rho_2} + c_1 \rho_2 (s_1 - s_2) \frac{\partial \tilde{T}}{\partial \rho_2} \right) \right] - \pi_3, \quad (2.82)$$

where

$$y = (\lambda - u)^2.$$

Now, from the two solutions  $y_1$  e  $y_2$  of the second order polynomial (2.82), we obtain

$$\lambda_{1,2} = u \pm \sqrt{y_1}; \quad \lambda_{3,4} = u \pm \sqrt{y_2},$$

where the terms  $y_1$  and  $y_2$  do not depends on the velocities of the two phases. Furthermore, from the expression we have derived for  $\frac{\partial \tilde{P}_i}{\partial \rho_i}$  and  $\frac{\partial \tilde{T}}{\partial \rho_i}$ , we have that

$$y_1 \rightarrow C_1^2 \quad \text{for } \alpha_1 \rightarrow 0, \quad (2.83)$$

$$y_2 \rightarrow C_2^2 \quad \text{for } \alpha_1 \rightarrow 1. \quad (2.84)$$

Thus, in the case of very dilute regime, two eigenvalues approach the usual characteristic velocities associated with the carrier phase, given by the velocity of the phase plus and minus the phase sound speed.

## 2.3 EQUATION OF STATE

In this section the equations of state employed in the model for gas-liquid flows are presented. These are obtained from a linearized form of the Mie-Grüneisen equations (Le Métayer et al., 2004, 2005; Menikoff and Plohr, 1989; Romenski et al., 2010).

For the gas phase, the perfect gas equation of state is used in the form:

$$e_g(\rho_g, s_g) = \bar{e}_g + c_{v,g} T_{0,g} \left( \frac{\rho_g}{\rho_{0,g}} \right)^{\gamma_g - 1} \exp \left( \frac{s_g - s_{0,g}}{c_{v,g}} \right), \quad (2.85)$$

where  $\bar{e}_g$  is a constant parameter representing the formation energy of the fluid,  $\rho_{0,g}$  is the reference density,  $T_{0,g}$  is the reference temperature,  $s_{0,g}$  is the entropy at the reference state  $(\rho_{0,g}, T_{0,g})$ ,  $\gamma_g$  is the adiabatic exponent and  $c_{v,g}$  is the specific heat capacity at constant volume. The pressure and temperature can be calculated from the equation of state using the expressions of Eq. (2.6), obtaining

$$\begin{aligned} P_g(\rho_g, s_g) &= \rho_g^2 \frac{\partial e_g}{\partial \rho_g} = (\gamma_g - 1) \rho_{0,g} c_{v,g} T_{0,g} \left( \frac{\rho_g}{\rho_{0,g}} \right)^{\gamma_g} \exp \left( \frac{s_g - s_{0,g}}{c_{v,g}} \right), \\ T_g(\rho_g, s_g) &= \frac{\partial e_g}{\partial s_g} = T_{0,g} \left( \frac{\rho_g}{\rho_{0,g}} \right)^{\gamma_g - 1} \exp \left( \frac{s_g - s_{0,g}}{c_{v,g}} \right). \end{aligned} \quad (2.86)$$

From the first equation, using Eq. (2.79), we obtain for the isentropic sound speed  $C_g(\rho_g, s_g)$  the following expression:

$$C_g^2 = \gamma_g (\gamma_g - 1) c_{v,g} T_{0,g} \left( \frac{\rho_g}{\rho_{0,g}} \right)^{\gamma_g} \exp \left( \frac{s_g - s_{0,g}}{c_{v,g}} \right), \quad (2.87)$$

and we can define a reference speed of sound  $C_{0,g}$  as the following function of the reference temperature  $T_{0,g}$ :

$$C_{0,g} = \sqrt{c_{v,g} T_{0,g} \gamma_g (\gamma_g - 1)}. \quad (2.88)$$

Then, the specific energy can be also written as

$$e_g(\rho_g, s_g) = \bar{e}_g + \frac{C_{0,g}^2}{\gamma_g (\gamma_g - 1)} \exp \left( \frac{s_g - s_{0,g}}{c_{v,g}} \right). \quad (2.89)$$

This expression for the specific energy is analogous to the expression presented in Romenski et al. (2010), with the difference of the presence of the two constants  $\bar{e}_g$ , representing the formation energy of the fluid, and  $s_{0,g}$ , added to the specific entropy in order to ensure the thermodynamic equilibrium when the chemical potentials of the two phases are equal Le Métayer et al. (2004).

Now, when dealing with a liquid phase, the additional parameter  $P_{0,l}$  denoting the reference pressure of the liquid phase is introduced and the following stiffened equation of state is adopted:

$$e_l(\rho_l, s_l) = \bar{e}_l + c_{v,l} T_{0,l} \left( \frac{\rho_l}{\rho_{0,l}} \right)^{\gamma_l - 1} \exp \left( \frac{s_l - s_{0,l}}{c_{v,l}} \right) + \frac{\rho_{0,l} C_{0,l}^2 - \gamma_l P_{0,l}}{\gamma_l \rho_l}. \quad (2.90)$$

As done for the gas phase, the pressure and temperature for the liquid phase are obtained using the relationship from Eq. (2.6):

$$\begin{aligned} P_l(\rho_l, s_l) &= (\gamma_l - 1)\rho_{0,l}c_{v,l}T_{0,l} \left( \frac{\rho_l}{\rho_{0,l}} \right)^{\gamma_l} \exp \left( \frac{s_l - s_{0,l}}{c_{v,l}} \right) - \frac{\rho_{0,l}C_{0,l}^2 - \gamma_l P_{0,l}}{\gamma_l}, \\ T_l(\rho_l, s_l) &= T_{0,l} \left( \frac{\rho_l}{\rho_{0,l}} \right)^{\gamma_l-1} \exp \left( \frac{s_l - s_{0,l}}{c_{v,l}} \right). \end{aligned} \quad (2.91)$$

We observe that, if we define for the gas phase a reference pressure in the following way:

$$P_{0,g} = \frac{\rho_{0,g}C_{0,g}}{\gamma_g}, \quad (2.92)$$

then the stiffened equation of state (2.90) is valid for also the gas. Furthermore, from this equation, the pressure for both the phases can be written as a function of the density and of the specific internal energy:

$$P_i(\rho_i, e_i) = (\gamma_i - 1)\rho_i(e_i - \bar{e}_i) - (\rho_{0,i}C_{0,i}^2 - \gamma_i P_{0,i}), \quad i \in \{g, l\}. \quad (2.93)$$

This expression has the same form of the equation of state utilized in Le Métayer et al. (2004) for the “Stiffened Gas” approximation, and it highlights the contribution of  $q_i = (\rho_{0,i}C_{0,i}^2 - \gamma_i P_{0,i})$  to the term  $(\gamma_i - 1)\rho_i(e_i - q_i)$  in the phase pressure, representing a repulsive effect present in all the media (gas, liquid and solid) due to the molecular agitation.

We observe also that it is possible to write the energy and the pressure of the two phases in a more convenient form as functions of the densities  $\rho_i$  and the common temperature  $T$  as:

$$e_i(\rho_i, T) = \bar{e}_i + c_{v,i}T + \frac{\rho_{0,i}C_{0,i}^2 - \gamma_i P_{0,i}}{\gamma_i \rho_i}, \quad (2.94)$$

$$P_i(\rho_i, T) = c_{v,i}(\gamma_i - 1)\rho_iT - \frac{\rho_{0,i}C_{0,i}^2 - \gamma_i P_{0,i}}{\gamma_i}, \quad (2.95)$$

$$s_i(\rho_i, T) = s_0 + c_{v,i} \ln \left[ \frac{T}{T_{0,i}} \left( \frac{\rho_{0,i}}{\rho_i} \right)^{\gamma_i-1} \right]. \quad (2.96)$$

Introducing the notation  $\bar{P}_i$  for the limit of the pressure of the  $i$ -th phase at absolute zero ( $T = 0$  K):

$$\bar{P}_i = \frac{\rho_{0,i}C_{0,i}^2 - \gamma_i P_{0,i}}{\gamma_i}, \quad (2.97)$$

we obtain the more compact form for the specific energy and the pressure:

$$e_i(\rho_i, T) = \bar{e}_i + c_{v,i}T + \frac{\bar{P}_i}{\rho_i}, \quad (2.98)$$

$$P_i(\rho_i, T) = c_{v,i}(\gamma_i - 1)\rho_iT - \bar{P}_i. \quad (2.99)$$

The negative term  $-\bar{P}_i$  in the equation for the pressure represents the effects of the molecular attraction guaranteeing the cohesion in the liquid and solid phases.

Using the expressions above for the specific energy, the pressure and the specific entropy as functions of the density and the temperature, we find the following expression for the chemical potentials  $\mu_i$ :

$$\mu_i = \bar{e}_i - T c_{v,i} \left( \frac{s_{0,i}}{\gamma_i} - \gamma_i + \ln \left[ \frac{T}{T_{0,i}} \left( \frac{\rho_{0,i}}{\rho_i} \right)^{\gamma_i-1} \right] \right), \quad (2.100)$$

or, in terms of the reference sound speed  $C_{0,i}$  instead of the reference temperature  $T_{0,i}$ :

$$\mu_i = \bar{e}_i - T c_{v,i} \left( \frac{s_{0,i}}{\gamma_i} - \gamma_i - \ln \left[ \frac{T c_{v,i} \gamma_i (\gamma_i - 1)}{C_{0,i}^2} \left( \frac{\rho_{0,i}}{\rho_i} \right)^{\gamma_i-1} \right] \right). \quad (2.101)$$

#### 2.4 COMPARISON OF MODELS

In the previous sections, a compressible two-phase flow model with two velocities, two pressures and a single temperature has been reported. This model has been derived using the principle of the thermodynamically compatible systems (see Appendix A), that allow us to write the system in conservative form. In the literature, there exist other models for compressible two-phase flow, which are based on the Baer-Nunziato model (Baer and Nunziato, 1986; Pelanti and LeVeque, 2006; Saurel and Abgrall, 1999; Saurel and Le Métayer, 2001; Zein et al., 2010). The approach used by Baer and Nunziato consists in considering the two-phase flow as two separate continua coupled by momentum and energy exchange. The resulting system of governing equations is still hyperbolic, but cannot be expressed in a conservative form.

The general two-phase flow model based on Baer and Nunziato equations consists of balance equations for mass (Eq. (2.1)), momentum (Eq. (2.2)) and energy (Eq. (2.3)) for each of the two phases, completed with a balance equation for the volume fraction (Eq. (2.4)).

The interfacial pressure is defined as the mixture pressure, while the interfacial velocity is defined as the velocity of the center of mass:

$$P_I = \alpha_1 P_1 + \alpha_2 P_2, \quad u_I = c_1 u_1 + c_2 u_2. \quad (2.102)$$

Now, we want to compare the one-dimensional Baer-Nunziato-type model with the one used in this work. In particular, rewriting the governing equations proposed in this work for each phase separately, we want compare the interfacial pressure and velocity deriving from the conservative model with those defined by Baer and Nunziato. The one-dimensional Baer-Nunziato-type model is given by the following governing equations:

$$\frac{\partial}{\partial t} (\alpha_i \rho_i) + \frac{\partial}{\partial x} (\alpha_i \rho_i u_i) = \Theta_i, \quad (2.103)$$

$$\frac{\partial}{\partial t} (\alpha_i \rho_i u_i) + \frac{\partial}{\partial x} (\alpha_i \rho_i u_i^2 + \alpha_i P_i) = P_I \frac{\partial}{\partial x} (\alpha_i) + \Gamma_i, \quad (2.104)$$

$$\frac{\partial}{\partial t} \left[ \alpha_i \rho_i \left( e_i + \frac{u_i^2}{2} \right) \right] + \frac{\partial}{\partial x} \left[ \alpha_i \rho_i u_i \left( e_i + \frac{u_i^2}{2} \right) + \alpha_i P_i u_i \right] = P_I u_I \frac{\partial}{\partial x} (\alpha_i) + \Omega_i, \quad (2.105)$$

$$\frac{\partial}{\partial t}(\alpha_1) + u_I \frac{\partial}{\partial x}(\alpha_1) = \Phi_1. \quad (2.106)$$

In the Eq. (2.45), we have already written the balance equation for the volume fraction of the model used in this thesis in the quasi-linear form. From the comparison with Eq. (2.106), we note that the interfacial velocity of both model are defined in the same way:  $u_I = u = c_1 u_1 + c_2 u_2$ .

To compare the definition of the interfacial pressure, instead, we consider the equation for the velocity of the first phase reported in Eq. (2.55). Multiplying it by  $\alpha_1 \rho_1$  and then adding and subtracting the term  $u_1 \frac{\partial \alpha_1 \rho_1}{\partial t}$  we obtain

$$\begin{aligned} & \alpha_1 \rho_1 \frac{\partial u_1}{\partial t} + u_1 \frac{\partial \alpha_1 \rho_1}{\partial t} - u_1 \frac{\partial \alpha_1 \rho_1}{\partial t} + \alpha_1 \rho_1 u_1 \frac{\partial}{\partial x} u_1 + \alpha_1 \frac{\partial}{\partial x} P_1 + \alpha_1 \rho_1 \frac{(P_1 - P_2)}{\rho} \frac{\partial}{\partial x} \alpha_1 + \\ & + \frac{\alpha_1 \rho_1 \alpha_2 \rho_2}{\rho} (s_2 - s_1) \frac{\partial}{\partial x} T = \alpha_1 \rho_1 (g + \theta(u_1 - u_2)) - \frac{\alpha_1 \rho_1 \alpha_2 \rho_2}{\rho^2} \lambda_0 \\ & \Downarrow \\ & \frac{\partial \alpha_1 \rho_1 u_1}{\partial t} + u_1 \frac{\partial \alpha_1 \rho_1 u_1}{\partial x} + \rho \theta u_1 + \alpha_1 \rho_1 u_1 \frac{\partial}{\partial x} u_1 + \alpha_1 \frac{\partial}{\partial x} P_1 + \alpha_1 \rho_1 \frac{(P_1 - P_2)}{\rho} \frac{\partial}{\partial x} \alpha_1 + \\ & + \frac{\alpha_1 \rho_1 \alpha_2 \rho_2}{\rho} (s_2 - s_1) \frac{\partial}{\partial x} T = \alpha_1 \rho_1 (g + \theta(u_1 - u_2)) - \frac{\alpha_1 \rho_1 \alpha_2 \rho_2}{\rho^2} \lambda_0 \\ & \Downarrow \\ & \frac{\partial \alpha_1 \rho_1 u_1}{\partial t} + \frac{\partial \alpha_1 \rho_1 u_1^2}{\partial x} + \rho \theta u_1 + \frac{\partial}{\partial x} \alpha_1 P_1 - P_1 \frac{\partial}{\partial x} \alpha_1 + \alpha_1 \rho_1 \frac{(P_1 - P_2)}{\rho} \frac{\partial}{\partial x} \alpha_1 + \\ & + \frac{\alpha_1 \rho_1 \alpha_2 \rho_2}{\rho} (s_2 - s_1) \frac{\partial}{\partial x} T = \alpha_1 \rho_1 (g + \theta(u_1 - u_2)) - \frac{\alpha_1 \rho_1 \alpha_2 \rho_2}{\rho^2} \lambda_0 \\ & \Downarrow \\ & \frac{\partial \alpha_1 \rho_1 u_1}{\partial t} + \frac{\partial (\alpha_1 \rho_1 u_1^2 + \alpha_1 P_1)}{\partial x} - \left[ P_1 - \alpha_1 \rho_1 \frac{(P_1 - P_2)}{\rho} \right] \frac{\partial}{\partial x} \alpha_1 + \\ & + \frac{\alpha_1 \rho_1 \alpha_2 \rho_2}{\rho} (s_2 - s_1) \frac{\partial}{\partial x} T = -\rho \theta u_1 + \alpha_1 \rho_1 (g + \theta(u_1 - u_2)) - \frac{\alpha_1 \rho_1 \alpha_2 \rho_2}{\rho^2} \lambda_0 \\ & \Downarrow \\ & \frac{\partial \alpha_1 \rho_1 u_1}{\partial t} + \frac{\partial (\alpha_1 \rho_1 u_1^2 + \alpha_1 P_1)}{\partial x} = \left[ \frac{(\alpha_2 \rho_2 P_1 + \alpha_1 \rho_1 P_2)}{\rho} \right] \frac{\partial}{\partial x} \alpha_1 - \\ & - \frac{\alpha_1 \rho_1 \alpha_2 \rho_2}{\rho} (s_2 - s_1) \frac{\partial}{\partial x} T - \rho \theta u_1 + \alpha_1 \rho_1 (g + \theta(u_1 - u_2)) - \frac{\alpha_1 \rho_1 \alpha_2 \rho_2}{\rho^2} \lambda_0. \end{aligned} \quad (2.107)$$

Therefore, from the last equality we obtain the expression for the interfacial pressure  $\hat{P}_I$  deriving from the conservative model:

$$\hat{P}_I = c_2 P_1 + c_1 P_2. \quad (2.108)$$

The interfacial pressure  $\hat{P}_I$  is different from the interfacial pressure  $P_I$  used in the Baer-Nunziato type models. Such a difference can produce different behavior of the solutions in concrete problems. However, in the case of very fast pressure relaxation ( $P_1 \approx P_2$ ) the solutions could be very close since both interfacial pressure converge to the same value.

# 3

---

## NUMERICAL SCHEMES FOR THE GOVERNING EQUATIONS

---

In the previous chapter we have introduced a two-phase compressible model, which governing equations can be expressed, using Eqs. (2.9,2.17,2.18), in the conservative form

$$\frac{\partial \mathbf{U}}{\partial t} + \nabla \cdot \mathbf{F}(\mathbf{U}) = \mathbf{S}(\mathbf{U}). \quad (3.1)$$

The solution of this system of partial differential equations, however, cannot be calculated analytically, thus a numerical approach is required. Eq. (3.1) represents the multidimensional formulation of the two-phase compressible model. For the sake of simplicity, in this chapter, we will restrict to the one-dimensional formulation to describe the numerical schemes:

$$\frac{\partial \mathbf{U}}{\partial t} + \frac{\partial}{\partial x} \mathbf{F}(\mathbf{U}) = \mathbf{S}(\mathbf{U}). \quad (3.2)$$

Even neglecting the source terms  $\mathbf{S}(\mathbf{U})$ , computing a correct numerical approximation of the solution of non-linear conservation laws is difficult.

In the work of Hou and LeFloch (1994) it is shown that non-conservative schemes (i.e. applied to systems of PDE not expressed in conservative form) do not converge to the correct solution if a shock wave is present in the solution of conservation laws. In particular, they have shown that, in the presence of shock waves, the solution of conservation laws obtained with non-conservative schemes actually is the solution of the same system of conservation laws but coupled with proper source terms.

Conservative schemes, instead, if convergent, converge to the correct solution, even in presence of shock waves. In fact, the Lax-Wendroff theorem states that if a conservative method is convergent, then it will converge to a weak solution of the conservation law (LeVeque, 1992).

In this thesis, since the governing equations are expressed in conservative form, the attention is focused on conservative methods, and in particular the schemes we present are based on the finite volume central methods. The advantages of using central schemes are the high resolution, the simplicity of implementation and the fact that we need only the spectral radius of the Jacobian matrix of the fluxes  $\mathbf{F}$  (or the maximum and minimum eigenvalue as we have for the scheme proposed by Kurganov et al. (2001)).

Furthermore, in conjunction with the finite volume central schemes, two different approaches used to solve the system (3.2) are illustrated:

- the *Splitting* (or fractional) approach,
- the *Runge-Kutta* approach.

Splitting methods are very attractive because of their simplicity and robustness. Strang splitting provides second order accuracy if each step is at least second order accurate (Strang, 1968). However, with this strategy, it is difficult to obtain higher order accuracy, and, furthermore, they lose in precision when the problem becomes stiff (Jin, 1995).

The Splitting approach used in this work consists in solving first the hyperbolic system

$$\frac{\partial \mathbf{U}}{\partial t} + \frac{\partial \mathbf{F}(\mathbf{U})}{\partial x} = 0, \quad (3.3)$$

and then the ODE system

$$\frac{\partial \mathbf{U}}{\partial t} = \mathbf{S}(\mathbf{U}), \quad (3.4)$$

both with a full time step. Thus, for each time step, we solve the hyperbolic part of the system, and then we use the obtained solution as the initial condition for the integration of the ODE system.

The other approach used in this work is based on Runge-Kutta schemes. Recently developed Runge-Kutta methods (Pareschi, 2002; Pareschi and Russo, 2000, 2005) provide basically the same advantages of the splitting schemes, without the drawback of the order restriction (Caflisch et al., 1997; Jin, 1995)

In the following sections we give more details about both approaches and how we decide to use them to solve numerically the two-phase compressible model presented in Chapter 2.

### 3.1 SPLITTING APPROACH

In this section we present the Splitting approach used to solve the system of partial differential equation

$$\frac{\partial \mathbf{U}}{\partial t} + \frac{\partial \mathbf{F}(\mathbf{U})}{\partial x} = \mathbf{S}(\mathbf{U}),$$

in which the source terms are decoupled from the hyperbolic system. In Pelanti (2005) it is shown that using a fractional step approach applied to multicomponent compressible flows gives the correct behavior of the coupled system and the correct sound speeds.

Assuming  $\mathbf{U}^n$  an approximation of the solution at time  $t^n$ , using the Splitting approach we divide the computation of  $\mathbf{U}^{n+1}$  at time  $t^{n+1} = t^n + \Delta t$  in two steps:

- 1) Compute  $(\mathbf{U}^{n+1})^*$  solving the homogeneous system of partial differential equation  $\mathbf{U}_t + [\mathbf{F}(\mathbf{U})]_x = 0$  with initial condition  $\mathbf{U}^n$  and time step  $\Delta t$ .
- 2) Compute  $\mathbf{U}^{n+1}$  integrating the ODE system  $\mathbf{U}_t = \mathbf{S}(\mathbf{U})$  with initial condition  $(\mathbf{U}^{n+1})^*$  and time step  $\Delta t$ .

Furthermore, in conjunction with the splitting approach, we adopt the segregated approach. This approach consists in solving all the equations of the ODE system one at a time (Jasak, 2006). Practically, during the step 2), when we compute the solution for one of the conservative variables, all the others are considered constant in time. These constant values are given by the solution of the hyperbolic system  $\mathbf{U}_t + [\mathbf{F}(\mathbf{U})]_x = 0$  calculated at the step 1).

### 3.1.1 Numerical methods for homogeneous systems of conservation laws

In this section several finite volume methods for solving homogeneous one-dimensional systems of conservation laws (3.3) are presented.

The system (3.3) is expressed in conservative form, thus, in order to solve it numerically, central schemes on collocated grids can be used.

Using a finite volume discretization, from Eq. (3.3) we get

$$\mathbf{U}_i^{n+1} = \mathbf{U}_i^n - \frac{\Delta t}{\Delta x} \left( \mathbf{F}_{i+\frac{1}{2}} - \mathbf{F}_{i-\frac{1}{2}} \right), \quad i = 1, \dots, m, \quad (3.5)$$

where  $\mathbf{U}_i^n$  is the integral average of the solution  $\mathbf{U}$  over the  $i$ -th cell  $[x_{i-\frac{1}{2}}, x_{i+\frac{1}{2}}]$  at time  $t^n$  and  $\mathbf{F}_{i\pm\frac{1}{2}}$  is given by

$$\mathbf{F}_{i\pm\frac{1}{2}} = \frac{1}{\Delta t} \int_{t^n}^{t^{n+1}} \mathbf{F}(\mathbf{U}(x_{i\pm\frac{1}{2}}, \tau)) d\tau. \quad (3.6)$$

Since the last integral cannot be computed exactly, a numerical integration is required. According to the choice of the numerical integrations  $\tilde{\mathbf{F}}_{i\pm\frac{1}{2}}$  of the Eq. (3.6) we can define different finite volumes schemes

$$\mathbf{U}_i^{n+1} = \mathbf{U}_i^n - \frac{\Delta t}{\Delta x} \left( \tilde{\mathbf{F}}_{i+\frac{1}{2}} - \tilde{\mathbf{F}}_{i-\frac{1}{2}} \right), \quad i = 1, \dots, m. \quad (3.7)$$

The numerical integrations  $\tilde{\mathbf{F}}_{i\pm\frac{1}{2}}$  are named *numerical fluxes*. Each finite volume method differs from the other mainly for the different choice of the numerical fluxes.

In order to obtain second order of accuracy, the MUSCL-Hancock technique with linear reconstruction is adopted here. This method is based on a *predictor/corrector* strategy, that consists in estimating the solution  $\mathbf{U}_{i+\frac{1}{2},L}^{n+\frac{1}{2}}$  and  $\mathbf{U}_{i+\frac{1}{2},R}^{n+\frac{1}{2}}$  at the two sides of the cells interfaces at an intermediate time  $t^{n+1/2}$  (*predictor step*) and using these values to evaluate the numerical fluxes and to compute the solution at the desired time  $t^{n+1}$  (*corrector step*).

The local data at the cells interfaces are computed in the predictor step using first a piecewise-linear reconstruction of the solution at time  $t^n$  and then evolving these values at time  $t^{n+\frac{1}{2}}$ . The linear-piecewise reconstruction  $\tilde{\mathbf{U}}^n(x)$  of the solution is defined as

$$\tilde{\mathbf{U}}^n(x) = \sum_i \tilde{\mathbf{U}}_i^n(x) = \sum_i [\mathbf{U}_i^n + (\mathbf{U}_i^n)'(x - x_i)] \cdot \chi_{[x_{i-1/2}, x_{i+1/2}]}(x), \quad (3.8)$$

where  $\tilde{\mathbf{U}}_i^n(x)$  is the linear reconstruction inside the  $i$ -th cell,  $\chi(x)$  is the characteristic function and  $(\mathbf{U}_i^n)'$  is an approximation of the first spatial derivative of the solution at the point  $x_i$  at the time  $t^n$ .

In order to prevent high derivative values and thus oscillations in the numerical solution, nonlinear slope limiter functions are adopted. In particular, in this work we adopt the minmod (denoted with *mm*) and Van Leer (Sweby (1984), denoted with *vl*) limiters, defined respectively by

$$(\mathbf{U}_i^n)' = \varphi_{mm}(\mathbf{U}_{i-1}^n, \mathbf{U}_i^n, \mathbf{U}_{i+1}^n) = \text{minmod} \left( \frac{\Delta \mathbf{U}_{i+\frac{1}{2}}^n}{\Delta x}, \frac{\Delta \mathbf{U}_{i-\frac{1}{2}}^n}{\Delta x} \right), \quad (3.9)$$

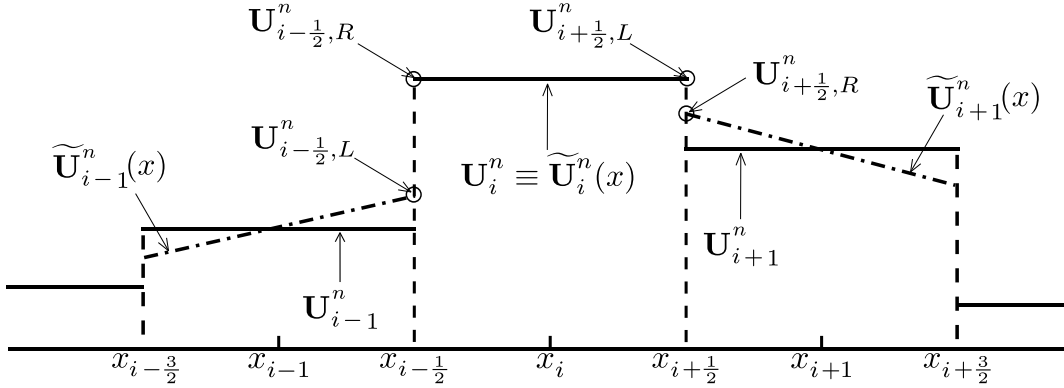


Figure 1: Schematic illustration of the linear reconstruction obtained using minmod limiter. The solid line corresponds to the average integral  $\mathbf{U}_i^n$  in the  $i$ -th cell, while the dash-dot line represent the linear reconstruction  $\tilde{\mathbf{U}}_i^n(x)$  inside the  $i$ -th cell.

$$\begin{aligned}
 (\mathbf{U}_i^n)' &= \varphi_{vl}(\mathbf{U}_{i-1}^n, \mathbf{U}_i^n, \mathbf{U}_{i+1}^n) = \\
 &= \begin{cases} \frac{2}{\Delta x} \cdot \frac{(\Delta \mathbf{U}_{i+\frac{1}{2}}^n)(\Delta \mathbf{U}_{i-\frac{1}{2}}^n)}{\Delta \mathbf{U}_{i+\frac{1}{2}}^n + \Delta \mathbf{U}_{i-\frac{1}{2}}^n}, & \text{if } (\Delta \mathbf{U}_{i+\frac{1}{2}}^n)(\Delta \mathbf{U}_{i-\frac{1}{2}}^n) > 0 \\ 0 & \text{otherwise} \end{cases} \quad (3.10)
 \end{aligned}$$

where

$$\minmod(x_1, x_2, \dots, x_n) = \begin{cases} \min_j \{x_j\} & \text{if } x_j > 0 \forall j \\ \max_j \{x_j\} & \text{if } x_j < 0 \forall j \\ 0 & \text{otherwise} \end{cases} \quad (3.11)$$

and

$$\Delta \mathbf{U}_{i+\frac{1}{2}}^n = \mathbf{U}_{i+1}^n - \mathbf{U}_i^n \quad \Delta \mathbf{U}_{i-\frac{1}{2}}^n = \mathbf{U}_i^n - \mathbf{U}_{i-1}^n.$$

The linear-piecewise reconstruction of the solution defined by Eq. (3.8) and by the choice of the slope limiter allows us to evaluate the left and right interface values as

$$\mathbf{U}_{i+\frac{1}{2},L}^n = \mathbf{U}_i^n + \frac{\Delta x}{2} (\mathbf{U}_i^n)', \quad \mathbf{U}_{i+\frac{1}{2},R}^n = \mathbf{U}_{i+1}^n - \frac{\Delta x}{2} (\mathbf{U}_{i+1}^n)'.$$

A schematic illustration of the linear reconstruction obtained using minmod limiter is reported in Fig.1.

The linear reconstruction is usually computed on the conservative variables  $\mathbf{U}_i^n$ , but sometimes, depending on the physical model and on the numerical simulations considered, unrealistic values could be obtained for some physical quantities derived from the conservative variables. To overcome this problem, instead of computing the linear reconstruction of the conservative variables, it is possible to perform it on a proper set of physical quantities (La Spina and de' Michieli Vitturi, 2012). More details will be given in Chapter 4.

Finally, once the linear reconstructions are computed, we evolve them in time using the following relations:

$$\mathbf{U}_{i+\frac{1}{2},L}^{n+\frac{1}{2}} = \mathbf{U}_{i+\frac{1}{2},L}^n - \frac{\Delta t}{2\Delta x} \left( \mathbf{F}(\mathbf{U}_{i+\frac{1}{2},L}^n) - \mathbf{F}(\mathbf{U}_{i-\frac{1}{2},R}^n) \right), \quad (3.12)$$

$$\mathbf{U}_{i+\frac{1}{2},R}^{n+\frac{1}{2}} = \mathbf{U}_{i+\frac{1}{2},R}^n - \frac{\Delta t}{2\Delta x} \left( \mathbf{F}(\mathbf{U}_{i+\frac{3}{2},L}^n) - \mathbf{F}(\mathbf{U}_{i+\frac{1}{2},R}^n) \right). \quad (3.13)$$

These interface values are used to evaluate the numerical fluxes for the corrector step. In the following paragraphs several numerical fluxes, that give us different finite volume schemes, are reported. We remark here that the numerical fluxes presented below are expressed without the time index, in fact they can be evaluated at any time required. For example, using the predictor/corrector strategy, as we did, the numerical fluxes for the corrector step have to be evaluated at time  $t^{n+\frac{1}{2}}$ , thus all the variable that define the numerical fluxes have to be evaluated at the same time.

### 3.1.1.1 Lax-Friedrichs numerical fluxes

The Lax-Friedrichs finite volume scheme (Lax, 2005) is presented here. The numerical fluxes that characterize this scheme are defined by the expression

$$\tilde{\mathbf{F}}_{i+\frac{1}{2}}^{(LF)} = \frac{1}{2} \left( \mathbf{F}(\mathbf{U}_{i+\frac{1}{2},L}) + \mathbf{F}(\mathbf{U}_{i+\frac{1}{2},R}) \right) - \frac{1}{2} \frac{\Delta x}{\Delta t} \left( \mathbf{U}_{i+\frac{1}{2},R} - \mathbf{U}_{i+\frac{1}{2},L} \right), \quad (3.14)$$

where  $\mathbf{U}_{i+\frac{1}{2},L}$  and  $\mathbf{U}_{i+\frac{1}{2},R}$  are left and right boundary values evaluated at the appropriate time.

### 3.1.1.2 GForce numerical fluxes

The GFORCE (Generalized FORCE) scheme represents an improvement of the Lax-Friedrichs scheme (Toro and Titarev, 2006). The numerical fluxes characterizing this scheme are defined as a convex combination of the Lax-Friedrichs and Lax-Wendroff numerical fluxes, i.e.

$$\tilde{\mathbf{F}}_{i+\frac{1}{2}}^{(GF)} = \omega \tilde{\mathbf{F}}_{i+\frac{1}{2}}^{(LF,loc)} + (1 - \omega) \tilde{\mathbf{F}}_{i+\frac{1}{2}}^{(LW,loc)}, \quad (3.15)$$

where  $\omega$  is a particular coefficient related to the local Courant number  $\nu^{(loc)}$  defined as

$$\omega = \frac{1}{1 + \nu^{(loc)}}.$$

The Lax-Wendroff fluxes are computed using the following expression:

$$\tilde{\mathbf{F}}_{i+\frac{1}{2}}^{(LW,loc)} = \mathbf{F} \left( \mathbf{U}_{i+\frac{1}{2}}^{(LW,loc)} \right), \quad (3.16)$$

with

$$\mathbf{U}_{i+\frac{1}{2}}^{(LW,loc)} = \frac{1}{2} \left( \mathbf{U}_{i+\frac{1}{2},L} + \mathbf{U}_{i+\frac{1}{2},R} \right) - \frac{1}{2} \frac{\Delta t_{i+\frac{1}{2}}^{(loc)}}{\Delta x} \left( \mathbf{F}(\mathbf{U}_{i+\frac{1}{2},R}) - \mathbf{F}(\mathbf{U}_{i+\frac{1}{2},L}) \right). \quad (3.17)$$

Note that the time step  $\Delta t_{i+\frac{1}{2}}^{(loc)}$  in the previous expressions in general is different from the global  $\Delta t$  used in Eq. (3.5) to compute the solution at time  $t^{n+1}$ . The local time step is calculated as

$$\Delta t_{i+\frac{1}{2}}^{(loc)} = \frac{\nu^{(loc)} \Delta x}{a_{i+\frac{1}{2}}},$$

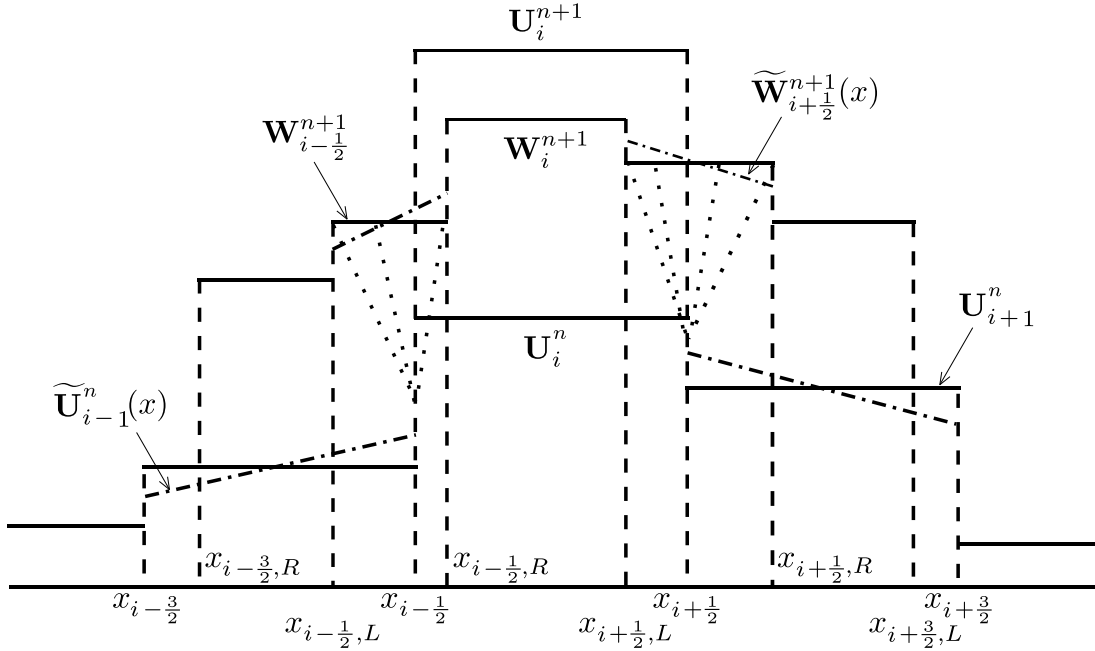


Figure 2: Schematic illustration of the fully discrete scheme of Kurganov, Noelle and Petrova.

where  $a_{i+\frac{1}{2}}$  is the speed of the fastest wave in the local data  $\mathbf{U}_{i+\frac{1}{2},L}$  and  $\mathbf{U}_{i+\frac{1}{2},R}$  while  $\nu^{(loc)}$  is the local Courant number (that usually is  $\nu^{(loc)} = 0.9$ ).

The speed of the fastest wave in the local data is defined as the maximum of the spectral radii  $\varrho_{i+\frac{1}{2}}$  of the jacobian matrix  $\frac{\partial \mathbf{F}}{\partial \mathbf{U}}$  evaluated at  $\mathbf{U}_{i+\frac{1}{2},R}$  and  $\mathbf{U}_{i+\frac{1}{2},L}$ , i.e.

$$a_{i+\frac{1}{2}} = \max(\varrho_{i+\frac{1}{2},L}, \varrho_{i+\frac{1}{2},R}). \quad (3.18)$$

The Lax-Friedrichs numerical fluxes  $\tilde{\mathbf{F}}_{i+\frac{1}{2}}^{(LF,loc)}$  are obtained from the Eq. (3.14) in which the global  $\Delta t$  is replaced by the local  $\Delta t_{i+\frac{1}{2}}^{(loc)}$ .

### 3.1.1.3 Kurganov, Noelle, Petrova numerical fluxes

The semidiscrete scheme proposed by Kurganov et al. (2001) is described below. Unlike we have done before, if we integrate Eq. (3.3) only respect the  $x$  variable we have

$$\frac{d}{dt} \mathbf{U}_i(t) = -\frac{\mathbf{F}(\mathbf{U}(x_{i+\frac{1}{2}}, t)) - \mathbf{F}(\mathbf{U}(x_{i-\frac{1}{2}}, t))}{\Delta x}, \quad (3.19)$$

where  $\mathbf{U}_i(t)$  is the integral average over the  $i$ -th cell  $[x_{i-\frac{1}{2}}, x_{i+\frac{1}{2}}]$  at time  $t$ . Being a finite volume method, our aim is determine the time-dependent numerical fluxes  $\tilde{\mathbf{F}}_{i\pm\frac{1}{2}}(t)$  that have to be used in the Eq. (3.19) in place of  $\mathbf{F}(\mathbf{U}(x_{i\pm\frac{1}{2}}, t))$ .

In order to determine the numerical fluxes, we start with the piecewise-linear reconstruction (3.8). With this reconstruction, some discontinuities could arise at the point

$x_{i+\frac{1}{2}}$  (see Fig.2). These discontinuities propagates with different right and left speed, that can be computed as

$$\begin{aligned} a_{i+\frac{1}{2}}^+ &= \max(\lambda_{i+\frac{1}{2},R}, \lambda_{i+\frac{1}{2},L}, 0), \\ a_{i+\frac{1}{2}}^- &= \min(\mu_{i+\frac{1}{2},R}, \mu_{i+\frac{1}{2},L}, 0), \end{aligned} \quad (3.20)$$

where  $\lambda_{i+\frac{1}{2},R}$  and  $\lambda_{i+\frac{1}{2},L}$  are the maximum eigenvalues of the jacobian matrix  $\frac{\partial \mathbf{F}}{\partial \mathbf{U}}$  evaluated respectively at  $\mathbf{U}_{i+\frac{1}{2},R}$  and  $\mathbf{U}_{i+\frac{1}{2},L}$  defined by

$$\begin{aligned} \mathbf{U}_{i+\frac{1}{2},R} &= \lim_{x \rightarrow (x_{i+\frac{1}{2}})^+} \tilde{\mathbf{U}}(x) = \lim_{x \rightarrow (x_{i+\frac{1}{2}})^+} \tilde{\mathbf{U}}_{i+1}(x), \\ \mathbf{U}_{i+\frac{1}{2},L} &= \lim_{x \rightarrow (x_{i+\frac{1}{2}})^-} \tilde{\mathbf{U}}(x) = \lim_{x \rightarrow (x_{i+\frac{1}{2}})^-} \tilde{\mathbf{U}}_i(x). \end{aligned} \quad (3.21)$$

while  $\mu_{i+\frac{1}{2},R}$  and  $\mu_{i+\frac{1}{2},L}$  are the minimum eigenvalues.

The left and right local speeds can be used also to determine particular rectangular domains, i.e.

$$J_i = [x_{i-\frac{1}{2},R}, x_{i+\frac{1}{2},L}] \quad (3.22)$$

and

$$J_{i+\frac{1}{2}} = [x_{i+\frac{1}{2},L}, x_{i+\frac{1}{2},R}], \quad (3.23)$$

where  $x_{i+\frac{1}{2},L} = x_{i+\frac{1}{2}} + a_{i+\frac{1}{2}}^- \Delta t$  and  $x_{i+\frac{1}{2},R} = x_{i+\frac{1}{2}} + a_{i+\frac{1}{2}}^+ \Delta t$ . The discontinuities in  $x_{i+\frac{1}{2}}$  propagates only inside the domain  $J_{i+\frac{1}{2}}$ , while  $\tilde{\mathbf{U}}(x)$  is smooth in the interval  $J_i$ . Then we define new cells averages

$$\mathbf{W}_i^{n+1} = \frac{1}{|J_i^n|} \left[ \int_{J_i^n} \tilde{\mathbf{U}}^n(x) dx - \int_{t^n}^{t^{n+1}} \left( \mathbf{F}(\mathbf{U}(x_{i+\frac{1}{2},L}, \tau) - \mathbf{F}(\mathbf{U}(x_{i-\frac{1}{2},R}, \tau)) dt \right] \quad (3.24)$$

and

$$\mathbf{W}_{i+\frac{1}{2}}^{n+1} = \frac{1}{|J_{i+\frac{1}{2}}^n|} \left[ \int_{J_{i+\frac{1}{2}}^n} \tilde{\mathbf{U}}^n(x) dx - \int_{t^n}^{t^{n+1}} \left( \mathbf{F}(\mathbf{U}(x_{i+\frac{1}{2},R}, \tau) - \mathbf{F}(\mathbf{U}(x_{i+\frac{1}{2},L}, \tau)) dt \right] \quad (3.25)$$

From these new cell averages, we reconstruct the piecewise polynomial interpolant

$$\tilde{\mathbf{W}}^{n+1}(x) = \sum_i \mathbf{W}_i^{n+1} \chi_{J_i^n}(x) + \tilde{\mathbf{W}}_{i+\frac{1}{2}}^{n+1}(x) \chi_{J_{i+\frac{1}{2}}^n}(x), \quad (3.26)$$

where  $\tilde{\mathbf{W}}_{i+\frac{1}{2}}^{n+1}(x)$  is a linear reconstruction of  $\mathbf{W}_{i+\frac{1}{2}}^{n+1}$  in the interval  $J_{i+\frac{1}{2}}^n$ . As we have done before, function limiter should be use to obtain this reconstruction. A linear reconstruction of  $\mathbf{W}_i^{n+1}$  is not needed since it will be averaged out.

From the computation of  $\tilde{\mathbf{W}}^{n+1}(x)$  we get a fully discrete scheme, where the approximation of the solution at time  $t^{n+1}$  is given by

$$\mathbf{U}_i^{n+1} = \frac{1}{\Delta x} \int_{x_{i-\frac{1}{2}}}^{x_{i+\frac{1}{2}}} \tilde{\mathbf{W}}^{n+1}(x) dx. \quad (3.27)$$

In order to obtain a semidiscrete scheme, we express  $\frac{d}{dt} \mathbf{U}_i(t)$  using Eq. (3.27) and thus we have

$$\frac{d}{dt} \mathbf{U}_i(t) = \lim_{\Delta t \rightarrow 0} \frac{\mathbf{U}_i^{n+1} - \mathbf{U}_i^n}{\Delta t} = \lim_{\Delta t \rightarrow 0} \frac{1}{\Delta t} \left[ \frac{1}{\Delta x} \int_{x_{i-\frac{1}{2}}}^{x_{i+\frac{1}{2}}} \tilde{\mathbf{W}}^{n+1}(x) dx - \mathbf{U}_i^n \right]. \quad (3.28)$$

Now, we suppose that the slopes  $(\mathbf{W}_{i+\frac{1}{2}}^{n+1})'$  of the linear reconstruction  $\tilde{\mathbf{W}}_{i+\frac{1}{2}}^{n+1}$  are uniformly bounded, independently of  $\Delta t$ . Thus, since the width of the Riemann fans is bounded by  $(a_{i+\frac{1}{2}}^+ - a_{i+\frac{1}{2}}^-)\Delta t$ , we obtain

$$\tilde{\mathbf{W}}_{i+\frac{1}{2}}^{n+1}(x) = \mathbf{W}_{i+\frac{1}{2}}^{n+1} + \mathcal{O}(\Delta t). \quad (3.29)$$

Using the previous expression, we get

$$\int_{x_{i-\frac{1}{2}}}^{x_{i-\frac{1}{2},R}} \tilde{\mathbf{W}}^{n+1}(x) dx = \int_{x_{i-\frac{1}{2}}}^{x_{i-\frac{1}{2},R}} \tilde{\mathbf{W}}_{i-\frac{1}{2}}^{n+1}(x) dx = a_{i-\frac{1}{2}}^+ \Delta t \mathbf{W}_{i-\frac{1}{2}}^{n+1} \quad (3.30)$$

and

$$\int_{x_{i+\frac{1}{2},L}}^{x_{i+\frac{1}{2}}} \tilde{\mathbf{W}}^{n+1}(x) dx = \int_{x_{i+\frac{1}{2},L}}^{x_{i+\frac{1}{2}}} \tilde{\mathbf{W}}_{i+\frac{1}{2}}^{n+1}(x) dx = a_{i+\frac{1}{2}}^- \Delta t \mathbf{W}_{i+\frac{1}{2}}^{n+1}. \quad (3.31)$$

Furthermore, from the Eq. (3.26) we have

$$\int_{x_{i-\frac{1}{2},R}}^{x_{i+\frac{1}{2},L}} \tilde{\mathbf{W}}^{n+1}(x) dx = \int_{x_{i-\frac{1}{2},R}}^{x_{i+\frac{1}{2},L}} \mathbf{W}_i^{n+1} dx = |J_i^n| \mathbf{W}_i^{n+1}. \quad (3.32)$$

Replacing Eqs. (3.30)–(3.32) in the Eq. (3.28) we obtain

$$\frac{d}{dt} \mathbf{U}_i(t) = \frac{a_{i-\frac{1}{2}}^+}{\Delta x} \lim_{\Delta t \rightarrow 0} \mathbf{W}_{i-\frac{1}{2}}^{n+1} + \lim_{\Delta t \rightarrow 0} \frac{1}{\Delta t} \left( \frac{|J_i^n|}{\Delta x} \mathbf{W}_i^{n+1} - \mathbf{U}_i^n \right) - \frac{a_{i+\frac{1}{2}}^-}{\Delta x} \lim_{\Delta t \rightarrow 0} \mathbf{W}_{i+\frac{1}{2}}^{n+1}. \quad (3.33)$$

Using Eq. (3.24) and (3.25) we get

$$\begin{aligned} \lim_{\Delta t \rightarrow 0} \frac{1}{\Delta t} \left( \frac{|J_i|}{\Delta x} \mathbf{W}_i^{n+1} - \mathbf{U}_i^n \right) &= \frac{a_{i+\frac{1}{2}}^- \mathbf{U}_{i+\frac{1}{2},L} - a_{i-\frac{1}{2}}^+ \mathbf{U}_{i-\frac{1}{2},R}}{\Delta x} - \\ &- \frac{\mathbf{F}(\mathbf{U}_{i+\frac{1}{2},L}) - \mathbf{F}(\mathbf{U}_{i-\frac{1}{2},R})}{\Delta x} \end{aligned} \quad (3.34)$$

and

$$\lim_{\Delta t \rightarrow 0} \mathbf{W}_{i+\frac{1}{2}}^{n+1} = \frac{a_{i+\frac{1}{2}}^+ \mathbf{U}_{i+\frac{1}{2},R} - a_{i+\frac{1}{2}}^- \mathbf{U}_{i+\frac{1}{2},L}}{a_{i+\frac{1}{2}}^+ - a_{i+\frac{1}{2}}^-} - \frac{\mathbf{F}(\mathbf{U}_{i+\frac{1}{2},R}) - \mathbf{F}(\mathbf{U}_{i+\frac{1}{2},L})}{a_{i+\frac{1}{2}}^+ - a_{i+\frac{1}{2}}^-}, \quad (3.35)$$

where  $\mathbf{U}_{i+\frac{1}{2},R}$  and  $\mathbf{U}_{i+\frac{1}{2},L}$  stand for the corresponding right and left values of the piecewise linear interpolant at time  $t$  defined in Eq. (3.21). Finally, replacing Eq. (3.34) and (3.35) in Eq. (3.33) we derive the semidiscrete central-upwind scheme

$$\frac{d}{dt} \mathbf{U}_i(t) = - \frac{\tilde{\mathbf{F}}_{i+\frac{1}{2}}^{(KNP)} - \tilde{\mathbf{F}}_{i-\frac{1}{2}}^{(KNP)}}{\Delta x}, \quad (3.36)$$

where  $\tilde{\mathbf{F}}_{i+\frac{1}{2}}^{(KNP)} \equiv \tilde{\mathbf{F}}_{i+\frac{1}{2}}^{(KNP)}(t)$  are the numerical fluxes at time  $t$  defined by

$$\tilde{\mathbf{F}}_{i+\frac{1}{2}}^{(KNP)} = \frac{a_{i+\frac{1}{2}}^+ \mathbf{F}(\mathbf{U}_{i+\frac{1}{2},L}) - a_{i+\frac{1}{2}}^- \mathbf{F}(\mathbf{U}_{i+\frac{1}{2},R})}{a_{i+\frac{1}{2}}^+ - a_{i+\frac{1}{2}}^-} + \frac{a_{i+\frac{1}{2}}^+ a_{i+\frac{1}{2}}^-}{a_{i+\frac{1}{2}}^+ - a_{i+\frac{1}{2}}^-} (\mathbf{U}_{i+\frac{1}{2},R} - \mathbf{U}_{i+\frac{1}{2},L}). \quad (3.37)$$

In the predictor/corrector framework, the second-order accuracy is achieved by means of MUSCL reconstruction in conjunction with a Hancock two-stage scheme for the time integration, using the predicted boundary values  $\mathbf{U}_{i+\frac{1}{2},L}^{n+\frac{1}{2}}$  and  $\mathbf{U}_{i+\frac{1}{2},R}^{n+\frac{1}{2}}$  at time  $t^{n+\frac{1}{2}}$  to evaluate the local speeds  $a_{i+\frac{1}{2}}^\pm$  and thus the numerical fluxes  $\tilde{\mathbf{F}}_{i+\frac{1}{2}}^{(KNP)}$  needed for the corrector step.

#### 3.1.1.4 Kurganov and Tadmor numerical fluxes

The Kurganov, Noelle and Petrova numerical fluxes reported in Eq. (3.37) are an improvement of the numerical fluxes presented by Kurganov and Tadmor (2000). These numerical fluxes can be obtained from Eq. (3.37) defining

$$\begin{aligned} a_{i+\frac{1}{2}}^+ &= a_{i+\frac{1}{2}}, \\ a_{i+\frac{1}{2}}^- &= -a_{i+\frac{1}{2}}, \end{aligned} \quad (3.38)$$

where  $a_{i+\frac{1}{2}}$  is the speed of the fastest wave in the local data  $\mathbf{U}_{i+\frac{1}{2},R}$  and  $\mathbf{U}_{i+\frac{1}{2},L}$  (see Eq. (3.18)). In this way, the Kurganov and Tadmor numerical fluxes become

$$\tilde{\mathbf{F}}_{i+\frac{1}{2}}^{(KT)} = \frac{1}{2} (\mathbf{F}(\mathbf{U}_{i+\frac{1}{2},L}) + \mathbf{F}(\mathbf{U}_{i+\frac{1}{2},R})) - \frac{1}{2} a_{i+\frac{1}{2}} (\mathbf{U}_{i+\frac{1}{2},R} - \mathbf{U}_{i+\frac{1}{2},L}). \quad (3.39)$$

#### 3.1.1.5 Modification of the Lax-Friedrichs numerical fluxes

In the previous paragraphs several numerical fluxes has been reported, from the very simple Lax-Friedrichs to the more complex Kurganov, Noelle and Petrova. In particular, the Lax-Friedrichs and the Kurganov and Tadmor numerical fluxes, respectively reported in Eq. (3.14) and (3.39), are very similar to each other. In fact in the Lax-Friedrichs scheme instead of  $a_{i+\frac{1}{2}}$ , is used the constant value  $\Delta x / \Delta t$ .

However, commonly the time step  $\Delta t$  is not defined as a constant value, but, for each iteration, it is computed as

$$\Delta t = \nu \cdot \min_{i=1,\dots,m} \left( \frac{\Delta x}{\varrho_i} \right), \quad (3.40)$$

where  $\varrho_i$  is the spectral radius of the jacobian matrix  $\frac{\partial \mathbf{F}}{\partial \mathbf{U}}$  evaluated at  $\mathbf{U}_i$  and  $\nu$  is the Courant number. Thus, we can write

$$\frac{\Delta x}{\Delta t} = \frac{1}{\nu} \cdot \max_{i=1,\dots,m} (\varrho_i). \quad (3.41)$$

In order to maintain the stability of the numerical schemes presented, the Courant number must not be greater than 0.5. Hence  $\Delta x / \Delta t$  is at least twice of  $\max (\varrho_i)$  and this makes the solution more diffusive. For this reason we define the new numerical fluxes

$$\begin{aligned} \tilde{\mathbf{F}}_{i+\frac{1}{2}}^{(LFMod)} &= \frac{1}{2} (\mathbf{F}(\mathbf{U}_{i+\frac{1}{2},L}) + \mathbf{F}(\mathbf{U}_{i+\frac{1}{2},R})) - \frac{1}{2} \left( \max_{i=1,\dots,m} \varrho_i \right) (\mathbf{U}_{i+\frac{1}{2},R} - \mathbf{U}_{i+\frac{1}{2},L}) = \\ &= \frac{1}{2} (\mathbf{F}(\mathbf{U}_{i+\frac{1}{2},L}) + \mathbf{F}(\mathbf{U}_{i+\frac{1}{2},R})) - \frac{1}{2} \frac{\Delta x}{\Delta t} \nu (\mathbf{U}_{i+\frac{1}{2},R} - \mathbf{U}_{i+\frac{1}{2},L}). \end{aligned} \quad (3.42)$$

In the Chapter 4 we will present several numerical tests, in order to asses the robustness and the accuracy of the numerical schemes proposed, and it will be shown that these numerical fluxes are much less diffusive with respect the standard Lax-Friedrichs numerical fluxes.

### 3.1.2 Integration of the source terms

The numerical methods illustrated in the previous section solve the step 1) of the splitting approach, i.e. the homogeneous part of the system (2.10)–(2.15)  $\mathbf{U}_t + \mathbf{F}(\mathbf{U})_x = 0$ . In this section we deal about the step 2) of the Splitting approach, i.e. the integration of the ODE system  $\mathbf{U}_t = \mathbf{S}(\mathbf{U})$  with  $(\mathbf{U}^{n+1})^*$  as initial condition.

For the Single Temperature model presented in Section 2, the ODE system is given by

$$\frac{\partial}{\partial t} \begin{pmatrix} \rho \\ \rho\alpha_1 \\ \rho_1\alpha_1 \\ \rho u \\ w \\ \rho \left(E + \frac{u^2}{2}\right) \end{pmatrix} = \frac{\partial}{\partial t} \begin{pmatrix} U_1 \\ U_2 \\ U_3 \\ U_4 \\ U_5 \\ U_6 \end{pmatrix} = \begin{pmatrix} 0 \\ -\frac{1}{\tau^{(p)}}(P_2 - P_1) \\ -\frac{1}{\tau^{(c)}}\rho \left[\mu_1 - \mu_2 + (1 - 2c)\frac{w^2}{2}\right] \\ \rho g \\ -\frac{1}{\tau^{(f)}}\frac{c(1 - c)w}{\rho} \\ \rho ug \end{pmatrix}.$$

As known, there exist several numerical methods to compute the solution of ODE systems, but in this work, when possible, we will compute the solution analytically, otherwise we will use a numerical integration. In fact, with the segregated approach, we assume that all the equations of the ODE system are independent from the others, that means that we can solve separately all the equations. In this way, under suitable condition, we will able to integrate some of them analytically.

In the following paragraphs, we will use the notation  $U_i \equiv (U_i^{(n+1)})^*$  to indicate the initial constant value of the conservative variable  $i$  obtained from the step 1) of the splitting approach, while we will explicitly show the time dependency for those variable that are not constant in time during the integration. Finally, we will indicate with  $U_j^{(n+1)}$  the solution of the time integration for variable  $j$  that we want to compute.

#### 3.1.2.1 Velocity Relaxation

The integration of the relative velocity differential equation

$$\frac{\partial U_5(t)}{\partial t} = \frac{\partial w(t)}{\partial t} = -\frac{1}{\tau^{(f)}} \frac{c(1 - c)w(t)}{\rho} \quad (3.43)$$

is reported here.

In order to integrate it analytically we assume that  $\tau^{(f)}$  is a constant coefficient. Furthermore, adopting a segregated approach for the integration of the source terms, all the conservative variables except  $w(t) = U_5(t)$  are assumed constant in time. Thus, writing

the source term for the relative velocity as function of the conservative variables, we have

$$\frac{\partial U_5(t)}{\partial t} = -\frac{1}{\tau^{(f)}} \frac{1}{U_1} \frac{U_3}{U_1} \left(1 - \frac{U_3}{U_1}\right) U_5(t) \implies U_5^{(n+1)} = U_5 e^{-\zeta \frac{1}{U_1} \frac{U_3}{U_1} \left(1 - \frac{U_3}{U_1}\right) \Delta t},$$

where we used the relations  $\rho = U_1$  and  $c = U_3/U_1$ .

We note here that, rewriting the governing equations in order to have separated momentum equations for each phases (see Eq. (2.107)), the drag force between the two phases can be expressed in terms of the velocity relaxation term. In fact, naming  $F_d$  the drag force, we have

$$F_d = \frac{1}{\tau^{(f)}} c_1^2 c_2^2 w. \quad (3.44)$$

### 3.1.2.2 Pressure Relaxation

The differential equation that we have to solve for the relaxation of the phases pressures is the following:

$$\frac{\partial U_2(t)}{\partial t} = \frac{\partial}{\partial t} [\alpha_1(t)\rho] = -\frac{1}{\tau^{(p)}} (P_2 - P_1).$$

Again, we want to express the right-hand side of the equation in terms of the conservative variables. First of all, as observed for the relaxation of the velocities, using a segregated approach  $\rho = U_1$  is constant in time during the integration of this source term, so we can write

$$\frac{\partial \alpha_1(t)}{\partial t} = \frac{1}{U_1 \tau^{(p)}} (P_1 - P_2). \quad (3.45)$$

Now, from the equation of state in the compact form (2.99) we have

$$P_1(\rho_1, T) = c_{v,1}(\gamma_1 - 1)\rho_1 T - \bar{P}_1 = \frac{1}{\alpha_1(t)} c_{v,1}(\gamma_1 - 1) U_3 T - \bar{P}_1 \quad (3.46)$$

and

$$P_2(\rho_2, T) = c_{v,2}(\gamma_2 - 1)\rho_2 T - \bar{P}_2 = \frac{1}{1 - \alpha_1(t)} c_{v,2}(\gamma_2 - 1)(U_1 - U_3)T - \bar{P}_2. \quad (3.47)$$

If we express the temperature in term of  $\alpha_1$ , Eq. (3.45) becomes an ordinary differential equation in function of the only variable  $\alpha_1$ .

The mixture temperature can be computed as follows. From the conservative variables we get

$$u_1 = \frac{U_4 + U_5(U_1 - U_3)}{U_1} \quad \text{and} \quad u_2 = \frac{U_4 - U_5 U_3}{U_1}. \quad (3.48)$$

Furthermore, from the expression for  $U_6$  we obtain

$$\begin{aligned} U_3 e_1 + (U_1 - U_3) e_2 &= U_6 - U_3 \frac{u_1^2}{2} - (U_1 - U_3) \frac{u_2^2}{2} = \\ &= U_6 - U_3 \frac{U_4^2 + U_5^2(U_1 - U_3)^2 + 2U_4 U_5(U_1 - U_3)}{2U_1^2} - \end{aligned}$$

$$\begin{aligned}
& - (U_1 - U_3) \frac{U_4^2 + U_3^2 U_5^2 - 2U_3 U_4 U_5}{2U_1^2} = \\
& = U_6 - \frac{U_3 U_4^2 + U_1^2 U_3 U_5^2 + U_3^3 U_5^2 - 2U_1 U_3^2 U_5^2 + 2U_1 U_3 U_4 U_5 - 2U_3^2 U_4 U_5}{2U_1^2} \\
& \quad - \frac{U_1 U_4^2 - U_3 U_4^2 + U_1 U_3^2 U_5^2 - U_3^3 U_5^2 - 2U_1 U_3 U_4 U_5 + 2U_3^2 U_4 U_5}{2U_1^2} = \\
& = U_6 - \frac{U_4^2}{2U_1} - \frac{U_5^2 U_3 (U_1 - U_3)}{2U_1}.
\end{aligned}$$

Using the expression (2.98) for the specific internal energies, we find

$$\begin{aligned}
& T (U_3 c_{v,1} + (U_1 - U_3) c_{v,2}) + \alpha_1(t) \bar{P}_1 + (1 - \alpha_1(t)) \bar{P}_2 + \\
& + U_3 \bar{e}_1 + (U_1 - U_3) \bar{e}_2 = U_6 - \frac{U_4^2}{2U_1} - \frac{U_5^2 U_3 (U_1 - U_3)}{2U_1}, \tag{3.49}
\end{aligned}$$

and, introducing the notation  $\hat{A}$  and  $\hat{B}$  for the following two terms

$$\begin{aligned}
\hat{A} &= \frac{1}{c_{v,mix}} \left[ U_6 - \frac{U_4^2}{2U_1} - U_5^2 \frac{U_3 (U_1 - U_3)}{2U_1} - \bar{P}_2 - U_3 \bar{e}_1 - (U_1 - U_3) \bar{e}_2 \right], \\
\hat{B} &= \frac{1}{c_{v,mix}} [\bar{P}_1 - \bar{P}_2],
\end{aligned}$$

where  $c_{v,mix} = U_3 c_{v,1} + (U_1 - U_3) c_{v,2}$ , we can express the mixture temperature as a linear function of  $\alpha_1(t)$

$$T = \hat{A} - \alpha_1(t) \hat{B}. \tag{3.50}$$

Now, if we replace Eq. (3.50) in the pressure expression (3.46) and (3.47) we get

$$P_1(\alpha_1(t)) = \frac{1}{\alpha_1(t)} (\gamma_1 - 1) U_3 c_{v,1} [\hat{A} - \alpha_1(t) \hat{B}] - \bar{P}_1$$

and

$$P_2(\alpha_1(t)) = \frac{1}{1 - \alpha_1(t)} (\gamma_2 - 1) (U_1 - U_3) c_{v,2} [\hat{A} - \alpha_1(t) \hat{B}] - \bar{P}_2.$$

Since we are adopting a segregated approach for the integration of the source terms, all the terms appearing in the expressions of  $P_1$  and  $P_2$  but  $\alpha_1(t)$  are constant in time during the integration of the pressures relaxation term and the ordinary differential equation (3.45) can be written as

$$\frac{d\alpha_1(t)}{dt} = \frac{1}{\alpha_1(t)} \hat{C} - \frac{1}{1 - \alpha_1(t)} \hat{D} - \hat{E}, \tag{3.51}$$

where

$$\hat{C} = \frac{1}{U_1 \tau^{(p)}} (\gamma_1 - 1) U_3 c_{v,1} \hat{A},$$

$$\hat{D} = \frac{1}{U_1 \tau^{(p)}} (\gamma_2 - 1) (U_1 - U_3) c_{v,2} (\hat{A} - \hat{B}),$$

$$\hat{E} = \frac{1}{U_1 \tau^{(p)}} [(\gamma_1 - 1) U_3 c_{v,1} \hat{B} + (\gamma_2 - 1) (U_1 - U_3) c_{v,2} \hat{B} + \bar{P}_1 - \bar{P}_2].$$

Assuming that  $\tau^{(p)}$  is a constant parameter, then the coefficients  $\hat{C}$ ,  $\hat{D}$  and  $\hat{E}$  of the ordinary differential equation (3.51) are constant in time.

From the Eq (3.51) we get

$$-\frac{(\alpha_1(t))^2 - \alpha_1(t)}{\hat{E}(\alpha_1(t))^2 - (\hat{C} + \hat{D} + \hat{E})\alpha_1(t) + \hat{C}} d\alpha_1 = dt,$$

and integrating over the interval  $[t_0, t]$  we have

$$\begin{aligned} & \int_{\alpha(t_0)}^{\alpha(t)} \frac{\alpha_1^2 - \alpha_1}{\alpha_1^2 - \hat{F}\alpha_1 + \hat{G}} d\alpha_1 = \\ &= \alpha_1(t) - \alpha_1(t_0) + \int_{\alpha(t_0)}^{\alpha(t)} \frac{(\hat{F} - 1)\alpha_1 - \hat{G}}{\alpha_1^2 - \hat{F}\alpha_1 + \hat{G}} d\alpha_1 = -\hat{E}(t - t_0) \\ & \quad \Downarrow \\ & \alpha_1^{(n+1)} - \frac{U_2}{U_1} + \int_{\frac{U_2}{U_1}}^{\alpha^{(n+1)}} \frac{(\hat{F} - 1)\alpha_1 - \hat{G}}{\alpha_1^2 - \hat{F}\alpha_1 + \hat{G}} d\alpha_1 = -\hat{E}\Delta t, \end{aligned} \quad (3.52)$$

where we set  $\hat{F} = (\hat{C} + \hat{D} + \hat{E})/\hat{E}$  and  $\hat{G} = \hat{C}/\hat{E}$ .

We remind that, with the notation used,  $U_1$  and  $U_2$  in the previous expression are the initial constant values obtained from the solution of the hyperbolic part of the governing equations, while  $\alpha_1^{(n+1)}$  is the variable that we have to compute.

Since any rational function can be integrated analytically, the last equation of (3.52) can be written as  $\Psi(\alpha_1^{(n+1)}) = 0$  with  $\Psi$  an analytic function. Thus we can use a functional iterative method like bisection, or the second order Newton-Raphson method to compute the volume fraction  $\alpha_1^{(n+1)}$ . Once the volume fraction is computed, we update the conservative variable  $U_2(t)$  as

$$U_2^{(n+1)} = U_1 \alpha_1^{(n+1)}.$$

### 3.1.2.3 Phase exchange

For the application regarding the phase exchange presented in this thesis, we consider the gas phase being exactly the vapor phase of the liquid. Furthermore, we assume the characteristic times of phase pressures and velocities equalizing being negligible compared to the characteristic time of phase transition, and thus the pressure and the velocity relaxations instantaneous ( $\tau^{(p)} = 0$  and  $\tau^{(f)} = 0$ ). With these assumptions, the equations for the integration of the source terms of the volume fraction and the mass fraction of the first phase and the equation of the relative velocity become:

$$P_2 - P_1 = 0, \quad (3.53)$$

$$w = 0, \quad (3.54)$$

$$\frac{\partial}{\partial t} U_3(t) = \frac{\partial}{\partial t} [\alpha_1(t)\rho_1(t)] = -\frac{\rho}{\tau^{(c)}} (\mu_1 - \mu_2). \quad (3.55)$$

According to the sign of the difference of the Gibbs free energies, it is possible to have evaporation or condensation, and the reaction ends when the difference becomes

zero. Thus the equilibrium density of the liquid phase (or gas phase) is the density that we have when the difference of the Gibbs energies is zero.

We show here that it is possible to derive, when the two conditions (3.53) and (3.54) hold, an expression of the source term for the mass fraction of the first phase as a function of  $U_3(t)$  only.

First of all, we observe that from Eq. (2.100) it is possible to write the chemical potential  $\mu_i$  as function of the density  $\rho_i$  and the common temperature  $T$  only. Now, from Eq. (3.49), we obtain

$$\begin{aligned} & T(U_3(t)c_{v,1} + (U_1 - U_3(t))c_{v,2}) + \alpha_1(t)\bar{P}_1 + (1 - \alpha_1(t))\bar{P}_2 + \\ & + U_3(t)\bar{e}_1 + (U_1 - U_3(t))\bar{e}_2 = U_6 - \frac{U_4^2}{2U_1} - \frac{U_5^2 U_3(t)(U_1 - U_3(t))}{2U_1}, \end{aligned}$$

where the only variables changing during the integration of the phase exchange term are  $U_3(t)$  and  $\alpha_1(t)$ .

If we assume that the relative motion of phases can be neglected, then the conservative variable  $U_5$  can be set to zero (Eq. (3.54)). With this assumption, we can derive the equation for the temperature as

$$T = \frac{U_6 - \frac{1}{2}\frac{U_4^2}{U_1} - U_3(t)\bar{e}_1 - \alpha_1(t)\bar{P}_1 - (U_1 - U_3(t))\bar{e}_2 - (1 - \alpha_1(t))\bar{P}_2}{U_3(t)c_{v,1} + (U_1 - U_3(t))c_{v,2}}, \quad (3.56)$$

where the only variables changing during the integration of the phase exchange term are  $U_3(t)$  and  $\alpha_1(t)$ .

Now, using the condition on the local pressures given by Eq. (3.53) for the thermodynamic equilibrium, and the Eq. (2.99) for the pressures expressed in terms of the densities and the temperature, we have:

$$\rho_1(\gamma_1 - 1)c_{v,1}T - \bar{P}_1 = \rho_2(\gamma_2 - 1)c_{v,2}T - \bar{P}_2. \quad (3.57)$$

Using the definition of the variable  $U_3(t)$  and the conservation of the mixture density  $U_1 = \rho$ , we can write the density of the two phases as functions of the constant variable  $U_1$  and the two variables  $U_3(t)$  and  $\alpha_1(t)$ :

$$\rho_1 \equiv \rho_1(U_3(t), \alpha_1(t)) = \frac{U_3(t)}{\alpha_1(t)}, \quad \rho_2 \equiv \rho_2(U_3(t), \alpha_1(t)) = \frac{U_1 - U_3(t)}{1 - \alpha_1(t)} \quad (3.58)$$

and, substituting these expressions into the equation (3.57), we obtain

$$T = \frac{\alpha_1(t)(1 - \alpha_1(t))(\bar{P}_1 - \bar{P}_2)}{(1 - \alpha_1(t))U_3(t)(\gamma_1 - 1)c_{v,1} - \alpha_1(t)(U_1 - U_3(t))(\gamma_2 - 1)c_{v,2}}. \quad (3.59)$$

Again, as for the other expression of the mixture temperature given by Eq. (3.56), the only variables changing during the integration of the phase relaxation term are  $U_3(t)$  and  $\alpha_1(t)$ . Furthermore, from the equations (3.56) and (3.59) we get

$$\begin{aligned} & \frac{U_6 - \frac{1}{2}\frac{U_4^2}{U_1} - U_3(t)\bar{e}_1 - \alpha_1(t)\bar{P}_1 - (U_1 - U_3(t))\bar{e}_2 - (1 - \alpha_1(t))\bar{P}_2}{U_3(t)c_{v,1} + (U_1 - U_3(t))c_{v,2}} = \\ & = \frac{\alpha_1(t)(1 - \alpha_1(t))(\bar{P}_1 - \bar{P}_2)}{(1 - \alpha_1(t))U_3(t)(\gamma_1 - 1)c_{v,1} - \alpha_1(t)(U_1 - U_3(t))(\gamma_2 - 1)c_{v,2}}. \end{aligned} \quad (3.60)$$

From this equation we can explicit  $\alpha_1$  as a function of  $U_3$

$$\alpha_1(t) \equiv \alpha_1(U_3(t)) \quad (3.61)$$

and substituting Eq. (3.61) in Eqs. (3.56) and (3.58), we can finally express the temperature and the densities as function of  $U_3(t)$ , i.e.  $T \equiv T(U_3(t))$ ,  $\rho_1 \equiv \rho_1(U_3(t))$  and  $\rho_2 \equiv \rho_2(U_3(t))$  respectively. Moreover, from the Eq. (2.100) we can write also the chemical potentials  $\mu_1$  and  $\mu_2$  in terms of  $U_3(t)$  only. Thus, under the assumptions of negligible relative velocity and small characteristic time of pressure relaxation compared to that of phase transition, the difference of the chemical potentials in the right hand side of Eq. (3.55) can be written as function of the conservative variable  $U_3(t)$  only.

Finally to integrate the ordinary differential equation (3.55), a second-order Crank-Nicolson method has been applied:

$$\begin{aligned} & \left( U_3^{(n+1)} - U_3 \right) \tau_c = \\ & = -\frac{U_1 \Delta t}{2} \left[ (\mu_1(U_3) - \mu_2(U_3)) + \left( \mu_1 \left( U_3^{(n+1)} \right) - \mu_2 \left( U_3^{(n+1)} \right) \right) \right]. \end{aligned} \quad (3.62)$$

We remind that, in the previous expression,  $U_1$  and  $U_3$  are the initial constant values obtained from the solution of the hyperbolic part of the governing equations, while  $U_3^{(n+1)}$  is the variable that we have to compute.

We remark, also, that  $0 < U_3^{(n+1)} < U_1$ , since the two-phase model would be degenerate if  $\alpha_1 = 0$  or  $\alpha_1 = 1$ . Hence, we can use any iterative methods, like bisection, inside the interval  $(0, U_1)$  to compute the solution  $U_3^{(n+1)}$  of the Eq. (3.62).

Once the conservative variable  $U_3^{(n+1)}$  is determined, we use it to update also  $U_2^{(n+1)}$  as  $\alpha(U_3^{(n+1)}) \cdot U_1$ , since  $\alpha(U_3^{(n+1)})$  is the correct value that makes the pressures equal after the phase exchange.

#### 3.1.2.4 Gravitational force

Finally, the integration of gravitational forces is reported here. We have to solve the differential equations

$$\frac{\partial U_4(t)}{\partial t} = \rho g \quad \text{and} \quad \frac{\partial U_6(t)}{\partial t} = \rho g u. \quad (3.63)$$

Since we have adopted a segregated approach, the two differential equations can be considered independent, and thus we have

$$\begin{aligned} U_4^{(n+1)} &= U_4 + g U_1 \Delta t, \\ U_6^{(n+1)} &= U_6 + g U_4 \Delta t. \end{aligned} \quad (3.64)$$

## 3.2 RUNGE-KUTTA APPROACH

In the previous sections we have described a numerical method to solve the system of partial differential equations (2.19)–(2.24) using an operator splitting approach. Furthermore, using the segregated approach and considering constant relaxation coefficients,

the integration of some source terms can be done analytically, making the solution more accurate and easier to compute. In general, however, assume constant relaxation coefficients could be a strong restriction. Therefore, considering non constant relaxation coefficients could make no possible to calculate an analytical solution of the ODE system. Furthermore, due to the stiffness nature of the governing equations, an explicit integration of the source terms could cause a strong instability in the solution. For these reasons a stable numerical method to integrate  $\mathbf{U}_t = \mathbf{S}(\mathbf{U})$  is required.

In this section it will be described an Implicit-Explicit (IMEX) Runge-Kutta scheme to solve the complete system (2.19)–(2.24). These methods have been developed to solve stiff systems of partial differential equations written in the form

$$\frac{\partial \mathbf{U}}{\partial t} + \mathbf{G}(\mathbf{U}) = \frac{1}{\tau} \mathbf{R}(\mathbf{U}), \quad (3.65)$$

where  $\tau > 0$  is a constant called “stiffness parameter”. System (3.65) may represent a system of  $N$  ODE’s or a discretization of a system of PDE’s, such as, for example, convection-diffusion equations, reaction-diffusion equations or hyperbolic systems with relaxation.

Defining the vector of relaxation terms  $\mathbf{R}(\mathbf{U})$  as

$$\mathbf{R}(\mathbf{U}) = \tau \begin{pmatrix} 0 \\ -\frac{1}{\tau^{(p)}}(P_2 - P_1) \\ -\frac{1}{\tau^{(c)}}\rho \left[ \mu_1 - \mu_2 + (1 - 2c)\frac{w^2}{2} \right] \\ 0 \\ -\frac{1}{\tau^{(f)}}\frac{c(1 - c)w}{\rho} \\ 0 \end{pmatrix}, \quad (3.66)$$

with  $\tau = \min(\tau^{(p)}, \tau^{(c)}, \tau^{(f)})$ , the system (3.2) can be expressed as in (3.65), where

$$\mathbf{G}(\mathbf{U}) = \frac{\partial}{\partial x} \mathbf{F}(\mathbf{U}) - \left[ \mathbf{S}(\mathbf{U}) - \frac{1}{\tau} \mathbf{R}(\mathbf{U}) \right] = \frac{\partial}{\partial x} \mathbf{F}(\mathbf{U}) - \hat{\mathbf{S}}(\mathbf{U}) \quad (3.67)$$

and

$$\hat{\mathbf{S}}(\mathbf{U}) = \begin{pmatrix} 0 \\ 0 \\ 0 \\ \rho g \\ 0 \\ \rho gu \end{pmatrix}. \quad (3.68)$$

An IMEX Runge-Kutta scheme consists of applying an implicit discretization to the relaxation terms and an explicit one to the non stiff terms. Applying the scheme to the system (3.65) we obtain

$$\mathbf{U}^{(j)} = \mathbf{U}^n - \Delta t \sum_{k=1}^{j-1} \tilde{a}_{jk} \mathbf{G}(\mathbf{U}^{(k)}) + \Delta t \cdot \frac{1}{\tau} \sum_{k=1}^{\nu} a_{jk} \mathbf{R}(\mathbf{U}^{(k)}), \quad j = 1, \dots, \nu \quad (3.69)$$

$$\mathbf{U}^{n+1} = \mathbf{U}^n - \Delta t \sum_{k=1}^{\nu} \tilde{b}_k \mathbf{G}(\mathbf{U}^{(k)}) + \Delta t \cdot \frac{1}{\tau} \sum_{k=1}^{\nu} b_k \mathbf{R}(\mathbf{U}^{(k)}). \quad (3.70)$$

The choice of the  $\nu \times \nu$  matrices  $\tilde{A} = (\tilde{a}_{jk})$ ,  $\tilde{a}_{jk} = 0$  for  $j \geq k$ , and  $A = (a_{jk})$  and of the vectors  $\tilde{b} = (\tilde{b}_1, \dots, \tilde{b}_\nu)^T$  and  $b = (b_1, \dots, b_\nu)^T$  differentiates the IMEX Runge-Kutta schemes.

IMEX Runge-Kutta schemes can be represented by a *double tableau* in the usual Butcher notation,

$$\begin{array}{c|c} \tilde{c} & \tilde{A} \\ \hline & \tilde{b}^T \end{array} \quad \begin{array}{c|c} c & A \\ \hline & b^T \end{array}, \quad (3.71)$$

where  $\tilde{c}$  and  $c$  are given by

$$\tilde{c}_j = \sum_{k=1}^{j-1} \tilde{a}_{jk}, \quad c_j = \sum_{k=1}^j a_{jk}. \quad (3.72)$$

Here we report the order conditions for IMEX Runge-Kutta schemes up to order  $p = 3$ :

- First Order

$$\sum_{k=1}^\nu \tilde{b}_k = 1, \quad \sum_{k=1}^\nu b_k = 1. \quad (3.73)$$

- Second Order

$$\sum_{k=1}^\nu \tilde{b}_k \tilde{c}_k = \frac{1}{2}, \quad \sum_{k=1}^\nu b_k \tilde{c}_k = \frac{1}{2}, \quad \sum_{k=1}^\nu \tilde{b}_k c_k = \frac{1}{2}, \quad \sum_{k=1}^\nu b_k c_k = \frac{1}{2}, \quad (3.74)$$

- Third Order

$$\begin{aligned} \sum_{j,k=1}^\nu \tilde{a}_{jk} \tilde{b}_k \tilde{c}_k &= \frac{1}{6}, \quad \sum_{k=1}^\nu \tilde{b}_k \tilde{c}_k \tilde{c}_k = \frac{1}{3}, \quad \sum_{j,k=1}^\nu a_{jk} b_k c_k = \frac{1}{6}, \quad \sum_{k=1}^\nu b_k c_k c_k = \frac{1}{3}, \\ \sum_{j,k=1}^\nu \tilde{a}_{jk} \tilde{b}_k c_k &= \frac{1}{6}, \quad \sum_{j,k=1}^\nu a_{jk} \tilde{b}_k \tilde{c}_k = \frac{1}{6}, \quad \sum_{j,k=1}^\nu a_{jk} \tilde{b}_k c_k = \frac{1}{6}, \\ \sum_{j,k=1}^\nu \tilde{a}_{jk} b_k c_k &= \frac{1}{6}, \quad \sum_{j,k=1}^\nu a_{jk} b_k \tilde{c}_k = \frac{1}{6}, \quad \sum_{j,k=1}^\nu \tilde{a}_{jk} b_k \tilde{c}_k = \frac{1}{6}, \\ \sum_{k=1}^\nu \tilde{b}_k c_k c_k &= \frac{1}{3}, \quad \sum_{k=1}^\nu \tilde{b}_k \tilde{c}_k c_k = \frac{1}{3}, \quad \sum_{k=1}^\nu b_k \tilde{c}_k \tilde{c}_k = \frac{1}{3}, \quad \sum_{k=1}^\nu b_k \tilde{c}_k c_k = \frac{1}{3}. \end{aligned} \quad (3.75)$$

In the following tables, the Butcher tableau for second and third order IMEX schemes used in this thesis are illustrated. In all these schemes the implicit tableau corresponds to an L-stable scheme, that is  $b^T A^{-1} e = 1$ , where  $e$  is a vector whose components are all equal to 1. The notation  $(s, \sigma, p)$ , where  $s$  indicates the number of stages of the implicit scheme,  $\sigma$  the number of stages of the explicit scheme and  $p$  is the order of the IMEX scheme, is used.

All the IMEX schemes used in this work satisfy a particular condition, i.e.  $a_{jk} = 0$  for  $j > k$ . This family of IMEX schemes are called Direct Implicit Runge-Kutta (DIRK) schemes. Furthermore the schemes reported in the tables satisfy the additional condition  $b_k = a_{\nu,k}$  and  $\tilde{b}_k = \tilde{a}_{\nu,k}$  for  $k = 1, \dots, \nu$ . In this way the equation (3.70) can be replaced by the more simple expression

$$\mathbf{U}^{n+1} = \mathbf{U}^{(\nu)}. \quad (3.76)$$

Finally, to apply the IMEX Runge-Kutta schemes to the system of partial differential equation (2.19)–(2.24) we need a suitable spatial discretization of Eq. (3.67), and in particular of the term  $\mathbf{F}(\mathbf{U})_x$ . This can be done using, for example, the numerical fluxes  $\tilde{\mathbf{F}}_{i\pm\frac{1}{2}}$  defined in the previous sections, i.e. the Lax-Friedrichs (3.14), the GForce (3.15), the Kurganov, Noelle, Petrova (3.37), the Kurganov and Tadmor (3.39) or the modification of the Lax-Friedrichs (3.42) numerical fluxes.

0	0	0		0	0	0
1	1	0		1	0	1
	1	0			0	1

Table 1: Tableau Implicit-Explicit Euler IEE(1,1,1)

0	0	0	0	0	0	0	0
γ	γ	0	0	γ	0	γ	0
1	δ	1 - δ	0	1	0	1 - γ	γ
	δ	1 - δ	0		0	1 - γ	γ

$$\gamma = 1 - \frac{1}{\sqrt{2}}, \delta = 1 - \frac{1}{2\gamma}$$

Table 2: Tableau Asher, Ruuth, Spiteri ARS(2,2,2)

0	0	0	0	0	0	0	0
1/2	1/2	0	0	0	1/2	0	1/2
1/3	1/3	0	0	0	1/3	0	1/3
1	0	1	0	0	1	0	3/4
	0	1	0	0		0	3/4
						0	1/4

Table 3: Tableau Liotta, Romano, Russo LRR(3,2,2)

0	0	0	0	0	0	0	0
1	1	0	0	0	1	0	1/2
2/3	4/9	2/9	0	0	2/3	5/18	-1/9
1	1/4	0	3/4	0	1	1/2	0
1	1/4	0	3/4	0	1	1/4	0
	1/4	0	3/4	0		1/4	0
						3/4	-1/2
							1/2

Table 4: Tableau Boscarino, Pareschi, Russo BPR(5,3,3)

### 3.2.1 Computation of the solution using IMEX DIRK schemes

When using DIRK schemes, at each internal Runge-Kutta step we have to solve an implicit problem for all the cells of the domain. Infact, applying a DIRK scheme to the partial differential equation (2.19)–(2.24) we obtain

$$\mathbf{U}_i^{(j)} = \mathbf{U}_i^n - \Delta t \sum_{k=1}^{j-1} \tilde{a}_{jk} \left( \frac{\tilde{\mathbf{F}}_{i+\frac{1}{2}}^{(k)} - \tilde{\mathbf{F}}_{i-\frac{1}{2}}^{(k)}}{\Delta x} - \hat{\mathbf{S}}(\mathbf{U}_i^{(k)}) \right) + \Delta t \cdot \frac{1}{\tau} \sum_{k=1}^j a_{jk} \mathbf{R}(\mathbf{U}_i^{(k)}), \quad (3.77)$$

$$\mathbf{U}_i^{n+1} = \mathbf{U}_i^n - \Delta t \sum_{k=1}^v \tilde{b}_k \left( \frac{\tilde{\mathbf{F}}_{i+\frac{1}{2}}^{(k)} - \tilde{\mathbf{F}}_{i-\frac{1}{2}}^{(k)}}{\Delta x} - \hat{\mathbf{S}}(\mathbf{U}_i^{(k)}) \right) + \Delta t \cdot \frac{1}{\tau} \sum_{k=1}^v b_k \mathbf{R}(\mathbf{U}_i^{(k)}), \quad (3.78)$$

for all  $j = 1, \dots, v$ . Furthermore, since in the equation (3.66) no differential operators are present,  $\mathbf{R}(\mathbf{U}_i^{(k)})$  depends only on the solution in the cell  $i$ . Thus, for each Runge-Kutta step, we have to solve  $n$  independent implicit problems, one for each cell of the domain. All the implicit problems can be solved using a functional iterative method, like Newton-Raphson. For simplicity, we rewrite the equation (3.77) as follows:

$$\begin{aligned} \mathbf{U}_i^{(j)} &= \mathbf{U}_i^n - \Delta t \sum_{k=1}^{j-1} \tilde{a}_{jk} \left( \frac{\tilde{\mathbf{F}}_{i+\frac{1}{2}}^{(k)} - \tilde{\mathbf{F}}_{i-\frac{1}{2}}^{(k)}}{\Delta x} - \hat{\mathbf{S}}(\mathbf{U}_i^{(k)}) \right) + \\ &+ \Delta t \cdot \frac{1}{\tau} \sum_{k=1}^{j-1} a_{jk} \mathbf{R}(\mathbf{U}_i^{(k)}) + \Delta t \cdot \frac{1}{\tau} a_{jj} \mathbf{R}(\mathbf{U}_i^{(j)}) \\ &\quad \downarrow \\ \mathbf{U}_i^{(j)} - \Lambda_i - \Delta t \cdot \frac{1}{\tau} a_{jj} \mathbf{R}(\mathbf{U}_i^{(j)}) &= 0 \\ &\quad \downarrow \\ \Gamma(\mathbf{U}_i^{(j)}) &= 0. \end{aligned} \quad (3.79)$$

The term  $\Lambda_i$  contains the explicit part of the equation (3.77), thus it can be calculated once during the computation of the solution  $\mathbf{U}_i^{(j)}$  with the iterative method.

Now, applying the Newton-Raphson method to  $\Gamma(\mathbf{x}) = 0$  we obtain

$$\begin{cases} \mathbf{x}_{(k+1)} = \mathbf{x}_{(k)} - J_{|\mathbf{x}_{(k)}}^{-1} \cdot \Gamma(\mathbf{x}_{(k)}) \\ \mathbf{x}_{(0)} = \mathbf{U}_i^n \end{cases} \quad (3.80)$$

where  $J_{|\mathbf{x}_{(k)}}^{-1}$  is the inverse of the Jacobian of the function  $\Gamma$  evaluated at  $\mathbf{x}_{(k)}$ . We underline here that the inversion of the Jacobian is not very expensive in terms of computational costs, since  $J$  is a  $m \times m$  matrix where  $m$  is the number of the equation of the system (2.19)–(2.24).

### 3.2.2 Derivative approximation through complex numbers

The solution of the system (3.80) requires an accurate evaluation of the Jacobian matrix  $J$ , i.e. the partial derivatives of  $\Gamma$  with respect to the components of  $\mathbf{x}$ . Due to the strong non-linearity of  $\mathbf{R}(\mathbf{U})$ , this task requires a particular attention and analysis.

Let us consider a function  $f(x) : \mathbb{R} \rightarrow \mathbb{R}$ ,  $f \in C^1(\mathbb{R})$ . A common method to estimate the first derivative is the forward-difference formula

$$f'(x) \approx \frac{f(x+h) - f(x)}{h}, \quad (3.81)$$

where  $h$  is the finite-difference interval. This is a first-order approximation, but using the Taylor series expansion and increasing the stencil of the approximation, it is possible to have high order approximation.

However, when estimating sensitivities using finite-difference formulas we are faced with the “step-size dilemma”, that is the desire to choose a small step size to minimize truncation error while avoiding the use of a step so small that errors due to subtractive cancellation become dominant.

A way to overcome this problem is to use the complex functions. The first use of complex variables to estimate derivatives starts with the work of Lyness and Moler (1967) and Lyness (1967). They introduce a reliable method for calculating the derivatives of an analytic function, and later Squire and Trapp (1998) obtain a very simple expression for estimating the first derivative. It has been shown that this estimation is very accurate, extremely robust and easy to implement, with a reasonable computational cost. Recently it has been used for sensitivity analysis in computational fluid dynamics (CFD) by Anderson et al. (2001). Further research on the subject has been carried out by Martins et al. (2001, 2000, 2003).

Let's see more in detail the theory behind the estimation of derivatives using complex variables. Consider a function  $g(x) : \mathbb{C} \rightarrow \mathbb{C}$ ,  $g \in C^1(\mathbb{C})$ . Then the Cauchy-Riemann equalities hold:

$$\frac{\partial u}{\partial x} = \frac{\partial v}{\partial y}, \quad \frac{\partial u}{\partial y} = -\frac{\partial v}{\partial x}, \quad (3.82)$$

where  $g(z) = u(x+iy) + iv(x+iy)$ ,  $\Re(g(x+iy)) = u(x+iy)$  and  $\Im(g(x+iy)) = v(x+iy)$ . Thanks to this equalities we can write

$$\left. \frac{\partial u}{\partial x} \right|_{(x+iy)} = \lim_{h \rightarrow 0} \frac{v(x+i(y+h)) - v(x+iy)}{h}, \quad (3.83)$$

where  $h$  is a real number. Since the function  $f \in C^1(\mathbb{R})$ , we can extend it to the complex plane and define a new function  $\tilde{f} : \mathbb{C} \rightarrow \mathbb{C}$  such that  $\tilde{f}(x) = f(x)$ ,  $\forall x \in \mathbb{R}$ . In this way, using the relation (3.83) we have

$$\left. \frac{\partial \Re(\tilde{f})}{\partial x} \right|_{(x+iy)} = \lim_{h \rightarrow 0} \frac{\Im(\tilde{f}(x+i(y+h))) - \Im(\tilde{f}(x+iy))}{h} \quad (3.84)$$

and finally posing  $y = 0$  we obtain

$$\begin{aligned} \left. \frac{\partial \Re(\tilde{f})}{\partial x} \right|_{(x)} &= \lim_{h \rightarrow 0} \frac{\Im(\tilde{f}(x+ih)) - \Im(\tilde{f}(x))}{h} \\ &\Downarrow \\ \left. \frac{\partial f}{\partial x} \right|_{(x)} &= \lim_{h \rightarrow 0} \frac{\Im(\tilde{f}(x+ih))}{h}. \end{aligned} \quad (3.85)$$

For a small discrete  $h$ , this can be approximated by

$$\frac{\partial f}{\partial x} \Big|_{(x)} \approx (f'(x))_{CS} = \frac{\Im(\tilde{f}(x + ih))}{h}. \quad (3.86)$$

This is called the *complex-step derivative approximation*. This estimation is not subject to subtractive cancellation errors, since it does not involve a difference operation. To see the improvements with respect the finite differences, we try to approximate the first derivative of the analytic function

$$f(x) = \frac{x^2}{1+x^4} \quad (3.87)$$

at  $x = 0.25$ . We compare the complex-step derivative approximation with the first order forward differences

$$(f'(x))_{F_1} = \frac{f(x+h) - f(x)}{h}, \quad (3.88)$$

the first order backward differences

$$(f'(x))_{B_1} = \frac{f(x) - f(x-h)}{h}, \quad (3.89)$$

the second order central differences

$$(f'(x))_{C_2} = \frac{f(x + \frac{h}{2}) - f(x - \frac{h}{2})}{h}, \quad (3.90)$$

the second order forward differences

$$(f'(x))_{F_2} = \frac{-f(x+2h) + 4f(x+h) - 3f(x)}{2h}, \quad (3.91)$$

the second order backward differences

$$(f'(x))_{B_2} = \frac{3f(x) - 4f(x-h) + f(x-2h)}{2h}, \quad (3.92)$$

and finally the forth order central differences

$$(f'(x))_{C_4} = \frac{-f(x+2h) + 8f(x+h) - 8f(x-h) + f(x-2h)}{12h}. \quad (3.93)$$

In the Fig.3 we report the normalized relative error

$$\epsilon = \left| \frac{(f'(x))_{est} - f'(x)}{f'(x)} \right| \quad (3.94)$$

of all the estimation presented above with respect the exact value  $f'(x)$  calculated at  $x = 0.25$ . As we can see, at the beginning the relative error of all the estimation decrease with the step-size, but at a certain point, for the finite differences, the subtractive cancellation errors become significant, and thus the relative error increases. With the complex step derivative approximation, instead, this does not happen, and the relative error continues to decrease until it reaches the machine working precision. Then, even decreasing the step size, the error remains almost constant. Thus, with the complex step derivative approximation we don't have anymore the "step-size dilemma" and we can

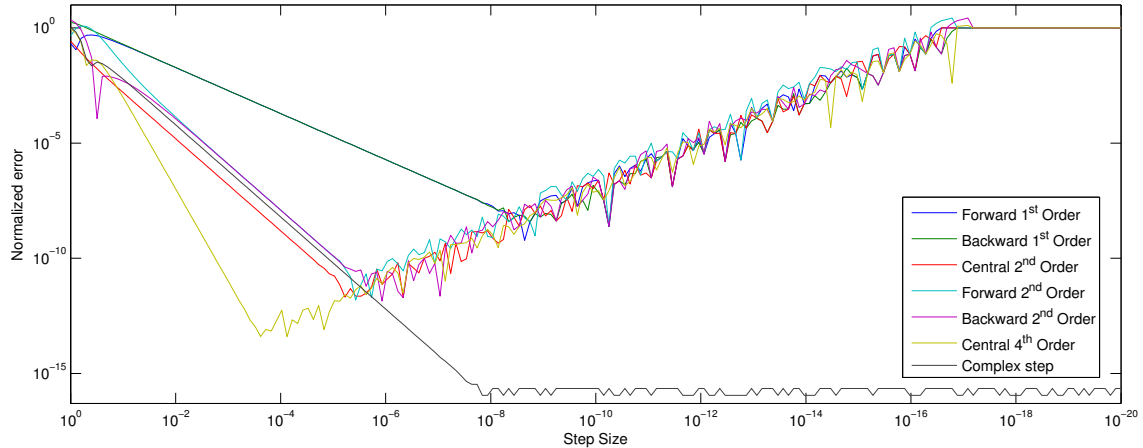


Figure 3: Normalized relative error of the derivative approximations with respect the exact value.

chose the machine working precision as step-size obtaining the highest accuracy for the approximation of the first derivative.

So, with the complex-step derivative approximation we can compute an approximation of the Jacobian  $J$  needed for the Newton-Raphson method with an error of the same order of the machine working precision. Infact, all we have to do is to extend the function  $\Gamma$  to the complex plane, introducing the new function  $\tilde{\Gamma} : \mathbb{C} \rightarrow \mathbb{C}$  and compute the Jacobian at  $\mathbf{x}$  as

$$J(\mathbf{x}) \cdot \mathbf{e}_j = \frac{\Im(\tilde{\Gamma}(\mathbf{x} + i h \mathbf{e}_j))}{h}, \quad (3.95)$$

where  $(\mathbf{e}_j)_{j=1,\dots,m}$  are the vectors canonical basis.

# 4

---

## NUMERICAL TESTS

---

In this section we apply the numerical schemes presented in the previous chapter to the single temperature model for several 1D Riemann problems for an air/water (Romenski et al., 2010; Romenski and Toro, 2004) and a water/steam (Zein et al., 2010) mixture. In the first tests the ability of the numerical schemes presented in Chapter 3 to resolve shock and rarefaction waves is evaluated. Then we analyze the behavior of the numerical schemes in the case of instantaneous and finite rate relaxations.

### 4.1 LINEAR RECONSTRUCTION

For these tests, due to the strong shocks present in the physical solutions, some problems could arise in the piecewise-linear reconstruction of the conservative variables. In fact, the reconstructed values at the interfaces could create unrealistic values of the primitive variables, like negative volume fractions or negative temperatures.

To overcome this problem, instead of computing directly the reconstruction of the conservative vector  $\mathbf{U} = (U_1, U_2, U_3, \vec{U}_4, \vec{U}_5, U_6) = (\rho, \rho\alpha_1, \rho_1\alpha_1, \rho\vec{u}, \vec{w}, \rho(E + |\vec{u}|^2/2))$ , we compute the piecewise-linear reconstruction of the set of physical variables  $\mathbf{Q} = (Q_1, Q_2, Q_3, \vec{Q}_4, \vec{Q}_5, Q_6) = (\alpha_1, P_1, P_2, \vec{u}_1, \vec{u}_2, T)$ .

With this choice of the vector  $\mathbf{Q}$ , there exists a bijection  $\phi$  such that  $\mathbf{Q} = \phi(\mathbf{U})$ , in fact, from the conservative vector  $\mathbf{U}$ , we can write

$$\begin{aligned} Q_1 &= \frac{U_2}{U_1}, \\ Q_6 &= \frac{U_6 - \frac{|\vec{U}_4|^2}{2U_1} - \frac{|\vec{U}_5|^2 U_3(U_1 - U_3)}{2U_1} - (\alpha_1 \bar{P}_1 + (1 - \alpha_1) \bar{P}_2 + U_3 \bar{e}_1 + (U_1 - U_3) \bar{e}_2)}{(U_3 c_{v,1} + (U_1 - U_3) c_{v,2}}}, \\ Q_2 &= c_{v,1}(\gamma_1 - 1) \frac{U_3 U_1}{U_2} Q_6 - \bar{P}_1, \\ Q_3 &= c_{v,2}(\gamma_2 - 1) \frac{(U_1 - U_3) U_1}{(U_1 - U_2)} Q_6 - \bar{P}_2, \\ \vec{Q}_4 &= \frac{\vec{U}_4 + \vec{U}_5(U_1 - U_3)}{U_1}, \\ \vec{Q}_5 &= \frac{\vec{U}_4 - \vec{U}_5 U_3}{U_1}. \end{aligned}$$

	$P_0$ (Pa)	$\rho_0$ (kg/m <sup>3</sup> )	$C_0$ (m/s)	$\gamma$	$c_v$ (J/(kg · K))	$\bar{e}$ (J/kg)	$s_0$ (J/(kg · K))
Water	$10^5$	1000	1625	4.4	951	0.0	0.0
Air	99911.429	1	374	1.4	714	0.0	0.0

Table 5: Parameters of the equation of state for water and air used in the Four Rarefaction, Four Shock, Air-Water Shock and Sonic Point test problem.

Similarly, from the set of physical variables  $\mathbf{Q}$ , we can uniquely determine the conservative variables  $\mathbf{U} = \phi^{-1}(\mathbf{Q})$ , in fact since

$$\rho_1(\mathbf{Q}) = \frac{Q_2 + \bar{P}_1}{c_{v,1}(\gamma_1 - 1)Q_6}, \quad \rho_2(\mathbf{Q}) = \frac{Q_3 + \bar{P}_2}{c_{v,2}(\gamma_2 - 1)Q_6},$$

we can write

$$U_1 = Q_1\rho_1(\mathbf{Q}) + (1 - Q_1)\rho_2(\mathbf{Q}),$$

$$U_2 = Q_1U_1,$$

$$U_3 = Q_1\rho_1(\mathbf{Q}),$$

$$\vec{U}_4 = U_3\vec{Q}_4 + (U_1 - U_3)\vec{Q}_5,$$

$$\vec{U}_5 = \vec{Q}_4 - \vec{Q}_5,$$

$$U_6 = U_3 \left( \bar{e}_1 + c_{v,1}Q_6 + \frac{\bar{P}_1}{\rho_1(\mathbf{Q})} + \frac{|\vec{Q}_4|^2}{2} \right) + (U_1 - U_3) \left( \bar{e}_2 + c_{v,2}Q_6 + \frac{\bar{P}_2}{\rho_2(\mathbf{Q})} + \frac{|\vec{Q}_5|^2}{2} \right).$$

Using the previous relations, we replace Eq. (3.8) for the piecewise-linear reconstruction with the expression

$$\tilde{\mathbf{U}}^n(x) = \sum_j \phi^{-1} \left( \left[ \phi(\mathbf{U}_j^n) + \left( \phi(\mathbf{U}_j^n) \right)' (x - x_j) \right] \right) \cdot \chi_{[x_{j-1/2}, x_{j+1/2}]}(x). \quad (4.1)$$

In this way we are sure that, from the reconstructed solution  $\tilde{\mathbf{U}}^n(x)$ , the physical quantities  $\alpha_1, P_1, P_2$  and  $T$  are not out-of-bounds.

## 4.2 ONE DIMENSIONAL FOUR RAREFACTION PROBLEM

The aim of the first test presented here is to analyze the behavior, in presence of rarefaction waves, of the schemes proposed.

The computational domain considered is [0, 1] m with a Riemann problem being defined with the interface located at  $x = 0.5$  m. The initial data of the test are similar to those described by Romenski and Toro (2004):

$$\begin{cases} \alpha_1 = 0.9, P_i = 10^9 \text{ Pa}, u_i = -300 \text{ m/s}, T = 355 \text{ K} & \forall x \in [0, 0.5) \text{ m} \\ \alpha_1 = 0.9, P_i = 10^9 \text{ Pa}, u_i = +300 \text{ m/s}, T = 355 \text{ K} & \forall x \in [0.5, 1] \text{ m} \end{cases},$$

for  $i = 1, 2$ . The indexes 1 and 2 are referred to the parameters of state of water and air, respectively, and the constants for the equations of state are given in Table 5.

For this test, no source terms are considered, hence we set  $\tau^{(p)} = \tau^{(c)} = \tau^{(f)} = \infty$  and  $g = 0$ . In this way we can compare the differences of the solutions of the homogeneous

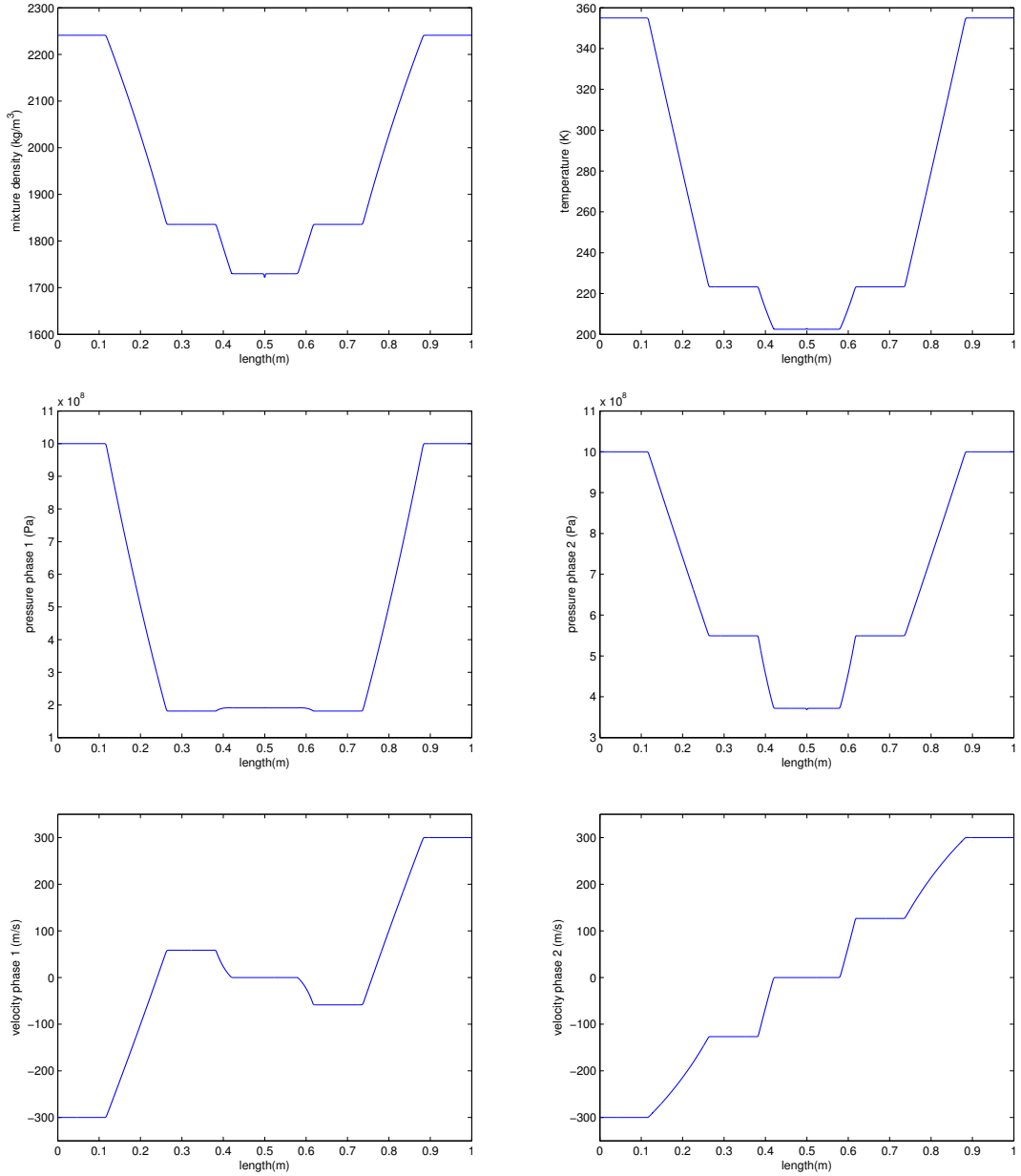


Figure 4: Four Rarefaction - Reference solution for mixture density (top left), mixture temperature (top right), pressure of phase 1 (middle left) and of phase 2 (middle right), velocity of phase 1 (bottom left) and of phase 2 (bottom right).

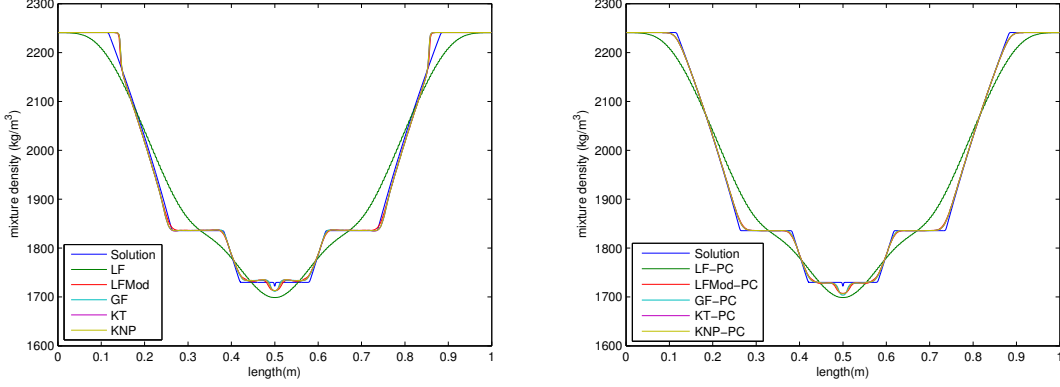


Figure 5: Four Rarefaction - Comparison between the reference solution for the mixture density (blue line), and the solutions computed using the splitting approach with LF (green line), LFMOD (red line), GF (cyan line), KT (magenta line) and KNP numerical fluxes (yellow line). On the left panel, the solutions are obtained without the predictor/corrector strategy, while on the right panel it has been used.

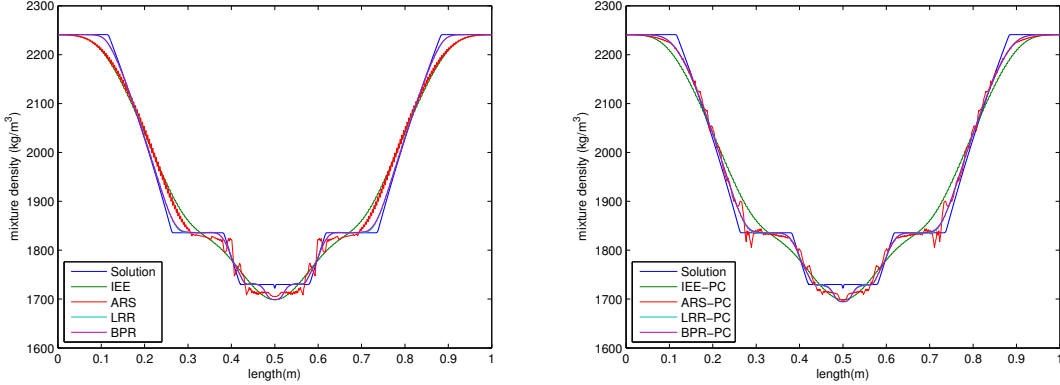


Figure 6: Four Rarefaction - Comparison between the reference solution for the mixture density (blue line), and the solutions computed using the DIRK schemes IEE (green line), ARS (red line), LRR (cyan line) and BPR (magenta line), all in conjunction with the LF numerical fluxes. On the left panel, the solutions are obtained without the predictor/corrector strategy, while on the right panel it has been used.

system of partial differential equations (3.3) obtained using the schemes proposed in this thesis.

The equations of state used for these tests are obtained from a linearized form of the Mie-Grüneisen equations (Le Métayer et al., 2004, 2005; Menikoff and Plohr, 1989; Romenski et al., 2010) and they are described in details in Section 2.3. The parameters of state used for this test are listed in Table 5. Note that the reference temperature can be computed from the data reported in the table as follows:

$$T_{0,i} = \frac{C_{0,i}^2}{\gamma_i(\gamma_i - 1)c_{v,i}}.$$

The results are computed at time  $2.0 \times 10^{-4}$  s using a CFL coefficient equal to 0.49. Transmissive boundary conditions are imposed at  $x = 0$  and  $x = 1$ .

In Fig. 4 it is reported the mixture density, the mixture temperature, the pressures and the velocities of both phases computed with a grid of 16000 cells. This solution is obtained using the splitting approach in conjunction with the predictor/corrector

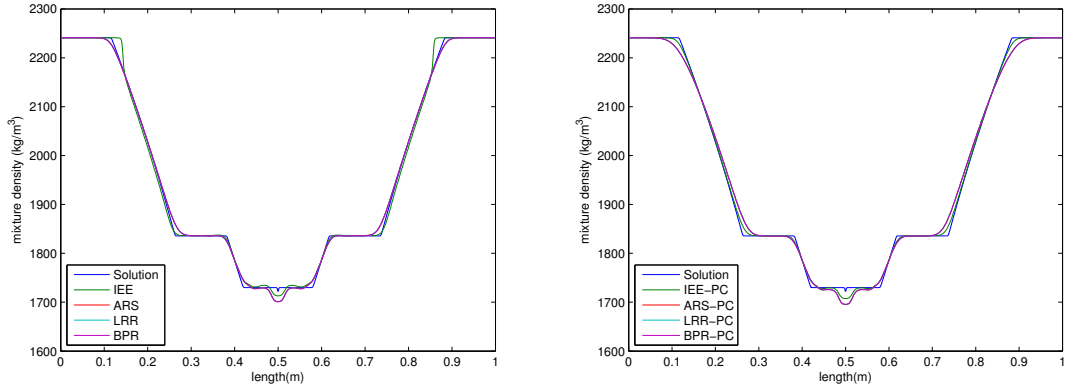


Figure 7: Four Rarefaction - Comparison between the reference solution for the mixture density (blue line), and the solutions computed using the DIRK schemes IEE (green line), ARS (red line), LRR (cyan line) and BPR (magenta line), all in conjunction with the LFMMod numerical fluxes. On the left panel, the solutions are obtained without the predictor/corrector strategy, while on the right panel it has been used.

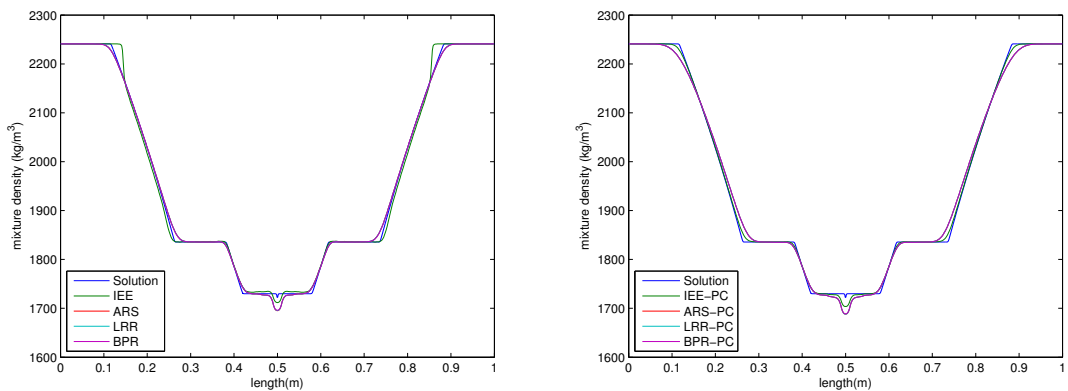


Figure 8: Four Rarefaction - Comparison between the reference solution for the mixture density (blue line), and the solutions computed using the DIRK schemes IEE (green line), ARS (red line), LRR (cyan line) and BPR (magenta line), all in conjunction with the GF numerical fluxes. On the left panel, the solutions are obtained without the predictor/corrector strategy, while on the right panel it has been used.

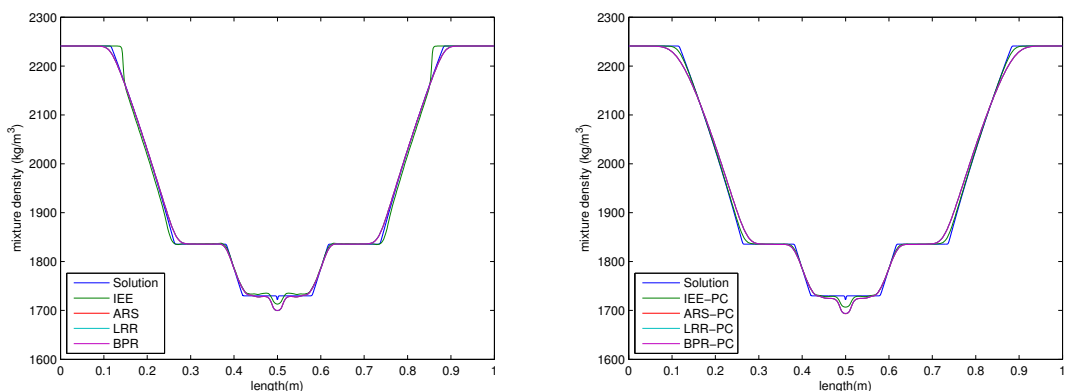


Figure 9: Four Rarefaction - Comparison between the reference solution for the mixture density (blue line), and the solutions computed using the DIRK schemes IEE (green line), ARS (red line), LRR (cyan line) and BPR (magenta line), all in conjunction with the KT numerical fluxes. On the left panel, the solutions are obtained without the predictor/corrector strategy, while on the right panel it has been used.

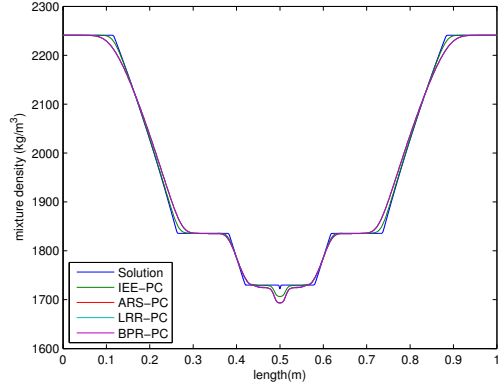
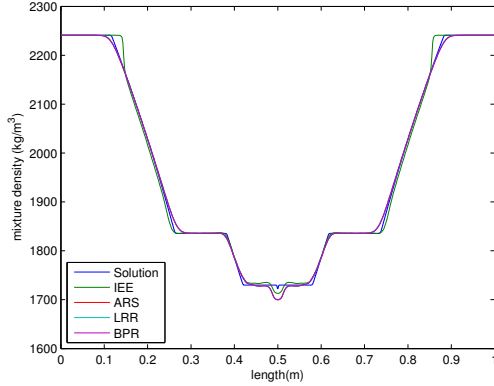


Figure 10: Four Rarefaction - Comparison between the reference solution for the mixture density (blue line), and the solutions computed using the DIRK schemes IEE (green line), ARS (red line), LRR (cyan line) and BPR (magenta line), all in conjunction with the KNP numerical fluxes. On the left panel, the solutions are obtained without the predictor/corrector strategy, while on the right panel it has been used.

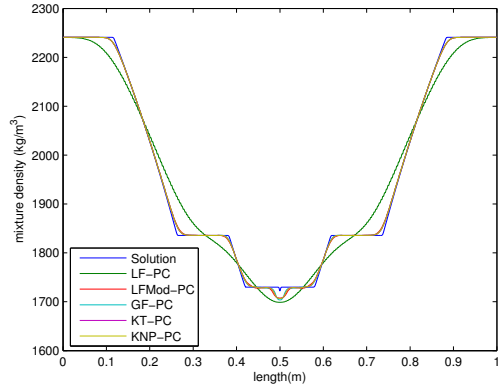
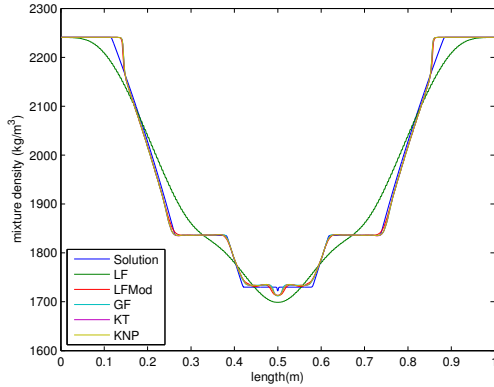


Figure 11: Four Rarefaction - Comparison between the reference solution for the mixture density (blue line), and the solutions computed using the DIRK IEE scheme in conjunction with LF (green line), LMod (red line), GF (cyan line), KT (magenta line) and KNP numerical fluxes (yellow line). On the left panel, the solutions are obtained without the predictor/corrector strategy, while on the right panel it has been used.

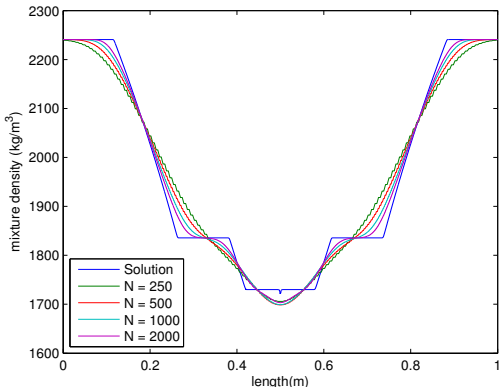
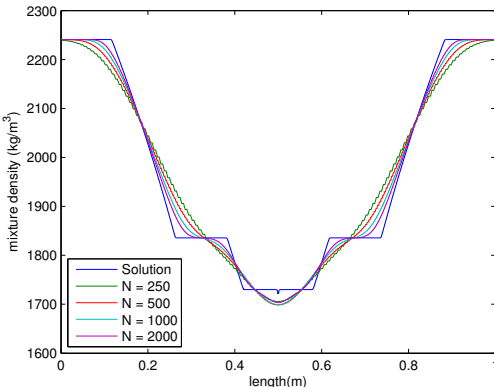


Figure 12: Four Rarefaction - Comparison between the reference solution for the mixture density (blue line) and the solutions obtained using different number of cells for the domain discretization: 250 (green line), 500 (red line), 1000 (cyan line) and 2000 (magenta line) cells. On the left panel we plot the solution obtained with the splitting approach, the predictor/corrector strategy and LF numerical fluxes is plotted, while on the right panel is reported the mixture density obtained with the DIRK scheme IEE in conjunction with LF numerical fluxes.

strategy and the Kurganov and Tadmor numerical fluxes and it will be considered as the reference solution.

As we can see from Fig. 4, the structure of the solution contains four rarefaction waves for the mixture quantities and for the quantities of each phase. Imposing a common temperature, we linked the two phases forcing them to have the respective rarefaction waves propagating with same velocity. Furthermore, the solution contains a low-density region in the middle. For a single-phase flow, it is well documented that the computation of low density flows is indeed very challenging. It is known that all linearized Riemann solvers, for example, will lead to the computation of negative densities (Einfeldt et al., 1991).

In Fig. 5 we plot the reference solution for the mixture density (blue line), and the solutions computed using the splitting approach with the Lax-Friedrichs (LF) numerical fluxes (green line), the modification of the Lax-Friedrichs (LFMod) numerical fluxes (red line), the Generalized FORCE (GF) numerical fluxes (cyan line), the Kurganov and Tadmor (KT) numerical fluxes (magenta line) and finally the Kurganov, Noelle and Petrova (KNP) numerical fluxes (yellow line).

From now on, if not explicitly indicated, the solutions plotted in all figures are computed using a grid of 500 cells (except for the reference solution) and minmod limiter. Furthermore on the right panel the predictor/corrector (PC) strategy is used, while on the left one is not.

As we can see from the Fig. 5 the solutions computed without the predictor/corrector strategy (left panel) are not able to solve properly the rarefaction waves (in  $x \approx 0.15$  and  $x \approx 0.85$  there is a changing in the inclination of the rarefaction waves), while using the predictor/corrector strategy (right panel) this problem disappeared. Furthermore we can see that the solution obtained using the LF numerical fluxes is quite diffusive, while the solutions obtained with the other schemes are very close to the reference solution.

In order to better compare the accuracy of the used schemes we compute the relative error as

$$err(sol_{scheme}, sol_{ref}) = \frac{\sum_j (sol_{scheme}(x_j) - sol_{ref}(x_j))^2}{\sum_j sol_{ref}(x_j)^2}. \quad (4.2)$$

In Table 6 the relative errors of the mixture density computed using the splitting approach and the different numerical fluxes presented in this work are reported. As expected, the fact that, using the splitting approach without the predictor/corrector strategy, the rarefaction waves are not properly solved reflects on the relative errors. In fact, as we can notice from the Table 6, the relative errors of the solutions in which the predictor/corrector strategy is used are smaller than the respective solutions obtained without the predictor/corrector strategy.

In Figs. 6-10, instead, we compare the reference solution for the mixture density (blue line) with the solutions computed using the DIRK schemes, IEE (green line), ARS (red line), LRR (cyan line) and BPR (magenta line). In each of them a different numerical flux is used (LF in Fig. 6, LFMod in Fig. 7, GF in Fig. 8, KT in Fig. 9 and KNP in Fig. 10) comparing the different DIRK schemes, i.e. IEE, ARS, LRR and BPR.

Finally in Fig. 11, for a fixed a DIRK schemes (the IEE for this test) we compare the reference solution with those obtained using the different numerical fluxes presented in this work.

N	LF	LFMod	GF	KT	KNP
250	3.4628e-4	4.1483e-5	4.8656e-5	4.8264e-5	4.8849e-5
500	2.0303e-4	2.4399e-5	2.8818e-5	2.8325e-5	2.8540e-5
1000	1.0915e-4	1.2983e-5	1.5775e-5	1.5026e-5	1.5565e-5
2000	5.3289e-5	6.7647e-6	8.5382e-6	8.0152e-6	8.8367e-6
N	LF-PC	LFMod-PC	GF-PC	KT-PC	KNP-PC
250	3.4628e-4	2.2444e-5	1.7743e-5	1.8540e-5	1.8781e-5
500	2.0303e-4	7.9079e-6	6.0681e-6	6.4359e-6	6.5106e-6
1000	1.0915e-4	2.6243e-6	2.0089e-6	2.1020e-6	2.1237e-6
2000	5.3289e-5	8.0214e-7	6.1463e-7	6.3944e-7	6.4632e-7

Table 6: Four Rarefaction - Relative errors between the reference mixture density and those computed using the splitting approach with the different numerical fluxes presented in this work and different domain discretizations.

DIRK IEE					
N	LF	LFMod	GF	KT	KNP
250	3.4628e-4	4.1483e-5	4.8657e-5	4.8264e-5	4.8849e-5
500	2.0303e-4	2.4399e-5	2.8818e-5	2.8325e-5	2.8540e-5
1000	1.0915e-4	1.2983e-5	1.5775e-5	1.5026e-5	1.5565e-5
2000	5.3289e-5	6.7647e-6	8.5382e-6	8.0152e-6	8.8368e-6
N	LF-PC	LFMod-PC	GF-PC	KT-PC	KNP-PC
250	3.4628e-4	2.2444e-5	1.7743e-5	1.8540e-5	1.8781e-5
500	2.0303e-4	7.9079e-6	6.0681e-6	6.4359e-6	6.5106e-6
1000	1.0915e-4	2.6243e-6	2.0089e-6	2.1020e-6	2.1237e-6
2000	5.3289e-5	8.0214e-7	6.1463e-7	6.3944e-7	6.4632e-7

Table 7: Four Rarefaction - Relative errors between the reference mixture density and those computed using the DIRK IEE scheme with the different numerical fluxes presented in this work and different domain discretizations.

DIRK ARS					
N	LF	LFMod	GF	KT	KNP
250	2.1491e-4	3.5372e-5	3.0480e-5	3.0433e-5	3.0516e-5
500	1.5080e-4	1.2518e-5	1.0648e-5	1.0698e-5	1.0772e-5
1000	9.1138e-5	4.2195e-6	3.6129e-6	3.5751e-6	3.6111e-6
2000	4.9746e-5	1.3434e-6	1.1734e-6	1.1422e-6	1.1569e-6
N	LF-PC	LFMod-PC	GF-PC	KT-PC	KNP-PC
250	1.2452e-4	8.7353e-5	8.4235e-5	8.3584e-5	8.3986e-5
500	7.1397e-5	3.7359e-5	3.6063e-5	3.5899e-5	3.6036e-5
1000	2.3038e-5	1.5328e-5	1.4889e-5	1.4779e-5	1.4820e-5
2000	9.3769e-6	6.1139e-6	5.9996e-6	5.9394e-6	5.9526e-6

Table 8: Four Rarefaction - Relative errors between the reference mixture density and those computed using the DIRK ARS scheme with the different numerical fluxes presented in this work and different domain discretizations.

DIRK LRR					
N	LF	LFMod	GF	KT	KNP
250	6.2973e-5	3.5166e-5	3.0277e-5	3.0355e-5	3.0464e-5
500	2.1979e-5	1.2457e-5	1.0587e-5	1.0671e-5	1.0740e-5
1000	7.5931e-6	4.2022e-6	3.5941e-6	3.5671e-6	3.5977e-6
2000	2.4601e-6	1.3397e-6	1.1671e-6	1.1388e-6	1.1521e-6
N	LF-PC	LFMod-PC	GF-PC	KT-PC	KNP-PC
250	1.1706e-4	8.7130e-5	8.4014e-5	8.3390e-5	8.3819e-5
500	4.7451e-5	3.7281e-5	3.5985e-5	3.5837e-5	3.5975e-5
1000	1.8976e-5	1.5304e-5	1.4863e-5	1.4758e-5	1.4800e-5
2000	7.3497e-6	6.1061e-6	5.9906e-6	5.9327e-6	5.9454e-6

Table 9: Four Rarefaction - Relative errors between the reference mixture density and those computed using the DIRK LRR scheme with the different numerical fluxes presented in this work and different domain discretizations.

DIRK BPR					
N	LF	LFMod	GF	KT	KNP
250	5.9966e-5	3.4403e-5	2.9087e-5	2.9358e-5	2.9528e-5
500	2.1023e-5	1.2208e-5	1.0180e-5	1.0340e-5	1.0414e-5
1000	7.3740e-6	4.1214e-6	3.4596e-6	3.4578e-6	3.4869e-6
2000	2.3984e-6	1.3121e-6	1.1211e-6	1.1020e-6	1.1140e-6
N	LF-PC	LFMod-PC	GF-PC	KT-PC	KNP-PC
250	1.1236e-4	8.6343e-5	8.2950e-5	8.2539e-5	8.2935e-5
500	4.6087e-5	3.6980e-5	3.5588e-5	3.5502e-5	3.5634e-5
1000	1.8653e-5	1.5195e-5	1.4718e-5	1.4636e-5	1.4675e-5
2000	7.2786e-6	6.0667e-6	5.9381e-6	5.8877e-6	5.8996e-6

Table 10: Four Rarefaction - Relative errors between the reference mixture density and those computed using the DIRK BPR scheme with the different numerical fluxes presented in this work and different domain discretizations.

N	LF	LFMod	GF	KT	KNP
250	-	-	-	-	-
500	1.3190	1.5073	1.4573	1.4782	1.4839
1000	1.4016	1.5646	1.5095	1.5473	1.5340
2000	1.5072	1.5494	1.4771	1.5163	1.4182
N	LF-PC	LFMod-PC	GF-PC	KT-PC	KNP-PC
250	-				
500	1.3190	1.9497	1.9230	1.9298	1.9264
1000	1.4016	1.9745	2.0076	2.0022	2.0026
2000	1.5072	2.0918	2.1276	2.1018	2.1023

Table 11: Four Rarefaction - Convergence rates for the mixture density computed with different domain discretization using the splitting approach with the numerical fluxes presented in this work.

DIRK IEE					
N	LF	LFMod	GF	KT	KNP
250	-	-	-	-	-
500	<b>1.3190</b>	<b>1.5073</b>	<b>1.4573</b>	<b>1.4782</b>	<b>1.4839</b>
1000	<b>1.4016</b>	<b>1.5646</b>	<b>1.5095</b>	<b>1.5473</b>	<b>1.5340</b>
2000	<b>1.5072</b>	<b>1.5494</b>	<b>1.4771</b>	<b>1.5163</b>	<b>1.4182</b>
N	LF-PC	LFMod-PC	GF-PC	KT-PC	KNP-PC
250	-	-	-	-	-
500	<b>1.3190</b>	<b>1.9497</b>	<b>1.9230</b>	<b>1.9298</b>	<b>1.9264</b>
1000	<b>1.4016</b>	<b>1.9745</b>	<b>2.0076</b>	<b>2.0022</b>	<b>2.0026</b>
2000	<b>1.5072</b>	<b>2.0918</b>	<b>2.1276</b>	<b>2.1018</b>	<b>2.1023</b>

Table 12: Four Rarefaction - Convergence rates for the mixture density computed with different domain discretization using the DIRK IEE scheme with the numerical fluxes presented in this work.

DIRK ARS					
N	LF	LFMod	GF	KT	KNP
250	-	-	-	-	-
500	<b>1.1291</b>	<b>1.9459</b>	<b>1.9038</b>	<b>1.9175</b>	<b>1.9071</b>
1000	<b>1.3505</b>	<b>1.9620</b>	<b>1.9809</b>	<b>1.9810</b>	<b>1.9796</b>
2000	<b>1.5753</b>	<b>2.0434</b>	<b>2.0638</b>	<b>2.0516</b>	<b>2.0517</b>
N	LF-PC	LFMod-PC	GF-PC	KT-PC	KNP-PC
250	-	-	-	-	-
500	<b>1.4520</b>	<b>1.6476</b>	<b>1.6364</b>	<b>1.6269</b>	<b>1.6271</b>
1000	<b>1.9030</b>	<b>1.6867</b>	<b>1.6774</b>	<b>1.6761</b>	<b>1.6766</b>
2000	<b>1.6510</b>	<b>1.7098</b>	<b>1.7013</b>	<b>1.7027</b>	<b>1.7029</b>

Table 13: Four Rarefaction - Convergence rates for the mixture density computed with different domain discretization using the DIRK ARS scheme with the numerical fluxes presented in this work.

DIRK LRR					
N	LF	LFMod	GF	KT	KNP
250	-	-	-	-	-
500	<b>1.9829</b>	<b>1.9452</b>	<b>1.9033</b>	<b>1.9175</b>	<b>1.9084</b>
1000	<b>1.9428</b>	<b>1.9619</b>	<b>1.9811</b>	<b>1.9805</b>	<b>1.9798</b>
2000	<b>2.0201</b>	<b>2.0427</b>	<b>2.0645</b>	<b>2.0524</b>	<b>2.0518</b>
N	LF-PC	LFMod-PC	GF-PC	KT-PC	KNP-PC
250	-	-	-	-	-
500	<b>1.7708</b>	<b>1.6470</b>	<b>1.6360</b>	<b>1.6265</b>	<b>1.6269</b>
1000	<b>1.7216</b>	<b>1.6865</b>	<b>1.6772</b>	<b>1.6760</b>	<b>1.6764</b>
2000	<b>1.7503</b>	<b>1.7096</b>	<b>1.7010</b>	<b>1.7025</b>	<b>1.7028</b>

Table 14: Four Rarefaction - Convergence rates for the mixture density computed with different domain discretization using the DIRK LRR scheme with the numerical fluxes presented in this work.

DIRK BPR					
N	LF	LFMod	GF	KT	KNP
250	-	-	-	-	-
500	1.9837	1.9461	1.9056	1.9201	1.9133
1000	1.9061	1.9629	1.9836	1.9833	1.9827
2000	2.0067	2.0479	2.0711	2.0582	2.0580
N	LF-PC	LFMod-PC	GF-PC	KT-PC	KNP-PC
250	-	-	-	-	-
500	1.7410	1.6457	1.6347	1.6260	1.6261
1000	1.6882	1.6858	1.6761	1.6751	1.6757
2000	1.7320	1.7093	1.7004	1.7019	1.7021

Table 15: Four Rarefaction - Convergence rates for the mixture density computed with different domain discretization using the DIRK BPR scheme with the numerical fluxes presented in this work.

Except for the solution computed using the LF numerical fluxes, that presents many oscillations, all the other solutions obtained with the DIRK schemes are quite good. Only for the DIRK IEE we find again the problem with the rarefaction waves that we have noticed using the splitting approach. However this is normal, since, when using the same numerical fluxes, the DIRK IEE scheme without source terms coincides with the splitting approach. For this reason when we apply the predictor/corrector strategy to the DIRK IEE the solution returns to be the correct one.

In the Tables 7-10, as we have done for the solutions computed using the splitting approach, the relative errors obtained using the DIRK schemes are collected.

We can see that the data reported in Tables 6 and 7 are the same, because of what we have said before about the splitting approach and the DIRK IEE schemes. Furthermore we can see that the relative errors obtained using the DIRK ARS, LRR and BPR schemes are very similar. In addition, although the predictor/corrector strategy increases the accuracy for the DIRK IEE, this is not true for the other DIRK schemes examined. Indeed, the relative errors of the DIRK ARS, LRR and BPR schemes with the predictor/corrector strategy are bigger than those obtained without it.

Finally, comparing all the relative errors collected, we can notice that the splitting approach is more accurate than DIRK schemes.

In order to have a better view of the proposed schemes, in addition to the relative error, we compute also the convergence rate of the schemes as

$$\text{rate}(\text{sol}_{N,\text{scheme}}, \text{sol}_{2N,\text{scheme}}, \text{sol}_{\text{ref}}) = \frac{\sum_j |\text{sol}_{N,\text{scheme}}(x_j) - \text{sol}_{\text{ref}}(x_j)|}{\sum_j |\text{sol}_{2N,\text{scheme}}(x_j) - \text{sol}_{\text{ref}}(x_j)|}. \quad (4.3)$$

In Tables 11-15 the convergence rates of all the schemes used in this test are reported. The data collected demonstrate that the predictor/corrector strategy increases also the convergence rate of the splitting schemes, while it decreases those of the DIRK schemes (except for DIRK IEE).

The effects of grid refinement are shown in Fig. 12, where we plot the reference mixture density (blue line) and those obtained using four different number of cells: 250 (green line), 500 (red line), 1000 (cyan line) and 2000 (magenta line) cells. On the left panel we plot the solution obtained with the splitting approach, the predictor/corrector

strategy and LF numerical fluxes, while on the right panel we report the mixture density obtained with the DIRK schemes IEE in conjunction with LF numerical fluxes.

The numerical results obtained for this test with the splitting approach in conjunction with the predictor/corrector strategy and with the DIRK schemes ARS, LRR and BPR look very satisfactory because all the expected features of the solution are well resolved. On the contrary, we observe that with the splitting approach without the predictor/corrector strategy (and consequently the DIRK scheme IEE) the solver is not able to reproduce correctly the rarefaction waves.

Finally, we note in all the solutions reported the presence of a little depression in the mixture density in a neighborhood of the point  $x = 0.5$  m. Increasing the number of cells and the end-time of the computation, this depression becomes smaller and smaller.

#### 4.3 ONE DIMENSIONAL FOUR SHOCK PROBLEM

The aim of the second test is to analyze the behavior and the robustness of the proposed schemes in presence of shock waves. Furthermore, we want to test the ability of the schemes to resolve the shock with high resolution and without spurious oscillations in the vicinity of the discontinuity. This test was presented in Romenski and Toro (2004) and applied to the single temperature model with some of the proposed numerical schemes in La Spina and de' Michieli Vitturi (2012).

We consider a Riemann problem with water and air as the phase 1 and 2 respectively. The computational domain (in meters) is  $[0, 1]$  with the Riemann problem being defined with the interface located at  $x = 0.5$ . The initial data of the test are the following:

$$\begin{cases} \alpha_1 = 0.9, P_i = 10^9 \text{ Pa}, u_i = +3000 \text{ m/s}, T = 355 \text{ K} & \forall x \in [0, 0.5) \text{ m} \\ \alpha_1 = 0.9, P_i = 10^9 \text{ Pa}, u_i = -3000 \text{ m/s}, T = 355 \text{ K} & \forall x \in [0.5, 1] \text{ m}. \end{cases}$$

for  $i = 1, 2$ . The constants for the equations of state are given in Table 5. For this test, as for the previous one, no source terms are considered, thus we set  $\tau^{(p)} = \tau^{(c)} = \tau^{(f)} = \infty$  and  $g = 0$ . The results are computed at time  $9.0 \times 10^{-5}$  s using a CFL coefficient equal to 0.49. Transmissive boundary conditions are imposed at  $x = 0$  and  $x = 1$ . Finally, the parameters of state used for this test are reported in Table 5

In Fig. 13 we plot the mixture density, the mixture temperature, the pressures and the velocities of both phases computed with a grid of 16000 cells. This solution is obtained using the splitting approach in conjunction with the LFMod numerical fluxes and it will be considered as the reference solution.

As we can see from Fig. 13, the structure of the solution contains four symmetric shock waves, two corresponding to the acoustic speed of the liquid phase and two corresponding to the acoustic speed of the gas phase (Romenski and Toro, 2004).

Fig. 14 presents the reference solution for the mixture density (blue line), and the solutions computed using the splitting approach and the LF (green line), the LFMod (red line), the GF (cyan line), the KT (magenta line) and the KNP (yellow line) numerical fluxes. As we can see, the solutions obtained without the predictor/corrector strategy (left panel) present many spurious oscillations that mostly disappear if we use that strategy (right panel).

In Figs. 15-19 the reference solution for the mixture density (blue line) is compared with the solutions computed using the different DIRK schemes proposed: IEE (green line), ARS (red line), LRR (cyan line) and BPR (magenta line). In Fig. 15 the solution

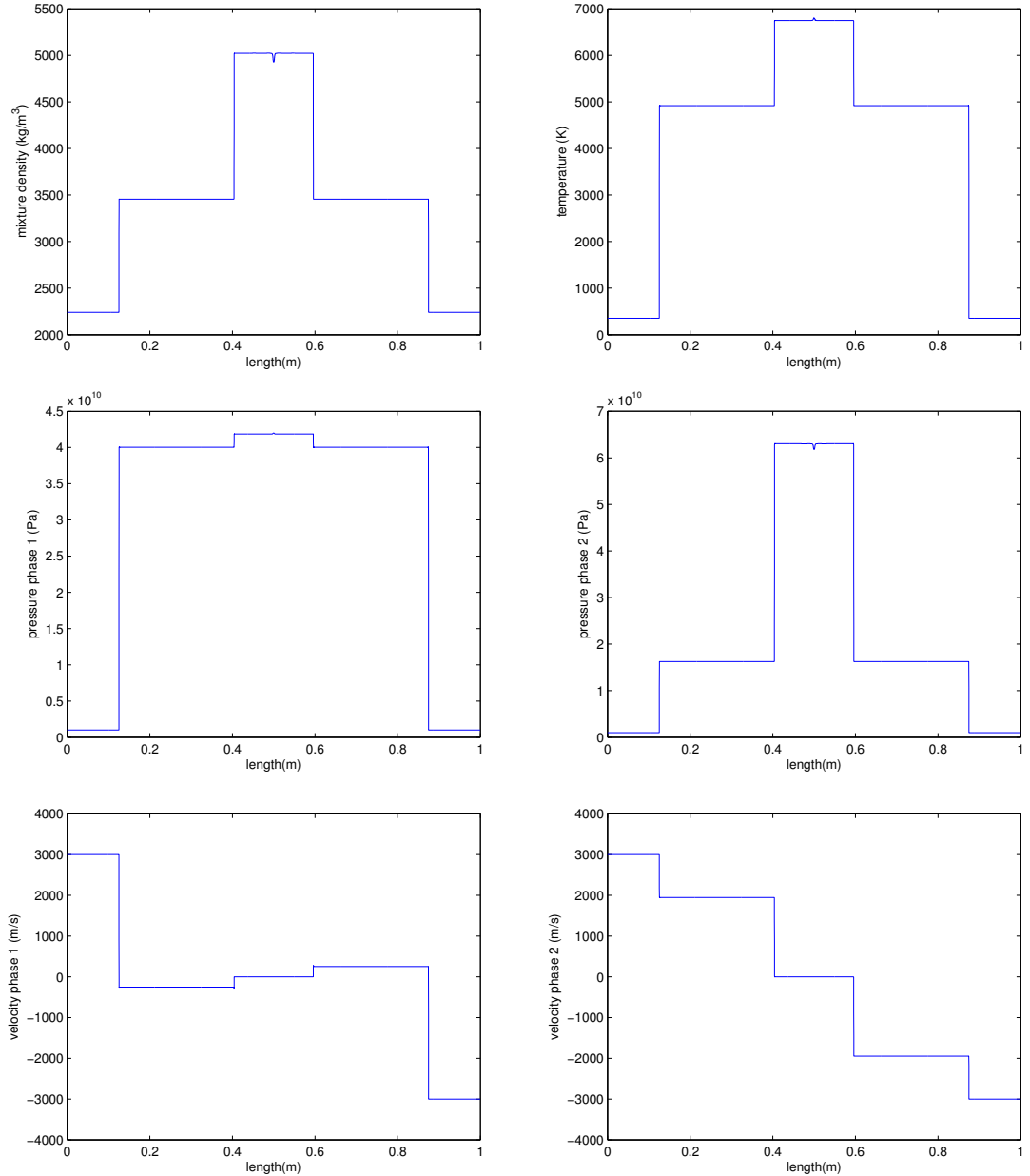


Figure 13: Four Shock - Reference solution for mixture density (top left), mixture temperature (top right), pressure of phase 1 (middle left) and of phase 2 (middle right), velocity of phase 1 (bottom left) and of phase 2 (bottom right).

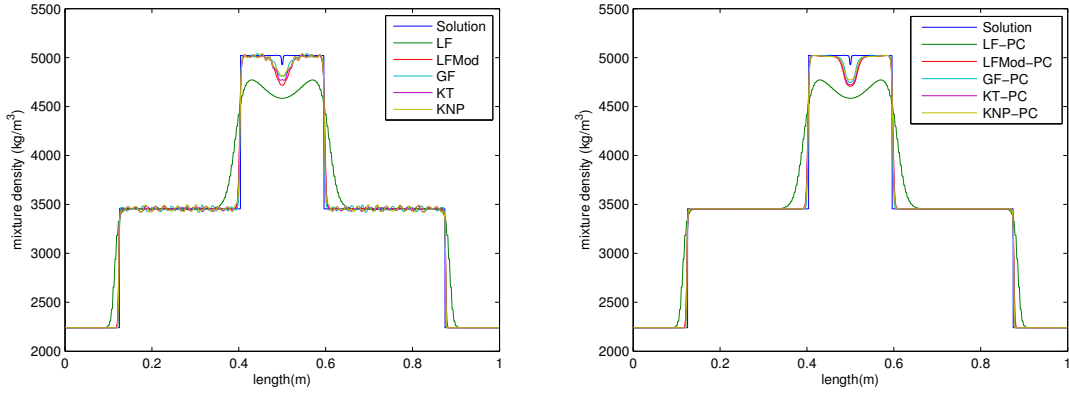


Figure 14: Four Shock - Comparison between the reference solution for the mixture density (blue line), and the solutions computed using the splitting approach with LF (green line), LFMod (red line), GF (cyan line), KT (magenta line) and KNP numerical fluxes (yellow line). On the left panel, the solutions are obtained without the predictor/corrector strategy, while on the right panel it has been used.

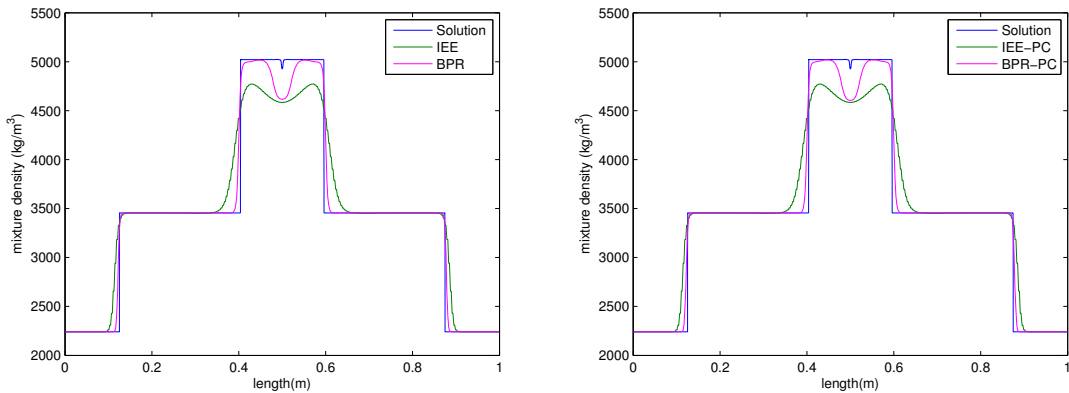


Figure 15: Four Shock - Comparison between the reference solution for the mixture density (blue line), and the solutions computed using the DIRK schemes IEE (green line) and BPR (magenta line), all in conjunction with the LF numerical fluxes. On the left panel, the solutions are obtained without the predictor/corrector strategy, while on the right panel it has been used.

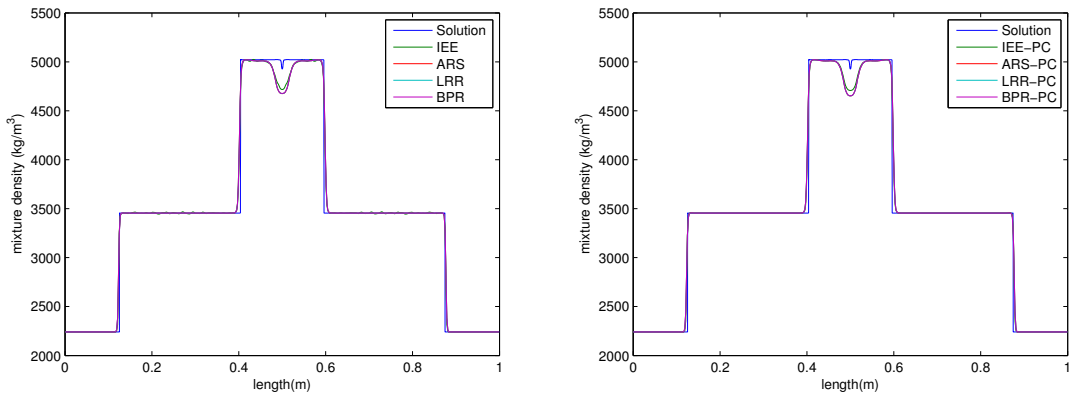


Figure 16: Four Shock - Comparison between the reference solution for the mixture density (blue line), and the solutions computed using the DIRK schemes IEE (green line), ARS (red line), LRR (cyan line) and BPR (magenta line), all in conjunction with the LFMod numerical fluxes. On the left panel, the solutions are obtained without the predictor/corrector strategy, while on the right panel it has been used.

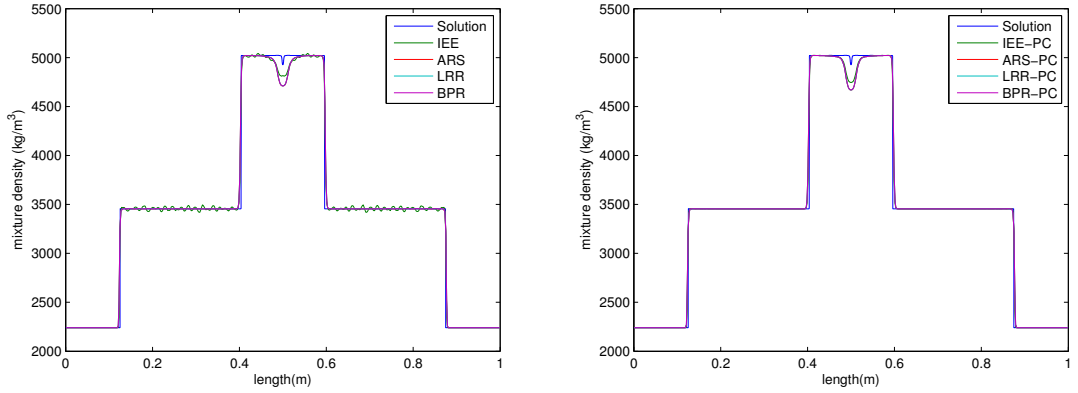


Figure 17: Four Shock - Comparison between the reference solution for the mixture density (blue line), and the solutions computed using the DIRK schemes IEE (green line), ARS (red line), LRR (cyan line) and BPR (magenta line), all in conjunction with the GF numerical fluxes. On the left panel, the solutions are obtained without the predictor/corrector strategy, while on the right panel it has been used.

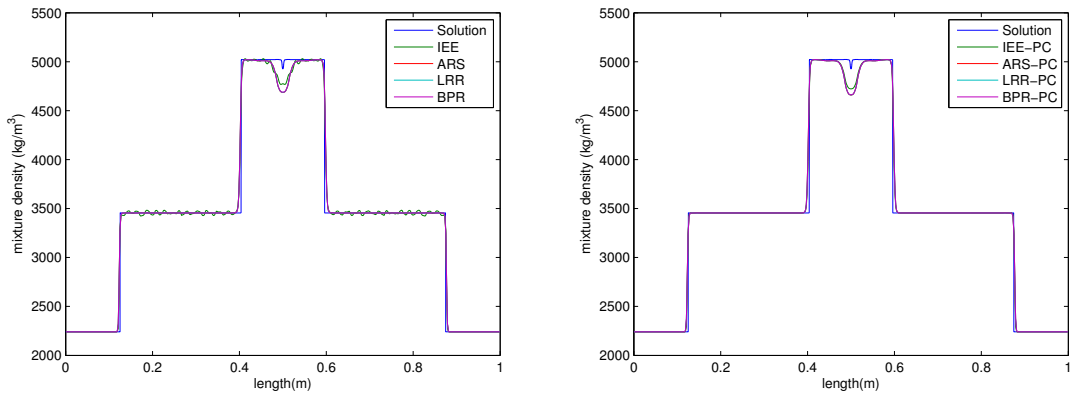


Figure 18: Four Shock - Comparison between the reference solution for the mixture density (blue line), and the solutions computed using the DIRK schemes IEE (green line), ARS (red line), LRR (cyan line) and BPR (magenta line), all in conjunction with the KT numerical fluxes. On the left panel, the solutions are obtained without the predictor/corrector strategy, while on the right panel it has been used.

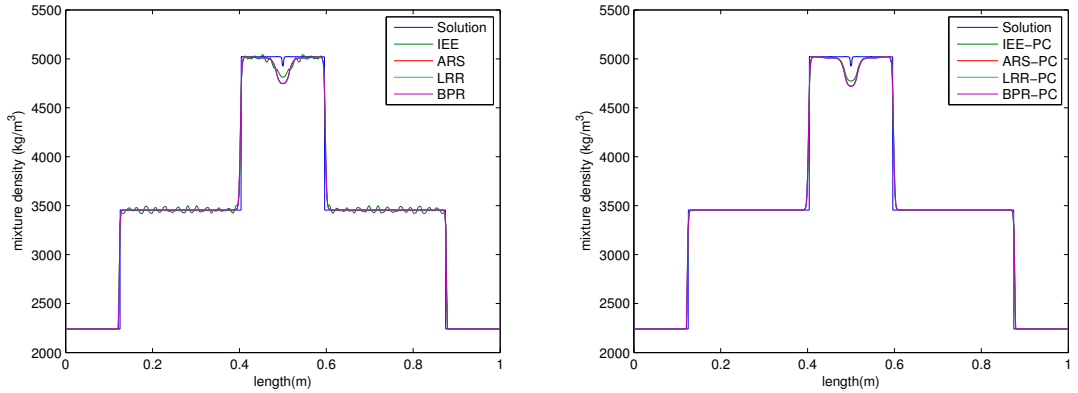


Figure 19: Four Shock - Comparison between the reference solution for the mixture density (blue line), and the solutions computed using the DIRK schemes IEE (green line), ARS (red line), LRR (cyan line) and BPR (magenta line), all in conjunction with the KNP numerical fluxes. On the left panel, the solutions are obtained without the predictor/corrector strategy, while on the right panel it has been used.

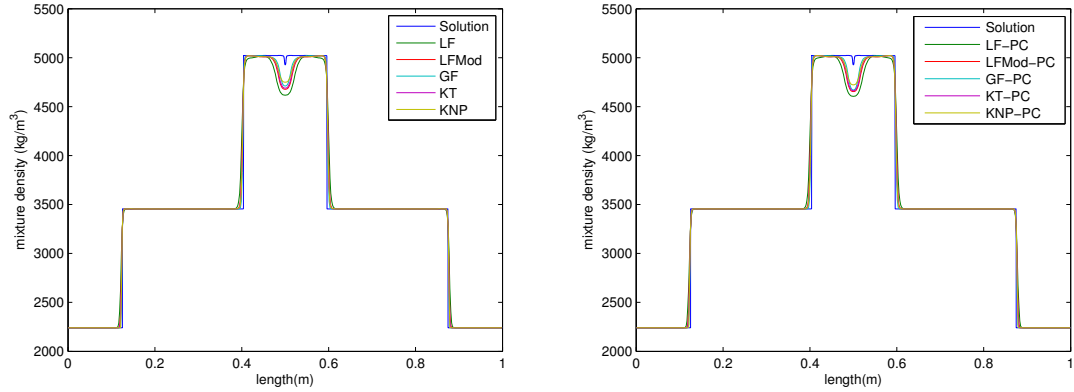


Figure 20: Four Shock - Comparison between the reference solution for the mixture density (blue line), and the solutions computed using the DIRK BPR scheme in conjunction with LF (green line), LMod (red line), GF (cyan line), KT (magenta line) and KNP numerical fluxes (yellow line). On the left panel, the solutions are obtained without the predictor/corrector strategy, while on the right panel it has been used.

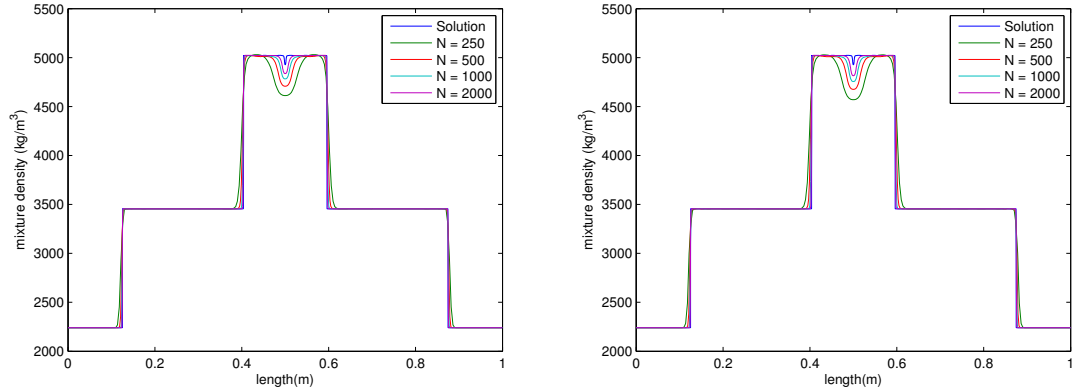


Figure 21: Four Shock - Comparison between the reference solution for the mixture density (blue line) and the solutions obtained using different number of cells for the domain discretization: 250 (green line), 500 (red line), 1000 (cyan line) and 2000 (magenta line) cells. On the left panel the solution obtained with the splitting approach, the predictor/corrector strategy and LMod numerical fluxes is plotted, while on the right panel is reported the mixture density obtained with the DIRK scheme ARS in conjunction with LMod numerical fluxes.

compared with the reference one is obtained using the LF numerical fluxes, in Fig. 16 with LMod, in Fig. 17 with GF, in Fig. 18 with KT and finally in Fig. 19 with KNP.

In Fig. 20, instead, the reference solution for the mixture density (blue line) is compared with the solutions obtained with the DIRK BPR scheme using the LF (green line), LMod (red line), GF (cyan line), KT (magenta line) and KNP (yellow line) numerical fluxes.

In the Fig. 15 the solutions reported are only those obtained with the DIRK IEE and BPR, because, for this test, using the ARS and LRR schemes in conjunction with the LF numerical fluxes the code crashes. In the previous test, we have seen in Fig. 6 that these two DIRK schemes with the LF numerical fluxes did not solve properly the strong rarefaction waves, showing many oscillation in the solutions. Thus we can conclude that the combination of DIRK ARS and LRR with the LF numerical fluxes does not produce acceptable results.

Anyway, the combination of DIRK ARS, LRR and BPR with the LMod, GF, KT and KNP gives good results. As we can see from Figs. 16-19, except for DIRK IEE, the

N	LF	LFMod	GF	KT	KNP
250	1.0454e-2	1.7816e-3	9.6228e-4	1.4927e-3	1.1956e-3
500	5.7723e-3	1.0688e-3	6.8120e-4	9.5514e-4	8.2518e-4
1000	2.7501e-3	3.9043e-4	2.8096e-4	4.5110e-4	4.3169e-4
2000	1.3898e-3	4.0815e-4	5.6021e-4	6.3105e-4	5.4746e-4
N	LF-PC	LFMod-PC	GF-PC	KT-PC	KNP-PC
250	1.0454e-2	1.8722e-3	1.1077e-3	1.5955e-3	1.2629e-3
500	5.7723e-3	1.0963e-3	7.4487e-4	9.7186e-4	8.3931e-4
1000	2.7501e-3	3.8396e-4	2.1686e-4	3.2528e-4	2.5906e-4
2000	1.3898e-3	2.1081e-4	1.2573e-4	1.8330e-4	1.6060e-4

Table 16: Four Shock - Relative errors between the reference mixture density and those computed using the splitting approach with the different numerical fluxes presented in this work and different domain discretizations.

solutions do not present spurious oscillations. Even for this test, where we do not apply source terms, the DIRK IEE schemes coincide with the respective scheme in the splitting approach.

Tables 16-20 report the relative errors obtained from all the schemes adopted in this work with different number of cells for the domain discretization. In the Table 16 the errors of the schemes that use the splitting approach are reported. We can see that the predictor/corrector strategy increases considerably the accuracy of the solutions (except for the LF schemes) only with an high number of cells. This happens because, with a low number of cells, the solutions near  $x = 0.5$  are far from the reference solution, thus the relative errors are dominated mainly by the error obtained in a neighbor of  $x = 0.5$ . Increasing the number of cells, the solutions converge towards the reference one, thus even the difference near  $x = 0.5$  becomes smaller and then the improvements obtained using the predictor/corrector strategy become visible in the relative errors.

About the relative error of the DIRK schemes, except for the DIRK IEE, the predictor/corrector strategy does not increase the accuracy of the solutions. Furthermore, as we have found in the previous test, the relative error of the DIRK schemes reported in Tables 18-20 are quite similar. Finally, from all the relative errors collected we can say that, even for this test, the splitting approach is more accurate than then the DIRK schemes, even if not significantly.

In Tables 21-25 the convergence rate of all the schemes used for this test are reported. Once again we can see that the predictor/corrector strategy gives better results in the splitting approach rather than in the Runge-Kutta approach.

Fig. 21 shows the effects of grid refinement, plotting the reference mixture density (blue line) and those obtained using four different number of cells: 250 (green line), 500 (red line), 1000 (cyan line) and 2000 (magenta line) cells. On the left panel the solution obtained with the splitting approach, the predictor/corrector strategy and LFMod numerical fluxes is plotted, while on the right panel we report the mixture density obtained with the DIRK schemes ARS in conjunction with LFMod numerical fluxes.

The last consideration for this test regards the presence of a little depression in the mixture density in a neighborhood of the point  $x = 0.5$  m, as we had in the previous test. Once again, increasing the number of cells and the end-time of the computation,

DIRK IEE					
N	LF	LFMod	GF	KT	KNP
250	1.0454e-2	1.7816e-3	9.6228e-4	1.4927e-3	1.1956e-3
500	5.7723e-3	1.0688e-3	6.8120e-4	9.5514e-4	8.2518e-4
1000	2.7501e-3	3.9043e-4	2.8096e-4	4.5110e-4	4.3169e-4
2000	1.3898e-3	4.0815e-4	5.6021e-4	6.3105e-4	5.4746e-4
N	LF-PC	LFMod-PC	GF-PC	KT-PC	KNP-PC
250	1.0454e-2	1.8722e-3	1.1077e-3	1.5955e-3	1.2629e-3
500	5.7723e-3	1.0963e-3	7.4487e-4	9.7186e-4	8.3931e-4
1000	2.7501e-3	3.8396e-4	2.1686e-4	3.2528e-4	2.5906e-4
2000	1.3898e-3	2.1081e-4	1.2573e-4	1.8330e-4	1.6060e-4

Table 17: Four Shock - Relative errors between the reference mixture density and those computed using the DIRK IEE scheme with the different numerical fluxes presented in this work and different domain discretizations.

DIRK ARS					
N	LF	LFMod	GF	KT	KNP
250	-	2.2271e-3	1.4074e-3	1.9311e-3	1.5321e-3
500	-	1.2658e-3	8.7864e-4	1.1249e-3	9.5394e-4
1000	-	4.6452e-4	2.8056e-4	3.9509e-4	3.1838e-4
2000	-	2.4485e-4	1.5754e-4	2.1386e-4	1.8494e-4
N	LF-PC	LFMod-PC	GF-PC	KT-PC	KNP-PC
250	-	2.3926e-3	1.6706e-3	2.1312e-3	1.7088e-3
500	-	1.3328e-3	9.7505e-4	1.2003e-3	1.0117e-3
1000	-	4.9653e-4	3.2725e-4	4.3392e-4	3.5446e-4
2000	-	2.5823e-4	1.7590e-4	2.2822e-4	1.9272e-4

Table 18: Four Shock - Relative errors between the reference mixture density and those computed using the DIRK ARS scheme with the different numerical fluxes presented in this work and different domain discretizations.

DIRK LRR					
N	LF	LFMod	GF	KT	KNP
250	-	2.2263e-3	1.4038e-3	1.9179e-3	1.5253e-3
500	-	1.2622e-3	8.7392e-4	1.1173e-3	9.4684e-4
1000	-	4.6197e-4	2.8014e-4	3.9421e-4	3.1850e-4
2000	-	2.4408e-4	1.5648e-4	2.1276e-4	1.8304e-4
N	LF-PC	LFMod-PC	GF-PC	KT-PC	KNP-PC
250	-	2.3925e-3	1.6684e-3	2.1215e-3	1.6984e-3
500	-	1.3347e-3	9.7547e-4	1.1973e-3	1.0102e-3
1000	-	4.9676e-4	3.2769e-4	4.3350e-4	3.5320e-4
2000	-	2.5845e-4	1.7616e-4	2.2792e-4	1.9264e-4

Table 19: Four Shock - Relative errors between the reference mixture density and those computed using the DIRK LRR scheme with the different numerical fluxes presented in this work and different domain discretizations.

DIRK BPR					
N	LF	LFMod	GF	KT	KNP
250	3.5215e-3	2.2007e-3	1.3853e-3	1.8925e-3	1.4997e-3
500	1.9105e-3	1.2476e-3	8.6317e-4	1.1059e-3	9.3576e-4
1000	7.6293e-4	4.5649e-4	2.7669e-4	3.8866e-4	3.1233e-4
2000	3.8929e-4	2.4191e-4	1.5359e-4	2.1032e-4	1.8022e-4
N	LF-PC	LFMod-PC	GF-PC	KT-PC	KNP-PC
250	3.6415e-3	2.3754e-3	1.6470e-3	2.0958e-3	1.6711e-3
500	1.9186e-3	1.3257e-3	9.6473e-4	1.1887e-3	1.0001e-3
1000	7.6991e-4	4.9209e-4	3.2318e-4	4.2879e-4	3.4684e-4
2000	3.8893e-4	2.5636e-4	1.7341e-4	2.2612e-4	1.9062e-4

Table 20: Four Rarefaction - Relative errors between the reference mixture density and those computed using the DIRK BPR scheme with the different numerical fluxes presented in this work and different domain discretizations.

N	LF	LFMod	GF	KT	KNP
250	-	-	-	-	-
500	1.6863	1.9271	1.4838	1.5723	1.4418
1000	1.8220	1.2309	0.9266	1.0292	0.9355
2000	1.9591	0.6763	0.5750	0.6285	0.7633
N	LF-PC	LFMod-PC	GF-PC	KT-PC	KNP-PC
250	-	-	-	-	-
500	1.6863	2.0434	2.0681	2.0351	2.0489
1000	1.8220	1.9404	1.9149	1.9325	1.9227
2000	1.9591	2.2005	2.3363	2.2320	2.2694

Table 21: Four Shock - Convergence rates for the mixture density computed with different domain discretization using the splitting approach with the numerical fluxes presented in this work.

DIRK IEE					
N	LF	LFMod	GF	KT	KNP
250	-	-	-	-	-
500	1.6863	1.9271	1.4838	1.5723	1.4418
1000	1.8220	1.2309	0.9266	1.0292	0.9355
2000	1.9591	0.6763	0.5750	0.6285	0.7633
N	LF-PC	LFMod-PC	GF-PC	KT-PC	KNP-PC
250	-	-	-	-	-
500	1.6863	2.0434	2.0681	2.0351	2.0489
1000	1.8220	1.9404	1.9149	1.9325	1.9227
2000	1.9591	2.2005	2.3363	2.2320	2.2694

Table 22: Four Shock - Convergence rates for the mixture density computed with different domain discretization using the DIRK IEE scheme with the numerical fluxes presented in this work.

DIRK ARS					
N	LF	LFMod	GF	KT	KNP
250	-	-	-	-	-
500	-	2.0212	2.0751	2.0261	2.0287
1000	-	1.9483	1.9339	1.9509	1.9439
2000	-	2.1984	2.3525	2.2285	2.2476
N	LF-PC	LFMod-PC	GF-PC	KT-PC	KNP-PC
250	-	-	-	-	-
500	-	2.0093	2.0724	2.0234	2.0254
1000	-	1.9510	1.9459	1.9465	1.9350
2000	-	2.1862	2.3307	2.2105	2.2424

Table 23: Four Shock - Convergence rates for the mixture density computed with different domain discretization using the DIRK ARS scheme with the numerical fluxes presented in this work.

DIRK LRR					
N	LF	LFMod	GF	KT	KNP
250	-	-	-	-	-
500	-	2.0194	2.0792	2.0255	2.0299
1000	-	1.9521	1.9251	1.9439	1.9360
2000	-	2.1939	2.3623	2.2281	2.2560
N	LF-PC	LFMod-PC	GF-PC	KT-PC	KNP-PC
250	-	-	-	-	-
500	-	2.0064	2.0710	2.0206	2.0186
1000	-	1.9540	1.9463	1.9445	1.9362
2000	-	2.1858	2.3320	2.2149	2.2424

Table 24: Four Shock - Convergence rates for the mixture density computed with different domain discretization using the DIRK LRR scheme with the numerical fluxes presented in this work.

DIRK BPR					
N	LF	LFMod	GF	KT	KNP
250	-	-	-	-	-
500	1.9672	2.0241	2.0754	2.0246	2.0333
1000	1.9441	1.9445	1.9215	1.9399	1.9305
2000	2.1050	2.1943	2.3531	2.2255	2.2563
N	LF-PC	LFMod-PC	GF-PC	KT-PC	KNP-PC
250	-	-	-	-	-
500	2.0000	2.0093	2.0708	2.0159	2.0162
1000	1.9365	1.9529	1.9411	1.9454	1.9364
2000	2.1092	2.1857	2.3321	2.2120	2.2400

Table 25: Four Shock - Convergence rates for the mixture density computed with different domain discretization using the DIRK BPR scheme with the numerical fluxes presented in this work.

this depression becomes smaller and smaller, hence we can conclude that the real exact solution of mixture density is the one in which there is no depression at point  $x = 0.5$ .

#### 4.4 ONE DIMENSIONAL AIR-WATER SHOCK PROBLEM

This test is an extension to two phases of the strong-shock Riemann problem described in Toro (2009), which was designed to assess the robustness and accuracy of numerical methods. Here we simulate an air-water shock tube problem, considering an initial solution in which are present pure water and pure air separated by an interface. In the numerical initial condition we have to assume that a minimum volume fraction  $\epsilon$  (here equal to  $10^{-7}$ ) of each phase is present in both sections. This assumption is needed since governing equations become degenerate for phase volume fraction of 0 or 1. Differently from the previous test, we consider here instantaneous relaxations for the velocities and pressures, which translates in  $\tau^{(p)} = \tau^{(f)} = 0$ . Imposing instantaneous relaxation for pressures and velocities we are forcing the two phases to have a common pressure and a common velocity. This numerical test will tell us the behavior of the numerical schemes presented in this work in presence of instantaneous relaxations.

The computational domain considered is  $[0, 1]$  m with a Riemann problem being defined with the interface located at  $x = 0.75$  m. The initial data of the test are the following:

$$\begin{cases} \alpha_1 = 1 - \epsilon, P_i = 10^9 \text{ Pa}, u_i = 0 \text{ m/s}, T = 495 \text{ K} & \forall x \in [0, 0.75) \text{ m} \\ \alpha_1 = \epsilon, P_i = 10^6 \text{ Pa}, u_i = 0 \text{ m/s}, T = 270 \text{ K} & \forall x \in [0.75, 1] \text{ m} \end{cases},$$

for  $i = 1, 2$  and  $\epsilon = 10^{-7}$ . The indexes 1 and 2 are referred to the parameters of state of water and air, respectively, and the constants for the equations of state are given in Table 5.

Transmissive boundary conditions are imposed at  $x = 0$  and  $x = 1$ . In this case the physical solution of the problem presents not only shock waves, but also rarefaction waves.

We present here the numerical solutions computed at time  $2.5 \times 10^{-4}$  s using a CFL coefficient equal to 0.49.

Fig. 22 shows the mixture density, the mixture temperature, the pressures and the velocities of both phases computed with a grid of 16000 cells. These plots are obtained using the splitting approach in conjunction with the LFMod numerical fluxes and they will be considered as reference solution to evaluate the accuracy of the different numerical schemes.

In Fig. 23 we plot the reference solution for the mixture density (blue line), and the solutions computed using the splitting approach and the LF, the LFMod, the GF, the KT and the KNP numerical fluxes (we remind that, except for the reference solution, in Figs. 23-29 a grid of 500 cells is used).

We can see that even in this case, the rarefaction wave, present in the reference solution for the mixture density, is not properly described in the splitting approach when the predictor/corrector strategy is not used.

As an additional test, we evaluate here the improvement in the accuracy of the solution when the integration of the source terms is done not only at the end of each time step, but also after the predictor step. Basically, once the local data at the cells interfaces

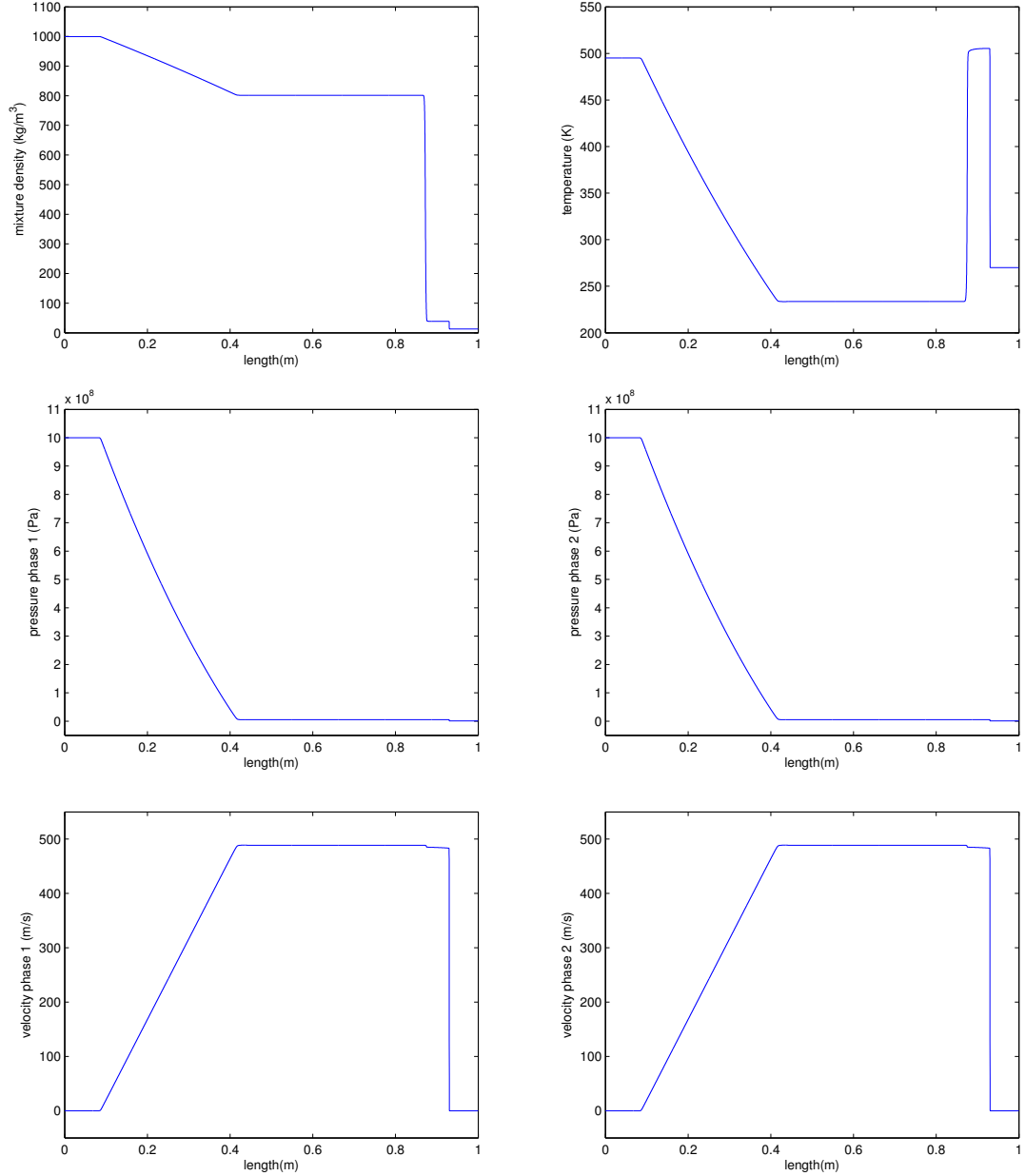


Figure 22: Air-Water Shock - Reference solution for mixture density (top left), mixture temperature (top right), pressure of phase 1 (middle left) and of phase 2 (middle right), velocity of phase 1 (bottom left) and of phase 2 (bottom right).

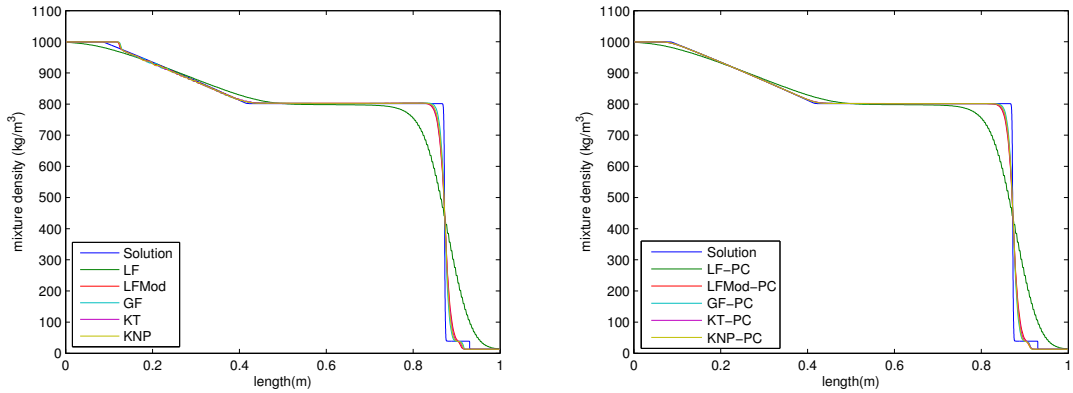


Figure 23: Air-Water Shock - Comparison between the reference solution for the mixture density (blue line), and the solutions computed using the splitting approach with LF (green line), LMod (red line), GF (cyan line), KT (magenta line) and KNP numerical fluxes (yellow line). On the left panel, the solutions are obtained without the predictor/corrector strategy, while on the right panel it has been used.

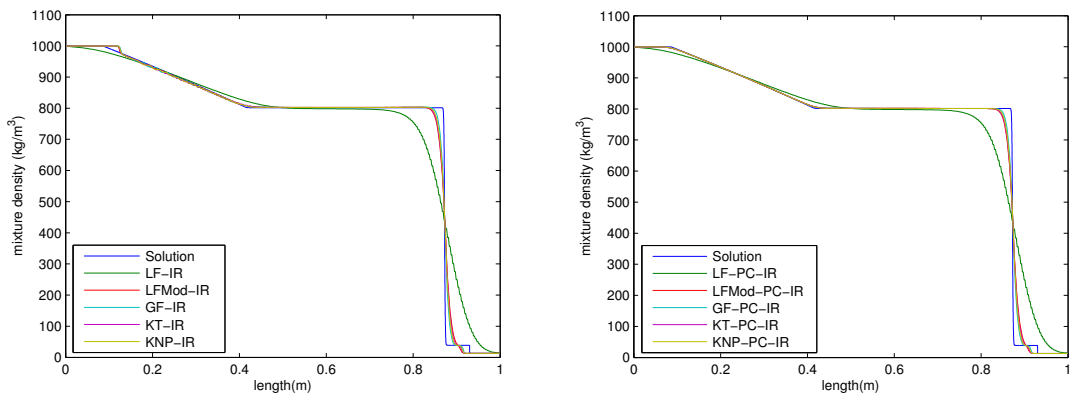


Figure 24: Air-Water Shock - Comparison between the reference solution for the mixture density (blue line), and the solutions computed using the splitting approach and the interfaces relaxations with LF (green line), LMod (red line), GF (cyan line), KT (magenta line) and KNP numerical fluxes (yellow line). On the left panel, the solutions are obtained without the predictor/corrector strategy, while on the right panel it has been used.

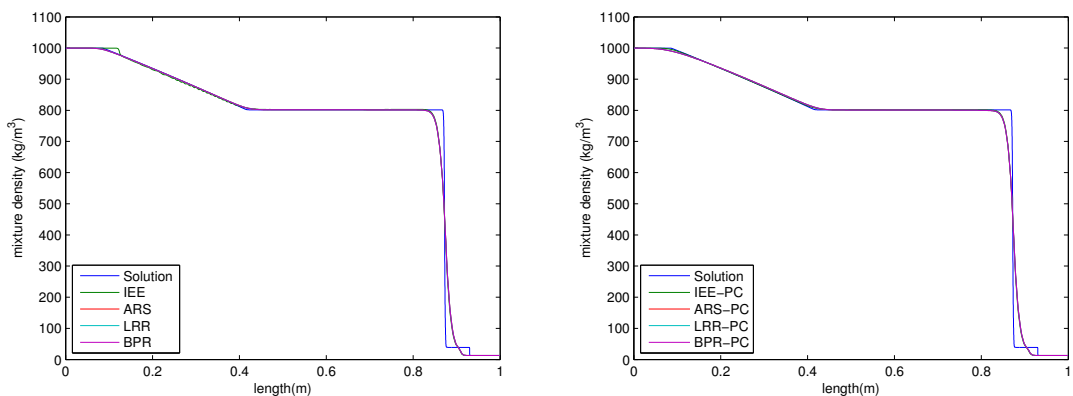


Figure 25: Air-Water Shock - Comparison between the reference solution for the mixture density (blue line), and the solutions computed using the DIRK schemes IEE (green line), ARS (red line), LRR (cyan line) and BPR (magenta line), all in conjunction with the LMod numerical fluxes. On the left panel, the solutions are obtained without the predictor/corrector strategy, while on the right panel it has been used.

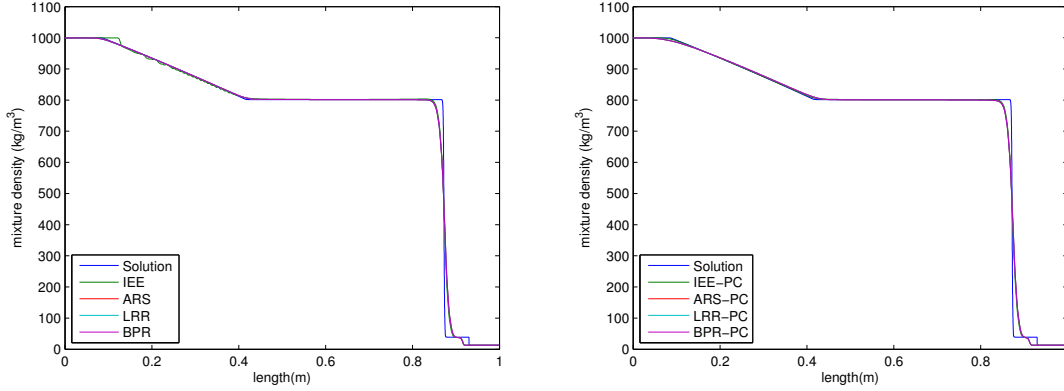


Figure 26: Air-Water Shock - Comparison between the reference solution for the mixture density (blue line), and the solutions computed using the DIRK schemes IEE (green line), ARS (red line), LRR (cyan line) and BPR (magenta line), all in conjunction with the GF numerical fluxes. On the left panel, the solutions are obtained without the predictor/corrector strategy, while on the right panel it has been used.

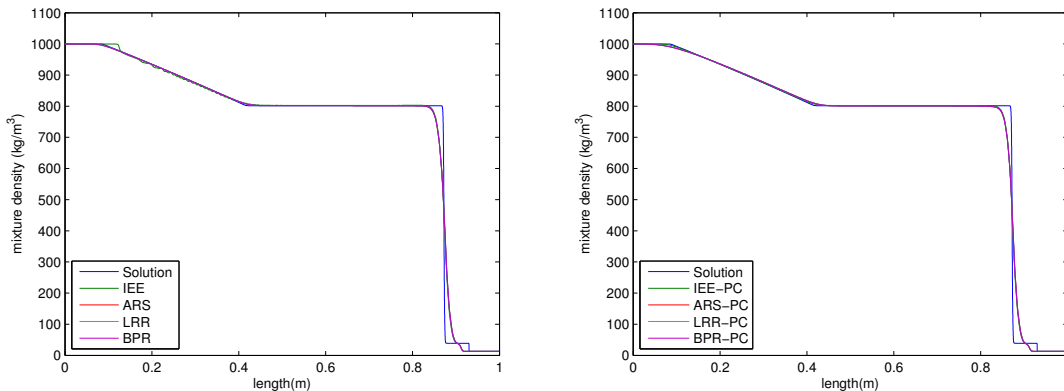


Figure 27: Air-Water Shock - Comparison between the reference solution for the mixture density (blue line), and the solutions computed using the DIRK schemes IEE (green line), ARS (red line), LRR (cyan line) and BPR (magenta line), all in conjunction with the KT numerical fluxes. On the left panel, the solutions are obtained without the predictor/corrector strategy, while on the right panel it has been used.

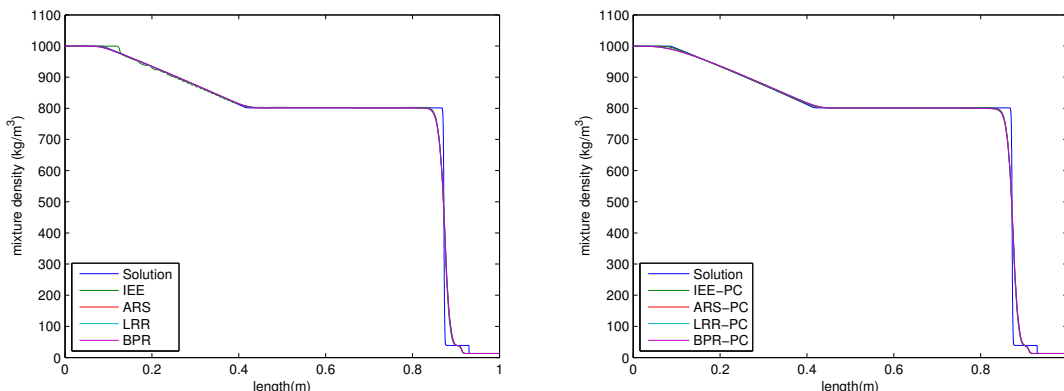


Figure 28: Air-Water Shock - Comparison between the reference solution for the mixture density (blue line), and the solutions computed using the DIRK schemes IEE (green line), ARS (red line), LRR (cyan line) and BPR (magenta line), all in conjunction with the KNP numerical fluxes. On the left panel, the solutions are obtained without the predictor/corrector strategy, while on the right panel it has been used.

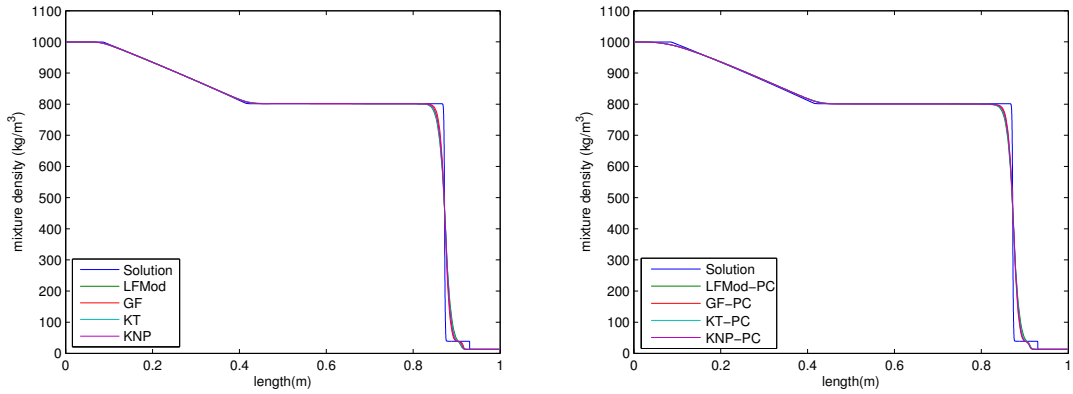


Figure 29: Air-Water Shock - Comparison between the reference solution for the mixture density (blue line), and the solutions computed using the DIRK ARS scheme in conjunction with LMod (green line), GF (red line), KT (cyan line), and KNP numerical fluxes (magenta line). On the left panel, the solutions are obtained without the predictor/corrector strategy, while on the right panel it has been used.

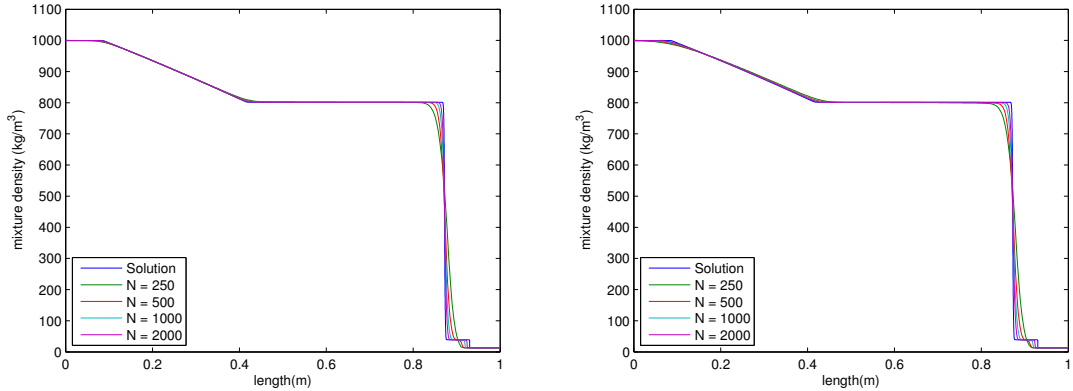


Figure 30: Air-Water Shock - Comparison between the reference solution for the mixture density (blue line) and the solutions obtained using different number of cells for the domain discretization: 250 (green line), 500 (red line), 1000 (cyan line) and 2000 (magenta line) cells. On the left panel the solution obtained with the splitting approach, the predictor/corrector strategy and the GF numerical fluxes is plotted, while on the right panel is reported the mixture density obtained with the DIRK scheme LRR in conjunction with GF numerical fluxes and the predictor/corrector strategy.

$\mathbf{U}_{i+\frac{1}{2},L}^{n+\frac{1}{2}}$  and  $\mathbf{U}_{i+\frac{1}{2},R}^{n+\frac{1}{2}}$  (Eqs. (3.12)-(3.13)) are computed, we integrate the ODE system (3.4) with  $\mathbf{U}_{i+\frac{1}{2},L}^{n+\frac{1}{2}}$  and  $\mathbf{U}_{i+\frac{1}{2},R}^{n+\frac{1}{2}}$  as initial conditions and half time step. Then the new cells interfaces obtained from the integration of the source terms are used to compute the local speeds and the numerical fluxes. We call this strategy *interface relaxation* (IR), since, in the model presented in this thesis, the source terms are mainly relaxation terms.

Fig. 24 shows the reference solution for the mixture density (blue line), and the solutions computed using the splitting approach with the interface relaxation and the LF, the LMod, the GF, the KT and the KNP numerical fluxes.

In Figs. 25-28 the reference solution for the mixture density (blue line) is compared with the solutions computed using the DIRK schemes. About the numerical fluxes chosen, we plot in Fig. 25 those computed with LMod, in Fig. 26 those calculated with GF, in Fig. 27 those obtained using KT and finally in Fig. 28 those computed with KNP.

N	LF	LFMod	GF	KT	KNP
250	1.2855e-2	3.2030e-3	2.7947e-3	3.1286e-3	2.9274e-3
500	8.7076e-3	1.8061e-3	1.1784e-3	1.6799e-3	1.4875e-3
1000	5.9074e-3	8.5080e-4	5.3291e-4	7.4864e-4	6.4556e-4
2000	3.9965e-3	3.9555e-4	2.0882e-4	3.4234e-4	2.8380e-4
N	LF-PC	LFMod-PC	GF-PC	KT-PC	KNP-PC
250	1.2855e-2	3.2875e-3	3.0556e-3	3.1945e-3	3.1133e-3
500	8.7076e-3	1.7780e-3	1.3458e-3	1.6340e-3	1.5436e-3
1000	5.9074e-3	9.4476e-4	6.6313e-4	8.5786e-4	7.8694e-4
2000	3.9965e-3	4.5227e-4	2.7799e-4	3.9986e-4	3.5045e-4
N	LF-IR	LFMod-IR	GF-IR	KT-IR	KNP-IR
250	1.2855e-2	3.2030e-3	2.7947e-3	3.1286e-3	2.9274e-3
500	8.7076e-3	1.8061e-3	1.1785e-3	1.6799e-3	1.4875e-3
1000	5.9074e-3	8.5080e-4	5.3291e-4	7.4864e-4	6.4556e-4
2000	3.9965e-3	3.9612e-4	2.0918e-4	3.4326e-4	2.8250e-4
N	LF-PC-IR	LFMod-PC-IR	GF-PC-IR	KT-PC-IR	KNP-PC-IR
250	1.2855e-2	3.3055e-3	2.9462e-3	3.2222e-3	3.0431e-3
500	8.7076e-3	1.8816e-3	1.3294e-3	1.7691e-3	1.6032e-3
1000	5.9074e-3	9.5354e-4	6.3593e-4	8.4793e-4	7.4611e-4
2000	3.9965e-3	4.5909e-4	2.6855e-4	4.0692e-4	3.4275e-4

Table 26: Air-Water Shock - Relative errors between the reference mixture density and those computed using the splitting approach with the different numerical fluxes presented in this work and different domain discretizations.

In Fig. 29 instead, the reference solution for the mixture density (blue line) is compared with the solutions obtained with the DIRK ARS using for the LF, LFMod, GF, KT and KNP numerical fluxes.

The solutions obtained with DIRK schemes in conjunction with LF numerical fluxes are missing since that simulations, at a certain time, produce a negative pressure and so the simulations end. Thus, from what we have obtained in these three preliminary tests we can conclude that the combination of the DIRK schemes proposed with the LF numerical fluxes does not produce accurate and robust numerical schemes.

Tables 26-30 report the relative errors obtained from all the schemes adopted in this work with different number of cells for the domain discretization. In the Table 26 are reported the errors of the schemes that use the splitting approach. This time, the improvements of the predictor/corrector strategy are not highlighted from the relative errors collected. This happens since the relative errors of the solutions are dominated by the errors computed near the discontinuities. Thus, although we can see from Figs. 22-23 that the rarefaction wave is properly described only with the predictor/corrector strategy (see in  $x \approx 0.15$  m), the improvements of the use of this strategy are not reflected (with the number of cells used for the simulations) in the relative errors. Increasing the number of cells, the relative error near the discontinuity becomes smaller and smaller and thus the error computed in the rarefaction wave becomes dominant.

Regarding the use of the integration of the relaxation terms after the predictor step, from Fig. 22 and 23 and from the relative errors collected we cannot see any improvement in using it.

DIRK IEE					
N	LF	LFMod	GF	KT	KNP
250	—	3.2030e-3	2.7947e-3	3.1286e-3	2.9274e-3
500	—	1.8061e-3	1.1784e-3	1.6799e-3	1.4875e-3
1000	—	8.5080e-4	5.3291e-4	7.4864e-4	6.4556e-4
2000	—	3.9425e-4	1.9842e-4	3.3730e-4	2.7071e-4
N	LF-PC	LFMod-PC	GF-PC	KT-PC	KNP-PC
250	—	3.2875e-3	3.0556e-3	3.1945e-3	3.1133e-3
500	—	1.7780e-3	1.3458e-3	1.6340e-3	1.5436e-3
1000	—	9.4476e-4	6.6313e-4	8.5786e-4	7.8694e-4
2000	—	4.5227e-4	2.7799e-4	3.9986e-4	3.5045e-4

Table 27: Air-Water Shock - Relative errors between the reference mixture density and those computed using the DIRK IEE scheme with the different numerical fluxes presented in this work and different domain discretizations.

DIRK ARS					
N	LF	LFMod	GF	KT	KNP
250	—	3.4017e-3	2.9547e-3	3.2901e-3	3.0765e-3
500	—	1.9180e-3	1.3662e-3	1.8011e-3	1.6342e-3
1000	—	9.6201e-4	6.5386e-4	8.6723e-4	7.6662e-4
2000	—	4.6519e-4	2.7871e-4	4.1633e-4	3.5365e-4
N	LF-PC	LFMod-PC	GF-PC	KT-PC	KNP-PC
250	—	3.4818e-3	3.1955e-3	3.3597e-3	3.2370e-3
500	—	1.8927e-3	1.5284e-3	1.7563e-3	1.6876e-3
1000	—	1.0533e-3	8.0287e-4	9.7916e-4	9.2009e-4
2000	—	5.2969e-4	3.7626e-4	4.8438e-4	4.4235e-4

Table 28: Air-Water Shock - Relative errors between the reference mixture density and those computed using the DIRK ARS scheme with the different numerical fluxes presented in this work and different domain discretizations.

DIRK LRR					
N	LF	LFMod	GF	KT	KNP
250	—	3.4007e-3	2.9584e-3	3.2902e-3	3.0796e-3
500	—	1.9172e-3	1.3669e-3	1.8005e-3	1.6343e-3
1000	—	9.6222e-4	6.5405e-4	8.6725e-4	7.6670e-4
2000	—	4.6522e-4	2.7878e-04	4.1630e-4	3.5357e-4
N	LF-PC	LFMod-PC	GF-PC	KT-PC	KNP-PC
250	—	3.4798e-3	3.2027e-3	3.3607e-3	3.2435e-3
500	—	1.8905e-3	1.5292e-3	1.7562e-3	1.6880e-3
1000	—	1.0535e-3	8.0313e-4	9.7922e-4	9.2024e-4
2000	—	5.2968e-4	3.7633e-4	4.8439e-4	4.4239e-4

Table 29: Air-Water Shock - Relative errors between the reference mixture density and those computed using the DIRK LRR scheme with the different numerical fluxes presented in this work and different domain discretizations.

DIRK BPR					
N	LF	LFMod	GF	KT	KNP
250	—	3.3879e-3	2.9694e-3	3.2852e-3	3.0781e-3
500	—	1.9161e-3	1.3680e-3	1.8026e-3	1.6368e-3
1000	—	9.6355e-4	6.5426e-4	8.6702e-4	7.6592e-4
2000	—	4.6536e-4	2.7875e-4	4.1648e-4	3.5355e-4
N	LF-PC	LFMod-PC	GF-PC	KT-PC	KNP-PC
250	—	3.4706e-3	3.2177e-3	3.3582e-3	3.2498e-3
500	—	1.8876e-3	1.5297e-3	1.7569e-3	1.6896e-3
1000	—	1.0544e-3	8.0325e-4	9.7924e-4	9.2017e-4
2000	—	5.2976e-4	3.7634e-4	4.8441e-4	4.4240e-4

Table 30: Air-Water Shock - Relative errors between the reference mixture density and those computed using the DIRK BPR scheme with the different numerical fluxes presented in this work and different domain discretizations.

N	LF	LFMod	GF	KT	KNP
250	—	—	—	—	—
500	1.4214	1.3681	1.6386	1.4400	1.4929
1000	1.4800	1.7121	1.6792	1.7337	1.7282
2000	1.4569	1.6437	1.4655	1.5923	1.3856
N	LF-PC	LFMod-PC	GF-PC	KT-PC	KNP-PC
250	—	—	—	—	—
500	1.4214	1.4710	1.6741	1.5357	1.5559
1000	1.4800	1.6241	1.6993	1.6419	1.6662
2000	1.4569	1.7381	1.8495	1.7601	1.8014
N	LF-IR	LFMod-IR	GF-IR	KT-IR	KNP-IR
250	—	—	—	—	—
500	1.4214	1.3681	1.6386	1.4400	1.4929
1000	1.4800	1.7121	1.6792	1.7337	1.7282
2000	1.4569	1.6236	1.4329	1.6272	1.4091
N	LF-PC-IR	LFMod-PC-IR	GF-PC-IR	KT-PC-IR	KNP-PC-IR
250	—	—	—	—	—
500	1.4214	1.4016	1.6543	1.4470	1.4939
1000	1.4800	1.6637	1.7346	1.7324	1.7650
2000	1.4569	1.7410	1.8384	1.7374	1.7698

Table 31: Air-Water Shock - Convergence rates for the mixture density computed with different domain discretization using the splitting approach with the numerical fluxes presented in this work.

DIRK IEE					
N	LF	LFMod	GF	KT	KNP
250	—	—	—	—	—
500	—	1.3681	1.6386	1.4400	1.4929
1000	—	1.7121	1.6792	1.7337	1.7282
2000	—	1.6880	1.6489	1.7078	1.6462
N	LF-PC	LFMod-PC	GF-PC	KT-PC	KNP-PC
250	—	—	—	—	—
500	—	1.4710	1.6741	1.5357	1.5559
1000	—	1.6241	1.6993	1.6419	1.6662
2000	—	1.7381	1.8495	1.7601	1.8014

Table 32: Air-Water Shock - Convergence rates for the mixture density computed with different domain discretization using the DIRK IEE scheme with the numerical fluxes presented in this work.

DIRK ARS					
N	LF	LFMod	GF	KT	KNP
250	—	—	—	—	—
500	—	1.4221	1.6316	1.4588	1.4899
1000	—	1.6821	1.7359	1.7318	1.7582
2000	—	1.7397	1.8327	1.7411	1.7699
N	LF-PC	LFMod-PC	GF-PC	KT-PC	KNP-PC
250	—	—	—	—	—
500	—	1.5013	1.5966	1.5371	1.5291
1000	—	1.5716	1.6244	1.5777	1.5934
2000	—	1.6812	1.7274	1.6931	1.7161

Table 33: Air-Water Shock - Convergence rates for the mixture density computed with different domain discretization using the DIRK ARS scheme with the numerical fluxes presented in this work.

DIRK LRR					
N	LF	LFMod	GF	KT	KNP
250	—	—	—	—	—
500	—	1.4219	1.6322	1.4593	1.4910
1000	—	1.6813	1.7363	1.7316	1.7585
2000	—	1.7398	1.8328	1.7412	1.7704
N	LF-PC	LFMod-PC	GF-PC	KT-PC	KNP-PC
250	—	—	—	—	—
500	—	1.5020	1.5980	1.5374	1.5307
1000	—	1.5705	1.6246	1.5777	1.5935
2000	—	1.6814	1.7275	1.6931	1.7162

Table 34: Air-Water Shock - Convergence rates for the mixture density computed with different domain discretization using the DIRK LRR scheme with the numerical fluxes presented in this work.

DIRK BPR					
N	LF	LFMod	GF	KT	KNP
250	—	—	—	—	—
500	—	1.4177	1.6411	1.4566	1.4922
1000	—	1.6778	1.7369	1.7321	1.7608
2000	—	1.7404	1.8330	1.7402	1.7690
N	LF-PC	LFMod-PC	GF-PC	KT-PC	KNP-PC
250	—	—	—	—	—
500	—	1.5012	1.6013	1.5362	1.5313
1000	—	1.5681	1.6247	1.5777	1.5943
2000	—	1.6820	1.7273	1.6930	1.7159

Table 35: Air-Water Shock - Convergence rates for the mixture density computed with different domain discretization using the DIRK BPR scheme with the numerical fluxes presented in this work.

About the DIRK schemes, as we have found in the previous test, the relative errors reported in Tables 28-30 are quite similar. Finally, analyzing all the relative errors collected, we notice that the solutions computed with the splitting approach and with the DIRK schemes are very similar. Thus we can conclude that the DIRK schemes are able to give accurate solutions even in presence of instantaneous relaxations.

Finally we report in Tables 31-35 the convergence rates, defined in Eq. (4.3), for the schemes adopted and in Fig. 30 the effects of grid refinement is shown, plotting the reference mixture density (blue line) and those obtained using four different number of cells: 250 (green line), 500 (red line), 1000 (cyan line) and 2000 (magenta line) cells. On the left panel the solution obtained with the splitting approach, the predictor/corrector strategy and the GF numerical fluxes is plotted, while on the right panel we report the mixture density obtained with the DIRK schemes LRR in conjunction with GF numerical fluxes and the predictor/corrector strategy.

#### 4.5 ONE DIMENSIONAL SONIC POINT TEST PROBLEM

In this test we investigate the effects of pressure and velocity relaxation on a flow regime containing a sonic point (Romenski et al., 2010), while the phase transition terms are ignored ( $\tau_c = +\infty$ ). In particular, while in the previous test we have studied the behavior of the schemes proposed in this thesis in presence of instantaneous relaxations, here we are interested in the results obtained with a finite rate pressure and velocity relaxation.

We consider a Riemann problem with water and air as the phase 1 and 2 respectively. The computational domain (in meters) is  $[0, 1]$  with the Riemann problem being defined with the interface located at  $x = 0.4$ . The initial data are given by:

$$\begin{cases} \alpha_1 = 0.05, P_i = 10^6 \text{ Pa}, u_i = 100 \text{ m/s}, T = 270 \text{ K} & \forall x \in [0, 0.4] \text{ m} \\ \alpha_1 = 0.05, P_i = 10^5 \text{ Pa}, u_i = 0 \text{ m/s}, T = 270 \text{ K} & \forall x \in [0.4, 1] \text{ m} \end{cases}$$

for  $i = 1, 2$ . The constants for the equations of state are given in Table 5.

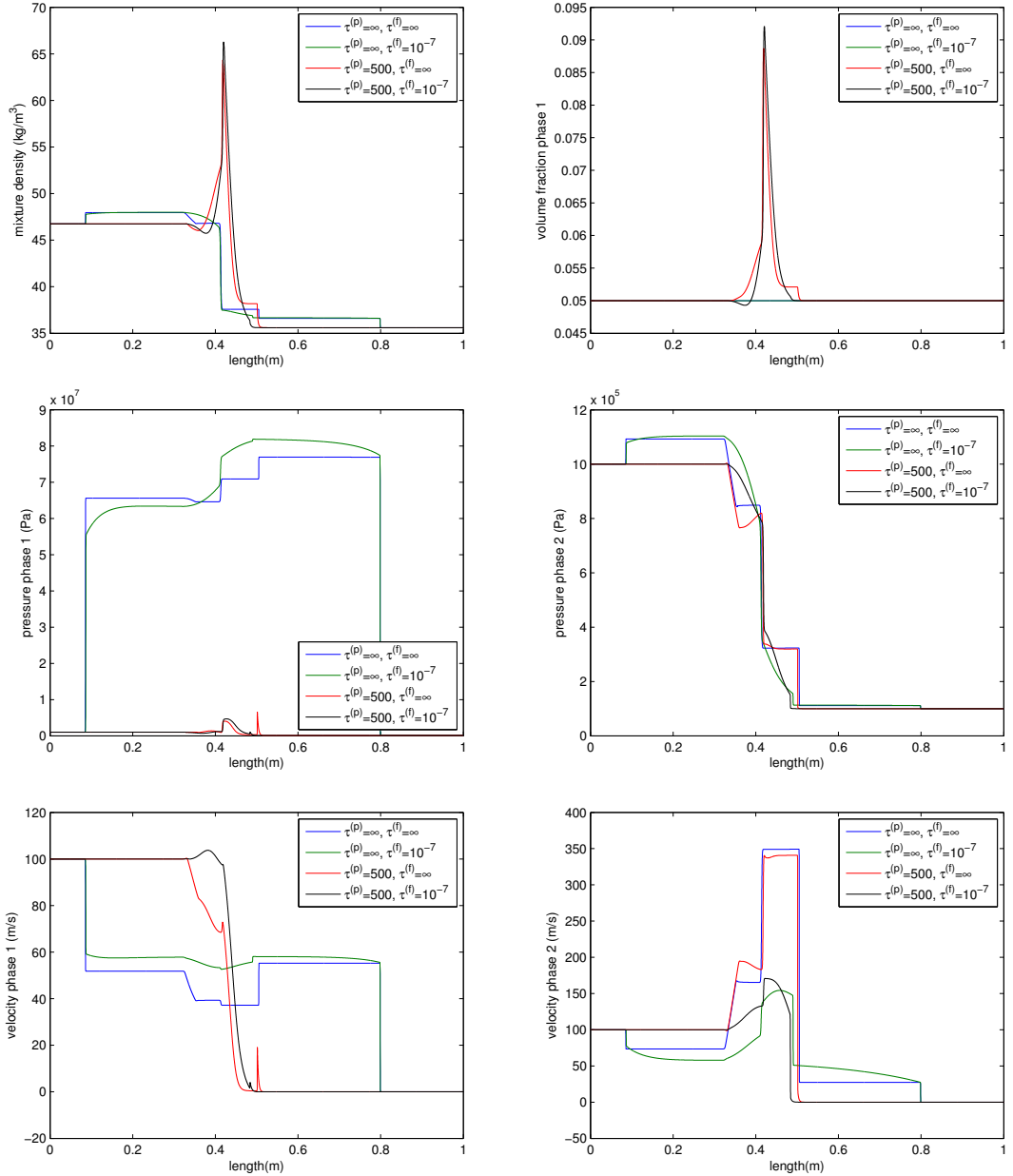


Figure 31: Sonic Point - Reference solution for mixture density (top left), volume fraction of phase 1 (top right), pressure of phase 1 (middle left) and of phase 2 (middle right), velocity of phase 1 (bottom left) and of phase 2 (bottom right). In each panel we compare the reference solutions obtained with  $\tau^{(p)} = \tau^{(f)} = \infty$  (blue line), with  $\tau^{(p)} = \infty, \tau^{(f)} = 10^{-7}$  (green line), with  $\tau^{(p)} = 500, \tau^{(f)} = \infty$  (red line) and finally with  $\tau^{(p)} = 500, \tau^{(f)} = 10^{-7}$  (black line).

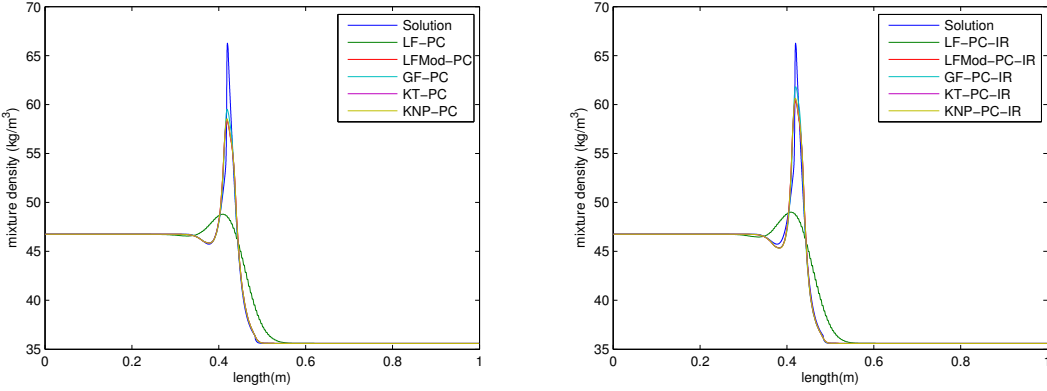


Figure 32: Sonic Point - Comparison between the reference solution for the mixture density (blue line), and the solutions computed using the splitting approach and the predictor/corrector strategy with LF (green line), LFMod (red line), GF (cyan line), KT (magenta line) and KNP numerical fluxes (yellow line). On the left panel, the solutions are obtained without the interfaces relaxations, while on the right panel they are included.

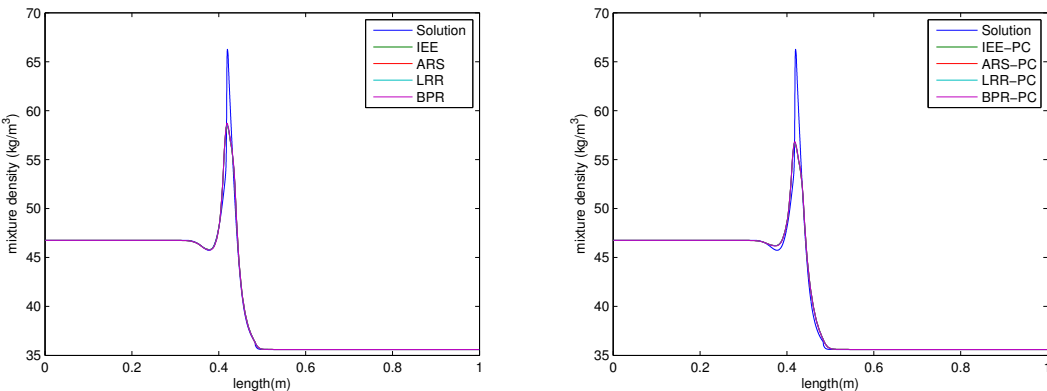


Figure 33: Sonic Point - Comparison between the reference solution for the mixture density (blue line), and the solutions computed using the DIRK schemes IEE (green line), ARS (red line), LRR (cyan line) and BPR (magenta line), all in conjunction with the LFMod numerical fluxes. On the left panel, the solutions are obtained without the predictor/corrector strategy, while on the right panel it has been used.

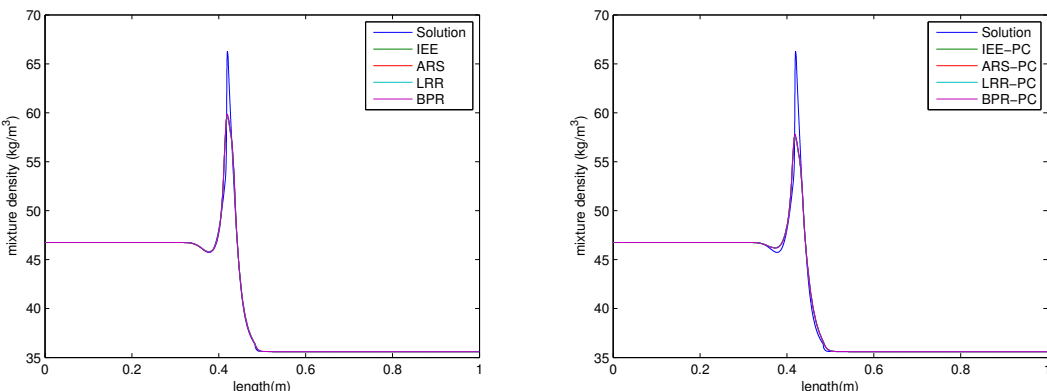


Figure 34: Sonic Point - Comparison between the reference solution for the mixture density (blue line), and the solutions computed using the DIRK schemes IEE (green line), ARS (red line), LRR (cyan line) and BPR (magenta line), all in conjunction with the GF numerical fluxes. On the left panel, the solutions are obtained without the predictor/corrector strategy, while on the right panel it has been used.

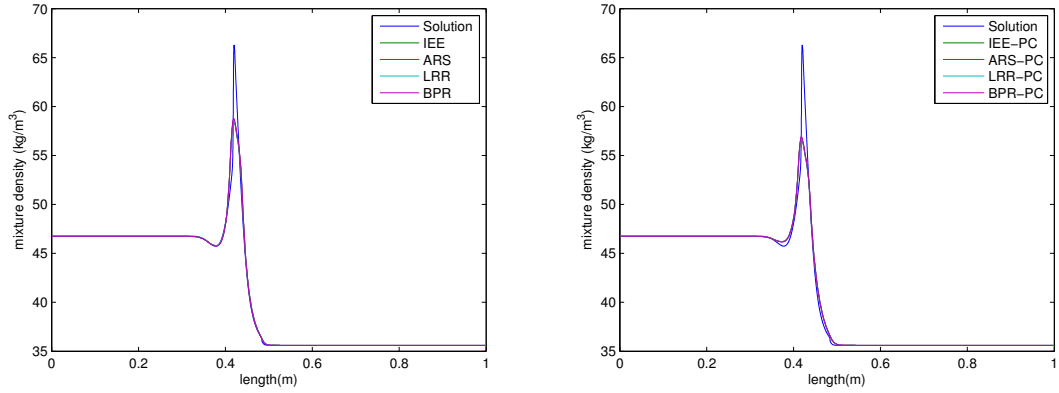


Figure 35: Sonic Point - Comparison between the reference solution for the mixture density (blue line), and the solutions computed using the DIRK schemes IEE (green line), ARS (red line), LRR (cyan line) and BPR (magenta line), all in conjunction with the KT numerical fluxes. On the left panel, the solutions are obtained without the predictor/corrector strategy, while on the right panel it has been used.

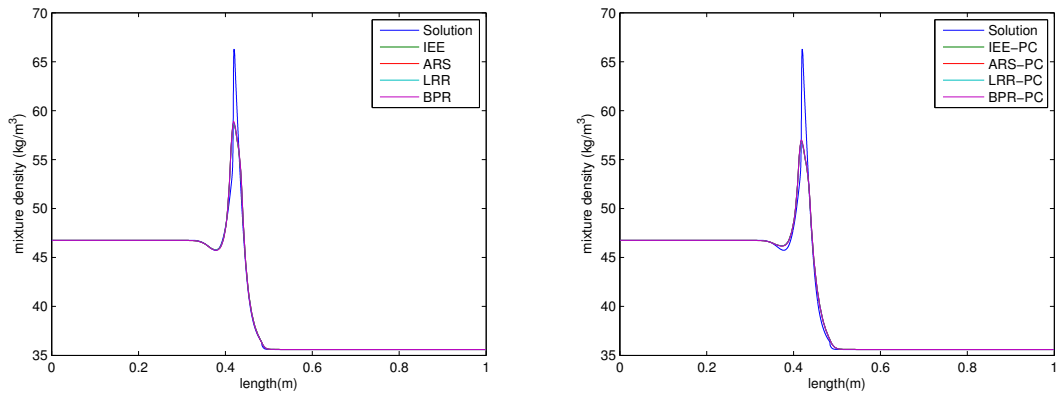


Figure 36: Sonic Point - Comparison between the reference solution for the mixture density (blue line), and the solutions computed using the DIRK schemes IEE (green line), ARS (red line), LRR (cyan line) and BPR (magenta line), all in conjunction with the KNP numerical fluxes. On the left panel, the solutions are obtained without the predictor/corrector strategy, while on the right panel it has been used.

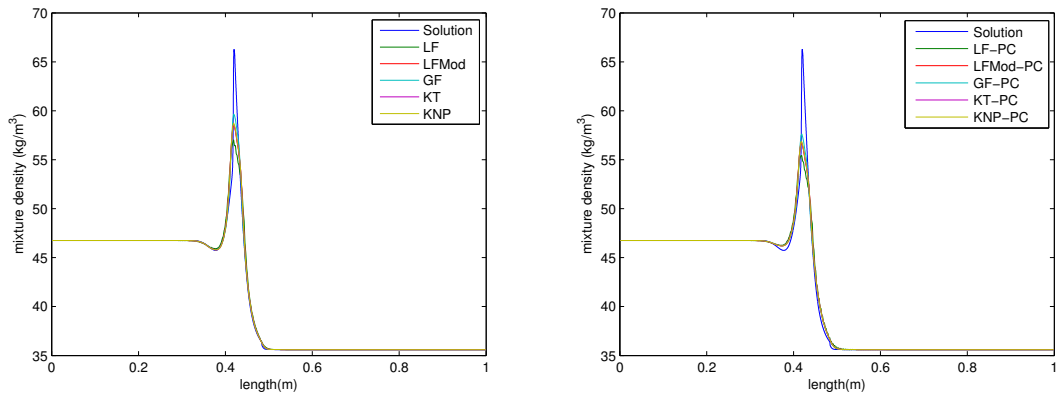


Figure 37: Sonic Point - Comparison between the reference solution for the mixture density (blue line), and the solutions computed using the DIRK LRR scheme in conjunction with LFMod (green line), GF (red line), KT (cyan line) and KNP numerical fluxes (magenta line). On the left panel, the solutions are obtained without the predictor/corrector strategy, while on the right panel it has been used.

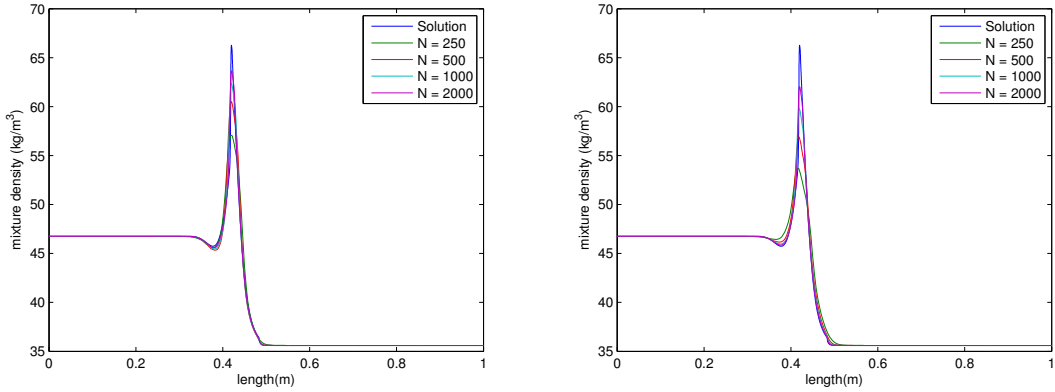


Figure 38: Sonic Point - Comparison between the reference solution for the mixture density (blue line) and the solutions obtained using different number of cells for the domain discretization: 250 (green line), 500 (red line), 1000 (cyan line) and 2000 (magenta line) cells. On the left panel the solution obtained with the splitting approach, the predictor/corrector strategy, the interfaces relaxations and KT numerical fluxes is plotted, while on the right panel is reported the mixture density obtained with the DIRK schemes BPR in conjunction with KT numerical fluxes and the predictor/corrector strategy.

Transmissive boundary conditions are imposed at  $x = 0$  and  $x = 1$ . The numerical solutions computed at time  $2.0 \times 10^{-4}$  s using a CFL coefficient equal to 0.49 are presented here.

Fig. 31 presents the solutions obtained with different values of pressure and velocity relaxation parameters  $\tau^{(p)}$  and  $\tau^{(f)}$  in order to compare the differences in the solutions caused by the finite rate relaxations. In particular, we plot the mixture density, the volume fraction of phase 1, the pressures and the velocities of both phases computed with a grid of 16000 cells. These are obtained using the modification of the Lax-Friedrichs scheme and will be considered as the reference solutions. In each panel we report the solutions without any relaxations ( $\tau^{(p)} = \tau^{(f)} = \infty$ ), with a finite rate relaxation for the velocities only ( $\tau^{(p)} = \infty, \tau^{(f)} = 10^{-7}$ ), with a finite rate relaxation for the pressures only ( $\tau^{(p)} = 5 \times 10^2, \tau^{(f)} = \infty$ ) and finally with both finite rate relaxations ( $\tau^{(p)} = 5 \times 10^2, \tau^{(f)} = 10^{-7}$ ).

For this test, we are interested in comparing the numerical schemes proposed in this thesis for finite rate relaxation for both pressures and velocity ( $\tau^{(p)} = 5 \times 10^2, \tau^{(f)} = 10^{-7}$ ). From the previous tests we have realized that the predictor/corrector strategy is fundamental in the splitting approach in order to recover the correct solution. For this reason, we have decided to not present anymore the solutions of the schemes in the splitting approach without the predictor/corrector strategy. The same decision has been made for the combination of the DIRK schemes with the LF numerical fluxes, thus from now on these will not be presented anymore.

Fig. 32 presents the reference solution for the mixture density (blue line), and the solutions computed using the splitting approach and the LFMod, the GF, the KT and the KNP numerical fluxes (we remind that, except for the reference solution, in Figs. 32-37 a grid of 500 cells is used). In the left panel are reported the solution obtained only with the predictor/corrector strategy, while in the right panel even the interface relaxation are included.

As we can see from Fig. 32, the solution computed with the interface relaxation is a little bit different from the solution obtained without it. The reference solution, near

N	LF-PC	LFMod-PC	GF-PC	KT-PC	KNP-PC
250	3.0333e-03	5.8607e-04	3.7606e-04	5.3707e-04	5.2324e-04
500	2.1537e-03	2.8436e-04	2.0227e-04	2.8007e-04	2.7435e-04
1000	1.3591e-03	1.3604e-04	9.3853e-05	1.3408e-04	1.3118e-04
2000	7.6954e-04	6.4557e-05	4.1036e-05	6.3567e-05	6.1848e-05
N	LF-PC-IR	LFMod-PC-IR	GF-PC-IR	KT-PC-IR	KNP-PC-IR
250	2.9723e-03	3.4798e-04	2.0473e-04	3.1172e-04	3.0168e-04
500	2.0926e-03	2.3442e-04	1.8636e-04	2.3412e-04	2.3185e-04
1000	1.2974e-03	1.3556e-04	9.9070e-05	1.3478e-04	1.3256e-04
2000	7.3147e-04	6.5200e-05	4.2629e-05	6.4406e-05	6.2797e-05

Table 36: Sonic Point - Relative errors between the reference mixture density and those computed using the splitting approach with the different numerical fluxes presented in this work and different domain discretizations.

DIRK IEE				
N	LFMod	GF	KT	KNP
250	5.2520e-04	3.2851e-04	4.7892e-04	4.6617e-04
500	2.7136e-04	1.9254e-04	2.6680e-04	2.6124e-04
1000	1.3295e-04	9.1182e-05	1.3104e-04	1.2809e-04
2000	6.3072e-05	3.9720e-05	6.2082e-05	6.0349e-05
N	LFMod-PC	GF-PC	KT-PC	KNP-PC
250	8.3660e-04	6.2821e-04	7.8852e-04	7.7510e-04
500	4.1768e-04	3.2536e-04	4.1138e-04	4.0452e-04
1000	1.7764e-04	1.3251e-04	1.7493e-04	1.7165e-04
2000	7.6853e-05	5.2742e-05	7.5738e-05	7.3941e-05

Table 37: Sonic Point - Relative errors between the reference mixture density and those computed using the DIRK IEE scheme with the different numerical fluxes presented in this work and different domain discretizations.

DIRK ARS				
N	LFMod	GF	KT	KNP
250	5.2884e-04	3.3143e-04	4.8243e-04	4.6962e-04
500	2.7260e-04	1.9317e-04	2.6800e-04	2.6242e-04
1000	1.3338e-04	9.1773e-05	1.3146e-04	1.2851e-04
2000	6.3465e-05	4.0206e-05	6.2471e-05	6.0744e-05
N	LFMod-PC	GF-PC	KT-PC	KNP-PC
250	8.4237e-04	6.3394e-04	7.9433e-04	7.8090e-04
500	4.2036e-04	3.2752e-04	4.1417e-04	4.0717e-04
1000	1.7855e-04	1.3345e-04	1.7583e-04	1.7255e-04
2000	7.7362e-05	5.3342e-05	7.6240e-05	7.4447e-05

Table 38: Sonic Point - Relative errors between the reference mixture density and those computed using the DIRK ARS scheme with the different numerical fluxes presented in this work and different domain discretizations.

DIRK LRR				
N	LFMod	GF	KT	KNP
250	5.2884e-04	3.3145e-04	4.8243e-04	4.6965e-04
500	2.7261e-04	1.9318e-04	2.6801e-04	2.6243e-04
1000	1.3338e-04	9.1767e-05	1.3146e-04	1.2851e-04
2000	6.3462e-05	4.0203e-05	6.2469e-05	6.0742e-05
N	LFMod-PC	GF-PC	KT-PC	KNP-PC
250	8.4230e-04	6.3387e-04	7.9426e-04	7.8084e-04
500	4.2035e-04	3.2750e-04	4.1416e-04	4.0716e-04
1000	1.7854e-04	1.3344e-04	1.7582e-04	1.7255e-04
2000	7.7360e-05	5.3339e-05	7.6239e-05	7.4445e-05

Table 39: Sonic Point - Relative errors between the reference mixture density and those computed using the DIRK LRR scheme with the different numerical fluxes presented in this work and different domain discretizations.

DIRK BPR				
N	LFMod	GF	KT	KNP
250	4.9567e-04	3.0410e-04	4.5054e-04	4.3808e-04
500	2.6476e-04	1.8744e-04	2.6057e-04	2.5521e-04
1000	1.3229e-04	9.0860e-05	1.3043e-04	1.2750e-04
2000	6.3249e-05	4.0013e-05	6.2261e-05	6.0536e-05
N	LFMod-PC	GF-PC	KT-PC	KNP-PC
250	8.0437e-04	5.9396e-04	7.5589e-04	7.4234e-04
500	4.0536e-04	3.1218e-04	3.9844e-04	3.9165e-04
1000	1.7520e-04	1.3020e-04	1.7252e-04	1.6926e-04
2000	7.6746e-05	5.2731e-05	7.5630e-05	7.3837e-05

Table 40: Sonic Point - Relative errors between the reference mixture density and those computed using the DIRK BPR scheme with the different numerical fluxes presented in this work and different domain discretizations.

N	LF-PC	LFMod-PC	GF-PC	KT-PC	KNP-PC
250	—	—	—	—	—
500	1.3234	2.1413	2.2185	2.0565	2.0631
1000	1.3780	1.6983	1.7007	1.6944	1.6922
2000	1.4789	1.6987	1.7746	1.7049	1.7099
N	LF-PC-IR	LFMod-PC-IR	GF-PC-IR	KT-PC-IR	KNP-PC-IR
250	—	—	—	—	—
500	1.3262	1.3472	1.0769	1.2618	1.2439
1000	1.3893	1.4188	1.5049	1.4329	1.4432
2000	1.4769	1.6942	1.7142	1.6973	1.7002

Table 41: Sonic Point - Convergence rates for the mixture density computed with different domain discretization using the splitting approach with the numerical fluxes presented in this work.

DIRK IEE				
N	LFMod	GF	KT	KNP
250	—	—	—	—
500	2.0659	2.0730	1.9676	1.9698
1000	1.6600	1.6875	1.6584	1.6606
2000	1.7015	1.7726	1.7087	1.7109
N	LFMod-PC	GF-PC	KT-PC	KNP-PC
250	—	—	—	—
500	1.7768	1.7840	1.7400	1.7467
1000	1.7680	1.7009	1.7636	1.7564
2000	1.6943	1.7711	1.6949	1.7000

Table 42: Sonic Point - Convergence rates for the mixture density computed with different domain discretization using the DIRK IEE scheme with the numerical fluxes presented in this work.

DIRK ARS				
N	LFMod	GF	KT	KNP
250	—	—	—	—
500	2.0568	2.0600	1.9600	1.9619
1000	1.6599	1.6893	1.6588	1.6610
2000	1.7000	1.7678	1.7071	1.7107
N	LFMod-PC	GF-PC	KT-PC	KNP-PC
250	—	—	—	—
500	1.7741	1.7854	1.7373	1.7443
1000	1.7678	1.6968	1.7634	1.7558
2000	1.6899	1.7651	1.6910	1.6962

Table 43: Sonic Point - Convergence rates for the mixture density computed with different domain discretization using the DIRK ARS scheme with the numerical fluxes presented in this work.

DIRK LRR				
N	LFMod	GF	KT	KNP
250	—	—	—	—
500	2.0568	2.0601	1.9599	1.9618
1000	1.6600	1.6895	1.6589	1.6610
2000	1.7001	1.7678	1.7072	1.7108
N	LFMod-PC	GF-PC	KT-PC	KNP-PC
250	—	—	—	—
500	1.7741	1.7854	1.7373	1.7443
1000	1.7678	1.6968	1.7635	1.7559
2000	1.6899	1.7650	1.6910	1.6962

Table 44: Sonic Point - Convergence rates for the mixture density computed with different domain discretization using the DIRK LRR scheme with the numerical fluxes presented in this work.

DIRK BPR				
N	LFMod	GF	KT	KNP
250	—	—	—	—
500	2.0161	1.9364	1.9058	1.8980
1000	1.6345	1.6698	1.6353	1.6379
2000	1.7028	1.7645	1.7113	1.7147
N	LFMod-PC	GF-PC	KT-PC	KNP-PC
250	—	—	—	—
500	1.7805	1.7996	1.7429	1.7495
1000	1.7606	1.6679	1.7514	1.7435
2000	1.6700	1.7437	1.6718	1.6769

Table 45: Sonic Point - Convergence rates for the mixture density computed with different domain discretization using the DIRK BPR scheme with the numerical fluxes presented in this work.

$x = 0.4$ , presents a relative minimum and maximum in the mixture density. We can see that the maximum of the mixture density obtained with the interface relaxation (right panel) is closer to the maximum density of the reference solution than that obtained without using it (left panel). On the contrary the minimum of the mixture density computed without the interface relaxation is closer than that in which the interface relaxation is not used. Because of that, as we can see from Table 36, the relative error of the solutions computed with or without the interface relaxation are quite similar.

In Fig. 33-36 the reference solution for the mixture density (blue line) is compared with the solutions computed using the DIRK schemes. About the numerical fluxes chosen, we plot in Fig. 33 those computed with LFMod, in Fig. 34 those calculated with GF, in Fig. 35 those obtained using KT and finally in Fig. 36 those computed with KNP.

In Fig. 37 instead, the reference solution for the mixture density (blue line) is compared with the solutions obtained with the DIRK LRR using for the LFMod, GF, KT and KNP numerical fluxes.

Once again the DIRK schemes seem to produce very similar solutions, and this evidence is highlighted by the relative error reported in Tables 37-40. Furthermore, even in the case of finite rate relaxations, the relative errors of the DIRK schemes are comparable to those obtained with the splitting approach.

Finally Tables 41-45 report the convergence rate of the schemes used in this test and in Fig. 38 the effects of grid refinement is shown, plotting the reference mixture density (blue line) and those obtained using four different number of cells: 250 (green line), 500 (red line), 1000 (cyan line) and 2000 (magenta line) cells. On the left panel we plot the solution obtained with the splitting approach, the predictor/corrector strategy, the interfaces relaxations and KT numerical fluxes, while on the right panel we report the mixture density obtained with the DIRK schemes BPR in conjunction with KT numerical fluxes and the predictor/corrector strategy.

#### 4.6 ONE DIMENSIONAL CAVITATION TUBE PROBLEM

In this test we consider a phase transition problem for a tube initially at atmospheric pressure and at a temperature of 355 K, filled with water and a small volumetric fraction

	$P_0$ (Pa)	$T_0$ (K)	$\gamma$	$C_0$ (m/s)	$c_v$ (J/(kg · K))	$\bar{e}$ (J/kg)	$s_0$ (J/(kg · K))
Water	$10^5$	373	2.514	1542.98	1677	-1.167e+6	1307
Vapor	$10^5$	373	1.324	501.37	1571	2.030e+6	7742

Table 46: Parameters of the equation of state for water and water vapor used in the Cavitation Tube test.

of water vapor. In this test the water cannot be treated as pure and phase transition only occurs if the pressure of the liquid phase is greater than the saturation pressure.

The initial condition is similar to the two-phase expansion tube test described in Zein et al. (2010), where a seven-equation model for two-phase flows is applied to model phase transition of metastable liquids. The left part of the tube is set to motion with a velocity  $u_l = -2$  m/s while the right part is set to motion with a velocity  $u_r = 2$  m/s. In such situation, the pressure, density and internal energy decrease across the rarefaction waves in order that the velocity reaches zero at the center of the domain. The pressure decreases until the saturation pressure at the local temperature is reached. Then the mass transfer appears, a part of liquid become gas, and the flow becomes a two-phase mixture. This problem has been studied also in Saurel and Le Métayer (2001) in a simplified situation where a small fraction of gas is initially present in the liquid (1% gas by volume) and the mass transfer in not considered. Here the effects of the phase exchange term is analyzed, in order to compare our results with both those presented in Saurel and Le Métayer (2001) and Zein et al. (2010).

The computational domain considered is [0, 1] m with a Riemann problem being defined with the interface located at  $x = 0.5$  m. The initial data for this numerical simulation are the following:

$$\begin{cases} \alpha_1 = 0.99, P_i = 10^5 \text{ Pa}, u_i = -2 \text{ m/s}, T = 355 \text{ K} & \forall x \in [0, 0.5] \text{ m} \\ \alpha_1 = 0.99, P_i = 10^5 \text{ Pa}, u_i = 2 \text{ m/s}, T = 355 \text{ K} & \forall x \in [0.5, 1] \text{ m} \end{cases}$$

for  $i = 1, 2$ . The indexes 1 and 2 are referred to the parameters of state of water and water vapor, respectively, and the constants for the equations of state are given in Table 46.

We present here the numerical solutions computed at time  $3.2 \times 10^{-3}$  s using a CFL coefficient equal to 0.49. Finally, we assume instantaneous relaxations for the pressures and velocities ( $\tau^{(p)} = \tau^{(f)} = 0$ ).

In Fig. 39 the reference solutions computed with and without the instantaneous evaporation are compared. More in detail, we plot the mixture density, the common temperature, the pressure, the velocity, and finally the volume and mass fraction of the vapor phase. In the previous tests presented in this work, the reference solutions has been computed using a grid of 16000 cells. For this test, the solution obtained with that grid is too diffusive and cannot be used as a reference one. For this reason the reference solution is calculated using the splitting approach in conjunction with the KNP numerical fluxes and a grid of 64000 cells. Furthermore, instead of using the Minmod limiter, the Van Leer limiter (3.10) is adopted. A reasonable agreement with the results obtained in (Zein et al., 2010) for a seven-equation model is achieved.

From now on, for this test, we consider only the solution obtained with the instantaneous evaporation, and we analyze the results computed with the schemes proposed in Chapter 3.

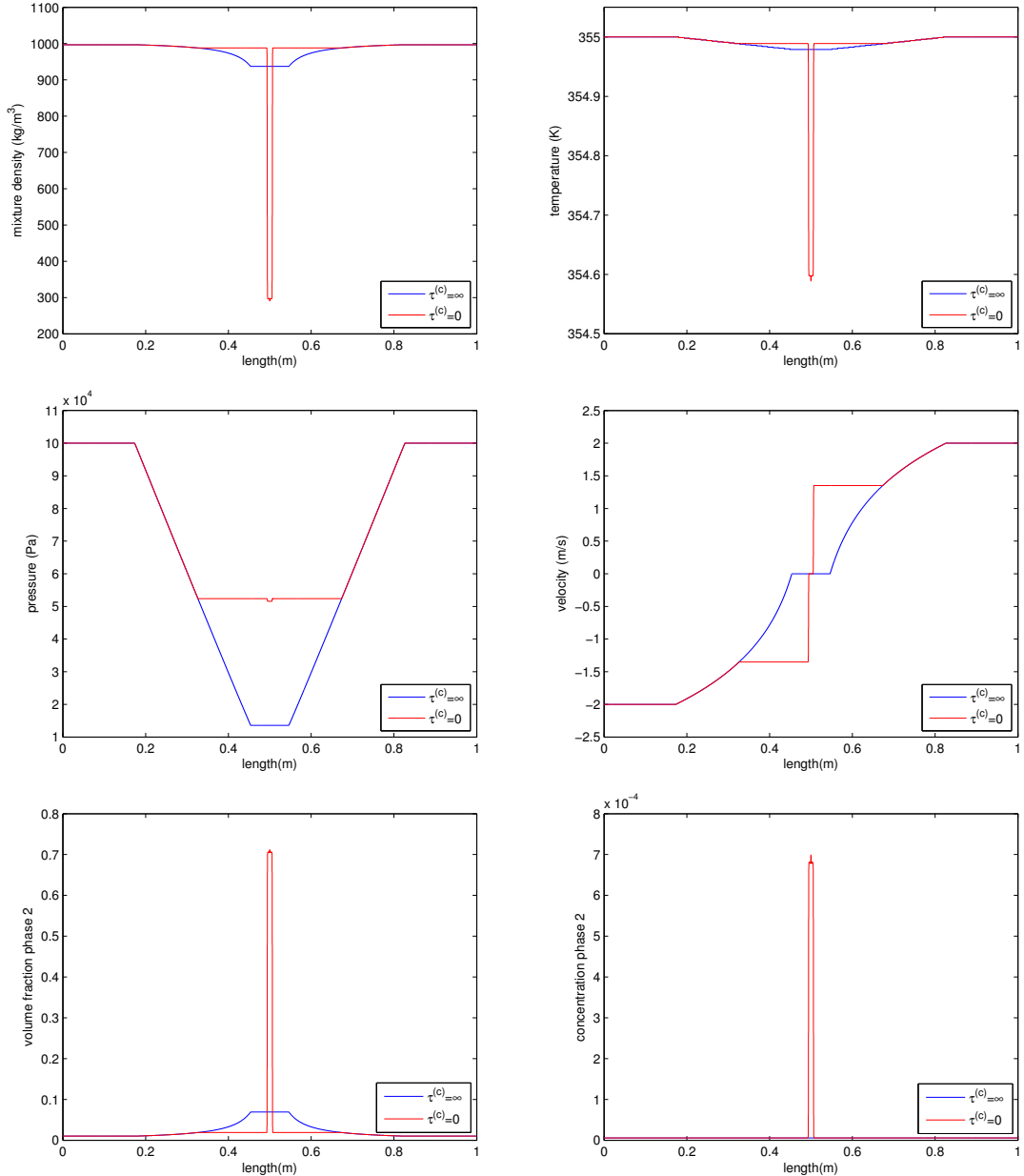


Figure 39: Cavitation Tube - Reference solution for mixture density (top left), mixture temperature (top right), mixture pressure (middle left) and mixture velocity (middle right), volume fraction (bottom left) and concentration (bottom right) both of phase 2. In each panel we reported the reference solutions obtained with  $\tau^{(p)} = \tau^{(f)} = 0$  and with  $\tau^{(c)} = \infty$  (blue line) and with  $\tau^{(c)} = 0$  (red line). Furthermore, the Van-Leer limiter has been used for both solutions.

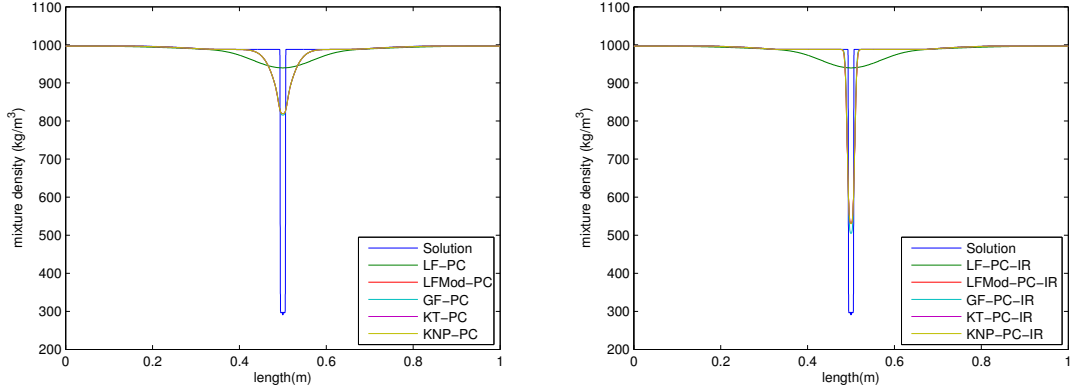


Figure 40: Cavitation Tube - Comparison between the reference solution for the mixture density (blue line), and the solutions computed using the splitting approach and the predictor/corrector strategy with LF (green line), LFMod (red line), GF (cyan line), KT (magenta line) and KNP numerical fluxes (yellow line). On the left panel, the solutions are obtained without the interfaces relaxations, while on the right panel they are included. Furthermore, the Van-Leer limiter has been used for all solutions.

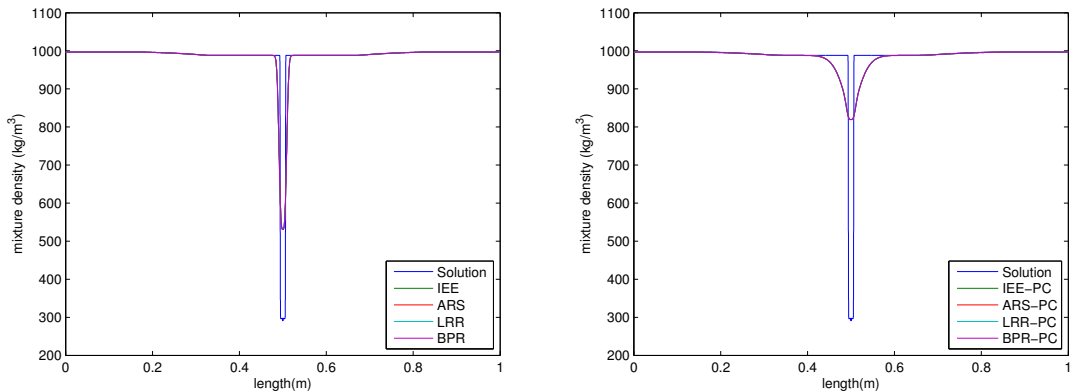


Figure 41: Cavitation Tube - Comparison between the reference solution for the mixture density (blue line), and the solutions computed using the DIRK schemes IEE (green line), ARS (red line), LRR (cyan line) and BPR (magenta line), all in conjunction with the LFMod numerical fluxes. On the left panel, the solutions are obtained without the predictor/corrector strategy, while on the right panel it has been used. Furthermore, the Van–Leer limiter has been used for all solutions.

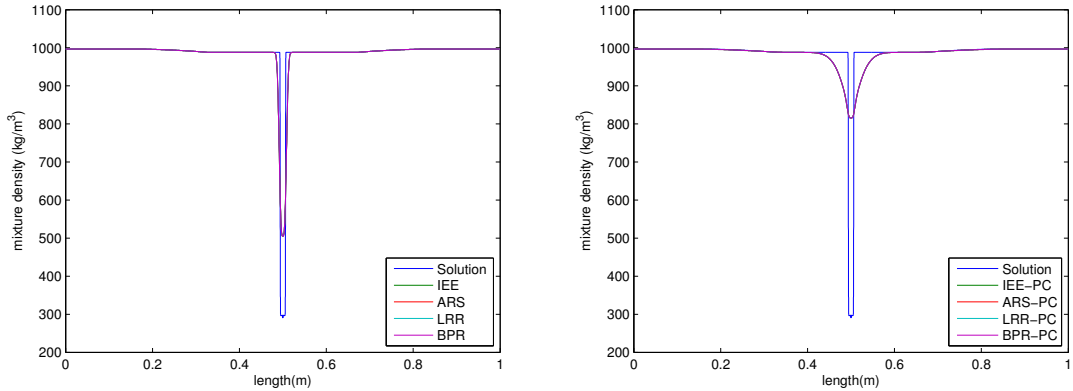


Figure 42: Cavitation Tube - Comparison between the reference solution for the mixture density (blue line), and the solutions computed using the DIRK schemes IEE (green line), ARS (red line), LRR (cyan line) and BPR (magenta line), all in conjunction with the GF numerical fluxes. On the left panel, the solutions are obtained without the predictor/corrector strategy, while on the right panel it has been used. Furthermore, the Van–Leer limiter has been used for all solutions.

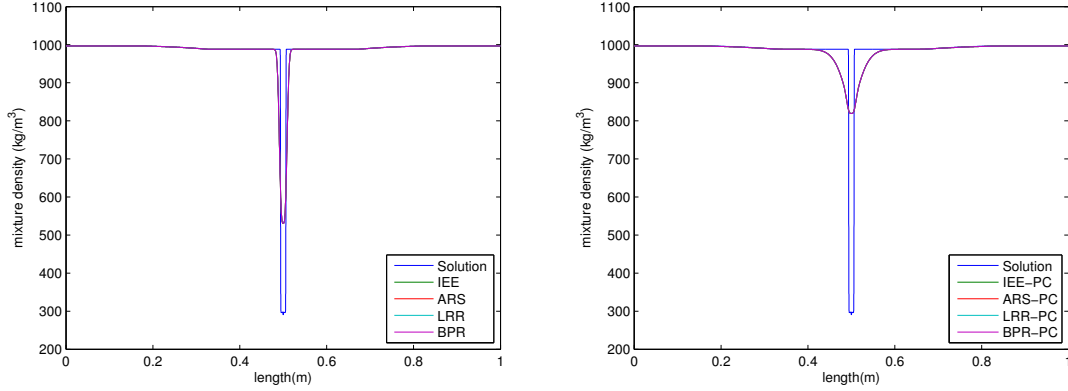


Figure 43: Cavitation Tube - Comparison between the reference solution for the mixture density (blue line), and the solutions computed using the DIRK schemes IEE (green line), ARS (red line), LRR (cyan line) and BPR (magenta line), all in conjunction with the KT numerical fluxes. On the left panel, the solutions are obtained without the predictor/corrector strategy, while on the right panel it has been used. Furthermore, the Van-Leer limiter has been used for all solutions.

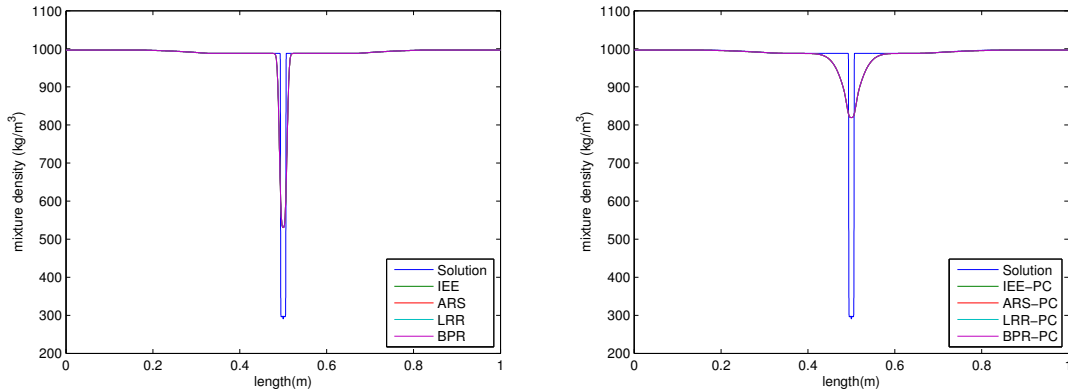


Figure 44: Cavitation Tube - Comparison between the reference solution for the mixture density (blue line), and the solutions computed using the DIRK schemes IEE (green line), ARS (red line), LRR (cyan line) and BPR (magenta line), all in conjunction with the KNP numerical fluxes. On the left panel, the solutions are obtained without the predictor/corrector strategy, while on the right panel it has been used. Furthermore, the Van-Leer limiter has been used for all solutions.

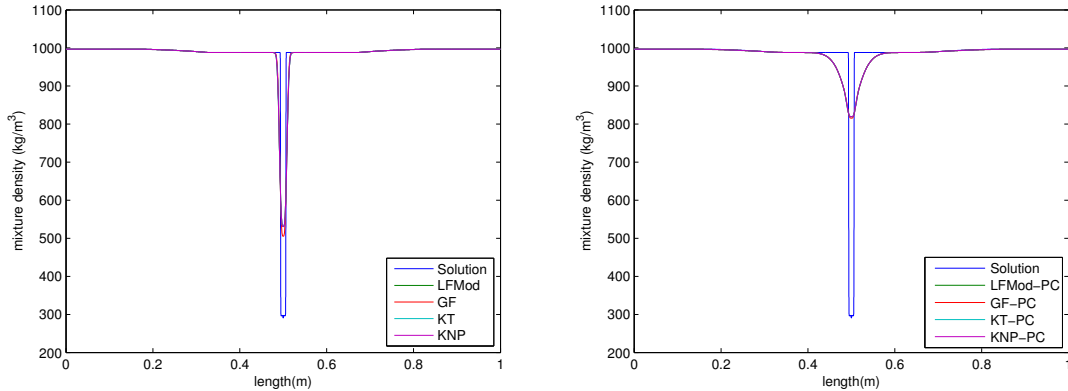


Figure 45: Cavitation Tube - Comparison between the reference solution for the mixture density (blue line), and the solutions computed using the DIRK BPR scheme in conjunction with LFMod (green line), GF (red line), KT (cyan line) and KNP numerical fluxes (magenta line). On the left panel, the solutions are obtained without the predictor/corrector strategy, while on the right panel it has been used. Furthermore, the Van-Leer limiter has been used for all solutions.

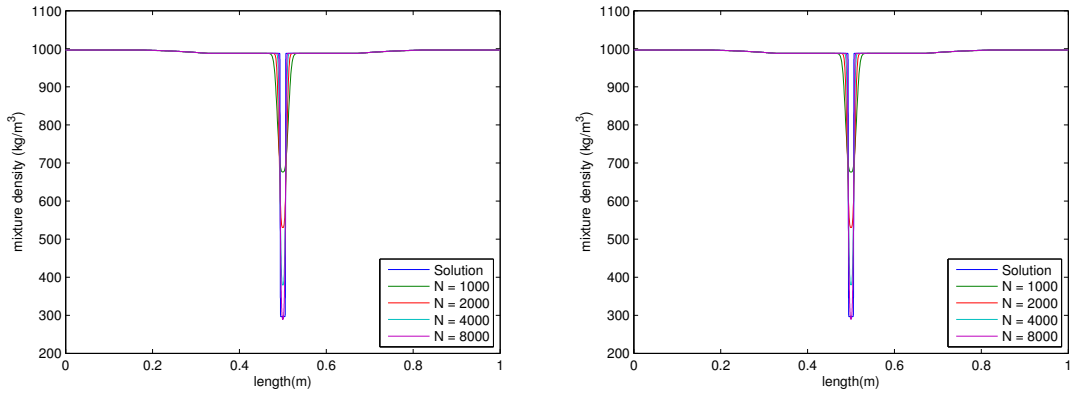


Figure 46: Cavitation Tube - Comparison between the reference solution for the mixture density (blue line) and the solutions obtained using different number of cells for the domain discretization: 1000 (green line), 2000 (red line), 4000 (cyan line) and 8000 (magenta line) cells. On the left panel the solution obtained with the splitting approach, the predictor/corrector strategy, the interfaces relaxations and KNP numerical fluxes has been plotted, while on the right panel is reported the mixture density obtained with the DIRK scheme ARS in conjunction with KNP numerical fluxes. Furthermore, the Van-Leer limiter has been used for all solutions.

N	LF-PC	LFMod-PC	GF-PC	KT-PC	KNP-PC
1000	5.4675e-03	4.4537e-03	4.4020e-03	4.4535e-03	4.4535e-03
2000	5.3184e-03	3.8895e-03	3.8395e-03	3.8893e-03	3.8892e-03
4000	5.1020e-03	3.2219e-03	3.1989e-03	3.2218e-03	3.2218e-03
8000	4.8080e-03	2.5591e-03	2.5625e-03	2.5591e-03	2.5591e-03
N	LF-PC-IR	LFMod-PC-IR	GF-PC-IR	KT-PC-IR	KNP-PC-IR
1000	5.4673e-03	2.6636e-03	2.4404e-03	2.6624e-03	2.6621e-03
2000	5.3181e-03	1.4115e-03	1.2342e-03	1.4104e-03	1.4102e-03
4000	5.1018e-03	5.6048e-04	4.9862e-04	5.6020e-04	5.6008e-04
8000	4.8080e-03	2.4786e-04	2.2355e-04	2.4781e-04	2.4775e-04

Table 47: Cavitation Tube - Relative errors between the reference mixture density and those computed using the splitting approach with the different numerical fluxes presented in this work and different domain discretizations.

Fig. 40 presents the reference solution for the mixture density (blue line), and the solutions computed using the splitting approach and the LF, LMod, the GF, the KT and the KNP numerical fluxes. In the left panel are reported the solution obtained only with the predictor/corrector strategy, while in the right panel the interface relaxation is also included.

As we can see from Fig. 40, the application of the interface relaxations gives less diffusive solutions with respect to those obtained without it. This reflects also in the relative errors reported in the Table 47, where we can notice that the relative errors of the solutions obtained with the interface relaxations are an order of magnitude less than those obtained without using it.

In Figs. 41-44 the reference solution for the mixture density (blue line) is compared with the solutions computed using the DIRK schemes. About the numerical fluxes chosen, we plot in Fig. 41 those computed with LMod, in Fig. 42 those calculated with GF, in Fig. 43 those obtained using KT and finally in Fig. 44 those computed with KNP.

DIRK IEE				
N	LFMod	GF	KT	KNP
1000	2.6652e-03	2.4427e-03	2.6640e-03	2.6636e-03
2000	1.4145e-03	1.2373e-03	1.4133e-03	1.4131e-03
4000	5.6251e-04	5.0047e-04	5.6225e-04	5.6213e-04
8000	2.4888e-04	2.2452e-04	2.4882e-04	2.4877e-04
N	LFMod-PC	GF-PC	KT-PC	KNP-PC
1000	4.4539e-03	4.4021e-03	4.4537e-03	4.4536e-03
2000	3.8896e-03	3.8396e-03	3.8894e-03	3.8894e-03
4000	3.2220e-03	3.1990e-03	3.2219e-03	3.2219e-03
8000	2.5592e-03	2.5626e-03	2.5592e-03	2.5592e-03

Table 48: Cavitation Tube - Relative errors between the reference mixture density and those computed using the DIRK IEE scheme with the different numerical fluxes presented in this work and different domain discretizations.

DIRK ARS				
N	LFMod	GF	KT	KNP
1000	2.6628e-03	2.4401e-03	2.6615e-03	2.6613e-03
2000	1.4121e-03	1.2350e-03	1.4109e-03	1.4107e-03
4000	5.6122e-04	4.9929e-04	5.6095e-04	5.6082e-04
8000	2.4806e-04	2.2375e-04	2.4800e-04	2.4794e-04
N	LFMod-PC	GF-PC	KT-PC	KNP-PC
1000	4.4534e-03	4.4016e-03	4.4532e-03	4.4531e-03
2000	3.8891e-03	3.8391e-03	3.8889e-03	3.8889e-03
4000	3.2216e-03	3.1986e-03	3.2215e-03	3.2215e-03
8000	2.5589e-03	2.5623e-03	2.5589e-03	2.5589e-03

Table 49: Cavitation Tube - Relative errors between the reference mixture density and those computed using the DIRK ARS scheme with the different numerical fluxes presented in this work and different domain discretizations.

DIRK LRR				
N	LFMod	GF	KT	KNP
1000	2.6638e-03	2.4413e-03	2.6626e-03	2.6623e-03
2000	1.4131e-03	1.2361e-03	1.4120e-03	1.4117e-03
4000	5.6181e-04	4.9986e-04	5.6153e-04	5.6140e-04
8000	2.4839e-04	2.2412e-04	2.4833e-04	2.4828e-04
N	LFMod-PC	GF-PC	KT-PC	KNP-PC
1000	4.4535e-03	4.4017e-03	4.4533e-03	4.4532e-03
2000	3.8892e-03	3.8391e-03	3.8890e-03	3.8890e-03
4000	3.2217e-03	3.1986e-03	3.2216e-03	3.2216e-03
8000	2.5590e-03	2.5624e-03	2.5590e-03	2.5590e-03

Table 50: Cavitation Tube - Relative errors between the reference mixture density and those computed using the DIRK LRR scheme with the different numerical fluxes presented in this work and different domain discretizations.

DIRK BPR				
N	LFMod	GF	KT	KNP
1000	2.6641e-03	2.4416e-03	2.6629e-03	2.6625e-03
2000	1.4133e-03	1.2364e-03	1.4123e-03	1.4120e-03
4000	5.6197e-04	5.0004e-04	5.6170e-04	5.6158e-04
8000	2.4848e-04	2.2424e-04	2.4842e-04	2.4836e-04
N	LFMod-PC	GF-PC	KT-PC	KNP-PC
1000	4.4535e-03	4.4017e-03	4.4533e-03	4.4533e-03
2000	3.8893e-03	3.8392e-03	3.8890e-03	3.8890e-03
4000	3.2217e-03	3.1987e-03	3.2216e-03	3.2216e-03
8000	2.5590e-03	2.5624e-03	2.5590e-03	2.5590e-03

Table 51: Cavitation Tube - Relative errors between the reference mixture density and those computed using the DIRK BPR scheme with the different numerical fluxes presented in this work and different domain discretizations.

N	LF-PC	LFMod-PC	GF-PC	KT-PC	KNP-PC
1000	—	—	—	—	—
2000	1.0251	1.0888	1.0892	1.0888	1.0888
4000	1.0265	1.1314	1.1279	1.1314	1.1314
8000	1.0438	1.1633	1.1594	1.1633	1.1633
N	LF-PC-IR	LFMod-PC-IR	GF-PC-IR	KT-PC-IR	KNP-PC-IR
1000	—	—	—	—	—
2000	1.0251	1.5187	1.5579	1.5189	1.5190
4000	1.0265	1.8829	1.8885	1.8826	1.8827
8000	1.0438	1.9806	1.9512	1.9802	1.9802

Table 52: Cavitation Tube - Convergence rates for the mixture density computed with different domain discretization using the splitting approach with the numerical fluxes presented in this work.

DIRK IEE				
N	LFMod	GF	KT	KNP
1000	—	—	—	—
2000	1.5175	1.5565	1.5178	1.5177
4000	1.8807	1.8862	1.8803	1.8804
8000	1.9799	1.9505	1.9795	1.9795
N	LFMod-PC	GF-PC	KT-PC	KNP-PC
1000	—	—	—	—
2000	1.0888	1.0892	1.0888	1.0888
4000	1.1314	1.1279	1.1314	1.1314
8000	1.1633	1.1594	1.1633	1.1633

Table 53: Cavitation Tube - Convergence rates for the mixture density computed with different domain discretization using the DIRK IEE scheme with the numerical fluxes presented in this work.

DIRK ARS				
N	LFMod	GF	KT	KNP
1000	—	—	—	—
2000	1.5182	1.5574	1.5185	1.5186
4000	1.8819	1.8876	1.8816	1.8817
8000	1.9817	1.9523	1.9813	1.9813
N	LFMod-PC	GF-PC	KT-PC	KNP-PC
1000	—	—	—	—
2000	1.0888	1.0892	1.0888	1.0888
4000	1.1314	1.1279	1.1314	1.1314
8000	1.1633	1.1594	1.1633	1.1633

Table 54: Cavitation Tube - Convergence rates for the mixture density computed with different domain discretization using the DIRK ARS scheme with the numerical fluxes presented in this work.

DIRK LRR				
N	LFMod	GF	KT	KNP
1000	—	—	—	—
2000	1.5179	1.5570	1.5182	1.5182
4000	1.8812	1.8869	1.8810	1.8811
8000	1.9812	1.9514	1.9808	1.9807
N	LFMod-PC	GF-PC	KT-PC	KNP-PC
1000	—	—	—	—
2000	1.0888	1.0892	1.0888	1.0888
4000	1.1314	1.1279	1.1314	1.1314
8000	1.1633	1.1594	1.1633	1.1633

Table 55: Cavitation Tube - Convergence rates for the mixture density computed with different domain discretization using the DIRK LRR scheme with the numerical fluxes presented in this work.

DIRK BPR				
N	LFMod	GF	KT	KNP
1000	—	—	—	—
2000	1.5179	1.5568	1.5181	1.5181
4000	1.8810	1.8866	1.8808	1.8809
8000	1.9811	1.9511	1.9807	1.9807
N	LFMod-PC	GF-PC	KT-PC	KNP-PC
1000	—	—	—	—
2000	1.0888	1.0892	1.0888	1.0888
4000	1.1315	1.1279	1.1314	1.1314
8000	1.1633	1.1594	1.1633	1.1633

Table 56: Cavitation Tube - Convergence rates for the mixture density computed with different domain discretization using the DIRK BPR scheme with the numerical fluxes presented in this work.

In Fig. 45 instead, the reference solution for the mixture density (blue line) is compared with the solutions obtained with the DIRK BPR using for the LMod, GF, KT and KNP numerical fluxes.

Once again the DIRK schemes seem to produce very similar solutions, and this evidence is highlighted by the relative error reported in Tables 48-51. As we can note from the Figs. 41-45 and from the data collected in Tables 48-51, the predictor/corrector strategy applied to the DIRK schemes produces more diffusive solutions with respect to those obtained without using it.

Finally in Tables 52-56 are reported the convergence rate of the schemes used in this test and Fig. 46 shows the effects of grid refinement, plotting the reference mixture density (blue line) and those obtained using four different number of cells: 1000 (green line), 2000 (red line), 4000 (cyan line) and 8000 (magenta line) cells. On the left panel we plot the solution obtained with the splitting approach, the predictor/corrector strategy, the interface relaxation and KNP numerical fluxes, while on the right panel we report the mixture density obtained with the DIRK schemes ARS in conjunction with KNP numerical fluxes. Furthermore, the Van-Leer limiter has been used for all solutions.

#### 4.7 CONCLUSIONS

In this chapter we have tested the numerical schemes presented in Chapter 3 with several Riemann problems. We have investigated the ability of the schemes to reproduce correctly the behavior of the solutions in presence of rarefaction and shock waves. Furthermore we have analyzed the solutions obtained considering instantaneous, finite-rate and no relaxations. From the results obtained, we can conclude that:

- the splitting approach has to be used in conjunction with the predictor/corrector strategy to properly resolve the rarefaction waves;
- the DIRK schemes in conjunction with LF numerical fluxes are not robust and are not able to compute the solution of problems that involve strong shock-waves;
- the application of the predictor/corrector strategy to the DIRK schemes does not result in a better accuracy on the solutions computed;
- the solutions obtained with the different DIRK schemes studied, except for the DIRK IEE, are almost identical, therefore the use of the DIRK ARS should be preferred due to the lower running time;
- the numerical fluxes investigated, except for the LF, produce quite similar solutions; sorting them from the most to the least accurate we have: GF, KNP, KT, LMod, LF; conversely, from the fastest to slowest the ranking is reversed: LF, LMod, KT, KNP, GF;
- finally, the accuracy of solutions obtained with the splitting approach in conjunction with the predictor/corrector strategy and the DIRK schemes is almost the same, therefore the former should be preferred due to a lower running time.



# 5

---

## MULTIDIMENSIONAL APPLICATIONS

---

For the multidimensional applications presented in this thesis, the implementation to the multidimensional case is extended using the open source CFD (Computational Fluid Dynamics) toolbox “OpenFOAM”(Open source Field Operation And Manipulation).

OpenFOAM is first and foremost a C++ library, used primarily to create executables, known as *applications*. The applications fall into two categories:

- solvers, designed to solve a specific problem in continuum mechanics;
- utilities, designed to perform tasks that involve data manipulation.

All solvers developed within OpenFOAM are, by default, three dimensional, but can be used for one- or two-dimensional problems by the application of particular conditions on boundaries lying in the plane of the direction(s) of no interest. Moreover the built-in functions are very simple to use and allow us to extend the numerical codes from the 1D formulation to the 3D case.

One of the strengths of OpenFOAM is that the new solvers and utilities, created by its users, inherit from the OpenFOAM framework some very useful features like the use of unstructured mesh and parallelization.

For this thesis OpenFOAM 2.1.1 is used. In this version, there are no solver for multiphase compressible flows with distinct pressures and velocities for the different phases. For this reason, two new solvers called respectively *twoPhaseCentralFoam* (based on the splitting approach) and *twoPhaseCentralFoamDIRK* (based on the Implicit-Explicit Runge-Kutta approach) solving the system of partial differential equations (2.8) have been implemented. The implementation of these solvers is based on the *rhoCentralFoam* solver included in OpenFOAM and described by Greenshields et al. (2010). It is a solver for the governing equations of a compressible single phase fluid based on finite volume central schemes. The numerical fluxes adopted in *rhoCentralFoam* are the KT and KNP numerical fluxes, but neither predictor/corrector strategy nor interfaces relaxation are implemented. Furthermore, in order to prevent unphysical solutions (for example negative pressures or temperature), in my solvers the linear reconstruction is done on a set of primitive variables, as described in Section 4.1. In Appendix B we present more in detail how the numerical schemes have been implemented using OpenFOAM framework.

The solvers have been tested on a desktop PC with a quad-core Intel® Core™ i7-3770 Processor (<http://ark.intel.com/products/65523>), on a High Performance Computing 64 multi core Shared Memory system (HPC-SM) at Istituto Nazionale di Geofisica e Vulcanologia (INGV), section of Pisa, Italy, and on the IBM PLX cluster at the High Performance Computing department of the Italian computing center CINECA,

in the framework of the ISCRA (Italian SuperComputing Resource Allocation) project GEOFOAM.

In this chapter three multidimensional numerical tests are illustrated: the first is an extension of the Air–Water Shock Problem presented in Section 4.4 and it is developed to asses the robustness of a numerical scheme and to compare the 1D and 2D solutions, while in the others we reproduce two laboratory experiments performed by Haas and Sturtevant (1987) comparing the numerical solutions with their results. Having analyzed the accuracy of the proposed schemes in the previous chapter, in the first test we use one scheme for each of the approaches presented in this thesis in order to asses the robustness of the splitting and Runge-Kutta approach when performing multidimensional simulations. Finally, for the other two tests, in order to compare the numerical solutions with the laboratory experiments, a single numerical method is chosen.

### 5.1 AIR-WATER EXPLOSION PROBLEM 2D

This test is an extension to the bidimensional case of the monodimensional Air-Water Shock problem presented in Section 4.4. Here, we consider a closed box  $[-1, 1] \times [-1, 1] \text{ m}^2$  in which the center region is filled with water at high pressure and temperature. The water is surrounded by air at lower pressure and temperature. Differently from the monodimensional version of the problem, where we have imposed transmissive boundary conditions, for this test we use reflective boundary conditions. In this way nothing can go outside the domain and therefore we will see the reflections of the shock waves after reaching the walls of the box.

We consider here instantaneous relaxations for the velocities and pressures, which translates in  $\tau^{(p)} = \tau^{(f)} = 0$  (i.e. we are forcing the two phases to have a common pressure and a common velocity). With these assumptions, the relative velocity  $\vec{w} = 0$ , thus the steady state equation (2.16) for the vorticity of relative velocity and the term  $\vec{u} \times \vec{\omega}$  in the relative velocity balance equation in the multidimensional system can be neglected.

The initial data of the test are the following:

$$\begin{cases} \alpha_1 = 1 - \epsilon, P_i = 10^9 \text{ Pa}, u_i = \vec{0} \text{ m/s}, T = 495 \text{ K} & \text{if } \max(|x|, |y|) \leq 0.75 \text{ m} \\ \alpha_1 = \epsilon, P_i = 10^6 \text{ Pa}, u_1 = \vec{0} \text{ m/s}, T = 270 \text{ K} & \text{otherwise} \end{cases},$$

for  $i = 1, 2$  and  $\epsilon = 10^{-7}$ . The indexes 1 and 2 are referred to the parameters of state of water and air, respectively, and the constants for the equations of state are given in Table 5.

Note that if we restrict ourself to a 1D section parallel to the  $x$ -axis with  $x \geq 0$  then we have the same initial condition of the Air-Water Shock problem proposed in Section 4.4.

The finite volume computational grid used for the numerical simulation is composed by  $1000 \times 1000$  cells and the splitting approach in conjunction with the predictor/corrector strategy and the DIRK scheme ARS, both with KT numerical fluxes have been tested. The numerical simulations are performed in parallel using respectively  $6 \times 6$  (for the splitting approach) and  $7 \times 7$  (for the Runge-Kutta approach) cores on the HPC-SM cluster at Istituto Nazionale di Geofisica e Vulcanologia (INGV), section of Pisa, Italy.

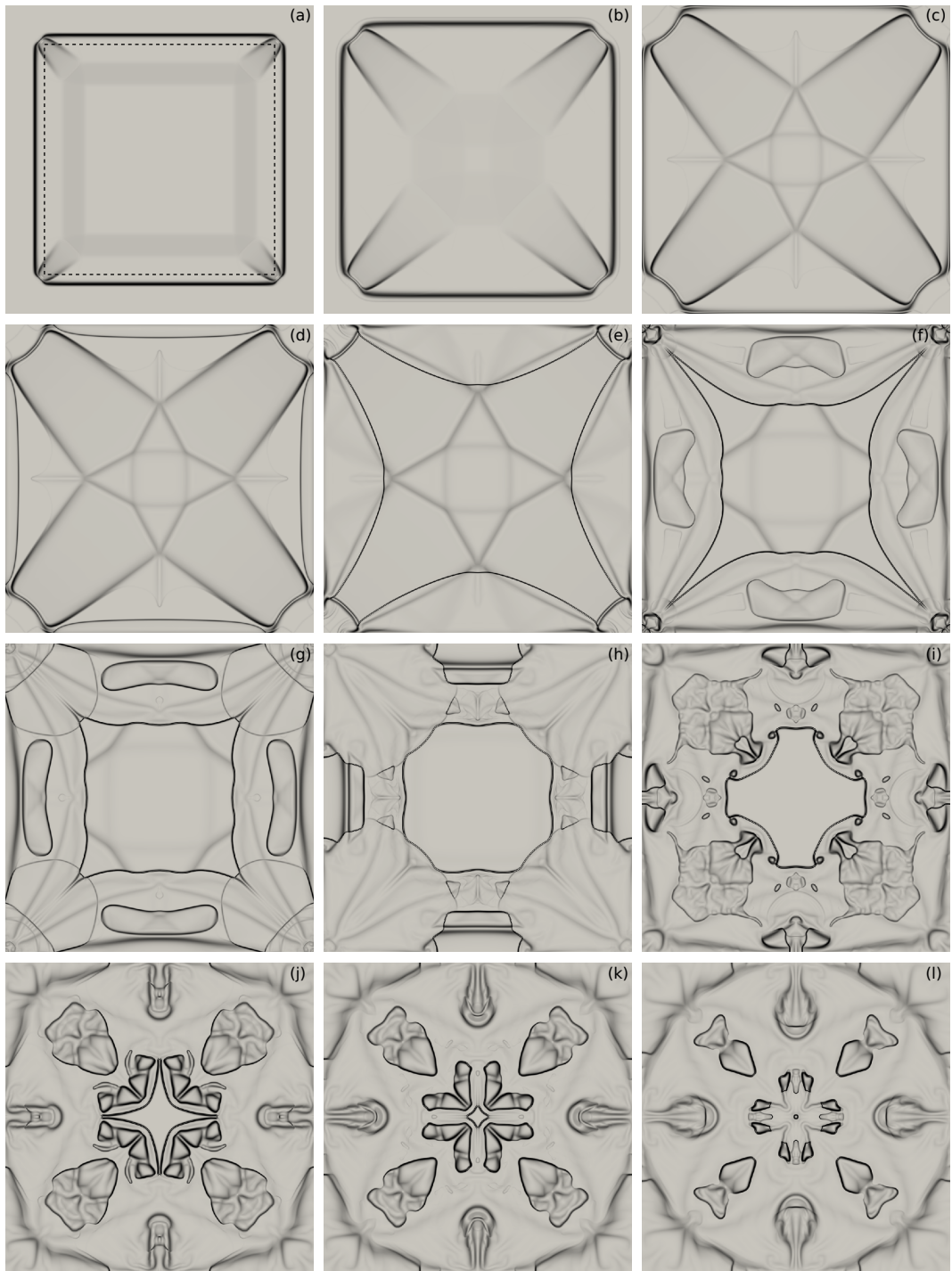


Figure 47: Air-Water Explosion: Emulated Schlieren images generated from the numerical results plotting  $|\nabla\rho|$  in a nonlinear graymap at different times: 0.0001 s (a), 0.00025 s (b), 0.0005 s (c), 0.00055 s (d), 0.0007 s (e), 0.001 s (f), 0.0012 s (g), 0.0015 s (h), 0.0020 s (i), 0.0025 s (j), 0.0027 s (k), 0.003 s (l). The dashed square in (a) is the reminder of the initial separation interface between water and air.

Figs. 47 reports emulated Schlieren images generated from the numerical results, obtained using DIRK scheme ARS. We plot  $|\nabla\rho|$  in a nonlinear graymap at different times: 0.0001 s (a), 0.00025 s (b), 0.0005 s (c), 0.00055 s (d), 0.0007 s (e), 0.001 s (f), 0.0012 s (g), 0.0015 s (h), 0.0020 s (i), 0.0025 s (j), 0.0027 s (k), 0.003 s (l). The dashed square in

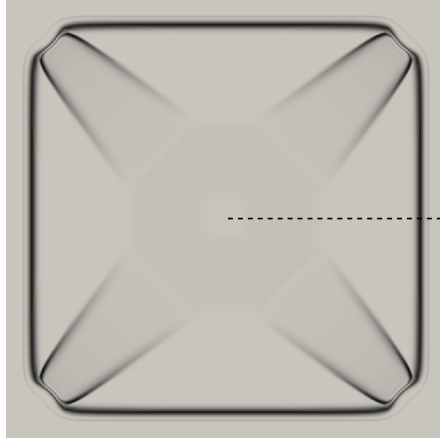


Figure 48: Air-Water Explosion: Emulated Schlieren image generated from the numerical results plotting  $|\nabla\rho|$  in a nonlinear graymap at time  $2.5 \times 10^{-4}$  s. The dashed line represents the domain  $(x, y) \in [0, 1] \times \{0\}$  from which will be extracted the 1D profile that will be compared with the solution of the 1D Air-Water Shock problem.

Fig. 47-(a) is the reminder of the initial separation interface between water and air. The solution obtained with the splitting approach is not presented, since the results are very similar to those obtained with the Runge-Kutta approach.

At the initial stage of the simulation, due to the high pressure of the water, strong shock waves propagate through the surrounding air towards the walls of the box (black square in Fig. 47-(a)). Furthermore, we can see rarefaction waves that propagate towards the center of the box (darker gray square in Fig. 47-(a)). In Fig. 47-(b), we can see that, near the strong shock waves, other weak shock waves, that travel in the same direction of the strong ones, become visible (the darker gray line that surrounds the black square). We can notice that it is the same behavior of the monodimensional version of this test, where we had two shock waves that propagates in one direction and a rarefaction one that travels in the opposite direction. In about 0.0005 s, Fig. 47-(c), the strong shock wave reaches the walls of the box and, due to the reflective boundary conditions, bounces back (Fig. 47-(d)). When the overpressured water, initially confined in the central box, expands radially, the surrounding air starts to compress and, after 0.0010 s, most of air is restricted at the four corners of the box (Figs. 47-(e),(f)). Then, the pressure of air in the four corners becomes a very high and four shock waves are generated propagating towards to center of the box(Figs. 47-(g),(h)). Finally, in Figs. 47-(i),(j),(k),(l) we can see the complex structure of the shock waves caused by different reflections with the walls of the box and interactions with pre-existent shock waves.

As said previously, this test is an extension of the monodimensional test Air-Water Shock problem presented before. The emulated Schlieren image reported in Fig. 47-(b) shows that the solution at the time  $2.5 \times 10^{-4}$  s has the same behavior of the results computed for the monodimensional test. Furthermore we can see that, at that time, the front of the shocks in the  $x$ -axis remains orthogonal to the direction of propagation. Thus, extracting from the two-dimensional domain the results at  $\{(x, y) \in [0, 1] \times \{0\}\}$  (dashed line in Fig. 48), we expect to see, at least until to the shock waves reach the boundaries of the domain, the same solution obtained for the Air-Water Shock problem. Due to the different boundary conditions used for the two tests, the solutions will have different behavior once the shock waves reach the boundary of the computational domain.

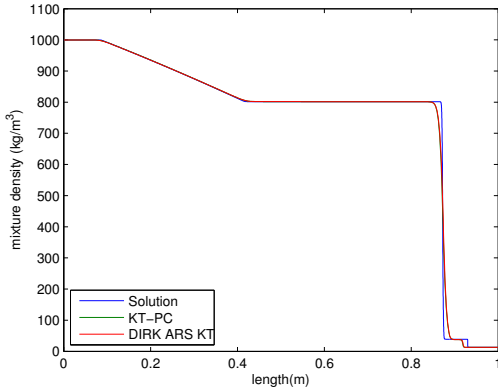


Figure 49: Air-Water Explosion: Comparison between the reference solution for the mixture density obtained from the monodimensional test Air-Water Shock problem (blue line) and those obtained from this test considering a grid of  $2000 \times 2000$  cells and extracting the data in the domain  $(x, y) \in [0, 1] \times \{0\}$ . The solutions are taken at time  $2.5 \times 10^{-4}$  s. These results are obtained using the splitting approach in conjunction with the KT numerical fluxes and the predictor/corrector strategy (green line) and the DIRK ARS scheme with the KT numerical fluxes (red line).

In order to compare the reference solution obtained for the 1D test in the previous chapter with the 2D solutions, obtained with the splitting and the Runge-Kutta approach respectively, we perform refined tests on a computational grid of  $2000 \times 2000$  cells. Then, a 1D profile defined by  $\{(x, y) \in [0, 1] \times \{0\}\}$  is extracted from the 2D solutions (Fig. 48). We compute the solution again with the splitting approach in conjunction with the predictor/corrector strategy and the DIRK scheme ARS, both with KT numerical fluxes. Furthermore the same partitioning strategy used before is adopted.

Fig. 49 presents the reference solution for the mixture density obtained with 16000 cells for the monodimensional test Air-Water Shock Problem (blue line), and those extracted from the 2D simulations obtained with the splitting approach in conjunction with the KT numerical fluxes and the predictor/corrector strategy (green line) and with the DIRK ARS and KT numerical fluxes (red line). The green line in the figure is not visible since is covered by the red line, that means that the solution with both approach are almost coincident. Furthermore, as expected, the results show the same profile of the reference solution of the monodimensional case.

In order to quantify the difference between the results obtained in this test with those of the monodimensional case, we compute the relative error not respect the reference solution, as reported in Eq. (4.2), but between the solutions computed with the same spatial discretization and the same numerical scheme. Therefore, the solutions of the monodimensional test chosen for the comparison are obtained with the same scheme (respectively KT-PC and DIRK ARS) and with a grid of 1000 cells. The relative error for the splitting approach in conjunction with KT numerical fluxes and the predictor/corrector strategy is  $8.0635e-7$  while that for the DIRK scheme ARS with KT numerical fluxes is  $9.4358e-6$ . Thus, the solutions extracted from the two-dimensional test are almost coincident with the correspondent solutions of the monodimensional case. The minimal difference is related to a lower time step in this simulation with respect the monodimensional case, caused, indeed, by the multidimensional nature of the simulation.

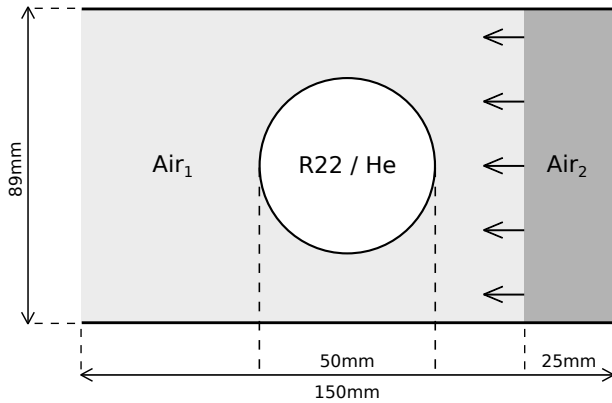


Figure 50: Schematic illustration of the domain and of the initial conditions used for the Shock-Bubble interaction problem.

	$P_0$ (Pa)	$T_0$ (K)	$\gamma$	$C_0$ (m/s)	$c_v$ (J/(kg · K))	$\bar{e}$ (J/kg)	$s_0$ (J/(kg · K))
R22	$10^5$	293	1.249	183.918515	371.211528	0.0	0.0
He	$10^5$	293	1.667	1006.57166	3110.00	0.0	0.0
Air	$10^5$	293	1.4	342.997170	717.609439	0.0	0.0

Table 57: Parameters of the equation of state for R22, He and air used in the Shock-Bubble interaction test.

## 5.2 SHOCK-BUBBLE INTERACTION PROBLEM 2D

As a second 2D test case for the numerical schemes proposed, we consider here the laboratory experiments presented by Haas and Sturtevant (1987), studying the interaction of a planar shock wave in air with a cylindrical volume of a second gas with different density and sound speed. The cylinder of the perturbing gas acts as an acoustic lens of index of refraction  $n = C_1/C_2$ , where  $C_1$  and  $C_2$  are the sound speeds of the two gases. In the laboratory experiments the waveform geometry and the deformation of the gas volume are visualized by shadowgraph photography, clearly showing the effects of refraction, reflection and diffraction of the initial shock wave.

Here, as done for a five-equations model for compressible two-fluid flow presented in Kreeft and Koren (Kreeft and Koren, 2010), we use the experiments done with Refrigerant 22 (R22) gas and Helium (He) as a benchmark for evaluating the accuracy of the computational schemes. R22 is a fluorocarbon ( $CHClF_2$ ) with a higher density and lower ratio of specific heat than air and the cylindrical volume filled with it acts as a strongly convergent lens when crossed by the shock wave. Helium, instead, has a much lower density and a higher ratio of specific heat than air, resulting in a speed of sound higher than air. As a result, the refracted shock runs ahead of the incoming shock.

### 5.2.1 R22 bubble

In this section the numerical simulation for the experiment with the R22 bubble is presented. The simulation is set as follows. We consider a cylindrical bubble of R22 with diameter  $d = 50$  mm located in the center of a tunnel with width 89 mm and length 150 mm, filled with air. We consider, also, a planar left-going shock wave at mach  $M_s = 1.22$

propagating through the air. A schematic illustration of the initial conditions for the numerical test is represented in Fig. 50.

Assuming that phase 1 is R22 while phase 2 is air, the initial conditions used for the simulation are the following:

$$\left\{ \begin{array}{ll} \alpha_1 = 1 - \epsilon, P_i = 10^5 \text{ Pa}, \vec{u}_i = \vec{0} \text{ m/s}, T = 293 \text{ K} & \text{R22 bubble} \\ \alpha_1 = \epsilon, P_i = 10^5 \text{ Pa}, \vec{u}_i = \vec{0} \text{ m/s}, T = 293 \text{ K} & \text{Air}_1 \text{ zone} \\ \alpha_1 = \epsilon, P_i = P_s, \vec{u}_i = \vec{u}_s, T = T_s & \text{Air}_2 \text{ zone} \end{array} \right.$$

for  $i = 1, 2$  and where we set  $\epsilon = 10^{-8}$ ,  $P_s = 157013.888 \text{ Pa}$ ,  $\vec{u}_s = (-114.460253, 0) \text{ m/s}$  and  $T_s = 334.3555 \text{ K}$ . The parameters needed for the equations of state are reported in Table 57.

At the inlet (right) and outlet (left) we impose transmissive boundary conditions, while reflective ones are imposed for the top and bottom walls of the tunnel.

Finally, as done in Kreeft and Koren (2010), a single pressure and velocity are used, that means  $\tau^{(p)} = \tau^{(f)} = 0$ . With these assumptions, the relative velocity  $\vec{w} = 0$ , thus the steady state equation (2.16) for the vorticity of relative velocity and the term  $\vec{u} \times \vec{\omega}$  in the relative velocity balance equation in the multi-dimensional system can be neglected.

For this test case the DIRK scheme ARS in conjunction with the KNP numerical fluxes is used. The grid used for the numerical simulation is formed by  $1200 \times 712$  cells. The numerical simulation has been performed in parallel using 8 threads in a desktop PC which has a quad-core Intel® Core™ i7-3770 Processor (<http://ark.intel.com/products/65523>). The time needed for the computation of the solution was about 37 hours.

In the right panels of Figs.51-52 we present the shadow photographs of the laboratory experiment with R22 and air of Haas and Sturtevant (1987). The shadowgraph technique, as well as Schlieren photography, is a visual process used to photograph the flow of fluids of varying densities, based on the distortions created by the optical inhomogeneities presents in transparent media (Settles, 2001). For this reason, it is well suited to capture the propagation of rarefaction and shock waves in the transparent media. R22 has a higher density and lower ratio of specific heat than air, resulting in an about two times lower speed of sound. The lower speed of sound causes the shock in the bubble, i.e. the refracted shock, to lag behind the incoming shock. Due to the circular shape of the bubble, the refracted shock is curved. For the same reason, the reflected wave, also a shock wave, is curved as well.

In the left panels of Figs.51-52 we emulate Schlieren image generated from the numerical results plotting  $|\nabla \rho|$  in a nonlinear graymap. Note that in the plots of the numerical results a black dashed circle has been added, representing the initial R22-air interface. Fig. 51 (a) shows,  $55\mu\text{s}$  after the time the shock has reached the right side of the bubble, the incident and reflected shock waves outside the cylinder and the convergent refracted shock inside, due to a speed of sound about two times lower than that in air. Density inside the cylinder also increases as the shock moves downstream. In Fig. 51 (b) the incoming shock wave in the air is diffracted into the shadow of cylinder and is connected to the refracted wave inside the R22 cylindrical bubble. In Fig. 51 (c) the two branches of the diffracted waves cross and the refracted shock focuses inside the bubble, resulting in a density peak of more than three times the initial density. In Fig.52, the refracted wave, after having focused in the most left point of the bubble, expands radially outside the cylinder, as shown in (d). High velocity created by the transmitted shock at its focus

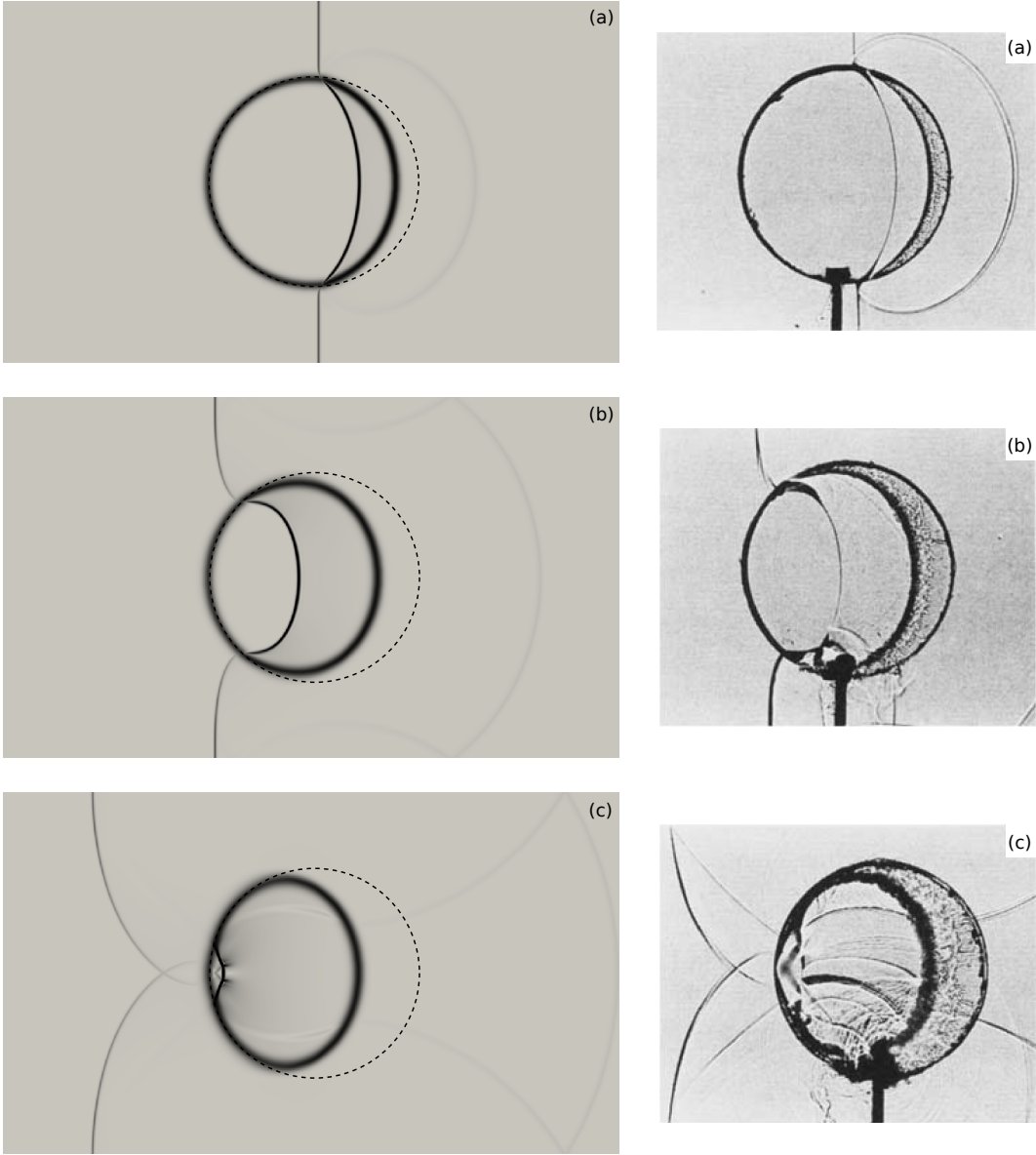


Figure 51: R22 bubble - Part 1: comparison between the numerical results (left panels) and laboratory experiments (right panels). On the left panels Schlieren images generated from the numerical results plotting  $|\nabla\rho|$  in a nonlinear graymap are emulated, while on the right panels the shadowgraph photographies obtained by Haas and Sturtevant in their laboratory experiment (Haas and Sturtevant, 1987) are reported. The results are taken at time:  $t = 55 \mu s$  (a),  $115 \mu s$  (b),  $187 \mu s$  (c) (where  $t=0$  the instant at which the shock reaches the bubble). The dashed circle on the left panels is the remainder of the initial bubble interface.

causes a central wedge to form along the symmetry axis, on the downstream R22-air interface (see Fig.52 (e)). Finally in Fig.52 (f) the waves resulting from the reflection of the transmitted shock from the top and bottom walls of the shock tube in their turn start to pass through the bubble.

The results of the run show a really good agreement between the simulation and the laboratory experiment presented by Haas and Sturtevant (1987). Physically correct solutions are obtained without any tuning or post-processing. The physical model appears to be accurate and the numerical method is robust being able to properly resolve detailed flow features. The two-fluid interface appears to be resolved in accurate posi-

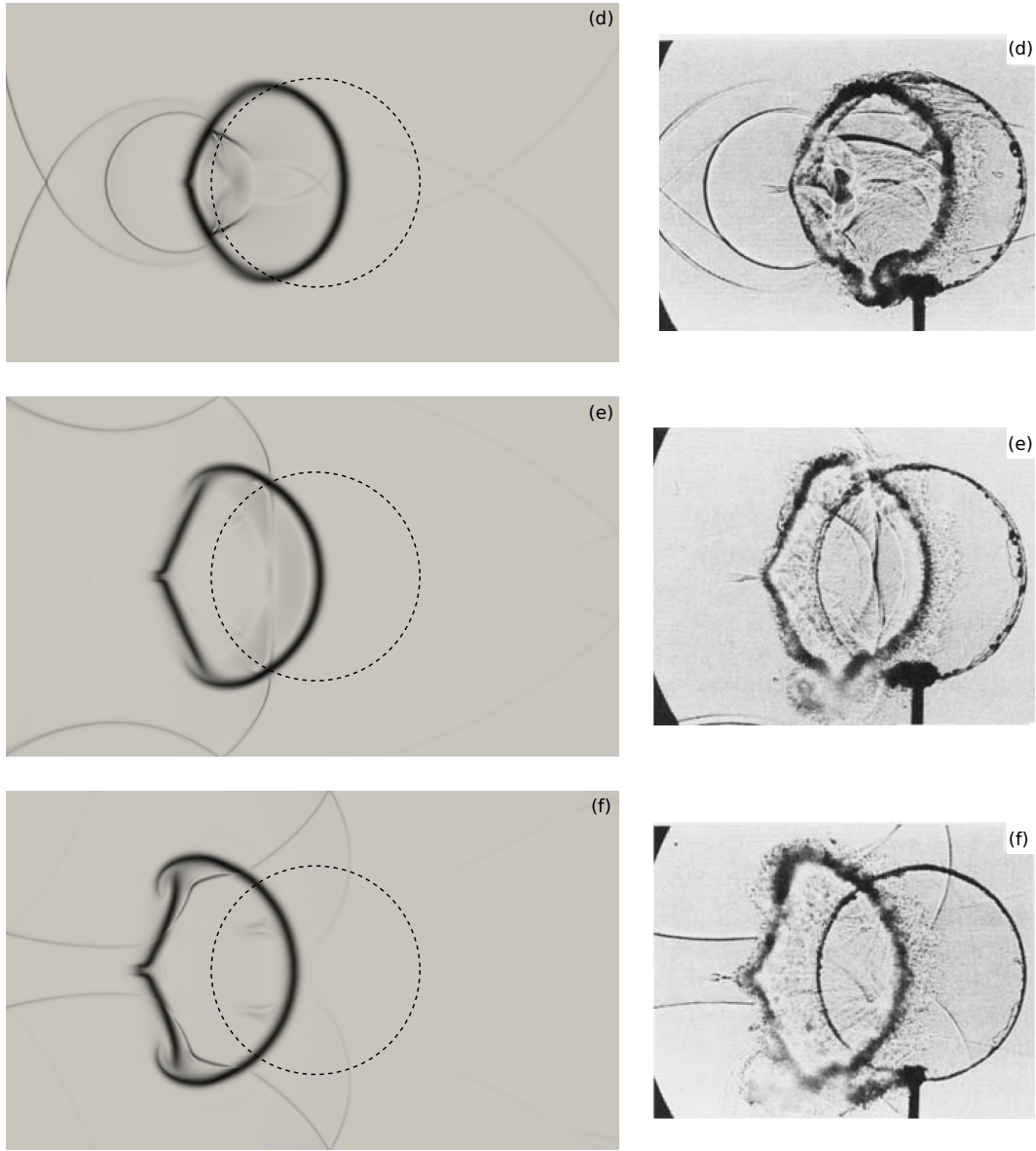


Figure 52: R22 bubble - Part 2: comparison between the numerical results (left panels) and laboratory experiments (right panels). On the left panels Schlieren images generated from the numerical results plotting  $|\nabla \rho|$  in a nonlinear graymap are emulated, while on the right panels the shadowgraph photographies obtained by Haas and Sturtevant in their laboratory experiment (Haas and Sturtevant, 1987) are reported. The results are taken at time:  $247 \mu\text{s}$  (d),  $342 \mu\text{s}$  (e),  $417 \mu\text{s}$  (f) (where  $t=0$  the instant at which the shock reaches the bubble). The dashed circle on the left panels is the remainder of the initial bubble interface.

tion and even rather sharply, despite the use of a mixture model, without any explicit description of the two-fluid flow topology.

### 5.2.2 Helium bubble

As a second shock-bubble interaction test we consider the case of the helium bubble. Haas and Sturtevant, in their experiment with the helium bubble, deduced from the obtained results that the bubble was not filled with pure helium, but it was contaminated significantly by air. In particular they deduced from the velocity of the shock wave inside

the bubble that it was a mixture of helium/air with mass concentration of air of around 0.28.

As in the previous test, we consider a cylindrical bubble of Helium with diameter  $d = 50\text{mm}$  located in the center of a tunnel with width 89 mm and length 150 mm, filled with air. We consider, also, a planar left-going shock wave of mach  $M_s = 1.22$  propagating through the air. In order to recreate the same experiment we slightly modified the initial condition for the numerical simulation:

$$\left\{ \begin{array}{ll} \alpha_1 = 1 - \epsilon_1, P_i = 10^5 \text{ Pa}, \vec{u}_i = \vec{0} \text{ m/s}, T = 293 \text{ K} & \text{He/Air bubble} \\ \alpha_1 = \epsilon, P_i = 10^5 \text{ Pa}, \vec{u}_i = \vec{0} \text{ m/s}, T = 293 \text{ K} & \text{Air}_1 \text{ zone} \\ \alpha_1 = \epsilon, P_i = P_s, \vec{u}_i = \vec{u}_s, T = T_s & \text{Air}_2 \text{ zone} \end{array} \right.$$

for  $i = 1, 2$  and where  $\epsilon, P_s, u_s, T_s$  are the same of the R22 bubble test case while  $\epsilon_1 = 0.051062268$ . With this correction we impose that the bubble is a mixture of helium and air with a mass concentration of air of 0.28. The parameters needed for the equations of state are reported in Table 57.

The boundary conditions and the relaxation parameters used in this case are the same of the R22 bubble test case. The grid used for the numerical simulation is composed by  $1200 \times 712$  cells. Here, differently from the previous test, we use the splitting approach in conjunction with the KT numerical fluxes and the predictor/corrector strategy. As for the previous test, the numerical simulation has been performed in parallel using 8 threads. The time needed for the computation of the solution was about 22 hours.

The right panels of Figs. 53-54 present the shadow photographs of the laboratory experiment with helium and air of Haas and Sturtevant (1987). Helium has a much lower density and a higher ratio of specific heat than air, resulting in a speed of sound higher than air. As a result, the refracted shock runs ahead of the incoming shock. The reflected wave is an expansion wave.

In the left panels of Figs. 53-54 we emulate Schlieren image generated from the numerical results plotting  $|\nabla \rho|$  in a nonlinear graymap. Note that in the plots of the numerical results a black dashed circle has been added, representing the initial He-air interface. Fig. 53 (a) shows,  $32\mu\text{s}$  after the time the shock has reached the right side of the bubble. As before, there is a curved refracted shock which lies inside the bubble, however, since the helium has a higher sound speed than the surrounding air the refracted shock now moves ahead of the incident shock. After  $52\mu\text{s}$ , as we can see from Fig. 53 (b), the difference in sound speeds between the bubble and the surrounding air becomes more apparent. In Fig. 53 (e), after  $72\mu\text{s}$ , the shock wave emerges entirely from the left side of the bubble. At  $102\mu\text{s}$  (Fig 54 (d)), the reflected wave has reflected from the walls of the shock tube. Note that, though the incident shock is still passing over the body, considerable distortion and motion of the helium volume has already occurred: the right-side of the bubble is almost flat, and it has expanded laterally as a consequence of the shock interaction. Finally, as time goes on (Fig 54 (e)-(f) respectively at time 245 and  $427\mu\text{s}$ ), the bubble becomes kidney shaped and spreads laterally in the process.

Comparing the results obtained from the run and the laboratory experiment presented in Haas and Sturtevant (1987) we note that the refracted shock wave which lies inside the bubble is moving faster in the numerical simulation rather than in the experiment. Although this difference, the dynamic represented in Fig. 53-54 by the numerical simulation shows a good agreement with the experiment of Haas and Sturtevant (1987).

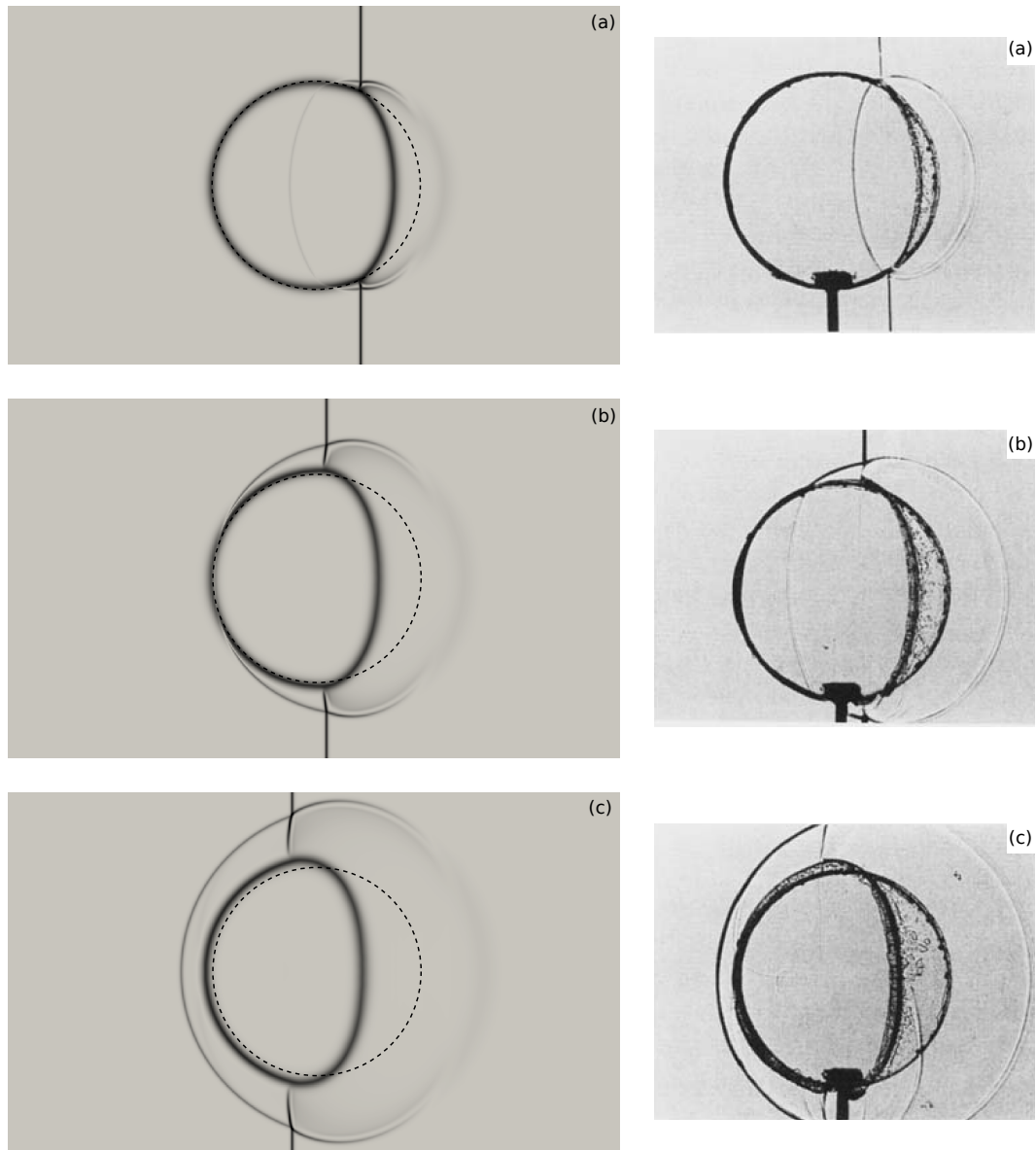


Figure 53: Helium bubble - Part 1: comparison between the numerical results (left panels) and laboratory experiments (right panels). On the left panels Schlieren images generated from the numerical results plotting  $|\nabla\rho|$  in a nonlinear graymap are emulated, while on the right panels the shadowgraph photographies obtained by Haas and Sturtevant in their laboratory experiment (Haas and Sturtevant, 1987) are reported. The results are taken at time:  $t = 32 \mu\text{s}$  (a),  $52 \mu\text{s}$  (b),  $72 \mu\text{s}$  (c) (where  $t=0$  the instant at which the shock reaches the bubble). The dashed circle on the left panels is the remainder of the initial bubble interface.

As for the R22 case, it appears that the physical model and the numerical method accurately resolve in space and time all the flow features (reflection, rarefaction and diffraction of the initial shock wave).

### 5.3 CONCLUSIONS

In this chapter we have presented two two-dimensional problem: the Air-Water Explosion and the Shock-Bubble Interaction problem. The first test is an extension of the monodimensional Air-Water Shock problem illustrated in the Chapter 4. Here we have

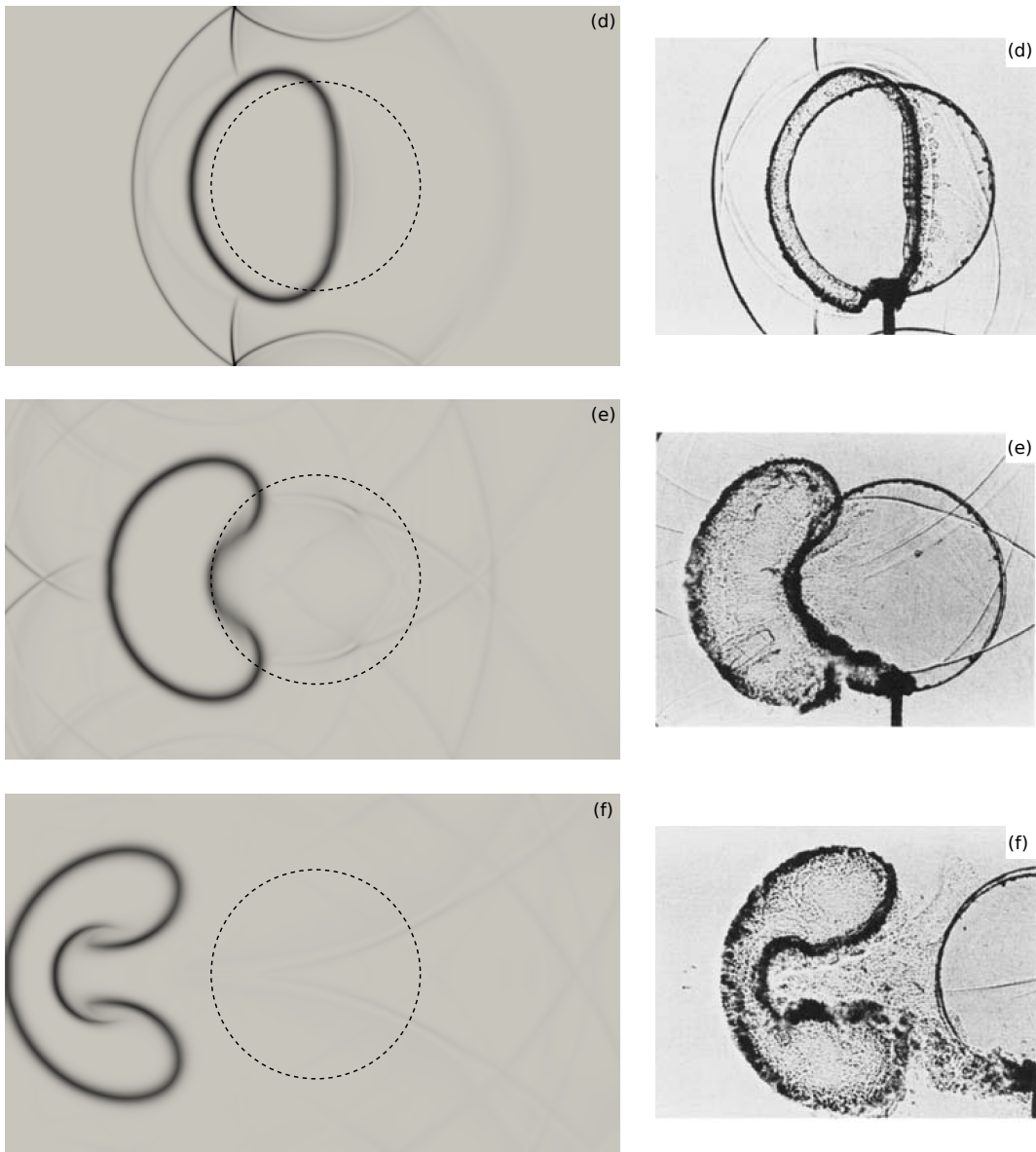


Figure 54: Helium bubble - Part 2: comparison between the numerical results (left panels) and laboratory experiments (right panels). On the left panels Schlieren images generated from the numerical results plotting  $|\nabla\rho|$  in a nonlinear graymap are emulated, while on the right panels the shadowgraph photographies obtained by Haas and Sturtevant in their laboratory experiment (Haas and Sturtevant, 1987) are reported. The results are taken at time:  $102 \mu\text{s}$  (d),  $245 \mu\text{s}$  (e),  $427 \mu\text{s}$  (f) (where  $t=0$  the instant at which the shock reaches the bubble). The dashed circle on the left panels is the remainder of the initial bubble interface.

investigated the robustness of the splitting approach in conjunction with the predictor corrector strategy and of the DIRK ARS scheme in the case of multidimensional problem. The second test, instead, consist of two numerical simulations representing some laboratory experiments performed by Haas and Sturtevant (1987). The numerical results have shown a good agreement with the real observations, demonstrating that the model and the numerical schemes reproduce correctly the laboratory experiments considered.

# 6

---

## VOLCANOLOGICAL APPLICATION

---

In this chapter the model described in Chapter 2 will be extended to the one-dimensional dynamics of explosive volcanic eruptions. Volcanic activity has formed three quarters of the surface rock on Earth, as well as extensive portions of the surface of Mars and the moon. Volcanoes erupt, exhibiting a wide range of eruption styles, when magma, a multiphase multicomponent mixture of liquid molten rock, volatile phases, solid crystals and clasts, migrates and escapes at the surface. Relatively slow effusive eruptions generate lava flows (low viscosity magma) and lava domes (high viscosity magma) and tend to evolve over days to decades. Alternatively, explosive eruptions can inject very large volumes of fragmented magma and volcanic gases high into the atmosphere over shorter periods (minutes to weeks to months). Although controls on eruption characteristics (style and scale) are not well-constrained, previous research suggests that the fluid mechanics governing magma ascent in the shallow subsurface (< 10 km depth) may in part control the transition from effusive to explosive eruption and variations in explosion scale (Jaupart and Allègre, 1991; Mason et al., 2006; Melnik and Sparks, 2002b, 2005; Woods and Koyaguchi, 1994).

In this chapter, we focus on conduit processes involved in the initial stages of explosive eruptions. In the context of volcanology the term explosive is used to denote any eruption in which magma is fragmented and ejected from a vent within a stream of gas. As the magma rises through the conduit toward the surface, the confining pressure decreases, causing dissolved volatile species, such as water and carbon dioxide, to exsolve from the melt to form bubbles, thus providing a driving force for the eruption (Pyle and Pyle, 1995; Sparks, 1978; Woods and Cardoso, 1997). It is high strain rates associated with acceleration of the bubbly mixture that ultimately causes the continuous body of liquid to break apart (or fragment) into a mixture of droplets or clots (pyroclasts) suspended in the gas (Alidibirov, 1994; Kueppers et al., 2006; Papale, 1999b; Sparks, 1978; Spieler et al., 2004; Zhang, 1999). Ascent and fragmentation are influenced not only by the nucleation and growth of gas bubbles, but also by magma rheology and brittle deformation. In fact, all processes and magma properties within the conduit interact and are coupled. Ultimately, it is the ability of gas trapped within growing bubbles to expand or to be lost by permeable gas flow from the viscous melt, which determines whether ascending magmas erupt effusively or explosively. If magma contains no dissolved volatiles, its eruptions will be effusive.

As stated previously, in this thesis we are mostly interested in the initial stages of explosive eruptions, in particular the beginning phases of Vulcanian explosions driven by the collapse of a dome overlying the conduit as for the 1997 eruptions at Soufrière Hills Volcano, Montserrat, UK (Druitt and Kokelaar, 2002). Vulcanian eruptions are named

for the 1888–1890 eruptions of Vulcano, Aeolian Islands, Italy (Mercalli, 1907), and are defined as short-lived, discrete explosions resulting from sudden decompression of a volcanic conduit that commonly contains high-pressure, vesiculated (bubbly) magma (Alidibirov, 1994; Druitt et al., 2002; Morrissey and Mastin, 2000; Self et al., 1979; Sparks et al., 1997; Stix et al., 1997; Woods, 1995). Resulting eruptions characteristically last only seconds to minutes and may produce buoyant columns, pyroclastic density currents or both.

The past decade has seen much progress in modeling magma ascent processes during explosive eruptions (Clarke et al., 2002a,b; Dufek and Bergantz, 2005; Koyaguchi and Mitani, 2005; Kozono and Koyaguchi, 2009; Macedonio et al., 2005; Massol and Jaupart, 1999; Massol et al., 2001; Mastin, 2002; Melnik and Sparks, 2002b; Melnik, 2000; Papale, 2001; Proussevitch and Sahagian, 1998; Sahagian, 2005; Woods and Koyaguchi, 1994). In contrast to the modeling of effusive eruptions, where changes in the solutions are more gentle, explosive eruptions require a proper treatment of shock and rarefaction waves to estimate the depth of magma fragmentation. Furthermore, a model for explosive eruptions should be able to properly describe very different regimes: a bubbly flow region where the gas is the dispersed phase with low volume fractions (below the fragmentation level), and a gas-pyroclasts region where the gas is the continuous carrier phase (above the fragmentation level). Furthermore, if the pressure at the top of the magma chamber is higher than the nucleation pressure, homogeneous magma without bubbles enters the conduit.

Due to the potential significance of the complexities described so far in controlling eruptive regime and style, we have decided to base the new conduit model on the theory of the thermodynamically compatible systems, in order to have a single set of equations able to: 1) treat both dilute and dense flow regimes without corresponding simplifications; 2) describe flow above and below the fragmentation level; 3) quantify the interaction between the phases forming the magmatic mixture by using two distinct pressures and velocities; 4) allow for multiple criteria for modeling the fragmentation transition and 5) accounts for disequilibrium degassing. While some of these processes have been separately implemented previously (Dufek and Bergantz, 2005; Melnik and Sparks, 2002b, 2005), the model presented in this thesis, and the corresponding code, are the first to combine them all.

The chapter is organized as follows: the first section presents the conduit model derived from the single temperature model as described in Chapter 2, and show that the new system of partial differential equations satisfies the hyperbolicity condition. Then we report the constitutive equations needed to close the system of partial differential equations. Finally an application of the model to explosive volcanic eruptions is illustrated.

## 6.1 CONDUIT MODEL

In this section we present the new model for magma ascent in a volcanic conduit, as an extension of the single temperature model. First of all, we briefly describe the eruptive mechanism and the physical processes we are interested in reproducing. In particular, in this thesis, we will focus on the initial stage of Vulcanian eruptions following the collapse of a lava dome. As the overlying dome collapses, the pressure at the top of the conduit decrease rapidly. Conditions soon thereafter exceed a critical condition

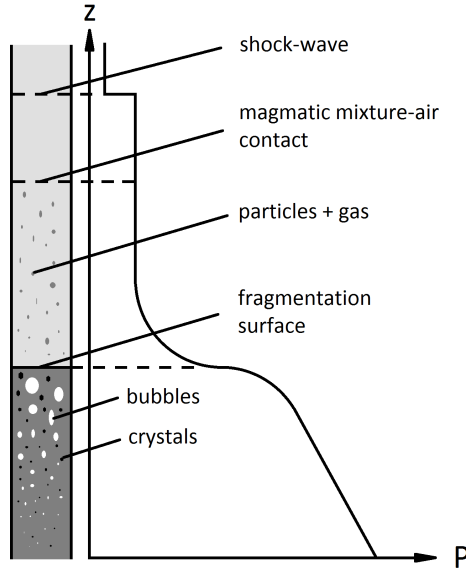


Figure 55: Schematic illustration of the conduit in the first stages of an eruption.

and explosive activity begins. A rarefaction wave propagates down in the conduit into vesiculated magma. As the rarefaction wave passes, the mixture accelerates and fragmentation occurs when a critical condition is reached, to be discussed below in detail. Fragmented magma forms a gas-particle dispersion, which accelerates upward to the conduit exit to form a volcanic columns in the atmosphere. Fig. 55 shows schematically the processes which occur in the conduit. For a more detailed description of the mechanism and the dynamics of vulcanian eruptions, the reader can refer to Clarke (2013).

This system has been treated in the past as a shock-tube (Chojnicki et al., 2006; Ishihara, 1985) to calculate the velocity of the expanding mixture according to equations of a shock-driven flow (Saad, 1985). Here we want to model the conduit processes described above using a modification of the single temperature model proposed in Romenski et al. (2010) and presented in detail in Chapter 2.

With respect to the original system of equations (2.19)–(2.24), for this application:

- a new transport equation for the dissolved gas is added,
- terms accounting for viscous effects are included,
- proper relaxation rates are considered.

As done for the single temperature model, the flow of the magmatic multi-phase multi-component mixture along the  $z$ -axis is treated as a continuum and the state of the two phases, denoted by the index  $i = 1, 2$ , is characterized by its volume fraction  $\alpha_i$ , mass density  $\rho_i$ , velocity  $u_i$ , and specific entropy  $s_i$ . Below the fragmentation level the first phase represents the mixture of melt, crystals and dissolved gas (carrier phase), while the second phase represents the bubbles of exsolved gases (dispersed phase). Above the fragmentation level the first phase represents the dispersed fragments of magma with dissolved gases, while the second phase is the mixture of exsolved gases (carrier phase). Thus, for the volume fractions, the saturation constraint holds:

$$\alpha_1 + \alpha_2 = 1. \quad (6.1)$$

Given that the second phase always refers to the exsolved gas phase, we will use without ambiguity the subscript  $g$  to refer to this phase, the subscript  $d$  to refer to the dissolved gas phase, and the subscript  $m$  to refer to melt (liquid+dissolved gas).

As is generally done for volcanic conduit models, eg de' Michieli Vitturi et al. (2010a, 2008); Melnik and Sparks (2002a,b), we assume here that the dissolved gas content does not affect the density and the equation of state of the melt.

The equations of state described in Section 2.3, obtained from a linearized form of the Mie-Grüneisen equations (Le Métayer et al., 2004, 2005; Menikoff and Plohr, 1989; Romenski et al., 2010), are reported here:

$$e_i(\rho_i, T) = \bar{e}_i + c_{v,i}T + \frac{\rho_{0,i}C_{0,i}^2 - \gamma_i P_{0,i}}{\gamma_i \rho_i}, \quad (6.2)$$

$$P_i(\rho_i, T) = c_{v,i}(\gamma_i - 1)\rho_i T - \frac{\rho_{0,i}C_{0,i}^2 - \gamma_i P_{0,i}}{\gamma_i}, \quad (6.3)$$

$$s_i(\rho_i, T) = s_0 + c_{v,i} \ln \left[ \frac{T}{T_{0,i}} \left( \frac{\rho_{0,i}}{\rho_i} \right)^{\gamma_i-1} \right]. \quad (6.4)$$

Given our interest in the multi-phase characteristics of the phenomenon, we assume here that the pressure and the velocity of the first phase can be different from those of the exsolved gas phase. For the temperatures, instead, a condition of equilibrium between the phases is assumed ( $T_1 = T_2$ ).

Finally, the parameters of state for the mixture are introduced:

$$\rho = \sum_{i=1}^2 \alpha_i \rho_i, \quad u = \sum_{i=1}^2 x_i u_i, \quad (6.5)$$

where  $\rho$  is the mixture density,  $u$  is the mixture velocity and  $c_i$  are the mass fractions of the carrier and dispersed phase.

Using the notations reported in Eq. (2.7) and following Romenski et al. (2010, 2007), we write the one-dimensional system of conservation equations derived from the theory of thermodynamically compatible systems, where dissipative non-equilibrium processes, such as pressure relaxation, inter-facial friction and gas exsolution, and volumetric force terms, such as gravity and viscosity, are included as source terms:

$$\frac{\partial \rho}{\partial t} + \frac{\partial \rho u}{\partial z} = 0, \quad (6.6)$$

$$\frac{\partial \rho \alpha_1}{\partial t} + \frac{\partial \rho u \alpha_1}{\partial z} = -\frac{1}{\tau^{(p)}} (P_2 - P_1), \quad (6.7)$$

$$\frac{\partial \alpha_1 \rho_1}{\partial t} + \frac{\partial \alpha_1 \rho_1 u_1}{\partial z} = -\frac{1}{\tau^{(d)}} (1 - \phi_f) (x_d - x_d^{eq}) \alpha_1 \rho_1, \quad (6.8)$$

$$\begin{aligned} \frac{\partial \rho u}{\partial t} + \frac{\partial (\alpha_1 \rho_1 u_1^2 + \alpha_2 \rho_2 u_2^2 + \alpha_1 P_1 + \alpha_2 P_2)}{\partial z} &= \\ &= -\rho g - (1 - \phi_f) \frac{8\mu_1 u_1}{R^2} - \phi_f \frac{8\mu_2 u_2}{R^2} \end{aligned}, \quad (6.9)$$

$$\frac{\partial w}{\partial t} + \frac{\partial}{\partial z} \left( \frac{u_1^2}{2} - \frac{u_2^2}{2} + e_1 + \frac{P_1}{\rho_1} - e_2 - \frac{P_2}{\rho_2} - (s_1 - s_2)T \right) = , \quad (6.10)$$

$$= -\frac{1}{\tau^{(f)}} \frac{c_1 c_2 w}{\rho} - (1 - \phi_f) \frac{8\mu_1 u_1}{\alpha_1 \rho_1 R^2} + \phi_f \frac{8\mu_2 u_2}{\alpha_2 \rho_2 R^2}$$

$$\frac{\partial}{\partial t} \left[ \rho \left( E + \frac{u^2}{2} \right) \right] + \frac{\partial}{\partial x} \left[ \alpha_1 \rho_1 u_1 \left( e_1 + \frac{p_1}{\rho_1} + \frac{u_1^2}{2} \right) + \alpha_2 \rho_2 u_2 \left( e_2 + \frac{p_2}{\rho_2} + \frac{u_2^2}{2} \right) - \rho c_1 c_2 w (s_1 - s_2) T \right] = -\rho g u - (1 - \phi_f) \frac{8\mu_1 u_1^2}{R^2} - \phi_f \frac{8\mu_2 u_2^2}{R^2} , \quad (6.11)$$

$$\frac{\partial}{\partial t} (\alpha_1 \rho_1 x_d) + \frac{\partial}{\partial x} (\alpha_1 \rho_1 x_d u_1) = -\frac{1}{\tau^{(d)}} (1 - \phi_f) (x_d - x_d^{eq}) \alpha_1 \rho_1 . \quad (6.12)$$

The equations of this system are the conservation laws of total mass, first phase volume fraction, first phase mass fraction, total momentum, relative velocity, total energy and dissolved gas mass fraction. The fragmentation efficiency  $\phi_f \in [0, 1]$  is a variable that allows us to consider the transition from the magma/bubble region ( $\phi_f = 0$ ) to the gas/particle zone ( $\phi_f = 1$ ). The viscosity terms included in the momentum, relative velocity and mixture energy equations are derived from the Poiseuille's approximation for 1D laminar flow.

In the last equation we use the notation  $x_d$  for the mass fraction of the dissolved gas in the first phase and  $x_d^{eq}$  for the equilibrium mass fraction.

The parameter  $\tau^{(p)}$  is the pressure relaxation rate,  $\tau^{(f)}$  is the velocity relaxation rate and  $\tau^{(d)}$  is the rate of exsolution of the dissolved gas. In the equation for momentum conservation  $g$  is the absolute value of the gravitational acceleration,  $\mu_1$  is the magma viscosity, which is a function of the melt viscosity and the crystal content,  $\mu_2$  is the gas viscosity, and  $R$  is the conduit radius, here assumed to be constant. In this model we assume that the crystal content is constant and it affects only the viscosity of the magma.

For effusive eruptions and explosive eruptions below the fragmentation level the main term of the viscous forces is given by the magma viscosity term ( $\phi_f = 0$ ), while for explosive eruptions above the fragmentation level the viscous forces depend only on the gas phase ( $\phi_f = 1$ ).

The model introduced is a modification of the single temperature model presented in Chapter 2, in which we have added a balance equation for the mass fraction of dissolved gas and altered some source terms. From a mathematical point of view, the addition of the balance law for the mass fraction of dissolved gas does not significantly change the characteristic polynomial. In fact, from the characteristic analysis, presented in the next session, it is shown that the eigenvalues of the conduit model (6.6)–(6.12) are the same as in the single temperature model described by Eqs. (2.19)–(2.24), with the addition of another characteristic speed  $u_1$ .

For the conduit model, as we have done for the single temperature model, it is possible to show that the system of equations admits an additional entropy balance law with the following form:

$$\frac{\partial \rho S}{\partial t} + \frac{\partial \rho u S}{\partial x} = \Pi , \quad (6.13)$$

where the right hand side  $\Pi$  is a positive term representing the entropy production.

### 6.1.1 Characteristic analysis

In this section, following the steps of the single temperature model, we study the hyperbolicity of the new model. The one-dimensional conservation form of the model can be summarized as

$$\frac{\partial \mathbf{Q}}{\partial t} + \frac{\partial \mathbf{F}(\mathbf{Q})}{\partial z} = \mathbf{S}(\mathbf{Q}), \quad (6.14)$$

where

$$\mathbf{Q} = \begin{pmatrix} \rho \\ \alpha_1 \rho \\ \alpha_1 \rho_1 \\ \rho u \\ w \\ \rho \left( E + \frac{u^2}{2} \right) \\ \alpha_1 \rho_1 x_d \end{pmatrix}, \quad (6.15)$$

$$\mathbf{F}(\mathbf{Q}) = \begin{pmatrix} \rho u \\ \alpha_1 \rho u \\ \alpha_1 \rho_1 u_1 \\ \alpha_1 \rho_1 u_1^2 + \alpha_2 \rho_2 u_2^2 + \alpha_1 P_1 + \alpha_2 P_2 \\ \frac{u_1^2}{2} - \frac{u_2^2}{2} + e_1 + \frac{P_1}{\rho_1} - e_2 - \frac{P_2}{\rho_2} - (s_1 - s_2)T \\ \sum_{i=1,2} \left[ \alpha_i \rho_i u_i \left( e_i + \frac{p_i}{\rho_i} + \frac{u_i^2}{2} \right) \right] - \rho c_1 c_2 w (s_1 - s_2)T \\ \alpha_1 \rho_1 x_d u_1 \end{pmatrix}, \quad (6.16)$$

$$\mathbf{S}(\mathbf{Q}) = \begin{pmatrix} 0 \\ -\frac{1}{\tau^{(p)}} (P_2 - P_1) \\ -\frac{1}{\tau^{(d)}} (1 - \phi_f) (x_d - x_d^{eq}) \alpha_1 \rho_1 \\ -\rho g - (1 - \phi_f) \frac{8\mu_1 u_1}{R^2} - \phi_f \frac{8\mu_2 u_2}{R^2} \\ -\frac{1}{\tau^{(f)}} \frac{c_1 c_2 w}{\rho} - (1 - \phi_f) \frac{8\mu_1 u_1}{\alpha_1 \rho_1 R^2} + \phi_f \frac{8\mu_2 u_2}{\alpha_2 \rho_2 R^2} \\ -\rho g u - (1 - \phi_f) \frac{8\mu_1 u_1^2}{R^2} - \phi_f \frac{8\mu_2 u_2^2}{R^2} \\ -\frac{1}{\tau^{(d)}} (1 - \phi_f) (x_d - x_d^{eq}) \alpha_1 \rho_1 \end{pmatrix}.$$

In order to study the eigenstructure of the equations we introduce another set of primitive variables:

$$\mathbf{W} = (v_1, \dots, v_7)^T = (\alpha_1, S, \rho_1, \rho_2, u_1, u_2, \rho_d^B)^T, \quad (6.17)$$

where  $\rho_d^B$  is the bulk density of the dissolved gas, i.e. the density referenced to the total volume.

As we have done in Section 2.2, we rewrite the system in an equivalent quasilinear form

$$\frac{\partial \mathbf{W}}{\partial t} + J(\mathbf{W}) \frac{\partial \mathbf{W}}{\partial z} = \mathbf{Y}(\mathbf{W}). \quad (6.18)$$

To obtain the matrix  $J(\mathbf{W})$  we must also write the equations of conservation for the primitive variables in quasilinear form. Although the source terms of the conduit model are different from the single temperature model presented in Chapter 2, the flux function in the first six equation is the same. Thus, ignoring the different source terms, the derivation of the quasilinear form for these equations is the same as that presented in Section 2.2. We can derive the quasilinear form of the balance law for the dissolved gas in a straightforward manner. In fact, noting that  $\alpha_1 \rho_1 x_d = \rho_d^B$ , we have

$$\frac{\partial \rho_d^B}{\partial t} + u_1 \frac{\partial \rho_d^B}{\partial z} + \rho_d^B \frac{\partial u_1}{\partial z} = \frac{1}{\tau^{(d)}} (1 - \phi_f) (x_d - x_d^{eq}) \alpha_1 \rho_1. \quad (6.19)$$

In this way, with the choice of the primitive variable (6.17), we have

$$J(\mathbf{W}) = \left[ \begin{array}{c|c} & \begin{matrix} 0 \\ 0 \\ 0 \\ 0 \\ 0 \\ 0 \end{matrix} \\ \hline B(\mathbf{V}) & \begin{matrix} 0 \\ 0 \\ 0 \\ 0 \\ 0 \\ u_1 \end{matrix} \end{array} \right], \quad (6.20)$$

where  $B(\mathbf{V})$  is the matrix reported in Eq. (2.62) and  $\mathbf{V}$  is the vector reported in Eq. (2.44). Therefore, the characteristic polynomial of  $J(\mathbf{W})$  is

$$\pi(\lambda) = (u_1 - \lambda) \det(B(\mathbf{V}) - \lambda I) = (u_1 - \lambda)(u - \lambda)^2 \tilde{\pi}(\lambda), \quad (6.21)$$

where  $\tilde{\pi}(\lambda)$  is the polynomial defined in Eq. (2.71).

As expected, we have formally derived, from the characteristic analysis presented here, that, with the addition of the balance law for the dissolved gas, the eigenvalues of the system (6.6)–(6.12) are the same as those in the model presented in Chapter 2 with the addition of an eigenvalue equal to  $u_1$ .

## 6.2 CONSTITUTIVE EQUATIONS

This section presents the constitutive equations for the conduit model (6.6)–(6.12). In general, solubility, rheology and fragmentation models differ for different eruptions and volcanic systems. Here we focus on constitutive equations appropriate for the physical and chemical properties of andesite melts, as is appropriate for the Soufrière Hills Volcano, Montserrat.

### 6.2.1 Volatiles and solubility

Volatiles play a central role in governing the ascent and eruption of magma. The decrease in pressure associated with magma rise reduces volatiles solubility, leading to bubble nucleation and growth, the latter a consequence of both volatile exsolution and expansion (Sparks, 1978). The dynamics of explosive eruptions are mediated by the initial volatile content of the magma and by the ability of gases to escape from the ascending magma.

The volatile solubility, that governs the exsolution of the gases dissolved in the magma, is primarily controlled by pressure, whereas other factors such as temperature and chemical variations play a minor role. Formulations for volatile solubility can be thermodynamic (Papale, 1999a; Papale et al., 2006) or empirical (Liu et al., 2005; Moore et al., 1998). In either case, calibration is achieved using measurements of dissolved volatile concentrations in quenched melts, equilibrated with a volatile phase of known composition at a fixed pressure and temperature.

In our model, kinetic disequilibrium in gas exsolution is modeled with an equation similar to those that describe the other relaxation processes considered in the single temperature model:

$$\frac{\partial}{\partial t} (\alpha_1 \rho_1 x_d) + \frac{\partial}{\partial x} (\alpha_1 \rho_1 x_d u_1) = -\frac{1}{\tau^{(d)}} (1 - \phi_f) (x_d - x_d^{eq}) \alpha_1 \rho_1.$$

The equilibrium mass concentration (relative to the crystal- and bubble-free magma) of the dissolved gas  $x_d^{eq}$  is defined by means of Henry's law

$$x_d^{eq} = \sigma \sqrt{p_g}, \quad (6.22)$$

where  $\sigma$  is the solubility constant of the gas (for water in silicic melts, for instance,  $\sigma = 4.11 \times 10^{-6} \text{ Pa}^{-\frac{1}{2}}$  (Burnham, 1979)).

The rate of phase transition is assumed to be proportional to the state disequilibrium, measured as the difference between the current mass fraction of the dissolved gas  $x_d$  and the mass fraction at equilibrium  $x_d^{eq}$ .

### 6.2.2 Magma Rheology

During magma ascent, even within a single volcanic eruption, viscosity can vary by several orders of magnitude. Viscosity mostly depends on the degree of polymerization, a function of chemical composition and volatile content (Giordano and Dingwell, 2003). For example, within realistic ranges of compositional variability, eruptive temperature, and volatile content, the viscosity of basaltic melts may vary between about 10 and  $10^3$   $\text{Pa}\cdot\text{s}$ , and silicic melts may vary between about  $10^4$  and  $10^{12}$   $\text{Pa}\cdot\text{s}$ . Changes in viscosity during individual eruptions are especially pronounced at low pressures where most of the water exsolves. In rhyolitic melts, the viscosity is controlled mainly by the temperature and by the water and crystal content (Giordano et al., 2008; Hui and Zhang, 2007; Zhang et al., 2007).

With the assumption of a Newtonian fluid, following de' Michieli Vitturi et al. (2010a), the viscosity of the liquid phase in the explosive regime below the fragmentation level is modeled as:

$$\mu_1 = \mu_{melt} \cdot \theta(\beta), \quad (6.23)$$

where  $\mu_{melt}$  is the viscosity of the bubble-free, crystal-free liquid phase and  $\theta$  is a factor which increases viscosity due to the presence of crystals (Caricchi et al., 2007; Lejeune and Richet, 1995).

We use an empirical relationship to estimate  $\mu_{melt}$  as a function of water concentration and temperature, as in Hess and Dingwell (1996) (based on the Vogel-Fulcher-Tammann equation):

$$\log(\mu_{melt}) = [-3.545 + 0.833 \ln(w_{H_2O})] + \frac{[9601 - 2368 \ln(w_{H_2O})]}{T - [195.7 + 32.25 \ln(w_{H_2O})]}, \quad (6.24)$$

where the viscosity  $\mu_{melt}$  is in  $\text{Pa}\cdot\text{s}$ ,  $w_{H_2O}$  is  $\text{H}_2\text{O}$  concentration in weight percent ( $w = 100 \cdot x_d$ ) and  $T$  is the temperature in Kelvin.

Furthermore, as crystallization proceeds, viscosity increases according to the empirical model described in (Melnik and Sparks, 1999):

$$\log\left(\frac{\theta}{\theta_0}\right) = \arctan(\omega_*(\beta - \beta_*)), \quad (6.25)$$

where  $\theta_0$ ,  $\omega_*$ ,  $\beta_*$  are proper constants. We remind the reader here that in this model we assumed a constant crystal content, i.e.  $\beta$  is constant. Other models for  $\theta_1$  were tested by Dingwell et al. (1993), Lejeune and Richet (1995), and Costa (2005), resulting in similar general trends for the parameter space explored here.

### 6.2.3 Magma fragmentation

Decompression during magma ascent causes volatiles to exsolve and form bubbles containing a supercritical fluid phase. Viscous magmas, such as rhyolite or crystal-rich magmas, do not allow bubbles to ascend buoyantly and may also hinder bubble growth. This condition can lead to significant gas overpressure and brittle magma fragmentation. During fragmentation in vulcanian, subplinian, and plinian eruptions, gas is released explosively into the atmosphere, carrying with it magma fragments known as pyroclasts.

Here we focus on “dry” magma fragmentation, which does not involve any interaction with non-magmatic water. The type and the efficiency of fragmentation process determines pyroclast size and how much magmatic gas is released per unit mass of magma. These values in turn, have implications for the volcanic jet, column and plume that are produced when the gas-pyroclast mixture exits the volcanic vent.

Fragmentation is thought to occur when specific conditions are reached within the conduit. In literature there exist several fragmentation criteria, but the most common are the critical volume fraction, the stress criterion and the strain-rate criterion.

Traditionally, it had been assumed that fragmentation occurs at a critical volume fraction, presumably due to the instability of thin bubble walls (Dufek and Bergantz, 2005; Gardner et al., 1996; Sparks, 1978; Verhoogen, 1951). According to a series of numerical solutions (Sparks, 1978), bubbles should stop growing long before explosive fragmentation, primarily because of increasing melt viscosity. The solutions led to the concept that bubble volume fraction never exceeds 66 – 83%. However, pyroclasts have vesicularities that range from 0 (obsidian) to > 98% (reticulite), implying that a fragmentation criterion governed by a critical volume fraction cannot always be applicable.

The stress criterion, on the other hand, is related to the volatile overpressure. This criterion is based on the view that fragmentation in high viscosity magmas takes place

when volatile overpressure exceeds the tensile strength of the melt and ruptures bubble walls. This concept can be expressed quantitatively as follows (Zhang, 1999):

$$(P_g - P_l) \frac{1 + 2\alpha_g}{2(1 - \alpha_g)} - P_l > \sigma_w, \quad (6.26)$$

where  $\sigma_w$  is the tensile strength of the bubble walls.

Following Mc Birney and Murase (1970) and Spieler et al. (2004), we formulate a simple relationship providing the overpressure fragmentation threshold  $(P_g - P_l)_{fr}$ , which shows a good fit to a broad range of experimental data:

$$(P_g - P_l)_{fr} = \frac{\sigma_w}{\alpha_g}. \quad (6.27)$$

Finally, the strain-rate criterion is based on the observation that silicate melts can fragment if deformation rates exceed the structural relaxation rate of melt. Essentially, under high acceleration or high strain-rate conditions, the magma relaxation or response time may exceed the time over which stresses are applied, causing the magma to behave in a brittle fashion, and leading to fragmentation. This concept can be expressed mathematically via the Maxwell relation (Papale, 1999b)

$$\frac{\partial u_l}{\partial z} = \kappa \frac{1}{\tau^{(m)}} = \kappa \frac{G_\infty}{\mu_1}, \quad (6.28)$$

where  $\kappa$  is an empirical constant generally equal to 0.01 (Gonnermann and Manga, 2003; Papale, 1999b),  $\tau^{(m)} = \mu_1/G_\infty$  is the magma relaxation time and  $G_\infty$  is the elastic modulus of the magma, which ranges from 3 to 30 GPa depending on composition and temperature.

In the proposed model all of the fragmentation criteria can be implemented, but for simplicity we have chosen the critical volume fraction criterion. Thus we assume that the fragmentation of the magma occurs when the volume fraction of the bubbles reaches a limit threshold  $\alpha_{2,f}$ . Following this criterion we define the fragmentation efficiency  $\phi_f$  as:

$$\phi_f = \begin{cases} 0 & \text{if } \alpha_2 < \alpha_{2,f} \\ 1 & \text{otherwise} \end{cases}. \quad (6.29)$$

This definition indicates that if the volume fraction is met, fragmentation is complete and perfectly efficient.

#### 6.2.4 Pressure relaxation

The model involves non-classical interaction terms regarding the pressure relaxation process. The term in Eq. (6.7),  $-\frac{1}{\tau^{(p)}}(P_2 - P_1)$ , represents the expansion of the volume fraction  $\alpha$  in order to reach pressure equilibrium. The physical meaning of this term is very simple. If the various phases are not in pressure equilibrium after the passage of a rarefaction or shock wave, the volume of each phase must vary in order to reach pressure equilibrium. The variable  $\tau^{(p)}$  controls the rate at which this equilibrium is reached. The existence of this variable has been demonstrated theoretically according the second law of thermodynamics and mechanics of irreversible process (Baer and Nunziato, 1986).

It has been shown by Saurel and Abgrall (1999) that these terms are crucial for the computation of pressure waves in two-phase mixtures (as in shock or detonation waves), but also of paramount importance for restoring the pressure interface condition when solving interfaces between compressible pure materials.

For a magmatic mixture rising in the conduit, bubble overpressure develops primarily because of viscous-limited growth of bubbles (Navon and Lyakhovsky, 1998; Prousevitch and Sahagian, 1996; Sparks, 1978). The gas phase expands in response to decreasing ambient magma pressure, while on the other hand, bubble-growth is resisted by surrounding high-viscosity melt, resulting in a trapped high-pressure gas phase.

In the conduit model proposed here, the variable  $\tau^{(p)}$  is assumed to be a function of the volumetric fractions, melt viscosity and mixture density in the magma/bubble region, while it is assumed to be constant in the gas/particle zone, i.e.

$$\tau^{(p)} = \tau_0^{(p)} \left[ (1 - \phi_f) \frac{\mu_1}{\rho \alpha_2 \alpha_1} + 0.001 \phi_f \right], \quad (6.30)$$

where  $\tau_0^{(p)}$  is a suitable constant. This constant, in conjunction with corresponding laboratory or field data, can be used to properly tune the pressure disequilibrium between phases. When  $\tau_0^{(p)}$  tends towards zero we are forcing both pressures to be equal, whereas when  $\tau_0^{(p)}$  tends towards infinity the pressures are completely decoupled.

### 6.2.5 Relative velocity

The efficiency of gas escape during the ascent of silicic magma governs the transition between effusive and explosive eruptions (Gonnermann and Manga, 2007; Woods and Koyaguchi, 1994). If the gas can escape rapidly from the magma, an effusive eruption occurs. On the other hand, when the gas stays trapped within the ascending magma, it provides the potential energy needed to fragment the magma and produce an explosive eruption.

Degruyter et al. (2012) suggest that outgassing during magma ascent can be described by Forchheimer's law (Rust and Cashman, 2004), an extension to Darcy's law, which accounts for the effects of turbulence:

$$\left| \frac{dP}{dz} \right| = \frac{\mu_g}{k_1} U + \frac{\rho_g}{k_2} U^2,$$

where  $z$  is the direction of flow,  $P$  is the pressure,  $U$  is the volume flux,  $\mu_g$  is the viscosity,  $\rho_g$  is the density of the gas phase. The Darcian permeability,  $k_1$ , and the inertial permeability,  $k_2$ , account for the influence of the geometry of the network of bubbles preserved in the juvenile pyroclasts.

In the conservative system proposed in this thesis, the relative velocity between the two phases is modeled through the interphase force defined by the velocity relaxation rate  $\tau^{(f)}$ . Below the fragmentation level (f.l.) we use Forchheimer's law to model the outgassing, while above the fragmentation depth we use the model reported in Yoshida

and Koyaguchi (1999), drag between gas and a population of pyroclasts. With these choices for the outgassing models, the velocity relaxation rate takes the form

$$\tau^{(f)} = \begin{cases} \left[ \frac{1}{\tau_0^{(f)}} \frac{\alpha_1 \alpha_2}{c_1^2 c_2^2} \left( \frac{\mu_2}{k_1} + \frac{\rho_2 |u_1 - u_2|}{k_2} \right) \right]^{-1} & \text{below f.l.} \\ \left[ \frac{1}{\tau_0^{(f)}} \frac{\alpha_1 \alpha_2}{c_1^2 c_2^2} \left( \frac{3C_d}{8r_a} \rho_2 |u_1 - u_2| \right) \right]^{-1} & \text{above f.l.} \end{cases}, \quad (6.31)$$

or in a more compact form

$$\frac{1}{\tau^{(f)}} = \frac{1}{\tau_0^{(f)}} \frac{\alpha_1 \alpha_2}{c_1^2 c_2^2} \left[ (1 - \phi_f) \left( \frac{\mu_2}{k_1} + \frac{\rho_2 |u_1 - u_2|}{k_2} \right) + \phi_f \left( \frac{3C_d}{8r_a} \rho_2 |u_1 - u_2| \right) \right], \quad (6.32)$$

where  $\tau_0^{(f)}$  is a suitable constant and

$$k_1 = \frac{(f_{tb} r_b)^2}{8} (\alpha_2)^m, \quad k_2 = \frac{f_{tb} r_b}{f_0} (\alpha_2)^{(1+3m)/2}. \quad (6.33)$$

Similarly to the pressure disequilibrium term, the constant  $\tau_0^{(f)}$  can be used to properly tune the velocity disequilibrium between phases, using appropriate calibration data. When  $\tau_0^{(f)}$  tends towards zero we are forcing both velocity to be equal, whereas, when  $\tau_0^{(f)}$  tends towards infinity the velocities are completely decoupled.

In Eq. (6.33),  $f_{tb}$  is the throat-bubble size ratio and  $r_b$  is the average bubble size, which, following Gonnermann and Manga (2005), can be determined from the bubble number density and the gas volume fraction according to

$$r_b = \left( \frac{\alpha_2}{\frac{4\pi}{3} N_d \alpha_1} \right)^{1/3}. \quad (6.34)$$

Bounds on the four parameters can be found in the literature:  $N_d = 10^8 - 10^{16} \text{ m}^{-3}$  (Giachetti et al., 2010; Klug and Cashman, 1994; Polacci et al., 2006; Sable et al., 2006);  $f_{tb} = 0.1 - 1$  (Degruyter et al., 2010; Saar and Manga, 1999);  $m = 1 - 10$  (Bernard et al., 2007; Le Pennec et al., 2001; Wright et al., 2009); and Degruyter et al. (2010) estimated  $f_0$  between 10 and 100 for pumices.

### 6.3 NUMERICAL TESTS

In this section the numerical solutions of the conduit model for the initial stages of explosive eruptions are presented. In Chapter 3 we have illustrated two approaches to numerically solve a system of partial differential equations with relaxation terms: the Splitting and the Runge-Kutta approach. Using the Splitting approach we have demonstrated that, under suitable conditions, the integration of the source terms can be done analytically (using the segregated approach and constant relaxation coefficients). However, with the conduit model, these conditions are not satisfied, thus a numerical integration of the source terms is required. Furthermore, due to the stiffness of the

Parameter	Symbol	Value	Information sources
Conduit length	$L$	5 km	Barclay et al. (1998)
Melt water content	$x_{d,0}$	0.05	Barclay et al. (1998)
Crystant content	$\beta$	0.60	Murphy et al. (2000)
Temperature	$T$	1123 K	Barclay et al. (1998)
Conduit radius	$R$	15 m	Devine et al. (1998)
Solubility	$\sigma$	$4.11 \times 10^{-6} \text{ Pa}^{-0.5}$	Burnham (1979)
Bubble number density	$N$	$10^{15}$	Degruyter et al. (2012)
Throat-bubble size ratio	$f_{tb}$	0.10	Degruyter et al. (2012)
Tortuosity factor	$m$	3.5	Degruyter et al. (2012)
Friction coefficient	$f_0$	10	Degruyter et al. (2012)
Ash particle size	$r_a$	0.001 m	Degruyter et al. (2012)
Gas-ash drag coefficient	$C_d$	0.8	Degruyter et al. (2012)
Gas-wall drag coefficient	$\lambda_w$	0.03	Degruyter et al. (2012)
	$\theta_0$	1.6	Melnik and Sparks (1999)
	$\beta_*$	0.62	Melnik and Sparks (1999)
	$\omega_*$	20.6	Melnik and Sparks (1999)
Fragmentation threshold	$\alpha_{2,f}$	0.6	Melnik and Sparks (2002b)

Table 58: Parameters of the conduit model used for the simulated eruption of Soufrière Hills Volcano.

relaxation terms, it is important to provide an implicit and stable numerical integration for the source terms.

The DIRK schemes presented in Section 3.2, based on the Runge-Kutta approach, provide an implicit and stable numerical integration for the source terms, thus all the numerical simulations of the conduit model are obtained using these schemes. For all the simulations presented in this section, the solutions are obtained using the DIRK KNP scheme with a grid of 1300 cells.

### 6.3.1 Explosive Eruptions at Soufrière Hills Volcano

In the numerical simulations that will be shown below, we will try to reproduce the initial stages of an explosive eruption. In particular we have focused the attention on the sub-Plinian eruption of 17 September 1996 and Vulcanian explosions of 3 August 1997 and 21 September 1997 at Soufrière Hills Volcano, Montserrat. These events are well described by Robertson et al. (1998) and Druitt et al. (2002). Vulcanian activity took place as a series of explosions with 13 explosions between 3 and 12 August and 75 explosions between 22 September and 21 October. Each series involved quasi-periodic behaviour, with rise of magma occurring between each explosion. Repeated Vulcanian explosions were short-lived, with the most intense activity occurring over a few tens of seconds (Druitt et al., 2002), followed by periods of strong ash-venting lasting typically 30 minutes to an hour. The explosions involved fountain collapse and generation of ground-hugging pumice-and-ash flows, simultaneously with plume rise. Ballistic clasts (up to 1.2m diameter) were ejected distances up to 1.6 km with observed velocities of  $110 - 140 \text{ ms}^{-1}$  (de' Michieli Vitturi et al., 2010b). Eruption column heights ranged from 3 km to a maximum of 15 km, with inferred peak discharge rates of hundreds to a few

	$P_0$ (Pa)	$\rho_0$ (kg/m <sup>3</sup> )	$C_0$ (m/s)	$\gamma$	$c_v$ (J/(kg K))	$\bar{e}$ (J/kg)	$s_0$ (J/(kg K))
Melt	$10^8$	2500	2000	2.3	1200	0.0	0.0
Gas	99911.43	1	374	1.4	1154.0	0.0	0.0

Table 59: Parameters of the equation of state for melt and gas. The reference density  $\rho_0$  for the melt is corrected due to the presence of the crystals.

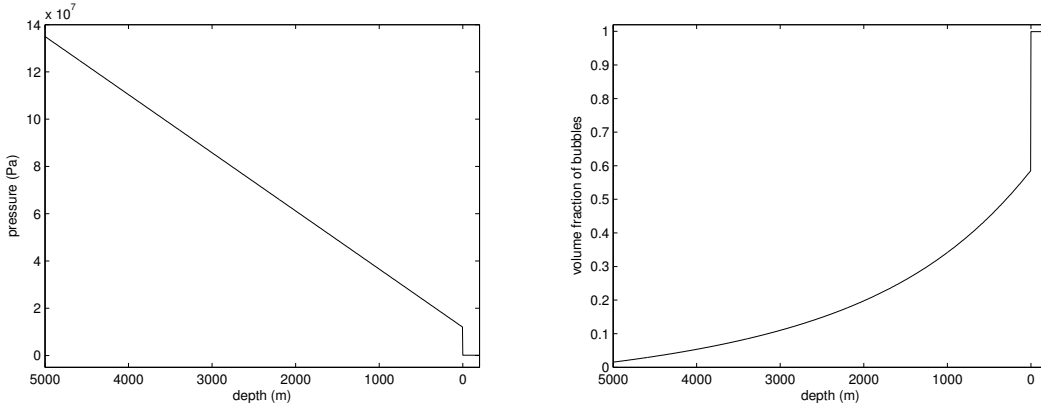


Figure 56: Initial profiles of pressure and bubbles volume fraction for the simulated eruption of Soufrière Hills Volcano.

thousand of cubic meters per second. Druitt et al. (2002) estimated a typical volume of ejecta as  $3 \times 10^5$  m<sup>3</sup> DRE (dense rock equivalent), although volumes of the largest individual explosions may have exceeded 10<sup>6</sup> m<sup>3</sup> DRE. If the conduit has a diameter of 30 m (Melnik and Sparks, 2002a) then typical drawdown depths were 200 – 1000 m.

The initial conditions for the numerical simulations of the conduit processes involved in the Vulcanian eruptions are similar to those used by Melnik and Sparks (2002b). First of all we consider an initial equilibrium between melt and exsolved gas pressures. Furthermore we assume constant temperature and zero velocities along the conduit because of the presence of a plugging dome. The common pressure is defined as a decreasing linear function from the magma chamber to the vent. On the contrary, the exsolved gas volume fraction is posed as a non-linear increasing function from the bottom of the conduit to the surface, remaining, however, under the fragmentation threshold. Therefore, unlike as done in Clarke et al. (2002b), at the beginning of the simulation, the magma is completely unfragmented. We also assume an initial constant crystal content of the melt. The parameters used for the initial condition are reported in Table 58, while the pre-eruptive profiles for pressures and exsolved gas volume fraction are plotted in Fig. 56. Furthermore, the parameters for the equations of state used in these simulations are reported in Table 59.

As done in Melnik and Sparks (2002b), in order to avoid difficulties with boundary conditions at the initial stages of the eruption, we extend the conduit of other 200 m. We assume that this zone, as we can see from Fig. 56, is occupied mainly by the exsolved gas phase at atmospheric pressure, while all the other quantities remain unchanged.

Finally, as boundary conditions, we assume that pressures, temperature and volume fraction of bubbles in the magma chamber (i.e. at the conduit inlet) remain constant

during the simulations and we also fixed the atmospheric pressure at the top of the computational domain for both phases.

#### 6.3.1.1 Instantaneous pressure and velocity relaxations

As a first test, in order to compare the numerical results with those obtained by Melnik and Sparks (2002b), we consider instantaneous relaxation for pressure and velocity ( $\tau_0^{(p)} = \tau_0^{(f)} = 0$ ). More specifically, we want to compare the solutions obtained with the proposed model to the simulations denoted in Melnik and Sparks (2002b) as “no mass transfer” and “equilibrium mass transfer”, i.e. different simulations performed; one without gas exsolution during ascent and one with instantaneous exsolution to the equilibrium value.

In the first run we consider a constant dissolved water content ( $x_d \equiv x_{d,0}$ ) for the whole simulation and exsolution is not taken into account (no mass transfer,  $\tau_0^{(d)} = \infty$ ). This end member case is representative of an eruption where the propagation of the fragmentation front is too fast for any further diffusive mass transfer from the melt into pre-existing vesicles, based on the initial conditions described above.

Fig. 57 presents profiles of pressure, volume fraction of bubbles, velocity, fragmentation efficiency, temperature and mixture density at different times. Fig. 58 presents the fragmentation level (left panel) and the discharge rate (right panel) at the top (blue line) and at the bottom (green line) of the conduit and its maximum value (red line) as function of time.

A rarefaction wave propagates into the conduit, accelerating the mixture and decompressing it. The fragmentation wave, which follows the rarefaction wave, splits the flow domain into two different regions, the bubbly magma and the gas-particle zone. The initial fragmentation wave velocity is 112 m/s, but it decreases to 12 m/s after 25 s. After about 9 minutes of eruption the fragmentation wave stops and then starts to rise gradually with the ascending magma.

The exit velocity at the top of the computational domain (where we fix atmospheric pressure), reaches a maximum value of 275 m/s after 1 s, then decrease rapidly to 185 m/s in 4 s and after that continues to decrease more gently reaching 91 m/s in about 9 minutes. We note that in Robertson et al. (1998) it is estimated that the launch velocity for ballistic clasts is comparable with the exit velocities obtained by our numerical simulation, where we have assumed a perfect coupling between the gas and the particles.

The modeled discharge rate goes from a maximum of  $30 \times 10^6$  kg/s in the first seconds of the eruption to an almost constant value of  $1.4 \times 10^6$  kg/s after 9 minutes. For comparison, with the same fragmentation threshold ( $\alpha_f = 0.6$ ), Melnik and Sparks (2002b) obtained a peak discharge rate of  $\approx 22 \times 10^6$  kg/s after a few seconds and a discharge rate of about  $2 \times 10^6$  kg/s after 9 minutes. Furthermore, we also observe good agreement with the mass flux in the first 30 s of the simulations in Clarke et al. (2002b), although they have a higher peak discharge rate in the very first seconds. On the contrary, the exit velocity reported by Clarke et al. (2002b) is significantly lower with respect to that computed in this test ( $\approx 115$  m/s vs 171 m/s after 30 s of simulated eruption).

Given that, the model proposed here also solves the energy equation (different from the model of Melnik and Sparks (2002b)), thus we are able to track the temperature evolution during the eruption. For this run, we observe, 1000 s after the onset of the

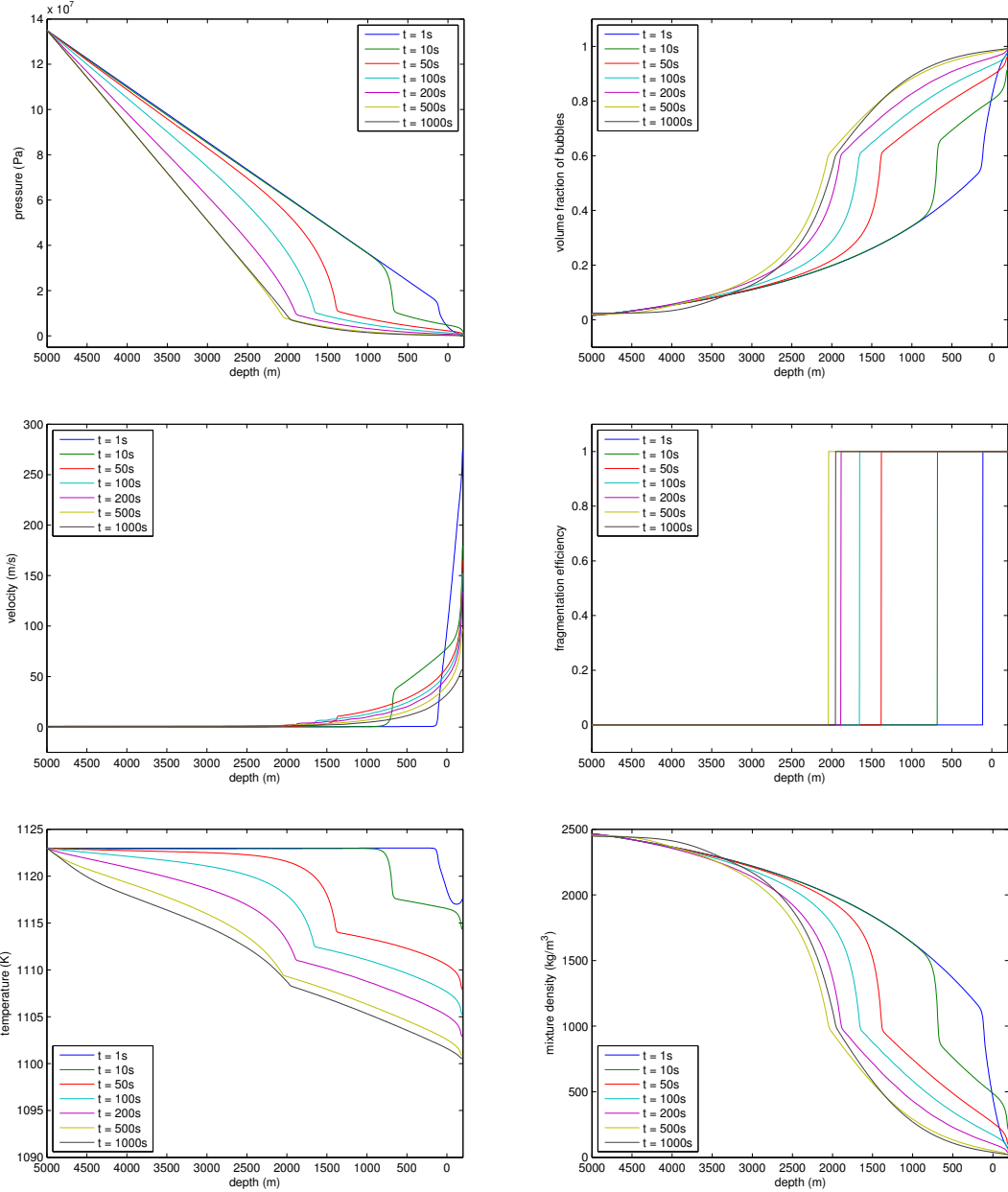


Figure 57: Profiles of pressure, volume fraction of bubbles, velocity, fragmentation efficiency, temperature and mixture density at different times assuming a single pressure and velocity and no mass transfer. These solutions are obtained using DIRK KNP scheme with a grid of 1300 cells.

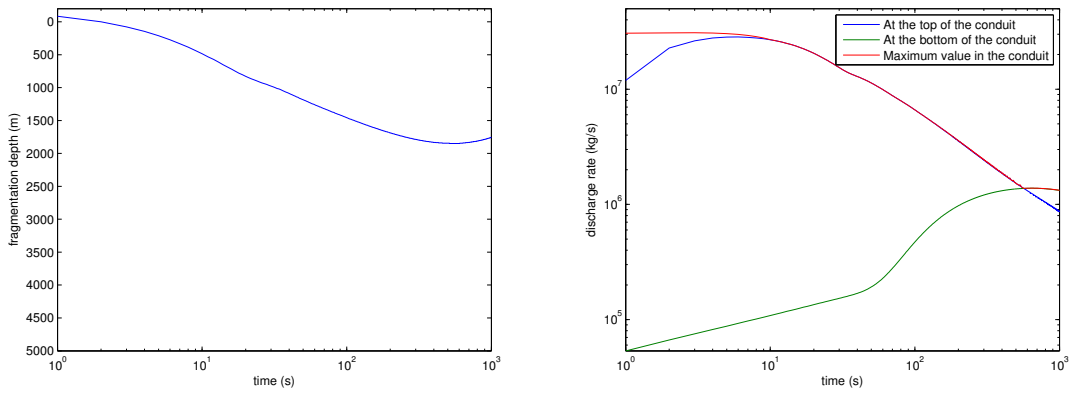


Figure 58: Fragmentation level (left panel) and discharge rate (right panel) at the top (blue line) and at the bottom (green line) of the conduit and its maximum value (red line) as function of time assuming a single pressure and velocity and no mass transfer.

eruption, a decrease in temperature at the top of the conduit of about 20 K and an almost linear increase in temperature with depth along the conduit. Such change in temperature can potentially produce feedback effects, changing the viscosity of the mixture and thus the ascent rate.

As a second test, we present a simulation with the same conditions as the first aside from the assumption of equilibrium mass transfer ( $\tau_0^{(d)} = 0$ ), as opposed to the “no mass transfer” assumption of the first example above. This end member case can be seen as representative of an eruption for which propagation of the fragmentation wave is sufficiently slow that diffusion has time to maintain equilibrium between the melt phase and the free-gas phase. As initial condition for this simulation, we assume an equilibrium profile in mass fraction of dissolved gas ( $x_d = x_d^{eq}(P_g)$ ) instead of a constant value.

Fig. 59 presents profiles of pressure, volume fraction of bubbles, velocity, fragmentation efficiency, temperature and mixture density at different times. Fig. 60 shows the fragmentation level (left panel) and the discharge rate (right panel) at the top (blue line) and at the bottom (green line) of the conduit and its maximum value (red line) as function of time.

As we can see, the general behavior of the solution is similar to that of the previous simulation, except that the fragmentation wave almost reaches the bottom of the conduit. The initial fragmentation wave velocity is lower than for the “no mass transfer” test (92 m/s vs 112 m/s), but after 25 s it is twice as fast and, after about 9 minutes, it continues to travel down in the conduit with a velocity of 0.8 m/s.

The exit velocity at the top of the computational domain, reaches a maximum value of 282 m/s after 1 s, then decrease rapidly to 193 m/s in 10 s and after that we notice, in contrast to the case of no mass transfer, an increase in the velocity, reaching 223 m/s by about 16 minutes into the simulation.

The discharge rate goes from a maximum of  $27 \times 10^6$  kg/s in the first seconds of the eruption to a value of  $5.6 \times 10^6$  kg/s at time 1000 s, similarly to Melnik and Sparks (2002b). Furthermore, as in the previous test, we observe, for the first 30 s of simulated eruption, a good agreement with the discharge rates obtained by Clarke et al. (2002b), but a higher exit velocity.

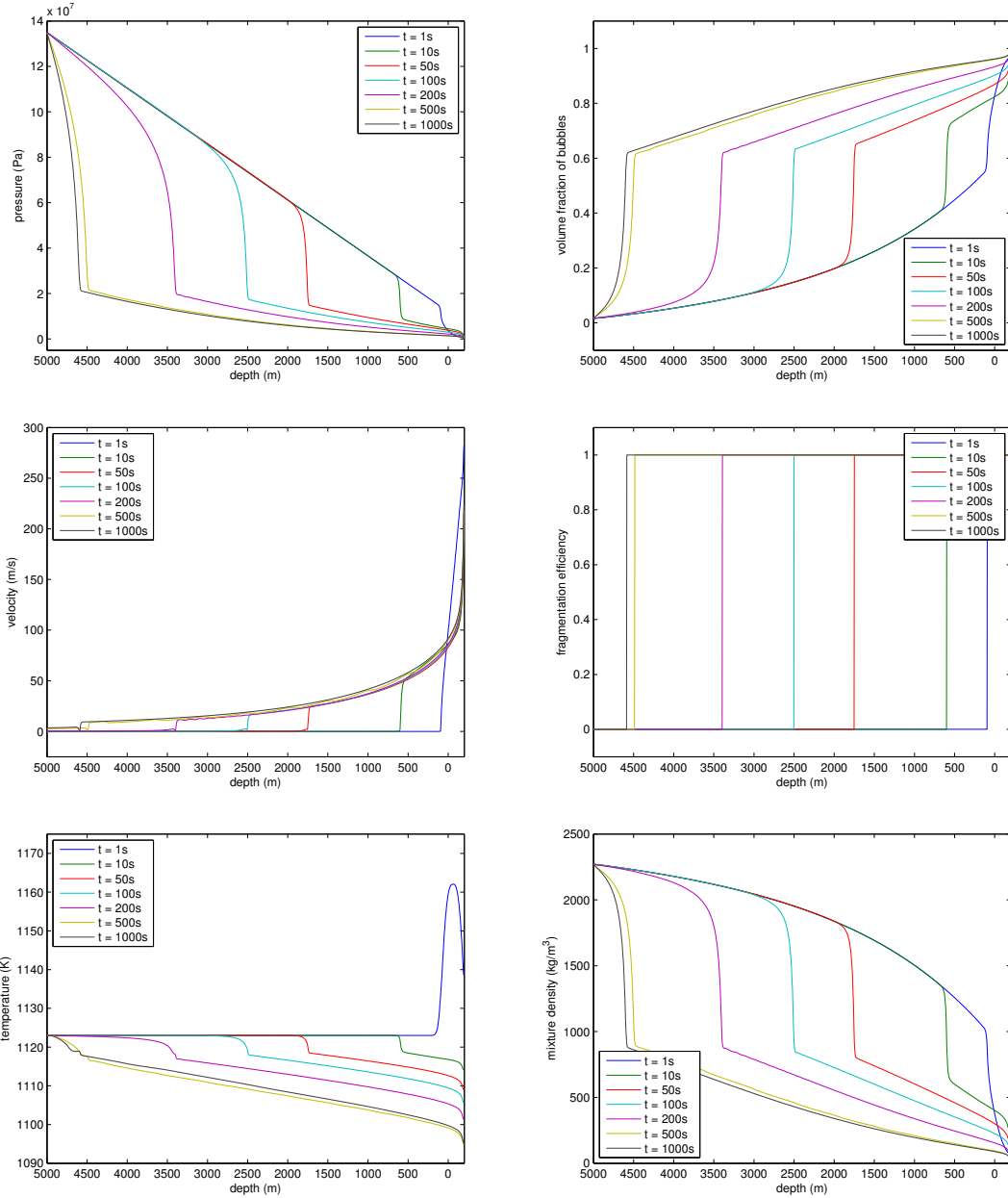


Figure 59: Profiles of pressure, volume fraction of bubbles, velocity, fragmentation efficiency, temperature and mixture density at different times assuming a single pressure and velocity and equilibrium mass transfer. These solutions are obtained using DIRK KNP scheme with a grid of 1300 cells.

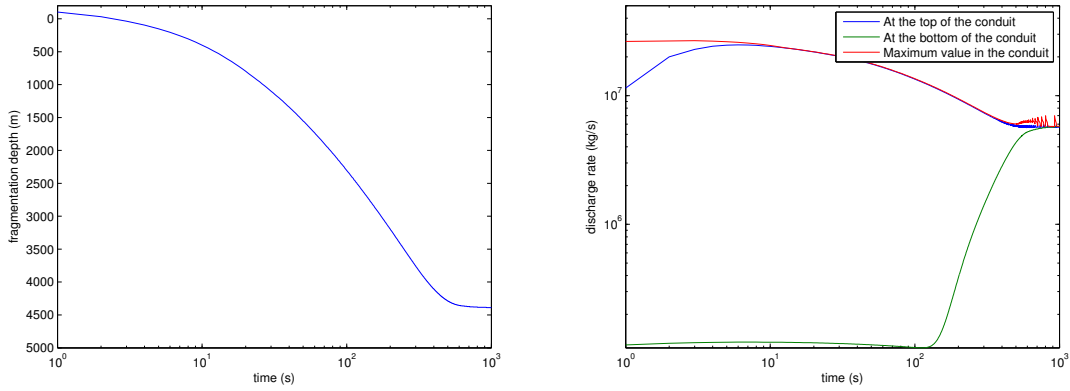


Figure 60: Fragmentation level (left panel) and discharge rate (right panel) at the top (blue line) and at the bottom (green line) of the conduit and its maximum value (red line) as function of time assuming a single pressure and velocity and equilibrium mass transfer.

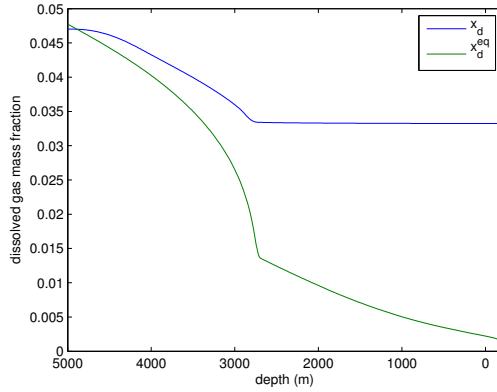


Figure 61: Profiles of dissolved water content  $x_d$  (blue line) and the equilibrium value  $x_d^{eq}$  (green line) at  $t = 1000$  s assuming a single pressure and velocity and a finite rate exsolution. These solutions are obtained using DIRK KNP scheme with a grid of 1300 cells.

From the comparison between these two tests, we can see the significant differences associated with these two different end-member assumptions, particularly in the behavior of the fragmentation wave. The assumption that most closely captures any natural case depends heavily on the viscosity of the magma, which is a function of crystals and dissolved gas content. Assuming equilibrium mass transfer, the dissolved gas content decreases with pressure (Henry's law, Eq. (6.22)), causing an increase in magma viscosity, allowing magma vesicularity to increase during the decompression process, and thus favoring the propagation of the fragmentation wave deeper in the conduit. We also remark that, in principle, the system can vary from no mass transfer to equilibrium mass transfer in both time and space. Immediately below the fragmentation level, the melt velocity is too fast for diffusive mass transfer from the melt into vesicles; conversely, deeper in the conduit, away from the fragmentation front, ascent velocity is low and diffusion has time to maintain equilibrium.

This variation is considered in the next simulation, where a finite rate for the gas exsolution is assumed. In the proposed model, the diffusive gas mass transfer is governed by the relaxation coefficient  $\tau^{(d)}$  that represents the time needed by the system to reach equilibrium for the mass fraction of dissolved gas (note that  $\tau^{(d)}$  is effectively a

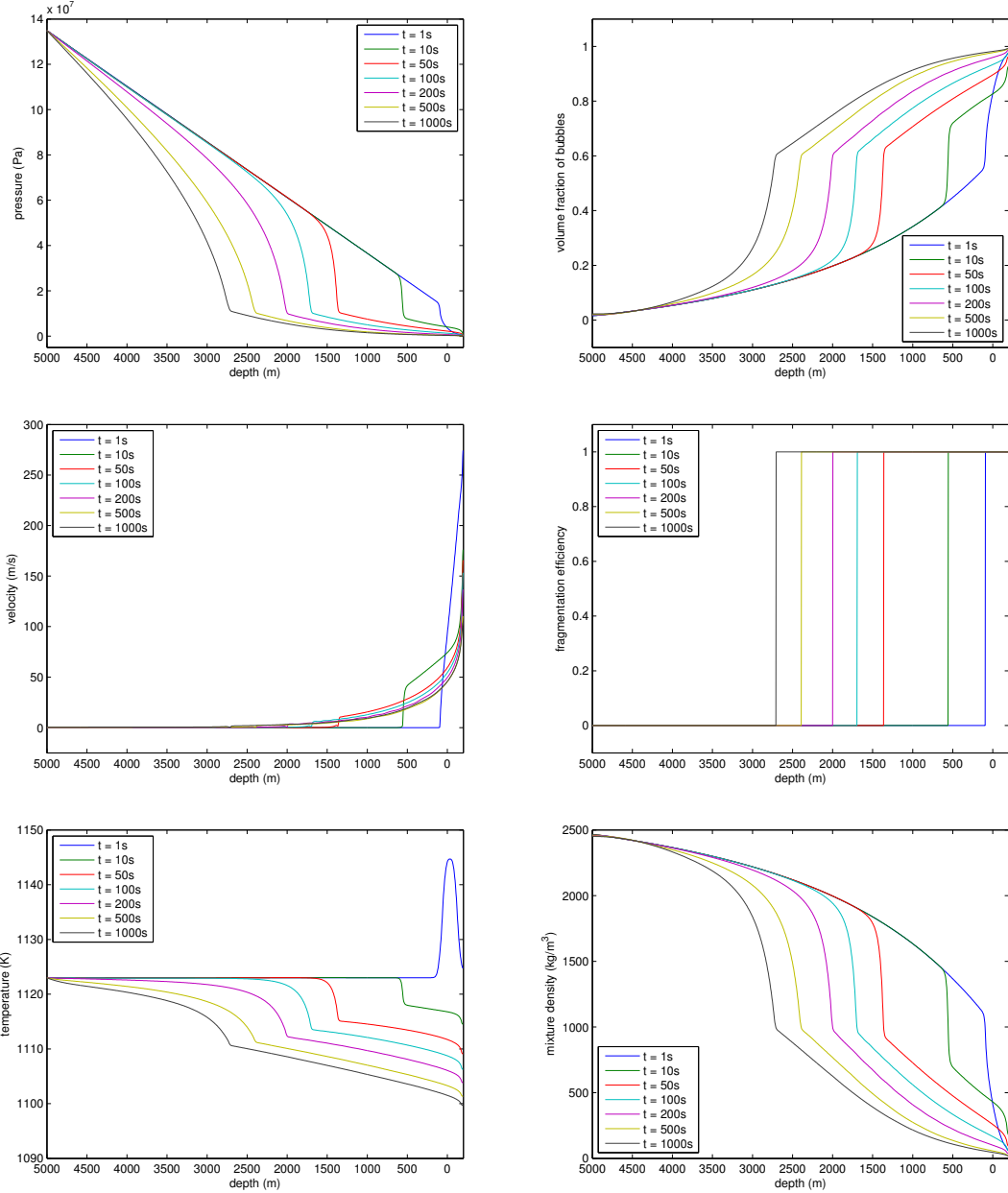


Figure 62: Profiles of pressure, volume fraction of bubbles, velocity, fragmentation efficiency, temperature and mixture density at different times assuming a single pressure and velocity and a disequilibrium mass transfer. These solutions are obtained using DIRK KNP scheme with a grid of 1300 cells.

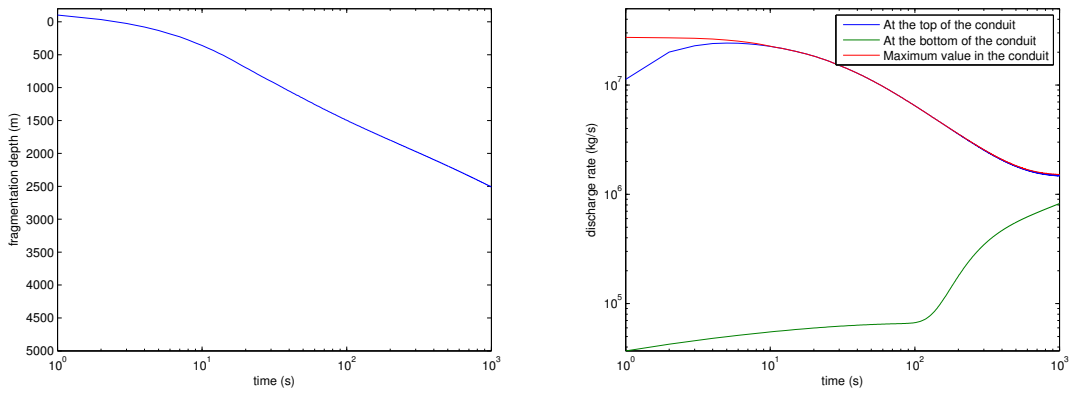


Figure 63: Fragmentation level (left panel) and discharge rate (right panel) at the top (blue line) and at the bottom (green line) of the conduit and its maximum value (red line) as function of time assuming a single pressure and velocity and a disequilibrium mass transfer.

time). We consider here a relaxation time  $\tau^{(d)}$  of the same order of the duration of the simulation, i.e. we set  $\tau^{(d)} = 1000$  s (de' Michieli Vitturi et al., 2013a). Furthermore, as done for the equilibrium case, we assume an initial condition  $x_d = x_d^{eq}$ . The effect of the finite rate exsolution is shown in Fig. 61, where both the dissolved water content  $x_d$  (blue line) and the equilibrium value  $x_d^{eq}$  (green line) are plotted for the solution at  $t = 1000$ s. At the conduit inlet, the blue line is below the green line, indicating an undersaturated magma. Then, shallower in the conduit and below the fragmentation level, the gap between the two line highlights the delay in the diffusive process due to the increasing ascent velocity. Above the fragmentation level, exsolution is not considered and the dissolved water content remains constant.

Fig. 62 show results of the run with finite-rate exsolution at different times, including profiles of pressure, volume fraction of bubbles, velocity, fragmentation efficiency, temperature and mixture density. Fig. 63 shows the fragmentation level (left panel) and the discharge rate (right panel) at the top (blue line) and at the bottom (green line) of the conduit and its maximum value (red line) as function of time.

As expected, the fragmentation wave propagates deeper with respect to the case of no mass transfer, but it is shallower than the case of equilibrium mass transfer. The initial fragmentation wave velocity is 92 m/s, and it decreases to 20 m/s after 25 s and to 0.8 m/s after about 9 minutes. After 1000 s of simulated eruption the fragmentation wave is still moving towards the magma chamber with a velocity of 0.5 m/s. An extended simulation shows that, after 2000 seconds, the fragmentation wave still continues its descent with a lower and lower speed (about 0.2 m/s at the end).

The exit velocity at the top of the computational domain, reaches a maximum value of 274 m/s after 1 s, then decrease rapidly to 175 m/s after 10 s and then continue to decrease reaching the minimum value of 104 m/s after 1000 s.

The discharge rate goes from a maximum of  $27 \times 10^6$  kg/s in the first seconds of the eruption to a minimum of  $1.4 \times 10^6$  kg/s.

In conclusion, from these simulations, we have observed that the effect of the gas exsolution play a key role in the propagation of the fragmentation wave along the volcanic conduit, changing significantly the fragmentation propagation and the maximum fragmentation depth.

### 6.3.1.2 Finite rate pressure and velocity relaxations

As observed with the previous tests, the choice between equilibrium, finite rate or no mass transfer can lead to different solutions. In particular, changing the disequilibrium of the mass transfer we can obtain a fragmentation wave that propagates deeper (moving towards the equilibrium mass transfer) or shallower (moving towards a complete disequilibrium).

In this section we are interested in the effects of other disequilibrium processes on the solution. In particular we want to relax the assumption of common pressure and velocity between phases, considering disequilibrium by setting the relaxation coefficients to  $\tau_0^{(p)} = 1$  and  $\tau_0^{(f)} = 1$ . Furthermore we investigate the solutions obtained for three different situations: no mass transfer, equilibrium mass transfer and finite rate mass transfer.

For the run with no mass transfer, Fig. 64 shows the mixture pressure, the pressure difference between gas and melt phase, the volume fraction of the bubbles, the fragmentation efficiency, the melt and the gas velocity, the temperature and finally the mixture density. The initial mass fraction of dissolved gas is constant along the conduit and equal to  $x_{d,0}$ .

In Fig. 64 we can see the effect of pressure and velocity disequilibrium. Using parameters reported in table 58 for the Darcian and the inertial permeability, the gas and melt remain coupled up to the fragmentation level, and then, in the gas/particle region, the gas phase moves faster with respect to the particles. On the contrary, the decoupling of pressures is evident only in the zone that precedes the fragmentation wave, where the gas pressure reaches an higher value with respect to the melt phase.

Fig. 65 presents the fragmentation level (left panel) and the discharge rate (right panel) at the top (blue line) and at the bottom (green line) of the conduit and its maximum value (red line) as function of time.

In the first 70 s, the fragmentation wave propagates down the conduit, reaching a maximum depth of 1380 m. After 70 s, the fragmentation wave starts to move back up the conduit toward the vent, and we observe a different solution behavior with respect to the case of instantaneous relaxation of pressures and velocities. For example, a local maximum appears in the volume fraction of the bubbles behind the fragmentation wave. Furthermore, with the advance in time, the discharge rate at the top of the domain decrease rapidly, and after 300 seconds of simulation it becomes negative. Thus, once the discharge rate reaches zero, we stop the numerical test.

The initial fragmentation wave velocity is 112 m/s, but it decreases to 12 m/s after 25 s and it stops after about 70 s and begins to move towards the vent of the conduit.

The velocity of the fragmented phase at the end of the computational domain, reaches a maximum value of 280 m/s after 1 s, then decrease rapidly to 173 m/s in 10 s continuing to decrease up to become zero in about 300 s.

Due to the effect of the velocity disequilibrium, the velocity of the gas phase is higher with respect to that of the fragmented phase. In fact, at the end of the computational domain, it reaches a maximum value of 405 m/s after 1 s, then decrease rapidly to 261 m/s in 10 s and reaching 81 m/s after 200 s of simulated eruption.

The discharge rate reaches a maximum value of  $30 \times 10^6$  kg/s in the first seconds of the eruption, similar to the value obtained for the run with instantaneous relaxation of pressure and velocity.

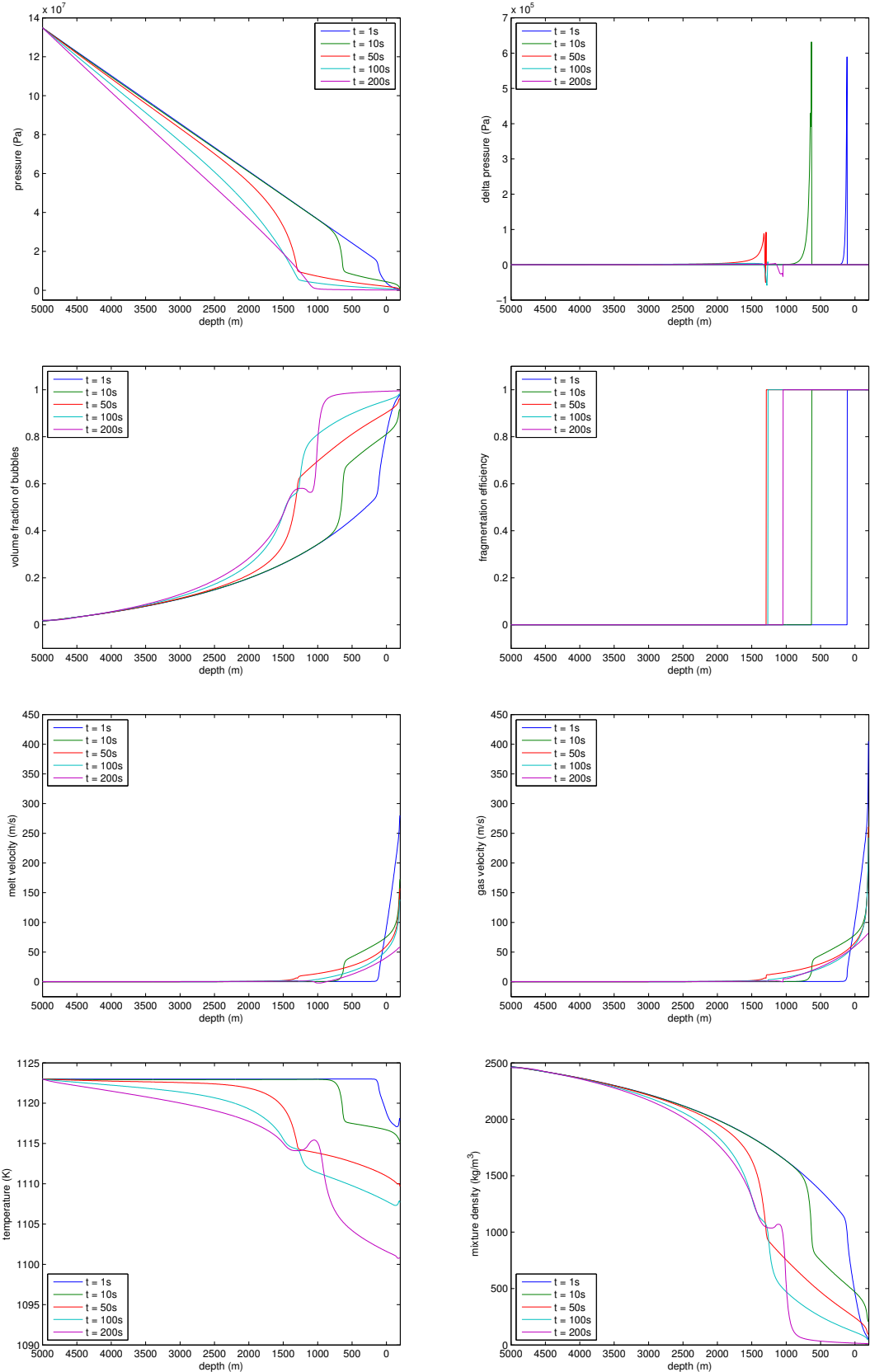


Figure 64: Profiles of mixture pressure, pressure difference between gas and melt phase, volume fraction of the bubbles, fragmentation efficiency, melt and gas velocity, temperature and mixture density at different times (up to 200 s) assuming the disequilibrium of pressures and velocities and no mass transfer. The solutions are obtained using DIRK KNP scheme with a grid of 1300 cells.

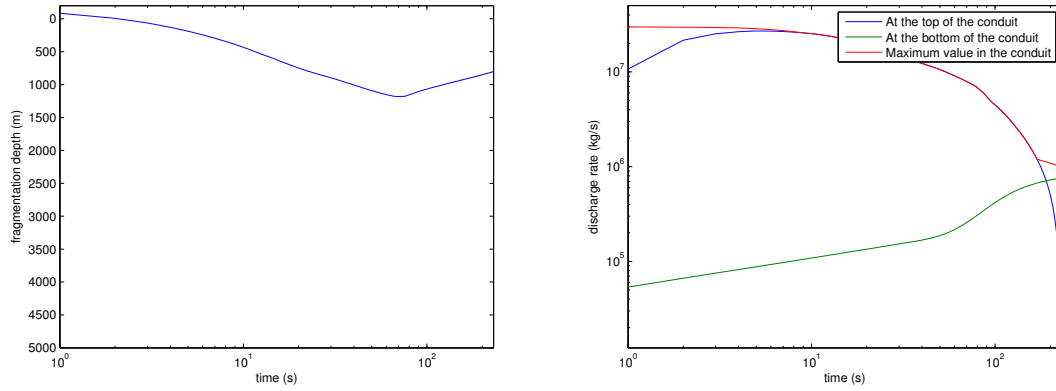


Figure 65: Fragmentation level (left panel) and discharge rate (right panel) at the top (blue line) and at the bottom (green line) of the conduit and its maximum value (red line) as function of time assuming the disequilibrium of pressures and velocities and no mass transfer.

Now, as done with the instantaneous pressure and velocity case, we analyze the solutions assuming equilibrium mass transfer. Furthermore, as initial condition for the mass fraction of the dissolved gas we use the equilibrium values ( $x_d = x_d^{eq}$ ).

Fig. 66 presents profiles of mixture pressure, pressure difference between gas and melt phase, volume fraction of the bubbles, fragmentation efficiency, melt and the gas velocity, temperature and finally the mixture density assuming equilibrium mass transfer. Fig. 67 shows the fragmentation level (left panel) and the discharge rate (right panel) at the top (blue line) and at the bottom (green line) of the conduit and its maximum value (red line) as function of time. As we have obtained in the case of instantaneous pressure and velocity relaxation, with the assumption of equilibrium mass transfer the fragmentation wave propagates far into the conduit, reaching almost the bottom of the conduit at the end of the simulation ( $t = 1000$  s).

The initial fragmentation wave velocity is 88 m/s, but it decreases to 24 m/s after 25 s and to 2 m/s after about 9 minutes. After 1000 s of simulated eruption, the fragmentation wave reaches 4440 m of depth with a velocity of 1.10 m/s.

The velocity of the fragmented phase at the end of the computational domain, reaches a maximum value of 278 m/s after 1 s, then decrease rapidly to 170 m/s in 10 s and after that we notice an increase in the velocity reaching 194 m/s in about 16 minutes.

Due to the effect of the velocity disequilibrium, the velocity of the gas phase is higher with respect to that of the fragmented phase. In fact, at the end of the computational domain, it reaches a maximum value of 405 m/s after 1 s, then decrease rapidly to 263 m/s in 10 s and then accelerate to 335 m/s in about 16 minutes.

The discharge rate goes from a maximum of  $25 \times 10^6$  kg/s in the first seconds of the eruption to a minimum of  $4.5 \times 10^6$  kg/s.

Comparing the results observed from this simulation with those obtained assuming instantaneous pressure and velocity relaxation, we notice similar profiles of the solutions and similar data for the discharge rate and for the velocity of the fragmentation wave. However, due to the effect of the finite rate relaxation for the velocity, we observe a decoupling between the exsolved gas and the fragmented phase (which is not present in the case of instantaneous velocity relaxation), that is particularly evident at the top of the computation domain (where we observe a lower exit velocity for the fragmented phase with respect the gas phase). The effect of the finite rate relaxation for pressure,

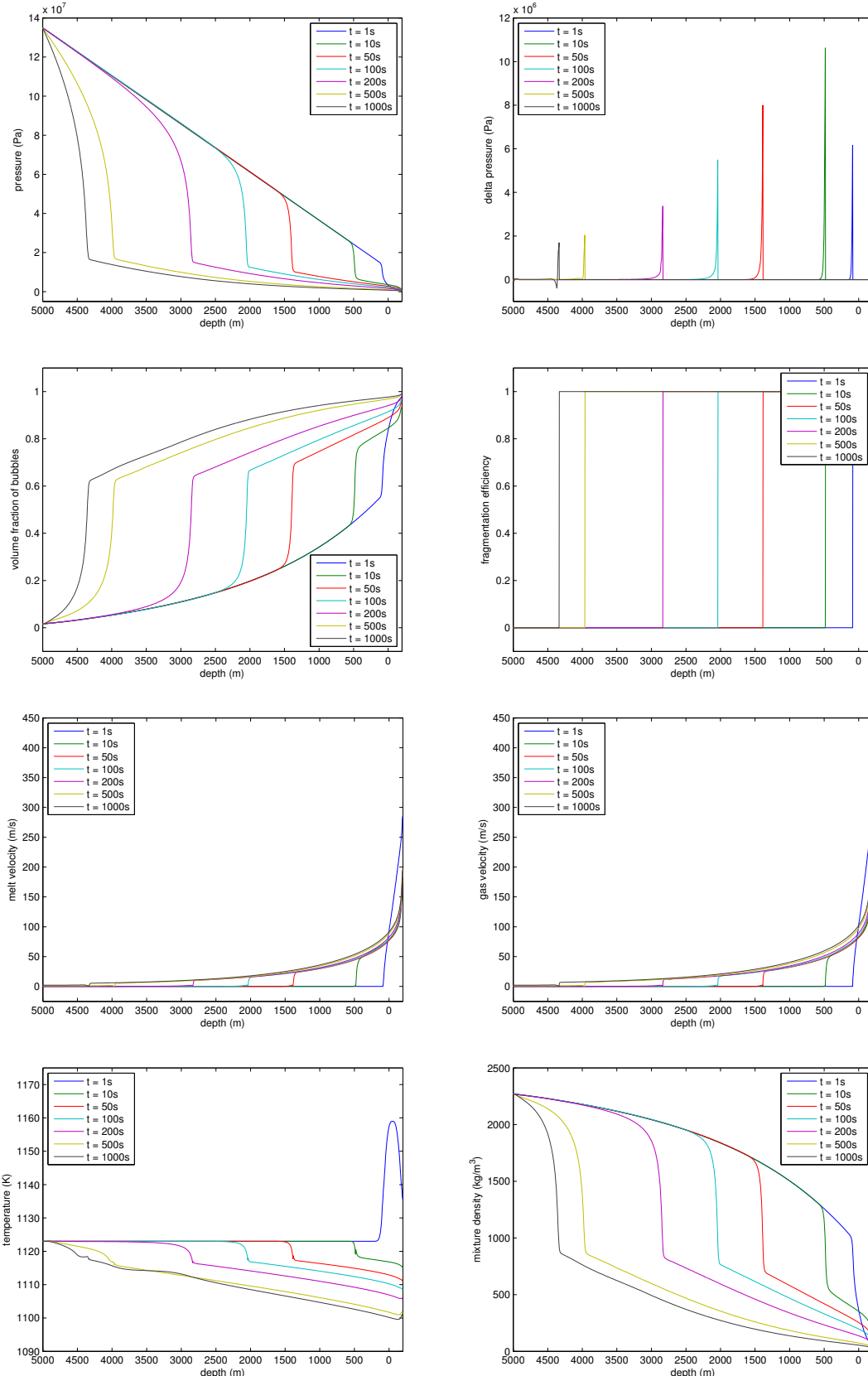


Figure 66: Profiles of mixture pressure, pressure difference between gas and melt phase, volume fraction of the bubbles, fragmentation efficiency, of melt and gas velocity, temperature and mixture density at different times assuming the disequilibrium of pressures and velocities and equilibrium mass transfer. The solutions are obtained using DIRK KNP scheme with a grid of 1300 cells.

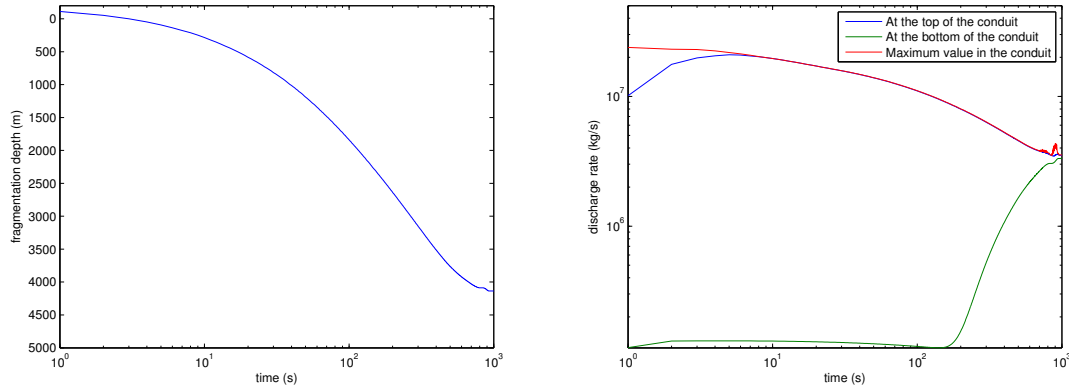


Figure 67: Fragmentation level (left panel) and discharge rate (right panel) at the top (blue line) and at the bottom (green line) of the conduit and its maximum value (red line) as function of time assuming the disequilibrium of pressures and velocities and equilibrium mass transfer.

instead, produces a peak of the overpressure of the bubbles with respect the melt that is located immediately below the fragmentation level. This peak propagates along the conduit going from a maximum of 10 MPa to a minimum of about 1.5 MPa (see top-right panel of Fig. 66).

As a final test we investigate the disequilibrium mass transfer case. We consider the relaxation time  $\tau^{(d)}$  of the same order of the duration of the simulation, i.e. we set  $\tau^{(d)} = 1000$  s. Furthermore, as done for the equilibrium case, we assume, as initial condition,  $x_d = x_d^{eq}$ .

Fig. 68 presents profiles of mixture pressure, pressure difference between gas and melt phase, volume fraction of the bubbles, fragmentation efficiency, melt and the gas velocity, temperature and finally the mixture density assuming disequilibrium mass transfer. Fig. 69 shows the fragmentation level (left panel) and the discharge rate (right panel) at the top (blue line) and at the bottom (green line) of the conduit and its maximum value (red line) as function of time.

As obtained in the case of single pressure and velocity, the fragmentation wave propagates deeper with respect the case of no mass transfer, but it is shallower than the case of equilibrium mass transfer.

The initial fragmentation wave velocity is 88 m/s, but it decreases to 20 m/s after 25 s and then continue to move more and more slow until the wave stops at a depth of 1568 m after about 130 s of simulated eruption. After that, the fragmentation wave starts to move back towards the vent. At time  $t = 200$  s the fragmentation wave is moving with a velocity of 1.33 m/s towards the exit of the conduit, but then its velocity decreases with the ascent. It reaches a velocity of 0.35 m/s after 500 s and 0.2 m/s at time  $t = 1000$  s.

The velocity of the fragmented phase at the end of the computational domain, reaches a maximum value of 275 m/s after 1 s, then decreases rapidly to 166 m/s in 10 s continuing to decrease up to 2.9 m/s at time  $t = 1000$  s.

The velocity of the gas, at the end of the computational domain, reaches a maximum value of 404 m/s after 1 s, then decreases rapidly to 259 m/s in 10 s and then continues to decrease up to 23 m/s at time  $t = 1000$  s.

Again, due to the effect of the finite rate relaxation for the velocity, we observe a lower exit velocity for the fragmented phase with respect the gas phase. The peak of the overpressure of the bubbles with respect the melt, produced by the finite relaxation

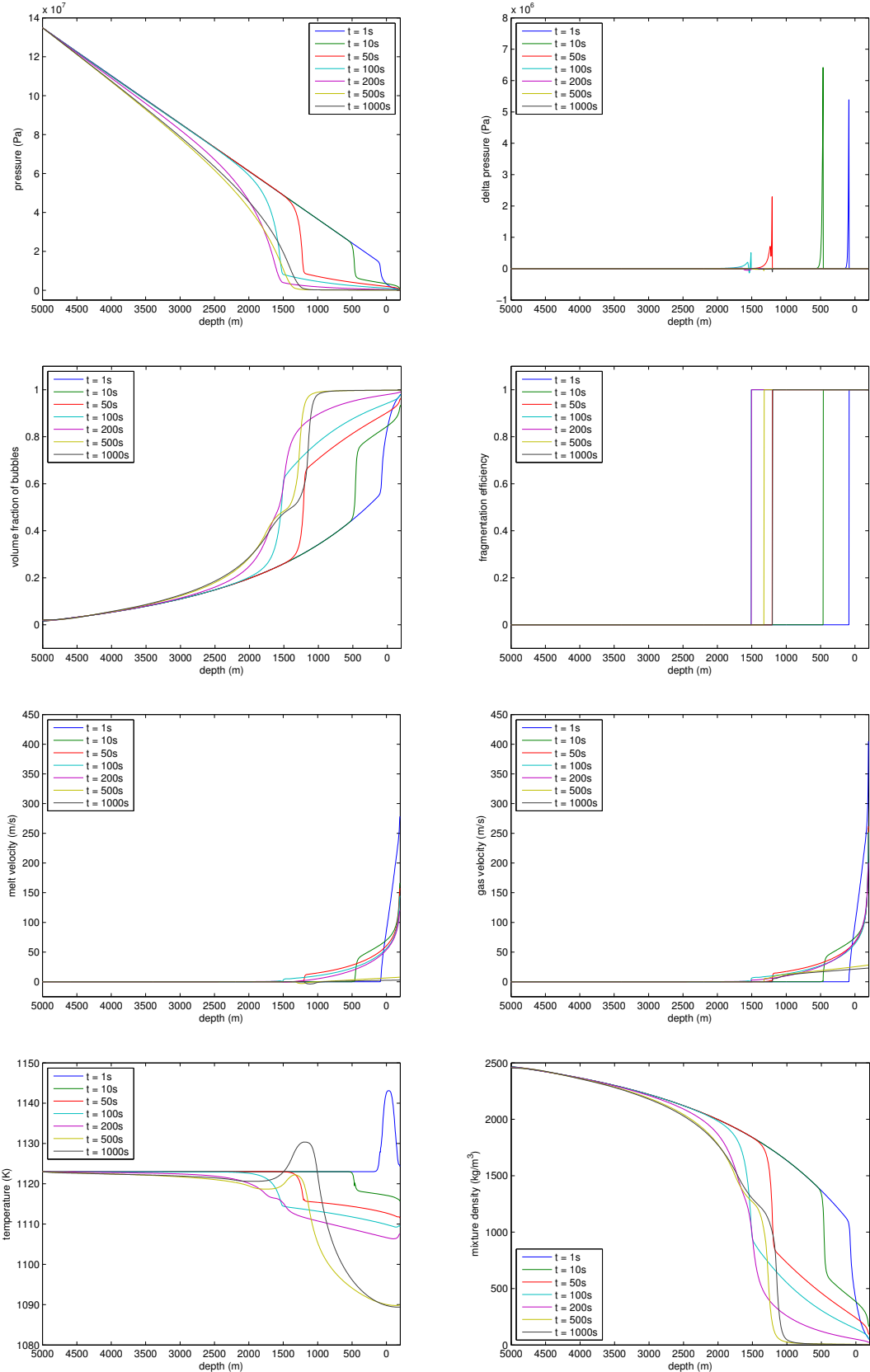


Figure 68: Profiles of mixture pressure, pressure difference between gas and melt phase, volume fraction of the bubbles, fragmentation efficiency, melt and gas velocity, temperature and mixture density at different times assuming the disequilibrium of pressures, velocities and mass transfer. The solutions are obtained using DIRK KNP scheme with a grid of 1300 cells.

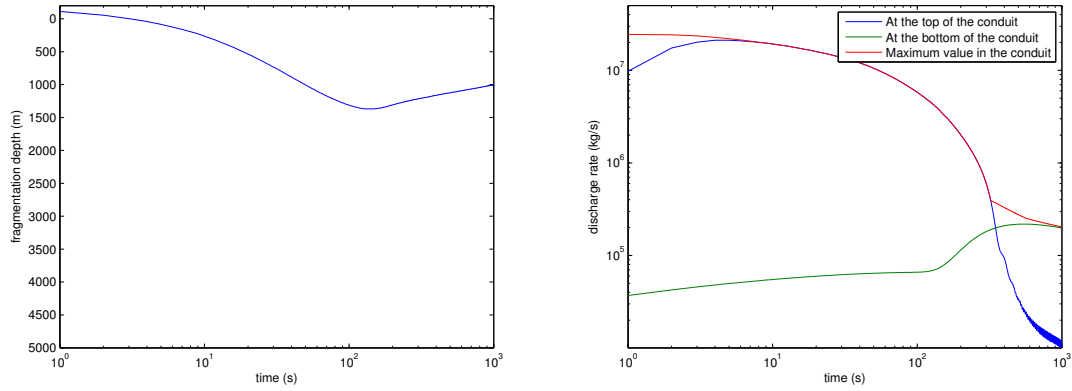


Figure 69: Fragmentation level (left panel) and discharge rate (right panel) at the top (blue line) and at the bottom (green line) of the conduit and its maximum value (red line) as function of time assuming the disequilibrium of pressures, of velocities and of mass transfer.

rate for pressure, propagates along the conduit going from a maximum of 6.5 MPa to a minimum of about 0.5 MPa.

The discharge rate goes from a maximum of  $25 \times 10^6$  kg/s in the first seconds of the eruption to a minimum of  $1.1 \times 10^4$  kg/s.

### 6.3.2 Conclusions

In this chapter a model to describe the one-dimensional dynamics of explosive volcanic eruptions has been presented. In particular we have focused on conduit processes involved in the initial stages of Vulcanian eruptions driven by the collapse of a dome overlying the conduit. Several numerical tests trying to reproduce the Vulcanian explosions of 3 August 1997 and 21 September 1997 at Soufrière Hills Volcano, Montserrat, have been presented and the effects of disequilibrium processes of pressures, velocities and mass transfer on the solutions have been investigated. In agreement with Melnik and Sparks (2002b), we have found that Vulcanian explosions are reproduced quite well in the limit of no mass transfer, where slowly rising magma develops a porosity in the conduit that evolves to critical conditions for explosive fragmentation. The short duration, the maximum fragmentation depth, the exit velocities, the discharge rates obtained from the proposed numerical model are comparable to those achieved by Melnik and Sparks (2002b) and those observed by Druitt et al. (2002). Furthermore, analyzing the first 30 s of simulated eruption, a good agreement between the discharge rate obtained by Clarke et al. (2002b) is observed, while we have noticed higher exit velocities with respect to that obtained by them.

In the limit of equilibrium mass transfer, we have observed deeper propagation of the fragmentation wave in the conduit. Melnik and Sparks (2002b) have interpreted this behavior as sub-Plinian activity, similar to that occurred on 17 September 1996 at Soufrière Hills Volcano.

Going beyond Melnik and Sparks (2002b), we have also investigated the effect of a finite-rate exsolution, better representing the real volcanic system in many cases. We have also investigated the effect of a fully multi-phase description of the volcanic system, where two pressures and two velocities are considered. The effect of the finite rate

relaxation for the velocity produces a decoupling between the exsolved gas and the fragmented phase. We have observed a lower exit velocity for the fragmented phase with respect the gas phase. The effect of the finite rate relaxation for pressure produces a peak of the overpressure of the bubbles with respect the melt that is located immediately below the fragmentation level and that propagates with it along the conduit.

Finally, unlike the model presented by Melnik and Sparks (2002b), the model proposed in this thesis solves also the energy equation, allowing us to observe the variations of the temperature in the volcanic conduit in the first stages of the eruption, which could have important implications for viscosity evolution and distribution within the conduit.



# 7

---

## CONCLUSIONS AND POSSIBLE RESEARCHES FOR FUTURE WORKS.

---

In this thesis the governing equations for a compressible two-phase flow model with two pressures, two velocities and a single temperature have been studied. A system of partial differential equations has been derived using the thermodynamically compatible system theory, which allowed us to write the governing equations in conservative form and ensured us the hyperbolicity of the system. For a more deeper analysis, we have computed the characteristic polynomial, showing how to efficiently compute, in the framework of a finite-volume central scheme, the minimum and the maximum eigenvalues. Furthermore, in the case of very dilute regime, it is shown that two eigenvalues approach the usual characteristic velocities associated with the carrier phase, given by the velocity of the phase plus and minus the phase sound speed. It is also proved that, from the governing equations, it is possible to derive a balance law for the entropy of the mixture, coupled with a non-negative source term. Then we have compared the proposed model with the classical Baer-Nunziato model, showing that, in the monodimensional case, the two systems lead to a different definition of the interfacial pressure.

To solve the governing equations, we have analyzed several numerical finite-volume central schemes, based on two approaches, respectively the splitting and the Runge–Kutta approach. The advantages and disadvantages of both approaches, when adopted to solve the presented compressible two-phase model, have been analyzed. For the splitting approach, for example, the simplicity of implementation is very attractive and, using the segregated approach, the integration of the relaxation terms, under suitable conditions, can be done analytically. However, when the conditions for the analytical integration of the relaxation terms are not satisfied, an implicit and stable integration scheme must be provided. To this aim, in this work, we have presented the DIRK (Diagonally Implicit Runge–Kutta) schemes, belonging to the family of Implicit-Explicit Runge–Kutta scheme developed to solve stiff systems of partial differential equations. However, since these schemes solve implicitly the relaxation terms, the computational cost is higher with respect the schemes developed with the splitting approach and this, of course, reflects on the execution time of a numerical simulation.

In order to check the robustness and the correctness of presented approaches in conjunction with different formulation for the finite-volume fluxes illustrated in this thesis (i.e. Lax–Friedrichs, GFORCE, Kurganov and Tadmor, Kurganov Noelle and Petrova and the modification of Lax–Friedrichs numerical fluxes), several numerical simulations have been performed. We have checked that the schemes are able to reproduce correctly the propagation of rarefaction and shock waves and the solutions obtained with instantaneous and finite relaxation rate have been analyzed. Some schemes do not give good

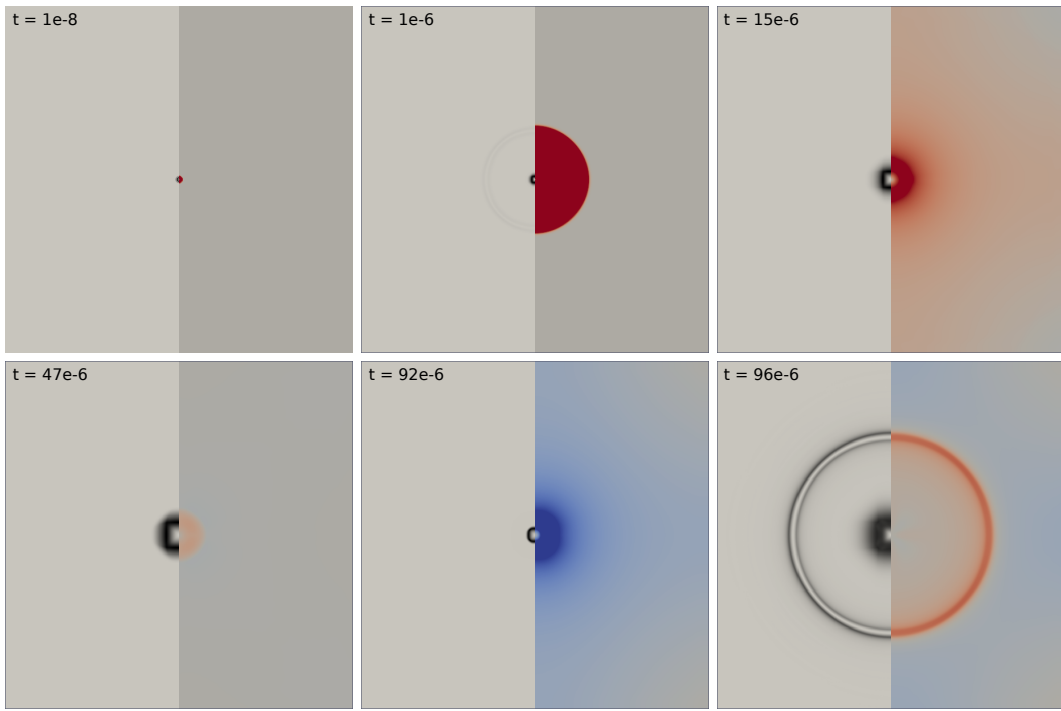


Figure 70: Laser Induced Cavitation Problem: Preliminary results presented at ICNAAM 2013 (de' Michieli Vitturi et al., 2013b). In each panel is reported on the left the emulated Schlieren images generated from the numerical results plotting  $|\nabla\rho|$  in a nonlinear graymap. On the right, instead, is reported the radial velocity, where the red color represents a positive velocity, while the blue color a negative one.

results, for example the Lax–Friedrichs numerical fluxes is too diffusive and the predictor/corrector strategy has to be used in the splitting approach to solve correctly the rarefaction waves. Nevertheless, most of the schemes presented gives excellent results, succeeding also in reproduce laboratory experiments like the interaction of shock waves with bubbles.

Another interesting laboratory experiment, investigated during the Ph.D. but not presented in this thesis, is the Laser–Induced Cavitation problem. Many studies related to this problem are dedicated to medical applications, especially in ophthalmology (Brujan et al., 2001; Brujan and Vogel, 2006; Vogel et al., 1996, 1990) and biomedicine. In the laboratory experiment a transparent box is filled with water (at ambient pressure and temperature) and, at a certain moment, a small region is irradiated with a laser pulse for a very short time. A shock wave, generated by the high pressure gradient, propagates, causing an expansion and a strong decrease of the pressure in the area previously irradiated by the laser and therefore the evaporation of the liquid. Then the gas bubble generated by the evaporation starts to expand and after a certain time, due to the high pressure of the surrounding water, the expansion ends and the bubble begins to collapse. Finally, when the bubble collapses entirely, a new shock wave is generated, and so we have the nucleation of a new bubble.

Due to the high pressure and temperature gradient resulting from energy released by the laser, the numerical simulation can be very stressful for the numerical schemes and see if the model are able to reproduce this experiment can be very interesting. Preliminary results have been presented at the ICNAAM 2013 (International Conference on

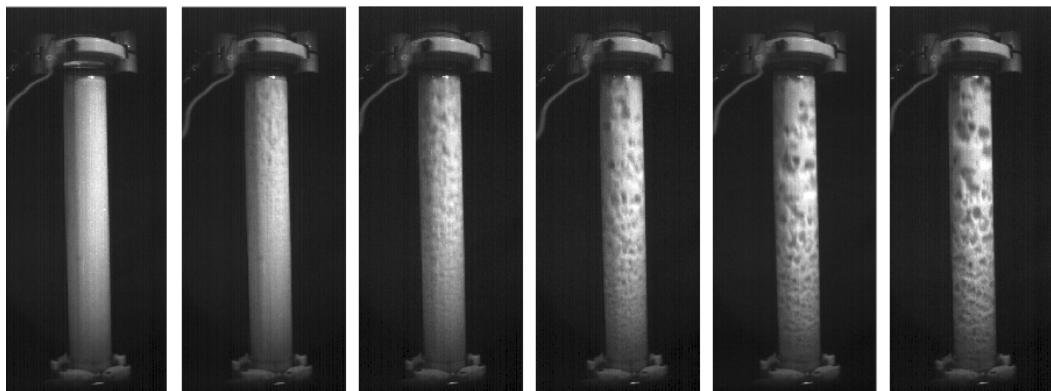


Figure 71: Photographies of a laboratory experiment regarding a shock-tube filled with gas and particles performed at the School of Earth and Exploration of the Arizona State University. The pictures represent the initial instants after the rupture of the diaphragm.

Numerical Analysis and Applied Mathematics) conference and are shown in Fig. 70 (de' Michieli Vitturi et al., 2013b).

We have also illustrated that the physical model can be adapted to a volcanological application, in particular to a conduit model for the magma ascent. The conduit model presented is obtained from the single temperature model adding a new transport equation for the dissolved gas and modifying properly the source and relaxation terms in order to include viscous effects and gas exsolution. We have shown that the addition of the transport equation for the dissolved mass fraction of gas does not change the hyperbolicity of the system. Again, for a more deeper analysis, the characteristic polynomial has been computed showing that the eigenvalues of the conduit model are the same of the single temperature model with the addition of another one.

The conduit model was able to reproduce the propagation of a fragmentation wave along the conduit, separating a gas-particle region from a bubbly flow region. Furthermore, we have noticed that the relaxation rate coefficients can modify significantly the profiles of the solutions. Thus, providing a correct model for the disequilibrium between the phases plays a key role in conduit dynamics. Preliminary results have been presented at EGU 2013 (European Geosciences Union) (de' Michieli Vitturi et al., 2013a).

In order to better understand the initial acceleration phase of vulcanian eruptions, it is also important to study the acceleration of gas-particle mixtures during explosive events. For this reason, I have worked also with an experimental shock-tube setup at the School of Earth and Exploration of the Arizona State University, in order to compare the laboratory measurements with the results of the numerical models and better constrain the drag of the gas phase on the particles for dense mixture (Fig. 71).

Finally, in the conduit model presented, we made the assumption of constant crystal content during the ascent of the magma. This is a reasonable assumption for explosive eruptions but not for effusive ones. For this reason, I am working on the extension of the model to effusive eruptions adding a new (or more) transport equation for the crystal with a proper disequilibrium process. Furthermore, real magmas contain several exsolved and dissolved gas phases, so take into account multiple gas can make the model more close to reality, allowing us to better understand the dynamics of volcanic eruptions.



# A

---

## THERMODYNAMICALLY COMPATIBLE SYSTEM GENERATING A TWO-PHASE FLOW MODEL

---

In this section a derivation of governing equations for a two-phase flow model based on the thermodynamically compatible systems theory is provided (Godunov and Romenskii, 2003; Romenski et al., 2010, 2007).

The derivation of the conservative governing equations for a continuous medium can be summarized in four key steps: (i) choose the physical variables characterizing the medium; (ii) define a set of thermodynamically compatible conservation laws written in terms of generating potentials and variables; (iii) establish a relationship between the generating potentials and variables with the physical variables and thermodynamic potential; (iv) introduce source terms in the system of governing equations.

Our aim is to represent the homogeneous system of conservation laws

$$\frac{\partial \mathbf{U}}{\partial t} + \frac{\partial}{\partial x_k} \mathbf{F}_k(\mathbf{U}) = 0 \quad (\text{A.1})$$

in the form

$$\frac{\partial L_{\mathbf{q}}}{\partial t} + \frac{\partial}{\partial x_k} \mathbf{F}_k(\mathbf{q}, L_{\mathbf{q}}) = 0, \quad (\text{A.2})$$

where  $\mathbf{q} = (q_1, \dots, q_m)^T$  is a vector of generating variables,  $L$  is the generating potential and  $L_{\mathbf{q}}$  is the vector of the partial derivatives of the generating potential with respect to the generating variables. The thermodynamic compatible system (A.2) can be transformed into a symmetric system, and if the generating potential  $L$  is a convex function, then the system is even hyperbolic. Therefore if the homogeneous system of conservation laws (A.1) can be written as in Eq. (A.2) with a convex generating potential, this will guarantee the hyperbolicity of the system.

First of all, we have to identify the physical quantities that better describe the medium. We want to model a compressible two-phase flow with a single temperature, thus the quantities that we consider are: the mixture density, the volume fraction of the first phase, the mass fraction of the first phase, the momentum of the mixture, the relative velocity and finally the mixture entropy.

Related to the physical quantities chosen, we consider the homogeneous thermodynamic compatible system written in the form

$$\frac{\partial}{\partial t} L_{q_1} + \frac{\partial}{\partial x_k} u^k L_{q_1} = 0, \quad (\text{A.3})$$

$$\frac{\partial}{\partial t} L_a + \frac{\partial}{\partial x_k} u^k L_a = 0, \quad (\text{A.4})$$

$$\frac{\partial}{\partial t} L_b + \frac{\partial}{\partial x_k} (u^k L_b + r_k) = 0, \quad (\text{A.5})$$

$$\frac{\partial}{\partial t} L_{r_i} + \frac{\partial}{\partial x_i} (u^j L_{r_j} + b) = 0, \quad i = 1, 2, 3 \quad (\text{A.6})$$

$$\frac{\partial}{\partial t} L_{u_i} + \frac{\partial}{\partial x_k} ((u^k L)_{u_i} + r_k L_{r_i} - \delta_{ik} r_j L_{r_j}) = 0, \quad i = 1, 2, 3 \quad (\text{A.7})$$

$$\frac{\partial}{\partial t} L_T + \frac{\partial}{\partial x_k} (u^k L_T) = 0, \quad (\text{A.8})$$

$$\frac{\partial}{\partial x_j} L_{r_k} - \frac{\partial}{\partial x_k} L_{r_j} = 0, \quad (\text{A.9})$$

where Eq. (A.3) represents the conservation law for the mass, the variables  $a$  and  $b$  represent the internal state of the medium governed by the Eq. (A.4) and (A.5). The conservation of the momentum of the mixture is represented by Eq. (A.7), while  $r = (r_1, r_2, r_3)$  is a vector that describe the relative motion of the mixture and it is governed by Eq. (A.6). The temperature of the medium is ruled by Eq. (A.8), and finally the last steady state equation (A.9) is added to the governing equations in order to provide the compatibility of the thermodynamic compatible system. One can prove that, differentiating the equation for  $L_{r_k}$  with respect  $x_j$  and subtract the equation for  $L_{r_j}$  after its differentiation with respect  $x_k$ , we have

$$\frac{\partial}{\partial t} \left( \frac{\partial}{\partial x_j} L_{r_k} + \frac{\partial}{\partial x_k} L_{r_j} \right) = 0. \quad (\text{A.10})$$

Thus, if at  $t = 0$  we have  $\frac{\partial}{\partial x_j} L_{r_k} + \frac{\partial}{\partial x_k} L_{r_j} = 0$  then we have the same equality for all  $t > 0$ .

Using a thermodynamically compatible system, it is possible to derive an additional (energy) conservation law. This equation can be obtained multiplying each equation of the system respectively with  $q_1, a, b, r_i, v_i, T, 2v_i r_k$  and then adding the products. In this way we have

$$\begin{aligned} & \frac{\partial}{\partial t} (q_1 L_{q_1} + a L_a + b L_b + r_i L_{r_i} + u_i L_{u_i} + T L_T - L) + \\ & + \frac{\partial}{\partial x_k} (u_k (q_1 L_{q_1} + a L_a + b L_b + u_i L_{u_i} + T L_T) + r_k u_j L_{r_j} + r_k b) = 0. \end{aligned} \quad (\text{A.11})$$

From the last equation we can define the energy of the medium as

$$\rho \left( E + \frac{u_i u_i}{2} \right) = q_1 L_{q_1} + a L_a + b L_b + r_i L_{r_i} + u_i L_{u_i} + T L_T - L, \quad (\text{A.12})$$

where  $\rho$  is the density of the mixture and  $E$  is specific internal energy of the mixture. Now, assuming that

$$L_{q_1} = \rho, \quad L_a = \rho \alpha, \quad L_b = \rho c, \quad L_{u_i} = \rho u_i, \quad L_{r_i} = w_i, \quad L_T = \rho S, \quad (\text{A.13})$$

we obtain the following equalities:

$$\begin{aligned}
d \left[ \rho \left( E + \frac{u_i u_i}{2} \right) \right] &= d [q_1 L_{q_1} + a L_a + b L_b + r_i L_{r_i} + u_i L_{u_i} + T L_T - L] \\
&\Downarrow \\
Ed\rho + \rho dE + d \left[ \frac{\rho u_i \rho u_i}{2\rho} \right] &= q_1 dL_{q_1} + a dL_a + b dL_b + r_i dL_{r_i} + u_i dL_{u_i} + T dL_T \\
&\Downarrow \\
\left[ E - \frac{u_i u_i}{2} \right] d\rho + u_i d(\rho u_i) + \rho dE &= \\
&= q_1 d\rho + a d(\rho \alpha) + b d(\rho c) + r_i d(w_i) + u_i d(\rho u_i) + T d(\rho S).
\end{aligned} \tag{A.14}$$

Assuming the  $E \equiv E(\rho, \alpha, c, w_i, S)$  (Eq. (2.34)), then we obtain

$$\begin{aligned}
dE &= E_\rho d\rho + E_\alpha d\alpha + E_c dc + E_{w_i} dw_i + E_S dS \\
&\Downarrow \\
\rho dE &= \rho E_\rho d\rho + \rho E_\alpha d\alpha + \rho E_c dc + \rho E_{w_i} dw_i + \rho E_S dS \\
&\Downarrow \\
\rho dE &= \rho E_\rho d\rho + E_\alpha d\rho \alpha - \alpha E_\alpha d\rho + E_c d\rho c - c E_c d\rho + \\
&\quad + \rho E_{w_i} dw_i + E_S d\rho S - S E_S d\rho.
\end{aligned} \tag{A.15}$$

Hence, from the two equations (A.14) and (A.15), comparing the differential terms we obtain

$$\begin{aligned}
q_1 &= \left[ E - \frac{u_i u_i}{2} + \rho E_\rho - \alpha E_\alpha - c E_c - S E_S \right], \\
a &= E_\alpha, \\
b &= E_c, \\
r_i &= \rho E_{w_i}, \\
u_i, \\
T &= E_S,
\end{aligned} \tag{A.16}$$

and finally from the Eq. (A.12) we find the generating potential

$$\begin{aligned}
L &= q_1 L_{q_1} + a L_a + b L_b + r_i L_{r_i} + u_i L_{u_i} + T L_T - \rho \left( E + \frac{u_i u_i}{2} \right) = \\
&= \left[ E - \frac{u_i u_i}{2} + \rho E_\rho - \alpha E_\alpha - c E_c - S E_S \right] \rho + \\
&\quad + E_\alpha \rho \alpha + E_c \rho c + \rho E_{w_i} w_i + u_i \rho u_i + E_S \rho S - \rho \left( E + \frac{u_i u_i}{2} \right) \\
&\Downarrow \\
L &= \rho^2 E_\rho + \rho w_i E_{w_i}.
\end{aligned} \tag{A.17}$$

With our choice of the generating variables, to obtain the symmetric system we add the term  $r_k \left( \frac{\partial}{\partial x_j} L_{r_k} - \frac{\partial}{\partial x_k} L_{r_j} \right) = 0$  to the equation for  $u_i$ , while  $u_i \left( \frac{\partial}{\partial x_i} L_{r_k} - \frac{\partial}{\partial x_k} L_{r_i} \right) = 0$  is added to the equation for  $r_k$ . In this way we get

$$\frac{\partial}{\partial t} L_{q_1} + \frac{\partial}{\partial x_k} (u^k L)_{q_1} = 0, \tag{A.18}$$

$$\frac{\partial}{\partial t} L_a + \frac{\partial}{\partial x_k} (u^k L)_a = 0, \quad (\text{A.19})$$

$$\frac{\partial}{\partial t} L_b + \frac{\partial}{\partial x_k} (u^k L)_b + \frac{\partial}{\partial x_k} r_k = 0, \quad (\text{A.20})$$

$$\frac{\partial}{\partial t} L_{r_i} + \frac{\partial}{\partial x_k} (u^k L)_{r_i} + L_{r_j} \frac{\partial}{\partial x_i} u_j - L_{r_i} \frac{\partial}{\partial x_k} u_k + \frac{\partial}{\partial x_i} b = 0, \quad i = 1, 2, 3 \quad (\text{A.21})$$

$$\frac{\partial}{\partial t} L_{u_i} + \frac{\partial}{\partial x_k} (u^k L)_{u_i} + L_{r_i} \frac{\partial}{\partial x_k} r_k - L_{r_j} \frac{\partial}{\partial x_i} r_j = 0, \quad i = 1, 2, 3 \quad (\text{A.22})$$

$$\frac{\partial}{\partial t} L_T + \frac{\partial}{\partial x_k} (u^k L)_T = 0, \quad (\text{A.23})$$

The above is a symmetric system and if  $L$  is a convex function then it is a symmetric hyperbolic system.

Finally, substituting the expressions for the generating variables (A.16) into (A.3)-(A.9) and into (A.11) we get

$$\frac{\partial}{\partial t} \rho + \frac{\partial}{\partial x_k} \rho u^k = 0, \quad (\text{A.24})$$

$$\frac{\partial}{\partial t} \rho \alpha + \frac{\partial}{\partial x_k} \rho \alpha u^k = 0, \quad (\text{A.25})$$

$$\frac{\partial}{\partial t} \rho c + \frac{\partial}{\partial x_k} \left( \rho c u^k + \rho E_{w_k} \right) = 0, \quad (\text{A.26})$$

$$\frac{\partial}{\partial t} w^k + \frac{\partial}{\partial x_k} \left( u^j w^j + E_c \right) = 0, \quad (\text{A.27})$$

$$\frac{\partial}{\partial t} \rho u^i + \frac{\partial}{\partial x_k} \left( \rho u^i u^k + \rho w^i E_{w_k} + \delta_{ik} \rho^2 E_\rho \right) = 0, \quad i = 1, 2, 3 \quad (\text{A.28})$$

$$\frac{\partial}{\partial t} \rho S + \frac{\partial}{\partial x_k} \left( \rho S u^k \right) = 0, \quad (\text{A.29})$$

$$\frac{\partial}{\partial x_j} w_k + \frac{\partial}{\partial x_k} w_j = 0, \quad (\text{A.30})$$

$$\frac{\partial}{\partial t} \left( \rho \left( E + \frac{u_i u_i}{2} \right) \right) + \frac{\partial}{\partial x_k} \left[ \rho u_k \left( E + \frac{u^i u^i}{2} + \rho E_\rho \right) + \rho E_{w_k} \left( u^j w^j + E_c \right) \right] = 0. \quad (\text{A.31})$$

Using the definition of the internal energy of the mixture and its partial derivatives (Eqs. (2.34) and (2.39)), substituting them into (A.24)-(A.31) and replacing the Eq. (A.29) with (A.31), we obtain the homogeneous part of the system of partial differential equations (2.10)-(2.16). Furthermore, again from Eqs. (2.34) and (2.39) we obtain the following expression for the generating potential:

$$L = P + \rho c (1 - c) w_i w_i. \quad (\text{A.32})$$

Since  $L$  is a convex function, then we can conclude that the system (2.10)-(2.15) is hyperbolic.

An explanation regarding how to incorporate some kinds of dissipative processes into the system can be found in Romenski et al. (2010, 2007); Romensky (2001).

# B

---

## OPENFOAM IMPLEMENTATION

---

OpenFOAM (Field Operation And Manipulation) is a free source CFD package written in C++ which uses classes and templates to manipulate and operate scalar, vectorial and tensorial fields (Weller, 1998).

OpenFOAM is programmed using an *object-oriented programming* (OOP), in which the programmer creates classes to represent conceptual objects in the code, classes that contain the data that make up the object. Another important feature of OOP is the relationships between the various classes, for example the relationship between an existing class and an extension of it. The extended class inherits all the properties of the base class. By doing this, existing classes can be given new behavior without the necessity of modifying the existing class itself (for example the class of the three-dimensional vectors can be extended to the class of the dimensioned vectors, a new class in which all the vectors have a proper unit). In particular, with OpenFOAM there exist data types that represent tensor fields and typical terms appearing in partial differential equations, constructed to behave like their mathematical counterparts and hiding the numerical details of the implementation by encapsulation. In fact, one of the strengths of OpenFOAM is that new solvers can be created by its users with some pre-requisite knowledge of the underlying method, physics and programming techniques involved, inheriting from the OpenFOAM framework some very useful features like the use of unstructured mesh and parallelization.

For these reasons, and also for the availability of proper numerical methods for the discretization of partial differential equations and for the solution of the resulting linear systems, OpenFOAM is as a good choice to handle CFD problems and develop new solvers. Its open-source characteristics are an advantage in the implementation of any addition or modification in the code. Moreover, all solvers developed within OpenFOAM are, by default, three dimensional, but can be used for one- or two-dimensional problems by the application of particular conditions on boundaries lying in the plane of the direction(s) of no interest.

Further information about OpenFOAM can be found on the website (<http://www.openfoam.com/>), while a documentation about the use of some solvers can be found in the User's Guide (<http://foam.sourceforge.net/docs/Guides-a4/UserGuide.pdf>).

Finally, it is also available the Programmer's Guide (<http://foam.sourceforge.net/docs/Guides-a4/ProgrammersGuide.pdf>), which is very useful for people that want to modify an existing code or write a new solver from the beginning.

In the following sections we first introduce some pre-requisites useful to better understand the implementation of the solvers (for example the structure of the variables, the mathematical operators, etc.). Then the implementation of the solvers presented

Operation	Mathematical Operator	OpenFOAM syntax
Addition	+	+
Subtraction	-	-
Scalar multiplication	.	*
Scalar division	/	/
Inner product	.	*
Cross product	$\times$	$\wedge$
Square	$(\cdot)^2$	sqr( )
Magnitude squared	$ \cdot ^2$	magSqr( )
Magnitude	$ \cdot $	mag( )
Component maximum	max( )	max( )
Component minimum	min( )	min( )

Table 60: Syntax of some mathematical operations in OpenFOAM

in this thesis is examined. We will not report entirely the codes in this thesis, but the solvers (and the initial conditions for the simulations presented in Chapters 4 and 5) will be available at this webpage: [www.pi.ingv.it/user/laspina](http://www.pi.ingv.it/user/laspina). The solvers, at the moment, are compatible with the version 2.1.1 of OpenFOAM.

### B.1 PRE-REQUISITES

In this section, some brief information needed for edit or write an OpenFOAM solver and to compute a simulation will be given. A more complete documentation can be found in the Programmer's Guide (<http://foam.sourceforge.net/docs/Guides-a4/ProgrammersGuide.pdf>) and in the User's Guide (<http://foam.sourceforge.net/docs/Guides-a4/UserGuide.pdf>)

One of the first thing we have to face when programming a new solver is the definition of a new variable. The algebraic variables in OpenFoam can be divided in three main categories: scalars, vectors and tensors. The scalar quantities are made of one component (for example the pressure or the temperature), the vectors are composed by three components (for example the velocities) and the tensors consists of nine components (for example the stress tensors) in a matrix form.

The standard mathematical operations that involve these variables are available in OpenFOAM and a list of the operations and the corresponding operators used is reported in Table 60.

Scalars vectors and tensors appearing in a model generally represent physical quantities with a proper unit. For this reason, in OpenFOAM it is possible to assign a dimension to a specific variable. This feature is very useful because OpenFOAM checks the dimensions of the variables before computing an operation and returns an error if we are doing incompatible operations with those variables, such as summing two variables which have different units.

All the units are defined as function of seven primitive units. In order we have: mass (kg), length (m), time (s), temperature (K), quantity (mol), current (A) and luminosity intensity (cd). So, if we want to define the vector  $velocity = (0, 1, 0) \text{ ms}^{-1}$  the syntax is:

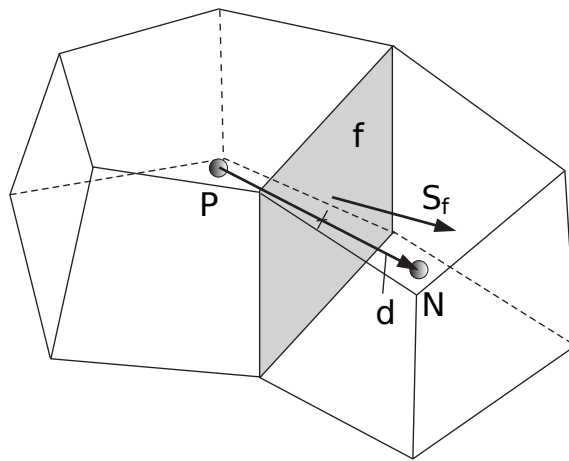


Figure 72: Schematic representation of two adjacent cells. Here  $P, N$  are the centroids of the two cells,  $f$  is the face that separates the two cells,  $S_f$  is a vector normal to face  $f$  which magnitude is equal to the area of  $f$  and  $d$  is the distance vector between  $P$  and  $N$ .

```
dimensionedVector velocity
(
    "velocity",
    dimensionSet(0, 1, -1, 0, 0, 0, 0),
    vector(0,1,0),
);
```

With the instruction `dimensionSet(0, 1, -1, 0, 0, 0, 0)` we are setting the units of the vector `velocity` as  $\text{ms}^{-1}$ . Note that the order of the units is that given before. The objects that represent the dimensioned algebraic variables are the `dimensioned<Type>` classes, where `<Type>` is one among `Scalar`, `Vector`, `Tensor`.

The variables presented before describe a single value of a particular physical quantity. However, in our domain, the physical quantities are not constant in the domain. Thus, instead of considering a single value, we are interested in considering a list (or a field) of values for that physical quantity. Lists of algebraic variables are defined in OpenFOAM by the template class `field<Type>`. For better code legibility, all instances of `field<Type>`, for example `fieldVector`, are renamed using `typedef` declarations as `<type>Field`, i.e. `scalarField`, `vectorField` and `tensorField`. As done before, even for the lists of variables it is possible to assign a dimension using the classes `dimensionedScalarField`, `dimensionedVectorField` and `dimensionedTensorField`.

The lists of variables are used to define the physical quantities in the discretized domain. OpenFOAM is based on the finite volume methods, thus the domain is discretized using cells or control volumes. The cells must be convex and contiguous, i.e. they do not overlap one another and completely fill the domain. An example of two cells is reported in Fig. 72.

Depending on the variable considered we can be interested to the values at the centroid of the cells, or at the centroid of the faces of the cells. OpenFOAM allow us to define a particular lists of variables defined at the centroid of the cells or at the centroid of the faces of the cells: `vol<Type>Field` and `surface<Type>Field`. In the finite volume framework the variables are assumed constant inside each cell, so they are defined as `vol<Type>Field`, while their reconstructions at the cells interfaces are treated as

Operator	Mathematical Operator	OpenFOAM syntax
Gradient	$\nabla(\chi)$	grad(chi)
Divergence	$\nabla \cdot (\chi)$	div(chi)
Curl	$\nabla \times (\phi)$	curl(phi)
Laplacian	$\nabla^2(\phi)$	laplacian(phi)
Time derivative	$\frac{\partial}{\partial t}(\phi)$	dtt(phi)

Table 61: Syntax for some differential operators in OpenFOAM.

`surface<Type>Field`. It is important to know that these variable are already defined as dimensioned, so for example it is no possible to define a `dimensionedVolScalarField` because a `volScalarField` is always dimensioned. An example of how to define a `volScalarField` is reported below:

```
volScalarField pressure
(
    IOobject
    (
        "pressure",
        runTime.timeName(),
        mesh
    ),
    mesh,
    dimensionedScalar("pressure",
        dimensionSet(1, 1, -2, 0, 0, 0, 0),
        scalar(1e6) )
);
```

With these instructions we have defined the variable `pressure` as constant in all cells centroids with a value of  $10^6$  Pa.

The classes `vol<Type>Field` and `surface<Type>Field` are very important when programming a new solver in the OpenFOAM framework, since they are designed expressly to be used with finite volume methods.

Finally, once the variables of our model are defined, we have to put them into the governing equations and discretize the differential terms appearing in the considered system of partial differential equations.

The syntax for some of the differential operators in OpenFOAM is reported in Table 61. The argument `phi` present in the table must be a `vol<Type>Field`, while `chi` can be also a `surface<Type>Field`.

The implicit discretization of an differential operator is obtained using the prefix `fvm::` (*Finite Volume Method*) before the differential operator, while for the explicit discretization `fvc::` (*Finite Volume Calculus*) is used. For example, with the instruction

```
fvm::ddt(phi) + fvc::div(chi)
```

we are discretizing the time derivative implicitly, while the divergence explicitly.

The explicit discretization of differential operators leads to lists of known terms while the implicit discretization returns a square matrix. Thus each partial differential equation is transformed into a linear system that has to be solved. Therefore the previous instruction is transformed into a linear system  $Ax = b$  in which  $x = \text{phi}$  is the unknown,  $b = -\text{fvc}::\text{div}(\text{chi})$  is the known term and  $A = \text{fvm}::\text{ddt}(\text{phi})$  is the matrix of the linear system.

The solution of this linear system can be obtained simply with the instructions

```
solve
(
    fvm::ddt(phi) + fvc::div(chi)
)
```

The discretization schemes used to obtain the linear system from the previous instruction are decided by the user modifying properly a file in the simulation folder.

In OpenFOAM the files needed to compute a simulation (called also *case*) are organized as follows:

- Case directory
  - constant directory
  - system directory
  - Solution directories (0,0.1,0.2,...)

In the `constant` directory we find several files containing the constant parameters needed by the considered solver. For example, in the cavity test case of the incompressible solver `icoFoam`, we find, in the `constant` folder, the file `transportProperties` in which the constant viscosity `nu` is defined. Furthermore, in the `constant` directory, we find another folder, `polyMesh`, in which is defined the discretization of spatial domain.

In the `system` directory, instead, we have the files needed for the execution of the solver. The most common are `controlDict` (in which we define, for example, the maximum time step, the end time of the simulation, etc.), `fvSchemes` (in which the numerical discretization schemes for the mathematical operators, such as the divergence or the laplacian operators, are specified) and `fvSolution` (in which we specify the numerical scheme used to compute the solution of the linear system obtained from the discretization of the differential operators).

The name of each solution directory corresponds to the time at which the solution is saved and in each directory we find several files representing the variables computed by the solver. Normally, before the beginning of the simulation, only the directory `0` is present, and the files in this folder are used to define the initial conditions and the boundary conditions needed for the solver.

To perform a numerical simulation, first of all we need to create the mesh. From within the case directory, this is done simply by executing from the command line the utility `blockMesh`. Then we can start the simulation by typing the name of the solver (for example `icoFoam`) and finally, once the simulation is concluded, we can see the results with `paraFoam`, that is the post-processing tool supplied with OpenFOAM.

Now that we have some familiarity with the nomenclature, with the functions and with the variables used in OpenFOAM we can start to give a look to the implementation of the numerical schemes presented in this thesis. We will not report entirely the

codes, but we will show the schematic procedures behind the two approaches presented, analyzing step by step the key points of the implementation.

## B.2 SOLVERS OVERVIEW

### B.2.1 *Splitting approach solver:* twoPhaseCentralFoam

In this section we discuss the implementation of the splitting approach schemes proposed in this work using the OpenFOAM framework. The implementation of this solver is based on the *rhoCentralFoam* solver included in OpenFOAM. The solver *rhoCentralFoam* is described by Greenshields et al. (2010). It is a solver for the governing equations of a compressible single phase fluid. For this reason the solver for the two-phase model based on the splitting approach has been called *twoPhaseCentralFoam*. The numerical fluxes adopted in *rhoCentralFoam* are the KT and KNP numerical fluxes, but no predictor/corrector strategy or interfaces relaxation are implemented in the existing solver. An overview of the implementation of the *twoPhaseCentralFoam* solver is presented below.

Given a numerical solution  $\mathbf{U}^t$  at the time  $t$ , the solution at the new time step is computed as follows:

- (i) Computation of the time step  $\Delta t$ .
- (ii) Linear reconstruction of  $\mathbf{U}^t$  at the cells interfaces.
- (iii) Computation of the predictor step at the cells interfaces.
- (iv) Application of the interface relaxation.
- (v) Calculation of the local speeds at the cells interfaces.
- (vi) Computation of the numerical fluxes.
- (vii) Computation of the solution  $(\mathbf{U}^{t+\Delta t})^*$  of the hyperbolic part of PDEs.
- (viii) Computation of the solution  $\mathbf{U}^{t+\Delta t}$  integrating the source terms.
- (ix) Correction of the solution at the boundaries.

In this way, starting from  $t = 0$  we can compute the solution at time  $t = \Delta t$ , and iterating the procedure we can obtain the solution at the time desired.

#### (i) Computation of the time step

The first point in the procedure presented above consists in the computation of the time step. In Eq. (3.40) we described, for the one-dimensional scheme, how to compute the time step as a function of the step size of the spatial discretization  $\Delta x$  (i.e. the minimum distance between two cell interfaces) and the speed of the fastest wave  $q_i$  (i.e. the spectral radius of the jacobian matrix  $\frac{\partial F}{\partial U}$  evaluated at  $\mathbf{U}_i^t$ ) for all cell  $i$ .

Using the OpenFOAM framework the numerical schemes are intrinsically three-dimensional thus we have to extend the computation of the time step to the 3D case.

One possibility is to consider three different 1D problem, obtained replacing the vectors  $\vec{u}$ ,  $\vec{w}$ ,  $\vec{u}_1$  and  $\vec{u}_2$  respectively with their  $x$ ,  $y$  and  $z$  component.

In this way, for each cell  $i$ , we can determine three different spectral radii, one for each directions:  $(\varrho_i)_x$ ,  $(\varrho_i)_y$  and  $(\varrho_i)_z$ . Thus we can define the vector  $\vec{\varrho}_i$  as

$$\vec{\varrho}_i = [(\varrho_i)_x, (\varrho_i)_y, (\varrho_i)_z]^T. \quad (\text{B.1})$$

For what concerns the spatial discretization, OpenFOAM allows us to define different shape or size for the cells of the domain, thus is not simple to define the step size for each cells. However, the cells must satisfy some properties, one of which is that every cell has to be convex (all properties of the cells are listed in the website <http://www.openfoam.org/docs/user/mesh-description.php>).

In order to estimate the step size of each cell, it is possible to define for each cell the maximum sphere contained in one cell with center located at the cell centroid. Since the sphere is contained inside the cell, its diameter is an approximation of the step size of that cell. Furthermore, since the cells are convex, for each of them, the radius of the sphere contained inside that cell is exactly the minimum distance between the centroid of the cell and the faces of the cell.

In OpenFOAM the built-in functions `mesh.C()` and `mesh.Cf()` return respectively the coordinates of the cells centroids and of the faces centroids of the mesh. Furthermore, the built-in function `mesh.Sf()` return a `surfaceVectorField` composed by the orthogonal vectors to the faces of the mesh, while the built-in function `mesh.magSf()` return a `surfaceScalarField` composed by the magnitude of the orthogonal vectors to the faces of the mesh. Thus, using this functions, we can calculate, for each cell  $cell_i$ , the radius  $r_{cell_i}$  of the biggest sphere included inside  $cell_i$  and which center coincides with the centroid of  $cell_i$ :

$$r_{cell_i, face_j} = |[mesh.C(cell_i) - mesh.Cf(face_j)] \cdot mesh.Sf(face_j)| / mesh.magSf(face_j)$$

$$r_{cell_i} = \min_{face_j \in \partial cell_i} r_{cell_i, face_j}.$$

Finally, we can define the time step as

$$\Delta t = \nu \cdot \min_{cell_i} \left( \frac{2r_{cell_i}}{|\vec{\varrho}_{cell_i}|} \right), \quad (\text{B.2})$$

where  $\nu$  is the Courant Number.

### *(ii) Linear reconstruction at the cells interfaces*

Once the time step is computed, we can proceed with the second step, the computation of the linear reconstruction at the cells interfaces. As described in Section 4.1, we apply the linear reconstruction to the physical variables. Thus, first of all, we have to calculate the physical variables from the conservative ones, then compute the linear reconstruction of the physical variables and finally come back to the conservative ones. OpenFOAM has already available a built-in function computing the linear reconstruction of fields from the centroid of the cells to the centroid of the faces: `fvc::interpolate`. As an example, we report here the instructions used to perform the linear reconstruction of the physical variable  $\alpha_1$  (i.e. the volume fraction of the first phase):

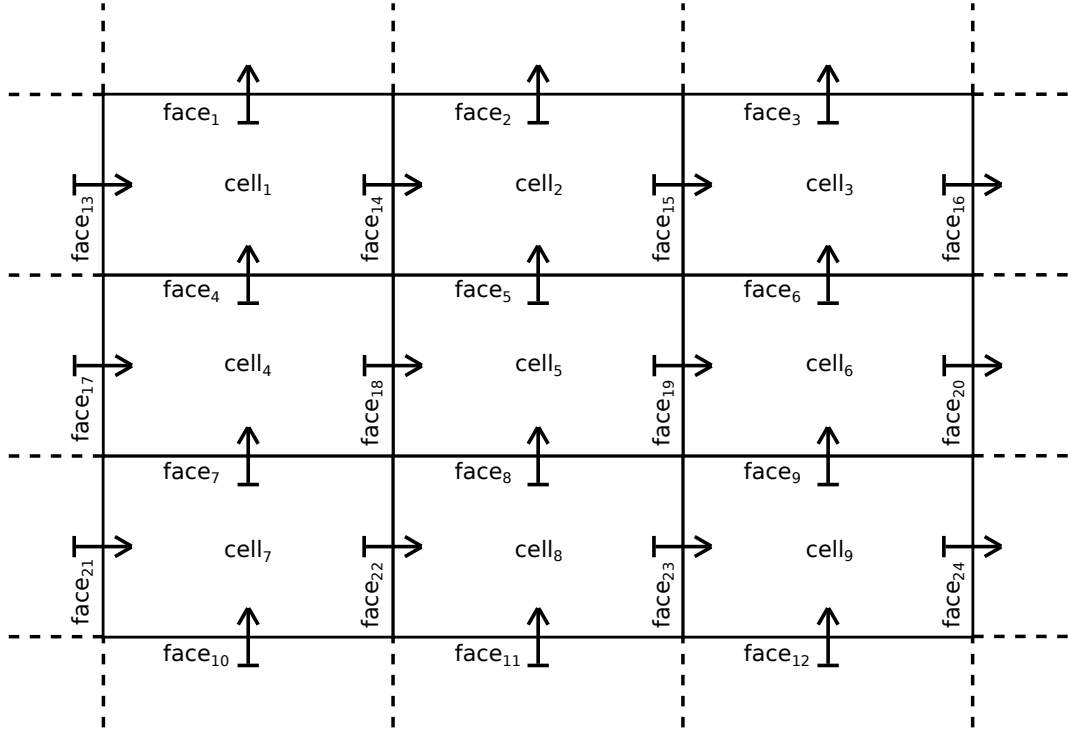


Figure 73: Schematic representation of a two-dimensional grid with uniform step-size. The arrows that intersect the interfaces between two adjacent cells are oriented according to the *owner/neighbor* direction.

```
alpha1_pos = fvc::interpolate(alpha1, pos, "reconstruct(alpha1)") ;
alpha1_neg = fvc::interpolate(alpha1, neg, "reconstruct(alpha1)") ;
```

In 1D we have defined the reconstructed variables at the two sides of each interfaces. In the implementation in OpenFOAM we have used for these reconstruction the same notation adopted in *rhoCentralFoam*, i.e. *\_pos* and *\_neg*. For each cell interface, OpenFOAM defines two functions: *owner* and *neighbor*. Each of them returns one of the two cells that are separated by that interface. Fig. 73 shows a schematic representation of a two-dimensional grid. In this illustration, for each face we have added an arrow, whose tail and head are located in the owner and neighbor cells of the face respectively. Then, for example, the face  $face_{18}$  has as owner the cell  $cell_4$  and as neighbor the cell  $cell_5$ . Using this notation we have

$$\begin{aligned} (\alpha_1, pos)_{face_{18}} &= (\alpha_1)_{cell_4} + (dist(cell_4, face_{18}), [(\alpha_1)_{cell_4}]') \\ (\alpha_1, neg)_{face_{18}} &= (\alpha_1)_{cell_5} - (dist(cell_5, face_{18}), [(\alpha_1)_{cell_5}]') \end{aligned}$$

where  $[(\alpha_1)_{cell_i}]'$  is an approximation of the first derivative at the  $cell_i$  and  $dist(cell_i, face_j)$  is the distance between the centroid of the cell  $cell_i$  and the centroid of the face  $face_j$ . In general, the linear reconstruction can be computed as follows:

$$\begin{aligned} (\alpha_1, pos)_{face_j} &= (\alpha_1)_{owner(face_j)} + [dist(owner(face_j), face_j)] [(\alpha_1)_{owner(face_j)}]', \\ (\alpha_1, neg)_{face_j} &= (\alpha_1)_{neighbor(face_j)} - [dist(neighbor(face_j), face_j)] [(\alpha_1)_{neighbor(face_j)}]'. \end{aligned} \quad (B.3)$$

Depending on the choice of the approximation of the first derivative, we can obtain different linear reconstructions. The user can choose several existing approximations

for the first derivative, among which we find approximations based on the Minmod or the Vanleer limiter used in this thesis. With OpenFOAM this can be done in the file `fvSchemes` in the directory `system` present in the case folder. An example of the syntax used to set the Minmod limiter is reported below:

```
interpolationSchemes
{
    reconstruct(alpha1) Minmod;
}
```

Restricting to the one dimensional case, if we assume that

$$face_j = j + \frac{1}{2}, \quad owner(face_j) = j, \quad neighbor(face_j) = j + 1, \quad (\text{B.4})$$

then

$$(\mathbf{U}_{neg})_{face_j} = (\mathbf{U})_{j+\frac{1}{2},R} \quad (\mathbf{U}_{pos})_{face_j} = (\mathbf{U})_{j+\frac{1}{2},L}. \quad (\text{B.5})$$

### (iii) Computation of the predictor step at the cells interfaces

At this point, if requested by the user, the predictor step of the predictor/corrector strategy will be applied. This can be done again in the file `fvSchemes`. To apply the predictor/corrector strategy we have to set to `true` the parameter `predictorCorrector`:

```
predictorCorrector true;
```

We remind here that the solver `rhoCentralFoam` does not use the predictor/corrector strategy.

As described in Chapter 2, in the predictor step we advance in time (with half time step) the linear reconstruction at the interfaces computed before. In 1D, the predictor step consists in calculating the solution at the cell interfaces at the time  $t^{n+1/2}$  according to the scheme presented in Eqs. (3.12)-(3.13). Using the expressions in Eq. (B.4)-(B.5) the 1D predictor step becomes

$$(\mathbf{U}_{pos})_{face_j}^{n+\frac{1}{2}} = (\mathbf{U}_{pos})_{face_j}^n - \frac{\Delta t}{2\Delta x} \left( \mathbf{F}((\mathbf{U}_{pos})_{face_j}^n) - \mathbf{F}((\mathbf{U}_{neg})_{face_{j-1}}^n) \right), \quad (\text{B.6})$$

$$(\mathbf{U}_{neg})_{face_j}^{n+\frac{1}{2}} = (\mathbf{U}_{neg})_{face_j}^n - \frac{\Delta t}{2\Delta x} \left( \mathbf{F}((\mathbf{U}_{pos})_{face_{j+1}}^n) - \mathbf{F}((\mathbf{U}_{neg})_{face_j}^n) \right). \quad (\text{B.7})$$

In Eq. (B.6),  $(\mathbf{U}_{pos})_{face_j}$  is reconstructed, according to Eq. (B.3), from the values of the variables inside the cell  $owner(face_j)$ . Similarly, in Eq. (B.7),  $(\mathbf{U}_{neg})_{face_j}$  is reconstructed from the values of the variables inside the cell  $neighbor(face_j)$ .

Using these considerations, we can define the three-dimensional predictor step as

$$(\mathbf{U}_{pos})_{face_j}^{n+\frac{1}{2}} = (\mathbf{U}_{pos})_{face_j}^n - \frac{0.5 \cdot \Delta t}{V(owner(face_j))} \int_{Vol(owner(face_j))} \nabla \cdot \mathbf{F}(\mathbf{U}) dV,$$

$$(\mathbf{U}_{neg})_{face_j}^{n+\frac{1}{2}} = (\mathbf{U}_{neg})_{face_j}^n - \frac{0.5 \cdot \Delta t}{V(neighbor(face_j))} \int_{Vol(neighbor(face_j))} \nabla \cdot \mathbf{F}(\mathbf{U}) dV,$$

where  $V(cell_i)$  is the volume of the cell  $cell_i$ .

The integrals in the above equations are linearized, as reported in the Programmer's Guide, using the Gauss theorem:

$$\int_{cell_i} \nabla \cdot \mathbf{F}(\mathbf{U}) dV = \int_{\partial cell_i} \mathbf{F}(\mathbf{U}) \cdot \vec{n} dS \approx \sum_{face_j \in cell_i} \Phi(\mathbf{U}, \vec{S}_{face_j}), \quad (B.8)$$

where

$$\Phi(\mathbf{U}, \vec{S}_{face_j}) = \begin{cases} \rho(\vec{u} \cdot \vec{S}_{face_j}) \\ \rho\alpha_1(\vec{u} \cdot \vec{S}_{face_j}) \\ \rho_1\alpha_1(\vec{u}_1 \cdot \vec{S}_{face_j}) \\ (\vec{u}_1 \cdot \vec{S}_{face_j})(\rho_1\alpha_1\vec{u}_1) + (\vec{u}_2 \cdot \vec{S}_{face_j})(\rho_2\alpha_2\vec{u}_2) + (\alpha_1 P_1 + \alpha_2 P_2)\vec{S}_{face_j} \\ (\vec{u}_1 \cdot \vec{S}_{face_j})\frac{\vec{u}_1}{2} - (\vec{u}_2 \cdot \vec{S}_{face_j})\frac{\vec{u}_2}{2} + \left(e_1 + \frac{P_1}{\rho_1} - e_2 - \frac{P_2}{\rho_2} - (s_1 - s_2)T\right)\vec{S}_{face_j} \\ \sum_{i=1}^2 \left[ \alpha_i \rho_i \left( e_i + \frac{|\vec{u}_i|^2}{2} + \frac{P_i}{\rho_i} \right) (\vec{u}_i \cdot \vec{S}_{face_j}) \right] - \rho c(1 - c)(s_1 - s_2)T(\vec{w} \cdot \vec{S}_{face_j}) \end{cases} \quad (B.9)$$

and  $\vec{S}_{face_j}$  is a vector normal to the face  $face_j$  pointing out of the owner cell, whose magnitude is that of the area of  $face_j$ . In OpenFOAM there is a built-in function that returns a field vectors similar to  $\vec{S}_{face_j}$ : `mesh.Sf()`. For each face  $face_j$ , `mesh.Sf()[face_j]` is a vector that has the magnitude and direction of  $\vec{S}_{face_j}$ , but instead of pointing out of the owner cell, is oriented in the direction owner-neighbor (as the arrows illustrated in Fig. 73).

Therefore, the three-dimensional predictor step can be computed as

$$(\mathbf{U}_{pos})_{face_j}^{n+\frac{1}{2}} = (\mathbf{U}_{pos})_{face_j}^n - \frac{0.5 \cdot \Delta t}{V(owner(face_j))} \cdot \left[ \left( \sum_{\{face_i | owner(face_i) = owner(face_j)\}} \Phi((\mathbf{U}_{pos})_{face_i}^n, mesh.Sf()[face_i]) \right) - \left( \sum_{\{face_i | neighbor(face_i) = owner(face_j)\}} \Phi((\mathbf{U}_{neg})_{face_i}^n, mesh.Sf()[face_i]) \right) \right], \quad (B.10)$$

$$(\mathbf{U}_{neg})_{face_j}^{n+\frac{1}{2}} = (\mathbf{U}_{neg})_{face_j}^n - \frac{0.5 \cdot \Delta t}{V(neighbor(face_j))} \cdot \left[ \left( \sum_{\{face_i | owner(face_i) = neighbor(face_j)\}} \Phi((\mathbf{U}_{pos})_{face_i}^n, mesh.Sf()[face_i]) \right) - \left( \sum_{\{face_i | neighbor(face_i) = neighbor(face_j)\}} \Phi((\mathbf{U}_{neg})_{face_i}^n, mesh.Sf()[face_i]) \right) \right]. \quad (B.11)$$

where the minus sign inside the square brackets is added to correct the orientation of the vector obtained with the built-in function `mesh.Sf()[face_i]`.

Thus, for example, if we consider the face  $face_{18}$  in Fig. 73, we have

$$\begin{aligned}
 (\mathbf{U}_{pos})_{face_{18}}^{n+\frac{1}{2}} &= (\mathbf{U}_{pos})_{face_{18}}^n - \frac{0.5 \cdot \Delta t}{V(cell_4)} \cdot \\
 &\cdot \left[ \Phi((\mathbf{U}_{pos})_{face_{18}}^n, mesh.Sf()[face_{18}]) + \Phi((\mathbf{U}_{pos})_{face_4}^n, mesh.Sf()[face_4]) - \right. \\
 &\left. - \Phi((\mathbf{U}_{neg})_{face_7}^n, mesh.Sf()[face_7]) - \Phi((\mathbf{U}_{neg})_{face_{17}}^n, mesh.Sf()[face_{17}]) \right], \\
 (\mathbf{U}_{neg})_{face_{18}}^{n+\frac{1}{2}} &= (\mathbf{U}_{neg})_{face_{18}}^n - \frac{0.5 \cdot \Delta t}{V(cell_5)} \cdot \\
 &\cdot \left[ \Phi((\mathbf{U}_{pos})_{face_{19}}^n, mesh.Sf()[face_{19}]) + \Phi((\mathbf{U}_{pos})_{face_5}^n, mesh.Sf()[face_5]) - \right. \\
 &\left. - \Phi((\mathbf{U}_{neg})_{face_8}^n, mesh.Sf()[face_8]) - \Phi((\mathbf{U}_{neg})_{face_{18}}^n, mesh.Sf()[face_{18}]) \right].
 \end{aligned}$$

We note that if we consider a mesh in which only one axis is discretized (for example  $x$  axis) with a constant step size, then Eq. (B.10)-(B.11) reduce to Eq. (B.6)-(B.7).

#### (iv) Application of the interfaces relaxations

Now, if requested by the user, the relaxation terms and the source terms will be applied to the local data at the cell interfaces. This can be done in the file `fvSchemes`. To apply the interface relaxation strategy the parameter `interphaseRelaxation` has to be set to `true`:

```
interphaseRelaxation true;
```

Note that this step is independent from the previous one. Thus, if the predictor/corrector strategy is used, then the interface relaxation will be applied to  $(\mathbf{U}_{pos})_{face_j}^{n+\frac{1}{2}}$  and  $(\mathbf{U}_{neg})_{face_j}^{n+\frac{1}{2}}$ , otherwise will be applied to  $(\mathbf{U}_{pos})_{face_j}^n$  and  $(\mathbf{U}_{neg})_{face_j}^n$ . In this part of the solver we have implemented the integration of the source terms (pressure relaxation, velocity relaxation, phase exchanges and gravity terms) we have discussed in Section 3.1.2.

#### (v) Calculation of the local speeds at the cells interfaces

At this point, from the local data computed after step (iv) of the procedure, we calculate the local speeds at the cells interfaces. Unlike we have done for the computation of the time step, for which the local speed have been calculated at the centroid of the con-

trol volumes, this time we need the vectors of the maximum and minimum eigenvalues of Jacobian evaluated at the cells interfaces, i.e.

$$\begin{aligned} (\vec{\lambda}_{pos})_{face_j} &= \left[ ((\lambda_{pos})_{face_j})_x, ((\lambda_{pos})_{face_j})_y, ((\lambda_{pos})_{face_j})_z \right]^T, \\ (\vec{\lambda}_{neg})_{face_j} &= \left[ ((\lambda_{neg})_{face_j})_x, ((\lambda_{neg})_{face_j})_y, ((\lambda_{neg})_{face_j})_z \right]^T, \\ (\vec{\mu}_{pos})_{face_j} &= \left[ ((\mu_{pos})_{face_j})_x, ((\mu_{pos})_{face_j})_y, ((\mu_{pos})_{face_j})_z \right]^T, \\ (\vec{\mu}_{neg})_{face_j} &= \left[ ((\mu_{neg})_{face_j})_x, ((\mu_{neg})_{face_j})_y, ((\mu_{neg})_{face_j})_z \right]^T, \end{aligned} \quad (B.12)$$

where with  $\lambda$  we are indicating the maximum eigenvalues, while with  $\mu$  the minimum ones. From these equations, we can define the local speeds as

$$\begin{aligned} (a^+)_{face_j} &= \max \left[ (\vec{\lambda}_{pos})_{face_j} \cdot mesh.Sf() [face_j], \right. \\ &\quad \left. (\vec{\lambda}_{neg})_{face_j} \cdot mesh.Sf() [face_j], 0.0 \right], \\ (a^-)_{face_j} &= \min \left[ (\vec{\mu}_{pos})_{face_j} \cdot mesh.Sf() [face_j], \right. \\ &\quad \left. (\vec{\mu}_{neg})_{face_j} \cdot mesh.Sf() [face_j], 0.0 \right]. \end{aligned} \quad (B.13)$$

We remark here that this step is avoided if the user choose the LF or LFMod numerical fluxes, since the local speeds at the cells interfaces are not needed. This makes the execution of the solver with LF and LFMod much faster with respect that using GF, KT or KNP.

#### (vi) Computation of the numerical fluxes

Once the local speeds are computed we can proceed with the computation of the numerical fluxes presented in Chapter 3. For example, using the notation introduced so far, the KNP numerical fluxes are computed as

$$\begin{aligned} \tilde{\mathbf{F}}_{face_j}^{(KNP)} &= [(a)_{pos}]_{face_j} \mathbf{F}((\mathbf{U}_{pos})_{face_j}) - [(a)_{neg}]_{face_j} \mathbf{F}((\mathbf{U}_{neg})_{face_j}) + \\ &\quad + (a^-)_{face_j} [(a)_{pos}]_{face_j} \left( \mathbf{U}_{i+\frac{1}{2},R} - \mathbf{U}_{i+\frac{1}{2},L} \right), \end{aligned} \quad (B.14)$$

where we have defined

$$\begin{aligned} [(a)_{pos}]_{face_j} &= \frac{(a^+)_{face_j}}{(a^+)_{face_j} - (a^-)_{face_j}}, \\ [(a)_{neg}]_{face_j} &= \frac{(a^-)_{face_j}}{(a^+)_{face_j} - (a^-)_{face_j}}. \end{aligned} \quad (B.15)$$

The user can choose the numerical fluxes in the file `fvSchemes`. An example of the instruction needed to use the KNP numerical fluxes is the following:

```
fluxScheme      KNP;
```

The possible choices available are the following: LF, LFMod, GF, KT and KNP.

(vii) Computation of the solution  $(\mathbf{U}^{t+\Delta t})^*$  of the hyperbolic part of PDEs

Finally we can compute the solution of the hyperbolic part of Eq. (2.8). In OpenFOAM this can be performed using the following instruction:

```
solve( fvm::ddt(U) + fvc::div(FLUX_U) );
```

where U is one of the conservative variables and FLUX\_U is the correspondent numerical flux computed previously. Thus, the previous instruction has to be performed for all conservative variables of the system. Furthermore OpenFOAM allow us to use several discretization for the time derivative or for the computation of the divergence. The user can choose the different discretization in the fvSchemes file. In order to have the same discretization used in Eq. (3.7) we have to set

```
ddtSchemes
{
    default      Euler;
}
```

and

```
divSchemes
{
    default      upwind;
}
```

(viii) Computation of the solution  $\mathbf{U}^{t+\Delta t}$  integrating the source terms

With the previous step we conclude the first part of the splitting approach. Now, in order to have the correct solution of Eq. (2.8), we have to integrate the ODE system  $\mathbf{U}_t = \mathbf{S}(\mathbf{U})$  with initial condition  $(\mathbf{U}^{t+\Delta t})_{cell_i}^*$  (that we have computed in the previous step) and time step  $\Delta t$ . This is done as described for the integration of the source/relaxation terms at the cell interfaces.

(ix) Correction of the solution at the boundaries

Once the integration of the source terms is completed, the calculation of the new solution is completed and then we can start again the process to advance of another time step. Before of that, although, we have to correct the solutions at the boundaries. This can be done using the OpenFOAM function

```
U.correctBoundaryConditions();
```

In this way the boundary values of the variable U will be corrected according to the boundary conditions specified in the 0 directory of the case folder. In general, the boundary conditions are specified for the physical variables. Thus we have to pass from the conservative variables to the physical ones, correct the boundary conditions for all of them and then go back to the conservative variables.

### B.2.2 Runge-Kutta approach solver: twoPhaseCentralFoamDIRK

In this section we describe the implementation of the Runge-Kutta approach in the OpenFOAM framework, based on the DIRK schemes proposed in this work in Section 3.2. We have considered only the DIRK schemes with the additional condition  $b_k = a_{\nu,k}$  and  $\tilde{b}_k = \tilde{a}_{\nu,k}$  for all the internal steps  $k = 1, \dots, \nu$  of the Runge-Kutta scheme. Thus, for each time step we compute

$$\mathbf{U}_i^{(j)} = \mathbf{U}_i^n - \Delta t \sum_{k=1}^{j-1} \tilde{a}_{jk} \left( \frac{\tilde{\mathbf{F}}_{i+\frac{1}{2}}^{(k)} - \tilde{\mathbf{F}}_{i-\frac{1}{2}}^{(k)}}{\Delta x} - \hat{\mathbf{S}}(\mathbf{U}_i^{(k)}) \right) + \Delta t \cdot \frac{1}{\tau} \sum_{k=1}^j a_{jk} \mathbf{R}(\mathbf{U}_i^{(k)}), \quad (\text{B.16})$$

for all  $j = 1, \dots, \nu$  and finally we advance in time posing  $\mathbf{U}^{n+1} = \mathbf{U}^{(\nu)}$ . In the previous equation  $\tilde{\mathbf{F}}_{i+\frac{1}{2}}$  is the vector of the numerical fluxes,  $\hat{\mathbf{S}}(\mathbf{U}_i)$  is the vector of the source terms (which, in this implementation, is composed only by the gravity terms) and  $\mathbf{R}(\mathbf{U}_i)$  is the vector of the relaxation terms.

The implementation of this solver is based on the *twoPhaseCentralFoam* presented in the previous section, thus we have named it *twoPhaseCentralFoamDIRK*.

An overview of the implementation of the *twoPhaseCentralFoamDIRK* solver is presented below. Given the solution  $\mathbf{U}^t$  at the time  $t$ , the new solution  $\mathbf{U}^{t+\Delta t}$  at the time  $t + \Delta t$  is computed as follows:

(i) Computation of the time step  $\Delta t$ .

For  $j = 1, \dots, \nu$

(ii) Computation of the numerical fluxes

(iii) Evaluation of the source and relaxation terms

(iv) Computation of the explicit terms in the DIRK schemes

(v) Computation of the solution  $\mathbf{U}_{cell_i}^{(j)}$

(vi) Correction of the solution at the boundaries

(vii) Set  $\mathbf{U}^{t+\Delta t} = \mathbf{U}^{(\nu)}$ .

(i) Computation of the time step

Before starting the Runge-Kutta iterations, we have to compute the time step. This will be done as described for the splitting approach, thus no further explanations are needed.

(ii) Computation of the numerical fluxes

For each internal Runge-Kutta step, we have first to compute the numerical fluxes used in Eq. (B.16). This step is implemented as we have done for the splitting approach, with the difference that the interface relaxation is not considered. That means that this step is done following (ii)., (iii)., (v). and (vi). of the *twoPhaseCentralFoam* solver.

## (iii) Evaluation of the source and relaxation terms

In this step we evaluate the source and relaxation terms with the solution  $\mathbf{U}_{cell_i}^{(j)}$  at the centroid of the cells. We remark that we are not integrating the source and relaxation terms as done in the splitting approach, but we are only evaluating them as functions of the conservative variable  $\mathbf{U}_{cell_i}^{(j)}$ .

## (iv) Computation of the explicit terms in the DIRK schemes

Now, as is done in Eq. (3.79), we separate the implicit terms of the Eq. (B.16) from the explicit ones, since these terms will not change during the steps of the iterative method used for the solution of the nonlinear system resulting from the implicit discretization and thus they can be computed once for each internal iteration of the Runge–Kutta scheme. To compute these terms we need to know which DIRK scheme has been chosen by the user. The choice of the DIRK scheme is done in the file `fvschemes`. An example of the instruction needed to use the DIRK ARS scheme is the following:

```
DIRKScheme      ARS;
```

The possible choices available are the following: IEE, ARS, LRR and BPR.

(v) Computation of the solution  $\mathbf{U}_{cell_i}^{(j+1)}$ 

This step is the core of the solver. It is the implementation of the Newton-Raphson method

$$\begin{cases} \mathbf{x}_{(l+1)} = \mathbf{x}_{(l)} - J_{|\mathbf{x}_{(l)}}^{-1} \cdot \Gamma(\mathbf{x}_{(l)}), \\ \mathbf{x}_{(0)} = \mathbf{U}_i^n, \end{cases} \quad (\text{B.17})$$

for  $l \geq 0$ , where

$$\begin{aligned} \Gamma(\mathbf{x}) &= \mathbf{x} - \Delta t \cdot \frac{1}{\tau} a_{jj} \mathbf{R}(\mathbf{x}) - \Lambda_i, \\ J &= \frac{\partial \Gamma}{\partial \mathbf{x}} = \mathbf{I} - \Delta t \cdot \frac{1}{\tau} a_{jj} \frac{\partial \mathbf{R}}{\partial \mathbf{x}} \approx \mathbf{I} - \Delta t \cdot \frac{1}{\tau} a_{jj} \frac{\Im(\tilde{\mathbf{R}}(\mathbf{x} + i h \mathbf{e}_n))}{h}, \end{aligned} \quad (\text{B.18})$$

$\tilde{\mathbf{R}}$  is the extension of the function of the relaxation terms to the complex plane,  $h$  is the step size for the discretization of the jacobian (here of the order of the machine working precision),  $i$  is the complex unity,  $(\mathbf{e}_n)_{n=1,\dots,m}$  is the canonical base of  $\mathbb{R}^m$  ( $m$  is the number of equations considered in the system) and  $a_{jj}$  are the diagonal coefficients of the matrix  $A$  defined by the DIRK scheme chosen and finally  $\Lambda_i$  are the explicit terms computed at the step (iv) of the procedure.

Once the jacobian  $J$  is calculated, we have to compute the vector

$$\Delta \mathbf{x}_{(l)} = J_{|\mathbf{x}_{(l)}}^{-1} \cdot \Gamma(\mathbf{x}_{(l)}) \iff (J_{|\mathbf{x}_{(l)}}) \Delta \mathbf{x}_{(l)} = \Gamma(\mathbf{x}_{(l)}). \quad (\text{B.19})$$

Therefore,  $\Delta \mathbf{x}_{(l)}$  is the solution of the linear system  $A \mathbf{y} = b$  where  $A = J_{|\mathbf{x}_{(l)}}$  and  $b = \Gamma(\mathbf{x}_{(l)})$ . With OpenFOAM it is possible to define an object that is composed by a matrix and a vector. This class of variables is called `simpleMatrix`. With the instruction

```
simpleMatrix<double> A(10);
```

we define a square matrix of double precision real numbers with 10 rows and columns. Furthermore, the column vector (of size 10)  $A.\text{solve}()$  is associated to  $A$ . Finally, with the instruction we obtain a vector  $\mathbf{y}$  which is the solution of the linear system  $A\mathbf{y} = A.\text{source}()$ . So, defining  $A = J|_{\mathbf{x}_{(l)}}$  and  $A.\text{source}() = \Gamma(\mathbf{x}_{(l)})$ , we can easily calculate the solution of the linear system  $\Delta\mathbf{x}_{(l)}$ . At this point we can compute the new guess for the solution of the nonlinear system as

$$\mathbf{x}_{(l+1)} = \mathbf{x}_{(l)} - \Delta\mathbf{x}_{(l)} \quad (\text{B.20})$$

and iterate this step of the procedure until  $\Delta\mathbf{x}_{(l+1)}$  or  $\Gamma(\mathbf{x}_{(l+1)})$  are small enough.

*(vi) Correction of the solution at the boundaries*

As done for the splitting approach, at the end of each Runge-Kutta step we have to correct the solutions at the boundaries. This can be done using the instruction

```
U.correctBoundaryConditions();
```

Since the boundary conditions are generally specified for the physical variables at first we have to pass from the conservative variables (obtained in the Runge-Kutta step) to the physical ones, then correct the boundaries accordingly to the specified boundary conditions, and finally go back to the conservative variables. After that, if we are at the final iteration of the Runge-Kutta, we save the obtained conservative variables and restart from step (i), otherwise we go to the step (ii) for the next the Runge-Kutta iteration.

---

## BIBLIOGRAPHY

---

- Alidibirov, M. A. (1994). A model for viscous magma fragmentation during volcanic blasts. *Bulletin of Volcanology*, 56(6-7):459–465.
- Anderson, W. K., Newman, J. C., Whitfield, D. L., and Nielsen, E. J. (2001). Sensitivity analysis for Navier-Stokes equations on unstructured meshes using complex variables. *AIAA journal*, 39(1):56–63.
- Andrianov, N., Saurel, R., and Warnecke, G. (2003). A simple method for compressible multiphase mixtures and interfaces. *International Journal for Numerical Methods in Fluids*, 41(2):109–131.
- Andrianov, N. and Warnecke, G. (2004). The Riemann problem for the Baer-Nunziato two-phase flow model. *Journal of Computational Physics*, 195(2):434–464.
- Arminjon, P., St-Cyr, A., and Madrane, A. (2002). New two- and three-dimensional non-oscillatory central finite volume methods on staggered Cartesian grids. *Applied numerical mathematics*, 40(3):367–390.
- Arminjon, P. and Touma, R. (2005). Central finite volume methods with constrained transport divergence treatment for ideal MHD. *Journal of Computational Physics*, 204(2):737–759.
- Baer, M. and Nunziato, J. (1986). A two-phase mixture theory for the deflagration-to-detonation transition (ddt) in reactive granular materials. *International Journal of Multiphase Flow*, 12(6):861–889.
- Barclay, J., Rutherford, M. J., Carroll, M. R., Murphy, M. D., Devine, J. D., Gardner, J., and Sparks, R. S. J. (1998). Experimental phase equilibria constraints on pre-eruptive storage conditions of the Soufriere Hills magma. *Geophysical Research Letters*, 25(18):3437–3440.
- Bernard, M.-L., Zamora, M., Géraud, Y., and Boudon, G. (2007). Transport properties of pyroclastic rocks from Montagne Pelée volcano (Martinique, Lesser Antilles). *Journal of Geophysical Research: Solid Earth* (1978–2012), 112(B5).
- Bianco, F., Puppo, G., and Russo, G. (1999). High order central schemes for hyperbolic systems of conservation laws. *SIAM Journal on Scientific Computing*, 21(1):294–322.
- Brujan, E.-A., Nahen, K., Schmidt, P., and Vogel, A. (2001). Dynamics of laser-induced cavitation bubbles near an elastic boundary. *Journal of Fluid Mechanics*, 433(1):251–281.
- Brujan, E.-A. and Vogel, A. (2006). Stress wave emission and cavitation bubble dynamics by nanosecond optical breakdown in a tissue phantom. *Journal of Fluid Mechanics*, 558(1):281–308.
- Burnham, C. W. (1979). Magmas and hydrothermal fluids. In L.Barnes, H., editor, *Geochemistry of Hydrothermal Ore Deposits*, 71–136. J.Wiley and Sons.

- Caflisch, R. E., Jin, S., and Russo, G. (1997). Uniformly accurate schemes for hyperbolic systems with relaxation. *SIAM Journal on Numerical Analysis*, 34(1):246–281.
- Caricchi, L., Burlini, L., Ulmer, P., Gerya, T., Vassalli, M., and Papale, P. (2007). Non-Newtonian rheology of crystal-bearing magmas and implications for magma ascent dynamics. *Earth and Planetary Science Letters*, 264(3–4):402–419.
- Chojnicki, K., Clarke, A. B., and Phillips, J. C. (2006). A shock-tube investigation of the dynamics of gas-particle mixtures: Implications for explosive volcanic eruptions. *Geophysical Research Letters*, 33(15):L15309.
- Clarke, A. B. (2013). Unsteady explosive activity: vulcanian eruptions. *Modeling Volcanic Processes: The Physics and Mathematics of Volcanism*, Cambridge Univ Press, 129–152.
- Clarke, A. B., Neri, A., Macedonio, G., and Voight, B. (2002a). Transient dynamics of Vulcanian explosions and column collapse. *Nature*, 415:897–901.
- Clarke, A. B., Neri, A., Macedonio, G., Voight, B., and Druitt, T. H. (2002b). Computational modelling of the transient dynamics of the August 1997 Vulcanian explosions at Soufrière Hills Volcano, Montserrat: influence of initial conduit conditions on near-vent pyroclastic dispersal. In Druitt, T. and Kokelaar, B., editors, *The Eruption of Soufrière Hills Volcano, Montserrat, from 1995 to 1999*, Geological Society, London, Memoirs, 21:319–348.
- Costa, A. (2005). Viscosity of high crystal content melts: Dependence on solid fraction. *Geophysical Research Letters*, 32(22).
- Courant, R., Isaacson, E., and Rees, M. (1952). On the solution of nonlinear hyperbolic differential equations by finite differences. *Communications on Pure and Applied Mathematics*, 5(3):243–255.
- Dal Maso, G., LeFloch, P. G., and Murat, F. (1995). Definition and weak stability of nonconservative products. *Journal de mathématiques pures et appliquées*, 74(6):483–548.
- de' Michieli Vitturi, M., Clarke, A., Neri, A., and Voight, B. (2010a). Transient effects of magma ascent dynamics along a geometrically variable dome-feeding conduit. *Earth and Planetary Science Letters*, 295(3–4):541–553.
- de' Michieli Vitturi, M., Clarke, A. B., Neri, A., and Voight, B. (2008). Effects of conduit geometry on magma ascent dynamics in dome-forming eruptions. *Earth and Planetary Science Letters*, 272(3–4):567–578.
- de' Michieli Vitturi, M., Clarke, A. B., Neri, A., Voight, B., and La Spina, G. (2013a). Investigating disequilibrium effects in magma ascent dynamics with a new multiphase flow model. In *EGU General Assembly Conference Abstracts*, 15:10536.
- de' Michieli Vitturi, M., La Spina, G., and Romenski, E. (2013b). A compressible single temperature conservative two-phase model with phase transitions. *11th International conference of numerical analysis and applied mathematics 2013, AIP Conference Proceedings*, 1558(1):112–115.

- de' Michieli Vitturi, M., Neri, A., Esposti Ongaro, T., Lo Savio, S., and Boschi, E. (2010b). Lagrangian modeling of large volcanic particles: Application to Vulcanian explosions. *Journal of Geophysical Research: Solid Earth (1978–2012)*, 115(B8).
- Degruyter, W., Bachmann, O., and Burgisser, A. (2010). Controls on magma permeability in the volcanic conduit during the climactic phase of the Kos Plateau Tuff eruption (Aegean arc). *Bulletin of volcanology*, 72(1):63–74.
- Degruyter, W., Bachmann, O., Burgisser, A., and Manga, M. (2012). The effects of outgassing on the transition between effusive and explosive silicic eruptions. *Earth and Planetary Science Letters*, 349:161–170.
- Del Zanna, L., Bucciantini, N., and Londrillo, P. (2002). An efficient shock-capturing central-type scheme for multidimensional relativistic flows. II. Magnetohydrodynamics. *Astronomy and Astrophysics*, 400:397–413.
- Devine, J., Rutherford, M., and Gardner, J. (1998). Petrologic determination of ascent rates for the 1995–1997 Soufrière Hills Volcano andesitic magma. *Geophysical Research Letters*, 25(19):3673–3676.
- Dingwell, D. B., Bagdassarov, N. S., Bussod, J., and Webb, S. L. (1993). Magma Rheology. In Luth, R. W., editor, *Short course handbook on experiments at high pressure and applications to the Earth's mantle*, Mineralogical Association of Canada, Edmonton, 21:131–196.
- Drew, D. A. and Passman, S. L. (1999). *Theory of multicomponent fluids*, Springer.
- Druitt, T. H., Calder, E. S., Cole, P. D., Hoblitt, R. P., Loughlin, S. C., Norton, G. E., Ritchie, L. J., Sparks, R. S. J., and Voight, B. (2002). Small-volume, highly mobile pyroclastic flows formed by rapid sedimentation from pyroclastic surges at Soufrière Hills Volcano, Montserrat: an important volcanic hazard. In Druitt, T. and Kokelaar, B., editors, *The Eruption of Soufrière Hills Volcano, Montserrat, from 1995 to 1999*, Geological Society, London, Memoirs, 263–279.
- Druitt, T. H. and Kokelaar, P., editors (2002). *The Eruption of Soufrière Hills Volcano, Montserrat, from 1995 to 1999*, Geological Society, London, Memoirs.
- Dufek, J. and Bergantz, G. W. (2005). Transient two-dimensional dynamics of the upper conduit of a rhyolitic eruption: A comparison of the closure models for the granular stress. *Journal of Volcanology and Geothermal Research*, 143:113–132.
- Einfeldt, B., Munz, C.-D., Roe, P. L., and Sjögreen, B. (1991). On Godunov-type methods near low densities. *Journal of computational physics*, 92(2):273–295.
- Embidi, P. and Baer, M. (1992). Mathematical analysis of a two-phase continuum mixture theory. *Continuum Mechanics and Thermodynamics*, 4:279–312.
- François, B. and François, J. (1999). Duality solutions for pressureless gases, monotone scalar conservation laws, and uniqueness. *Communications in partial differential equations*, 24(11–12):2173–2189.
- Gardner, J. E., Thomas, R. M., Jaupart, C., and Tait, S. (1996). Fragmentation of magma during plinian volcanic eruptions. *Bulletin of Volcanology*, 58(2–3):144–162.

- Giachetti, T., Druitt, T., Burgisser, A., Arbaret, L., and Galven, C. (2010). Bubble nucleation, growth and coalescence during the 1997 vulcanian explosions of Soufrière Hills Volcano, Montserrat. *Journal of Volcanology and Geothermal Research*, 193(3):215–231.
- Giordano, D. and Dingwell, D. (2003). Viscosity of hydrous etna basalt: implications for plinian-style basaltic eruptions. *Bulletin of Volcanology*, 65(1):8–14.
- Giordano, D., Russell, J. K., and Dingwell, D. B. (2008). Viscosity of magmatic liquids: a model. *Earth and Planetary Science Letters*, 271(1):123–134.
- Godunov, S. and Romenskii, E. (2003). *Elements of continuum mechanics and conservation laws*. Springer Us.
- Godunov, S. K. (1959). A difference method for numerical calculation of discontinuous solutions of the equations of hydrodynamics. *Matematicheskii Sbornik*, 89(3):271–306.
- Godunov, S. K. and Romensky, E. (1995). Thermodynamics, conservation laws and symmetric forms of differential equations in mechanics of continuous media. *Computational fluid dynamics review*, 95:19–31.
- Gonnermann, H. M. and Manga, M. (2003). Explosive volcanism may not be an inevitable consequence of magma fragmentation. *Nature*, 426(6965):432–435.
- Gonnermann, H. M. and Manga, M. (2005). Nonequilibrium magma degassing: results from modeling of the ca. 1340 ad eruption of mono craters, california. *Earth and Planetary Science Letters*, 238(1):1–16.
- Gonnermann, H. M. and Manga, M. (2007). The fluid mechanics inside a volcano. *Annual Reviews of Fluid Mechanics*, 39:321–356.
- Greenshields, C. J., Weller, H. G., Gasparini, L., and Reese, J. M. (2010). Implementation of semi-discrete, non-staggered central schemes in a colocated, polyhedral, finite volume framework, for high-speed viscous flows. *International Journal for Numerical Methods in Fluids*, 63(1):1–21.
- Guillard, H. and Duval, F. (2007). A darcy law for the drift velocity in a two-phase flow model. *Journal of Computational Physics*, 224(1):288–313.
- Haas, J. and Sturtevant, B. (1987). Interaction of weak shock waves with cylindrical and spherical gas inhomogeneities. *Journal of Fluid Mechanics*, 181:41–76.
- Harten, A., Lax, P. D., and Leer, B. v. (1983). On upstream differencing and Godunov-type schemes for hyperbolic conservation laws. *SIAM review*, 25(1):35–61.
- Hess, K.-U. and Dingwell, D. B. (1996). Viscosities of hydrous leucogranitic melts: A non-Arrhenian model. *American Mineralogist*, 81:1297–1300.
- Hou, T. Y. and LeFloch, P. G. (1994). Why nonconservative schemes converge to wrong solutions: error analysis. *Mathematics of computation*, 62(206):497–530.
- Hou, T. Y., Rosakis, P., and LeFloch, P. (1999). A level-set approach to the computation of twinning and phase-transition dynamics. *Journal of Computational Physics*, 150(2):302–331.

- Hui, H. and Zhang, Y. (2007). Toward a general viscosity equation for natural anhydrous and hydrous silicate melts. *Geochimica et Cosmochimica Acta*, 71(2):403–416.
- Ishihara, K. (1985). Dynamical analysis of volcanic explosion. *Journal of geodynamics*, 3(3):327–349.
- Ishii, M. (1975). *Thermo-fluid dynamic theory of two-phase flow*. Collection de la Direction des études et recherches d'Électricité de France. Eyrolles.
- Jasak, H. (2006). Numerical solution algorithms for compressible flows: Lecture notes. *Faculty of Mechanical Engineering and Naval Architecture*, 2007.
- Jaupart, C. and Allègre, C. J. (1991). Gas content, eruption rate and instabilities of eruption regime in silicic volcanoes. *Earth and Planetary Science Letters*, 102:413–429.
- Jin, S. (1995). Runge-Kutta methods for hyperbolic conservation laws with stiff relaxation terms. *Journal of Computational Physics*, 122(1):51–67.
- Klug, C. and Cashman, K. V. (1994). Vesiculation of May 18, 1980, Mount St. Helens magma. *Geology*, 22(5):468–472.
- Koyaguchi, T. and Mitani, N. K. (2005). A theoretical model for fragmentation of viscous bubbly magmas in shock tubes. *Journal of Geophysical Research: Solid Earth (1978–2012)*, 110(B10).
- Kozono, T. and Koyaguchi, T. (2009). Effects of relative motion between gas and liquid on 1-dimensional steady flow in silicic volcanic conduits: 2. Origin of diversity of eruption styles. *Journal of Volcanology and Geothermal Research*, 180(1):37–49.
- Kreeft, J. and Koren, B. (2010). A new formulation of Kapila's five-equation model for compressible two-fluid flow, and its numerical treatment. *Journal of Computational Physics*, 229(18):6220–6242.
- Kueppers, U., Scheu, B., Spieler, O., and Dingwell, D. B. (2006). Fragmentation efficiency of explosive volcanic eruptions: A study of experimentally generated pyroclasts. *Journal of Volcanology and Geothermal Research*, 153(1-2):125–135.
- Kurganov, A., Noelle, S., and Petrova, G. (2001). Semidiscrete central-upwind schemes for hyperbolic conservation laws and Hamilton–Jacobi equations. *SIAM Journal on Scientific Computing*, 23(3):707–740.
- Kurganov, A. and Petrova, G. (2001). A third-order semi-discrete genuinely multidimensional central scheme for hyperbolic conservation laws and related problems. *Numerische Mathematik*, 88(4):683–729.
- Kurganov, A. and Tadmor, E. (2000). New high-resolution central schemes for nonlinear conservation laws and convection-diffusion equations. *Journal of Computational Physics*, 160(1):241–282.
- La Spina, G. and de' Michieli Vitturi, M. (2012). High-resolution finite volume central schemes for a compressible two-phase model. *SIAM Journal on Scientific Computing*, 34(6):B861–B880.

- Lax, P. D. (2005). Hyperbolic systems of conservation laws II. In Sarnak, P. and Majda, A., editors, *Selected Papers Volume I*, Springer New York, 233–262.
- Le Métayer, O., Massoni, J., and Saurel, R. (2004). Élaboration des lois d'état d'un liquide et de sa vapeur pour les modèles d'écoulements diphasiques. *International Journal of Thermal Sciences*, 43(3):265 – 276.
- Le Métayer, O., Massoni, J., and Saurel, R. (2005). Modelling evaporation fronts with reactive Riemann solvers. *Journal of Computational Physics*, 205(2):567–610.
- Le Pennec, J.-L., Hermitte, D., Dana, I., Pezard, P., Coulon, C., Cochemé, J.-J., Mulyadi, E., Ollagnier, F., and Revest, C. (2001). Electrical conductivity and pore-space topology of Merapi Lavas: Implications for the degassing of porphyritic andesite magmas. *Geophysical research letters*, 28(22):4283–4286.
- Lefloch, P. G. and Tzavaras, A. E. (1999). Representation of weak limits and definition of nonconservative products. *SIAM journal on mathematical analysis*, 30(6):1309–1342.
- Lejeune, A. M. and Richet, P. (1995). Rheology of crystal-bearing silicate melts: An experimental study at high viscosities. *Journal of Geophysical Research: Solid Earth (1978–2012)*, 100:4215–4229.
- LeVeque, R. J. (1992). *Numerical methods for conservation laws*. Birkhäuser Basel, 2nd edition.
- Levy, D., Puppo, G., and Russo, G. (1999). Central WENO schemes for hyperbolic systems of conservation laws. *Mathematical Modelling and Numerical Analysis*, 33(3):547–571.
- Levy, D., Puppo, G., and Russo, G. (2002). A fourth-order central WENO scheme for multidimensional hyperbolic systems of conservation laws. *SIAM Journal on scientific computing*, 24(2):480–506.
- Lie, K.-A. and Noelle, S. (2003). An improved quadrature rule for the flux-computation in staggered central difference schemes in multidimensions. *Journal of scientific computing*, 18(1):69–81.
- Liu, X.-D. and Tadmor, E. (1998). Third order nonoscillatory central scheme for hyperbolic conservation laws. *Numerische Mathematik*, 79:397–425.
- Liu, Y., Zhang, Y., and Behrens, H. (2005). Solubility of H<sub>2</sub>O in rhyolitic melts at low pressures and a new empirical model for mixed H<sub>2</sub>O–CO<sub>2</sub> solubility in rhyolitic melts. *Journal of Volcanology and Geothermal Research*, 143(1–3):219–235.
- Lyness, J. (1967). Numerical algorithms based on the theory of complex variable. In *Proceedings of the 1967 22nd national conference*, ACM, 125–133.
- Lyness, J. N. and Moler, C. B. (1967). Numerical differentiation of analytic functions. *SIAM Journal on Numerical Analysis*, 4(2):202–210.
- Macedonio, G., Neri, A., Martí, J., and Folch, A. (2005). Temporal evolution of flow conditions in sustained magmatic explosive eruptions. *Journal of Volcanology and Geothermal Research*, 143:153–172.

- Martins, J., Sturdza, P., and Alonso, J. J. (2001). The connection between the complex-step derivative approximation and algorithmic differentiation. *AIAA paper*, 921:2001.
- Martins, J. R. R. A., Kroo, I. M., and Alonso, J. J. (2000). An automated method for sensitivity analysis using complex variables. In *AIAA paper 2000-0689, 38th Aerospace Sciences Meeting*, 2000–0689.
- Martins, J. R. R. A., Sturdza, P., and Alonso, J. J. (2003). The complex-step derivative approximation. *ACM Transactions on Mathematical Software*, 29(3):245–262.
- Mason, R. M., Starostin, A. B., Melnik, O. E., and Sparks, R. S. J. (2006). From Vulcanian explosions to sustained explosive eruptions: the role of diffusive mass transfer in conduit flow dynamics. *Journal of Volcanology and Geothermal Research*, 153:148–165.
- Massol, H. and Jaupart, C. (1999). The generation of gas overpressure in volcanic eruptions. *Earth and Planetary Science Letters*, 166(1–2):57–70.
- Massol, H., Jaupart, C., and Pepper, D. W. (2001). Ascent and decompression of viscous vesicular magma in a volcanic conduit. *Journal of Geophysical Research: Solid Earth (1978–2012)*, 106:16223–16240.
- Mastin, L. G. (2002). Insights into volcanic conduit flow from an open-source numerical model. *Geochemistry Geophysics Geosystems*, 3(7):1–18.
- McBirney, A. and Murase, T. (1970). Factors governing the formation of pyroclastic rocks. *Bulletin Volcanologique*, 34(2):372–384.
- Melnik, O. and Sparks, R. S. J. (1999). Nonlinear dynamics of lava dome extrusion. *Nature*, 402:37–41.
- Melnik, O. and Sparks, R. S. J. (2002a). Dynamics of magma ascent and lava extrusion at Soufrière Hills Volcano, Montserrat. In Druitt, T. and Kokelaar, B., editors, *The Eruption of Soufrière Hills Volcano, Montserrat, from 1995 to 1999*, Geological Society, London, Memoirs, 21:153–171.
- Melnik, O. and Sparks, R. S. J. (2002b). Modelling of conduit flow dynamics during explosive activity at Soufrière Hills Volcano, Montserrat. In Druitt, T. and Kokelaar, B., editors, *The Eruption of Soufrière Hills Volcano, Montserrat, from 1995 to 1999*, Geological Society, London, Memoirs, 21:307–317.
- Melnik, O. and Sparks, R. S. J. (2005). Controls on conduit magma flow dynamics during lava dome building eruptions. *Journal of Geophysical Research: Solid Earth (1978–2012)*, 110(B2).
- Melnik, O. E. (2000). Dynamics of two-phase conduit flow of high-viscosity gas-saturated magma: Large variations of Sustained Explosive eruption intensity. *Bulletin of Volcanology*, 62:153–170.
- Menikoff, R. and Plohr, B. J. (1989). The Riemann problem for fluid flow of real materials. *Reviews of modern physics*, 61:75–130.
- Mercalli, G. (1907). *Vulcani attivi della Terra*. Ulrico Hoepli.

- Moore, G., Vennemann, T., and Carmichael, I. (1998). An empirical model for the solubility of H<sub>2</sub>O in magmas to 3 kilobars. *American Mineralogist*, 83(1):36–42.
- Morrissey, M. and Mastin, L. (2000). Vulcanian eruptions. *Encyclopedia of volcanoes*, 463–475.
- Murphy, M., Sparks, R., Barclay, J., Carroll, M., and Brewer, T. (2000). Remobilization of andesite magma by intrusion of mafic magma at the Soufriere Hills Volcano, Montserrat, West Indies. *Journal of Petrology*, 41(1):21–42.
- Murrone, A. and Guillard, H. (2005). A five equation reduced model for compressible two phase flow problems. *Journal of Computational Physics*, 202(2):664 – 698.
- Navon, O. and Lyakhovsky, V. (1998). Vesiculation processes in silicic magmas. *The physics of explosive volcanic eruptions*, 27–50.
- Nessyahu, H. and Tadmor, E. (1990). Non-oscillatory central differencing for hyperbolic conservation laws. *Journal of Computational Physics*, 87(2):408–463.
- Papale, P. (1999a). Modeling of the solubility of a two-component H<sub>2</sub>O+CO<sub>2</sub> fluid in silicate liquids. *American Mineralogist*, 84(4):477–492.
- Papale, P. (1999b). Strain-induced magma fragmentation in explosive eruptions. *Nature*, 397:425–428.
- Papale, P. (2001). Dynamics of magma flow in volcanic conduits with variable fragmentation efficiency and nonequilibrium pumice degassing. *Journal of Geophysical Research: Solid Earth (1978–2012)*, 106(B6):11043–11065.
- Papale, P., Moretti, R., and Barbato, D. (2006). The compositional dependence of the saturation surface of H<sub>2</sub>O+CO<sub>2</sub> fluids in silicate melts. *Chemical Geology*, 229(1-3):78–95.
- Pareschi, L. (2002). Central differencing based numerical schemes for hyperbolic conservation laws with relaxation terms. *SIAM journal on numerical analysis*, 39(4):1395–1417.
- Pareschi, L. and Russo, G. (2000). Implicit-explicit Runge–Kutta schemes for stiff systems of differential equations. *Recent trends in numerical analysis*, 3:269–289.
- Pareschi, L. and Russo, G. (2005). Implicit-explicit Runge–Kutta schemes and applications to hyperbolic systems with relaxation. *Journal of Scientific computing*, 25(1):129–155.
- Pelanti, M. (2005). *Wave propagation algorithms for multicomponent compressible flows with applications to volcanic jets*. PhD thesis, University of Washington.
- Pelanti, M. and LeVeque, R. J. (2006). High-resolution finite volume methods for dusty gas jets and plumes. *SIAM Journal on Scientific Computing*, 28(4):1335–1360.
- Polacci, M., Baker, D. R., Mancini, L., Tromba, G., and Zanini, F. (2006). Three-dimensional investigation of volcanic textures by X-ray microtomography and implications for conduit processes. *Geophysical Research Letters*, 33(13).

- Proussevitch, A. and Sahagian, D. (1998). Dynamics and energetics of bubble growth in magmas: Analytical formulation and numerical modeling. *Journal of Geophysical Research: Solid Earth (1978–2012)*, 103(B8):18223–18251.
- Proussevitch, A. A. and Sahagian, D. L. (1996). Dynamics of coupled diffusive and decompressive bubble growth in magmatic systems. *Journal of Geophysical Research: Solid Earth (1978–2012)*, 101(B8):17447–17455.
- Pyle, D. and Pyle, D. (1995). Bubble migration and the initiation of volcanic eruptions. *Journal of volcanology and geothermal research*, 67(4):227–232.
- Resnyansky, A. (2003). A thermodynamically complete model for simulation of one-dimensional multi-phase flows. Technical report, DSTO Report DSTO-TR-1510, Edinburgh, SA, Australia.
- Resnyansky, A. (2006). A thermodynamically complete model for one-dimensional two-phase flows with heat exchange. Technical report, DSTO Report DSTO-TR-1862, Edinburgh, SA, Australia.
- Resnyansky, A., Bourne, N., Millett, J., and Brown, E. (2011). Constitutive modeling of shock response of polytetrafluoroethylene. *Journal of Applied Physics*, 110(3):033530–15.
- Resnyansky, A. D. and Bourne, N. K. (2004). Shock-wave compression of a porous material. *Journal of Applied Physics*, 95(4):1760–1769.
- Robertson, R., Cole, P., Sparks, R., Harford, C., Lejeune, A., McGuire, W., Miller, A., Murphy, M., Norton, G., Stevens, N., et al. (1998). The explosive eruption of Soufrière Hills Volcano, Montserrat, West Indies, 17 September, 1996. *Geophysical Research Letters*, 25(18):3429–3432.
- Roe, P. L. (1981). Approximate Riemann solvers, parameter vectors, and difference schemes. *Journal of Computational Physics*, 43(2):357–372.
- Romenski, E., Drikakis, D., and Toro, E. (2010). Conservative models and numerical methods for compressible two-phase flow. *Journal of Scientific Computing*, 42(1):68–95.
- Romenski, E., Resnyansky, A., and Toro, E. (2007). Conservative hyperbolic formulation for compressible two-phase flow with different phase pressures and temperatures. *Quarterly of applied mathematics*, 65(2):259–279.
- Romenski, E. and Toro, E. (2004). Compressible two-phase flows: Two-pressure models and numerical methods. *Computational Fluid Dynamics Journal*, 13(3):403–416.
- Romenski, E., Zeidan, D., Slaouti, A., and Toro, E. (2003). Hyperbolic conservative model for compressible two-phase flow. *Reprint of the Isaac Newton Institute for Mathematical Sciences, NI03022-NPA, Cambridge, UK*, 1–13.
- Romensky, E. (2001). Thermodynamics and hyperbolic systems of balance laws in continuum mechanics. In *Godunov methods*, Springer, 745–761.
- Romensky, E. I. (1998). Hyperbolic systems of thermodynamically compatible conservation laws in continuum mechanics. *Mathematical and Computer Modelling*, 28(10):115–130.

- Rust, A. and Cashman, K. (2004). Permeability of vesicular silicic magma: inertial and hysteresis effects. *Earth and Planetary Science Letters*, 228(1):93–107.
- Saad, M. A. (1985). Compressible fluid flow. *Englewood Cliffs, NJ, Prentice-Hall, Inc.*, 560 p.
- Saar, M. O. and Manga, M. (1999). Permeability-porosity relationship in vesicular basalts. *Geophysical Research Letters*, 26(1):111–114.
- Sable, J. E., Houghton, B. F., Del Carlo, P., and Coltelli, M. (2006). Changing conditions of magma ascent and fragmentation during the Etna 122 BC basaltic Plinian eruption: Evidence from clast microtextures. *Journal of Volcanology and Geothermal Research*, 158(3):333–354.
- Sahagian, D. (2005). Volcanic eruption mechanisms: Insights from intercomparison of models of conduit processes. *Journal of Volcanology and Geothermal Research*, 143(1–3):1–15.
- Saito, T., Marumoto, M., and Takayama, K. (2003). Numerical investigations of shock waves in gas-particle mixtures. *Shock Waves*, 13:299–322.
- Saurel, R. and Abgrall, R. (1999). A multiphase Godunov method for compressible multifluid and multiphase flows. *Journal of Computational Physics*, 150(2):425–467.
- Saurel, R. and Le Métayer, O. (2001). A multiphase model for compressible flows with interfaces, shocks, detonation waves and cavitation. *Journal of Fluid Mechanics*, 431:239–271.
- Scardovelli, R. and Zaleski, S. (1999). Direct numerical simulation of free-surface and interfacial flow. *Annual Review of Fluid Mechanics*, 31(1):567–603.
- Self, S., Wilson, L., and Nairn, I. A. (1979). Vulcanian eruption mechanism. *Nature*, 277:440–443.
- Settles, G. S. (2001). *Schlieren and Shadowgraph techniques*. Springer.
- Sod, G. A. (1978). A survey of several finite difference methods for systems of nonlinear hyperbolic conservation laws. *Journal of Computational Physics*, 27(1):1–31.
- Sparks, R. S. J. (1978). The dynamics of bubble formation and growth in magmas: A review and analysis. *Journal of Volcanology and Geothermal Research*, 3(1–2):1–37.
- Sparks, R. S. J., Bursik, M. I., Carey, S. N., Gilbert, J. E., Glaze, L., Sigurdsson, H., and Woods, A. W. (1997). *Volcanic plumes*. John Wiley & Sons Inc.
- Spieler, O., Kennedy, B., Kueppers, U., Dingwell, D., Scheu, B., and Taddeucci, J. (2004). The fragmentation threshold of pyroclastic rocks. *Earth and Planetary Science Letters*, 226(1–2):139–148.
- Squire, W. and Trapp, G. (1998). Using complex variables to estimate derivatives of real functions. *Siam Review*, 40(1):110–112.
- Stewart, H. B. and Wendroff, B. (1984). Two-phase flow: Models and methods. *Journal of Computational Physics*, 56(3):363–409.

- Stix, J., Torres, R. C., Narvaez, M. L., Cortes, G. B., Raigosa, J. A., Gomes, D. M., and Castonguay, R. (1997). A model of Vulcanian eruptions at Galeras volcano, Colombia. *Journal of Volcanology and Geothermal Research*, 77(1–4):285–303.
- Strang, G. (1968). On the construction and comparison of difference schemes. *SIAM Journal on Numerical Analysis*, 5(3):506–517.
- Sweby, P. K. (1984). High resolution schemes using flux limiters for hyperbolic conservation laws. *SIAM journal on numerical analysis*, 21(5):995–1011.
- Tokareva, S. and Toro, E. (2010). HLLC-type Riemann solver for the Baer-Nunziato equations of compressible two-phase flow. *Journal of Computational Physics*, 229(10):3573–3604.
- Toro, E. (2009). *Riemann solvers and numerical methods for fluid dynamics: a practical introduction*. Springer Verlag.
- Toro, E. and Titarev, V. (2006). Musta fluxes for systems of conservation laws. *Journal of Computational Physics*, 216(2):403–429.
- Tryggvason, G., Bunner, B., Esmaeeli, A., Juric, D., Al-Rawahi, N., Tauber, W., Han, J., Nas, S., and Jan, Y.-J. (2001). A front-tracking method for the computations of multiphase flow. *Journal of Computational Physics*, 169(2):708–759.
- Verhoogen, J. (1951). Mechanics of ash formation. *American Journal of Science*, 249(10):729–739.
- Vogel, A., Busch, S., and Parlitz, U. (1996). Shock wave emission and cavitation bubble generation by picosecond and nanosecond optical breakdown in water. *The Journal of the Acoustical Society of America*, 100:148.
- Vogel, A., Schweiger, P., Frieser, A., Asiyo, M. N., and Birngruber, R. (1990). Intraocular Nd: YAG laser surgery: laser-tissue interaction, damage range, and reduction of collateral effects. *Quantum Electronics, IEEE Journal of*, 26(12):2240–2260.
- Weller, H. G. (1998). A tensorial approach to computational continuum mechanics using object-oriented techniques. *Computers in Physics*, 12:620.
- Woods, A. W. (1995). A model of vulcanian explosions. *Nuclear Engineering and Design*, 155(1–2):345–357.
- Woods, A. W. and Cardoso, S. S. (1997). Triggering basaltic volcanic eruptions by bubble-melt separation. *Nature*, 385(6616):518–520.
- Woods, A. W. and Koyaguchi, T. (1994). Transitions between explosive and effusive eruptions of silicic magmas. *Nature*, 370:641–644.
- Wright, H., Cashman, K. V., Gottesfeld, E. H., and Roberts, J. J. (2009). Pore structure of volcanic clasts: Measurements of permeability and electrical conductivity. *Earth and Planetary Science Letters*, 280(1):93–104.
- Yoshida, S. and Koyaguchi, T. (1999). A new regime of volcanic eruption due to the relative motion between liquid and gas. *Journal of volcanology and geothermal research*, 89(1):303–315.

- Zeidan, D. (2003). *Mathematical and numerical study of two-phase flow models*. PhD thesis, Manchester Metropolitan University.
- Zeidan, D. (2011). Numerical resolution for a compressible two-phase flow model based on the theory of thermodynamically compatible systems. *Applied Mathematics and Computation*, 217(11):5023–5040.
- Zeidan, D., Romenski, E., Slaouti, A., and Toro, E. F. (2007). Numerical study of wave propagation in compressible two-phase flow. *International Journal for Numerical Methods in Fluids*, 54(4):393–417.
- Zeidan, D. and Slaouti, A. (2009). Validation of hyperbolic model for two-phase flow in conservative form. *International journal of computational fluid dynamics*, 23(9):623–641.
- Zein, A., Hantke, M., and Warnecke, G. (2010). Modeling phase transition for compressible two-phase flows applied to metastable liquids. *Journal of Computational Physics*, 229(8):2964–2998.
- Zhang, Y. (1999). A criterion for the fragmentation of bubbly magma based on brittle failure theory. *Nature*, 402:648–650.
- Zhang, Y., Xu, Z., Zhu, M., and Wang, H. (2007). Silicate melt properties and volcanic eruptions. *Reviews of Geophysics*, 45(4).